Modeling gas crossover in alkaline water electrolysers

S. Oikonomidis

TU Delft

Modeling gas crossover in alkaline water electrolysers

by

S. Oikonomidis

to obtain the degree of Master of Science in Mechanical Engineering
at the Delft University of Technology,
to be defended publicly on Monday October 3, 2022 at 9:00 AM.

Student number:	5346088	
Project duration:	December 6, 2021 – October 3, 2022	
Thesis committee:	Dr. Ir. M. Ramdin,	TU Delft, supervisor
	Prof. Dr. Ir. T.J.H. Vlugt,	TU Delft, supervisor
	Prof. Dr. Ir. W. de Jong,	TU Delft
	Dr. A. Rahbari,	XINTC B.V., supervisor

This thesis is confidential and cannot be made public until October 3, 2024.

TU Delft

Preface

This thesis is driven by my belief that sustainable energy will dominate the coming years and hydrogen will play a key role in it. Before starting this thesis, I was unaware of the strengths and weaknesses of alkaline water electrolysis, and the electrochemical processes. I believe that this project helped me to understand some of the fundamentals of alkaline water electrolysis, and not be afraid of the unknown. Finally, I hope that the outcome of this thesis will help XINTC Global in the years to come.

S. Oikonomidis
Delft, September 2022

Acknowledgments

First of all, I would like to express my gratitude to my daily supervisor from XINTC, Dr. A. Rahbari, for the extremely valuable feedback and remarks throughout the thesis project. The countless meetings, especially during the development of the models, made the whole process seem smooth even when I was having a hard time. Your guidance helped me to develop my programming skills and gave me the confidence to finalize this project.

Furthermore, I would like to show my appreciation to my thesis supervisors Dr. Ir. M. Ramdin and Prof. Dr. Ir. T.J.H. Vlugt. Your feedback during our progress meetings helped me to search and understand the mechanisms of gas crossover in greater depth.

I would also like to acknowledge the help of Dr. Ir. A. Bos and Owen Rietman from XINTC. Dr. Ir. A. Bos, helped me to discover the motivation behind this thesis. Owen Rietman helped me in performing the gas crossover experiments and impurity measurements.

I would also like to thank my friends in Greece and Delft, and Ioanna. Your support during the good and bad times that I had, helped me in overcoming the daily difficulties as a master's student.

Last but not least, I would like to express my gratitude to my family in Greece for their unlimited love and support during my master's studies at the Technical University of Delft. This journey would not be possible without you.

S. Oikonomidis
Delft, September 2022

Summary

Climate change due to the extensive use of fossil fuels has led to the deployment of alternative green ones, such as hydrogen. Green hydrogen is produced by renewable electricity and is CO_2-free. This thesis focuses on the production of hydrogen by implementing alkaline water electrolysis as the core technology.

Due to the intermittency of renewable sources, alkaline water electrolysers are forced to operate in their part-load range. The cathodic hydrogen species that remains dissolved in the liquid electrolyte can end up to the anodic compartment, and hence lower the purity of the produced gaseous oxygen. This phenomenon is prominent in the part-load range and is called gas crossover. When the concentration of hydrogen in oxygen reaches the Lower Explosive Limit which is 4 vol%, spontaneous combustion can occur. Therefore, the electrolyser is forced to shut down for safety reasons.

This thesis focuses on understanding the mass transfer mechanisms of gas crossover in alkaline water electrolysis, in the part-load range. A literature study has been conducted in which the gas crossover mechanisms are thoroughly analyzed. The mitigation of gas crossover can lead the operation to lower current density ranges. From the mitigation strategies, a focus is given on the “dynamic switching of the electrolyte cycles”. The dynamic switching of the electrolyte cycles is based on the periodic changeover of the operative electrolyte cycles between the partly-separated and the mixed mode. The anodic hydrogen content acquires a sinusoidal response, where the average value is less than the impurity in traditional operation.

The gas crossover steady-state and dynamic models are mathematically derived and developed in Python. The models consider the mechanisms of gas crossover through the diaphragm and the electrolyte mixing. Therefore, the anodic hydrogen and cathodic oxygen content are calculated in the steady state and dynamically. The dynamic switching of electrolyte cycles can be simulated with the dynamic model.

The experiments are conducted to define the anodic hydrogen and cathodic oxygen content in a single cell configuration. The first experiment outputs the steady-state impurity as a function of the current density. The steady-state impurities show a descending tendency with an increasing current density. Next, the dynamic switching is performed and the anodic hydrogen content is recorded as a function of time. The average impurity in the dynamic switching is smaller than the result in the steady-state experiment.

The steady-state model sufficiently validates the literature data and verifies the experimental results. The dynamic switching model validates the literature data. Furthermore, it verifies the experimental results, when a correction factor is applied to the total volume of the separator tanks. The correction factor is required because the experimental impurities were measured at the exit of the single cell, resulting in a faster system response. Finally, a sensitivity analysis is conducted to test the robustness of the dynamic model. The sensitivity analysis shows that the dynamic model can successfully simulate the operation of an alkaline water electrolyser.

Contents

List of Figures

List of Tables

Nomenclature

Constants

F Faraday's constant 96485, $[\mathrm{C\ mol^{-1}}]$

g Gravitational accelaration 9.81, $[\mathrm{m\ s^{-2}}]$

$M_{\mathrm{H_2O}}$ Molar mass of water 18.01528, $[\mathrm{g\ mol^{-1}}]$

M_{KOH} Molar mass of KOH 56.1056, $[\mathrm{g\ mol^{-1}}]$

n Charge transfer $n = 2$

R Universal gas constant 8.314, $[\mathrm{J\ mol^{-1}\ K^{-1}}]$

Greek symbols

δ_{L} Liquid film thickness, $[\mathrm{m}]$

γ Surface tension of KOH concentrated liquid electrolyte, $[\mathrm{N\ m^{-1}}]$

μ_{L} Dynamic viscosity of KOH concentrated liquid electrolyte, $[\mathrm{Pa\ s}]$

ν_i Stoichiometric number of species i. 1 for hydrogen, 0.5 for oxygen

$\rho_{\mathrm{H_2O}}$ Water density, $[\mathrm{kg\ m^{-3}}]$

ρ_{L} Density of KOH concentrated liquid electrolyte, $[\mathrm{kg\ m^{-3}}]$

τ Tortuosity of the porous media, [–]

θ Electrolyte temperature , $[^{\circ}\mathrm{C}]$

ε Porosity of the porous media , [–]

$\varepsilon^{j}_{\mathrm{g,out}}$ Gas hold-up fraction at the exit of compartment j, [–]

$\varepsilon^{j}_{\mathrm{g}}$ Gas hold-up fraction inside the compartment j, [–]

Other symbols

i Species, H_2 or O_2

j Compartment, anode or cathode

Symbols

$\dot{n}^{j}_{\mathrm{R},i}$ Reaction rate of species i, in the compartment j, $[\mathrm{mol\ s^{-1}}]$

$\dot{V}_{\mathrm{mix}}$ Liquid flow rate under mixed-mode operation, [$\mathrm{m^3\ s^{-1}}$]

$\dot{V}_{\mathrm{G}}^{j}$ Outlet gaseous volumetric flow rate, in the compartment j, [$\mathrm{m^3\ s^{-1}}$]

$\dot{V}_{\mathrm{L}}^{j}$ Inlet liquid volumetric flow rate, in the compartment j, [$\mathrm{m^3\ s^{-1}}$]

A_{d} Area of the diaphragm, [$\mathrm{m^2}$]

A_{el} Electrode area, [m^2]

A_{GL}^{j} Gas liquid interface, in the compartment j, ($\mathrm{m^2}$)

$c_{\mathrm{in},i}^{j}$ Inlet concentration of product i, in the compartment j, [$\mathrm{mol\ m^{-3}}$]

$c_{\mathrm{out},i}^{\mathrm{sep},j}$ Outlet concentration of species i in the gas separator of the compartment j, [$\mathrm{mol\ m^{-3}}$]

$c_{\mathrm{out},i}^{j}$ Outlet concentration of product i, in the compartment j, [$\mathrm{mol\ m^{-3}}$]

$c_{i,\mathrm{H_2O}}^{*,j}$ Equilibrium concentration of species i in pure water, in compartment j, [$\mathrm{mol\ m^{-3}}$]

$c_{i}^{*,j}$ Equilibrium concentration of species i, in compartment j, [$\mathrm{mol\ m^{-3}}$]

c_{i}^{mix} Inlet mixed-mode concentration of species i, [$\mathrm{mol\ m^{-3}}$]

d_{d} Thickness of the diaphragm, [m]

d_{b}^{j} Diameter of bubble in compartment j, [m]

$D_{i,\theta}$ Molecular diffusivity of species i, at temperature θ, in the KOH concentrated liquid electrolyte, [$\mathrm{m^2\ s^{-1}}$]

D_{i}^{eff} Effective diffusivity of species i, [$\mathrm{m^2\ s^{-1}}$]

$f_{\mathrm{G},i}$ Gas evolution efficiency of species i [–]

$h_{\mathrm{liq}}^{\mathrm{sep},j}$ Liquid volume fraction in the gas separator of the compartment j, [%]

H_i Henry's coefficient of species i, [atm]

J Applied current density, [$\mathrm{A\ m^{-2}}$]

$k_{\mathrm{L},i}^{j}$ Mass transfer coefficient of the gas-liquid film of species i, in compartment j, [$\mathrm{m\ s^{-1}}$]

$K_{\mathrm{S},i}$ Setchenov constant of species i, [–]

m Molality of KOH , [$\mathrm{mol\ kg^{-1}}$]

$N_{\mathrm{cross},i}$ Crossover flux of species i through the diaphragm, [$\mathrm{mol\ m^{-2}\ s^{-1}}$]

N_{M} MacMullin number, [–]

$N^{j}_{\mathrm{phys},i}$ Physisorption mass flux of species i, in the compartment j [$\mathrm{mol\ m^{-2}\ s^{-1}}$]

$N^{j,\mathrm{sep}}_{i,\mathrm{gas}}$ Moles of species i in the gaseous volume of gas separator of the compartment j, [mol]

$N^{j}_{i,\mathrm{gas}}$ Moles of species i in the gaseous volume of compartment j, [mol]

$N^{j,\mathrm{sep}}_{i,\mathrm{liq}}$ Moles of species i in the liquid volume of gas separator of the compartment j, [mol]

$N^{j}_{i,\mathrm{liq}}$ Moles of species i in the liquid volume of compartment j, [mol]

$p_{\mathrm{H_2O}}$ Water vapour partial pressure, [Pa]

p^{j} Pressure exerted on the liquid electrolyte by means of a pump in compartment j, [Pa]

$p^{j}_{\mathrm{in},i}$ Inlet partial pressure of species i in the compartment j, [Pa]

$p^{\mathrm{sep},j}_{\mathrm{out},i}$ Outlet partial pressure of species i in the gas separator of the compartment j, [Pa]

$p^{j}_{\mathrm{out},i}$ Outlet partial pressure of species i in the compartment j, [Pa]

p^{j}_{tot} Total pressure in the compartment j, [Pa]

R_{v} Volume ratio of the gas separator to the half-cell, [-]

Re^{j} Reynolds number in compartment j, [$-$]

$S_{\mathrm{b}}{}^{j}$ Surface area of a single bubble in compartment j, [$\mathrm{m^2}$]

Sc_i Schmidt number of species i, [$-$]

Sh^{j}_{i} Sherwood number of species i, in compartment j, [$-$]

T Temperature, [K]

t_{switch} Switching time, [min]

t_{tot} Total time of the experiment, [h]

u_{rs} Rising swarm velocity , [$\mathrm{m\ s^{-1}}$]

u_{r} Rising velocity of a single bubble, [$\mathrm{m\ s^{-1}}$]

V_{b} Volume of a single bubble in compartment j, [$\mathrm{m^3}$]

V_{hcell} Geometrical volume of the half cell, [$\mathrm{m^3}$]

$V^{\mathrm{sep},j}_{\mathrm{gas}}$ Gaseous volume inside the gas separator of its associated compartment j, [$\mathrm{m^3}$]

$V_{\text{gas}}^{\text{tot},j}$ Gaseous volume of the half-cell and the gas separator of compartment j, [L]

V_{gas}^{j} Gaseous volume inside the compartment j, [m^3]

$V_{\text{liq}}^{\text{sep},j}$ Liquid volume inside the gas separator of its associated compartment j, [m^3]

$V_{\text{liq}}^{\text{tot},j}$ Liquid volume of the half-cell and the gas separator of compartment j, [L]

V_{liq}^{j} Liquid volume inside the compartment j, [m^3]

V_{sep}^{j} Geometrical volume of the gas separator of its associated compartment j, [m^3]

w_{KOH} Mass fraction of potassium hydroxide in the electrolyte solution, [$-$]

$y_{\text{H}_2}^{\text{avg,mod}}$ Average calculated anodic hydrogen content, [vol%]

$y_{\text{H}_2}^{\text{avg}}$ Average experimental anodic hydrogen content, [vol%]

y_i Purity of species i, expressed as volume fraction fraction , [vol%]

1 Introduction

In this chapter, the motivation of the thesis is given. More specifically, the social-economic background necessitating the swift towards green hydrogen production is presented. The motivation is focused on Dutch society, but also provides some policies decided by the European Commission. Finally, the research questions are provided.

1.1. Motivation

Global warming is one of the greatest challenges of the 21st century [1]. It can be attributed to greenhouse gas (GHG) emissions that trap the heat in the atmosphere and cause the temperature to rise [2]. Some of the most well-known GHG are carbon dioxide (CO_2), methane (CH_4), nitrous oxide (N_2O), and fluorinated gases [2]. The emissions of GHG are due to the natural systems (e.g., forest fires, volcanoes, oceans) as well as the anthropogenic activity [3]. The anthropogenic activity consists of all the human activities which result in CO_2 emissions mainly from the combustion of fossil fuels and cement production. According to [3], the biggest contributor to GHG is anthropogenic activity accounting for 47.9-66.6% of the total global emissions. In addition, over the last century, the vast industrialization of modern societies resulted in a gradual increase of the global CO_2 emissions through the usage of fossil fuels [4]. Therefore, for a reduction in GHG emissions to occur, a transition from fossil fuels to sustainable ones is required.

Over the last years, a lot of transnational policies have been developed on decarbonizing energy-intense human activities. Among others, the most important include the Paris Agreement [5], and the European Green Deal [6]. Briefly, the Paris Agreement aims at limiting the temperature increase threshold to 1.5°C above pre-industrial levels. The European Green Deal is aligned with the Paris Agreement and aims for a “prosperous, modern, competitive and climate-neutral economy by 2050” by reducing carbon emissions by 49 - 55% in 2030 and by 80 - 95%, below 1990 levels. The Dutch government has committed to adopting the European Green Deal and meeting its goals [7].

1.1.1. Decarbonization initiatives in the Netherlands

Ambitious and innovative political decisions are required for such targets to be met. For the Dutch Government, the goals of the Paris Agreement are envisioned in the National Climate Agreement (Klimaat-en Energieverkenning, KEV) [8]. This report depicts the focus of the Dutch Government to decarbonize a series of anthropogenic activities. More specifically, the Government focuses on the decarbonization of the Built Environment, the Mobility Sector, the Industry Sector, the Agricultural Sector, and the Electricity Sector. Through the implementation of a large variety of technological solutions, it is expected to reach the goals referred to previously. Such solutions include sustainable heating sources (e.g., biomass, power to heat, and sustainable gases), the increase of the heavy fuel cell vehicles, and sustainable energy carriers along with the required infrastructure (e.g., refueling stations). In addition, it is expected that the transition to zero emissions in the Industry Sector will be accompanied by the application of Carbon Capture and Storage (CCS), and the extensive usage of hydrogen. In the Electricity Sector, besides the continuous installation of wind turbines in the North Sea, is also expected the conversion and storage of electricity into sustainable energy carriers including biogas and hydrogen. Consequently, from all the considerations above, it becomes clear that hydrogen will play a crucial role as a carbon-free energy carrier and feedstock for the Process Industry and the Mobility Sector during the next decades.

1.1.2. Hydrogen, the key element to the energy transition

The term hydrogen has its roots in the Greek language where ‘hydro’ means water, and ‘-gen’ means formation. The hydrogen molecule acquired its name due to the water formation upon its combustion. For that reason, the scientific community and the policymakers emphasize its adaptation as an energy carrier and feedstock towards net zero, not only in the Netherlands but in the whole European Union and globally [9–11]. However, hydrogen production may result in CO_2 emissions depending on the production technology used. Therefore, hydrogen can be categorized in different color shades depending on the production method [11].

Grey Hydrogen: It is produced via Steam Methane Reforming (SMR) or gasification when the feedstock is methane or coal. These methods emit a significant amount of CO_2 into the atmosphere via the previously mentioned fossil fuels. However, at the moment, they are the most cost-effective processes. Steam methane reforming is an endothermic reaction that produces H_2 and CO (Reaction 1.1). Subsequently, in the water-shift reaction, carbon monoxide and steam react and produce hydrogen and CO_2 (Reaction 1.2).

$$\mathrm{CH_4 + H_2O\,(+heat) \longrightarrow CO + 3H_2} \tag{1.1}$$

$$\mathrm{CO + H_2O \longrightarrow CO_2 + H_2\,(+heat)} \tag{1.2}$$

Blue Hydrogen: It is produced in the same way as grey hydrogen. However, CCS is additionally applied to reduce the CO_2 emissions. Experts claim [11], that the production method of blue hydrogen will be the transition technology towards net-zero because the pre-existing industrial facilities could retrofit CCS units to reduce the emissions. However, there will be 5-15% of CO_2 that will still be emitted into the

atmosphere making blue hydrogen unsuitable in the long term.

Turquoise Hydrogen: This production method uses Methane as feedstock, and by applying the pyrolysis process hydrogen is produced in the gaseous phase, and the carbon becomes solid carbon black. The storage of carbon black is much easier than gaseous CO_2 and at the same time there is a market that it can be sold. However, the production method of turquoise hydrogen is still at the experimental stage. The production of turquoise hydrogen is given by reaction 1.3.

$$\mathrm{CH_4\,(+heat)} \longrightarrow \mathrm{C_{(s)}} + 2\mathrm{H_2} \tag{1.3}$$

Green Hydrogen: It contains the term green because renewable electricity is used to produce hydrogen via the application of the water-splitting reaction in the electrolysis process (reaction 1.4). Green hydrogen meets all the suitability criteria for the realization of the energy transition, as its production does not give rise to CO_2 emissions, if the carbon intensity of the used electricity is zero.

$$\mathrm{H_2O} \longrightarrow \mathrm{H_2} + 0.5\mathrm{O_2} \tag{1.4}$$

This discussion leads to the conclusion that green hydrogen will be the key element for the energy transition. The market analysts claim that the global energy share of green hydrogen will reach 24% in 2050, and the European Union plans to reach 40 GW of electrolysers by 2030 by producing cost-effectively 10 million tons of green hydrogen [10]. The Netherlands plans to have a prominent role in the European Union as a key player in the green hydrogen production by taking advantage of the significant wind potential in the North Sea, which will be the first Hydrogen Valley in Europe [9]. Moreover, there are many projects between the Dutch industry and scientific institutions focusing on the scale-up of hydrogen applications. However, several requirements need to be addressed for the extensive application of Green Hydrogen to take place.

First, for green hydrogen to be more widely produced, low variable renewable energy (VRE) electricity costs are required. The electricity price is a crucial factor for the production cost of green hydrogen. In addition, there must be investment decisions in the lab-developed electrolysis technologies which could scale up. This fact could enable the reduction in the electrolysis capital expenditures (CAPEX), which have been reduced by 60% since 2010 [11]. Moreover, the rise of VRE sources over the last decades has enabled the requirement for a more flexible power grid. Due to the intermittency of renewable sources, there are fluctuations in the power system. Therefore, the electrolysers need to be able to immediately adjust to the grid-induced fluctuations by increasing or reducing their production. In such a way, the produced green hydrogen can be stored for long periods and can be used as an energy carrier when there is a lack of VRE sources.

Moreover, even if the requirements described above will be fulfilled, there are major bottlenecks. The most important one is the high production cost of green hydrogen. For example, even though the electricity price from onshore wind descended from 75 USD/MWh in 2010 to 48 in 2018, the production of green hydrogen from VRE sources is 2.5-5.5 €/kg while for grey hydrogen it is 1.5 €/kg depending on the natural gas price [10]. In addition, there is a lack of hydrogen infrastructure. Currently, the total length of dedicated hydrogen pipelines does not exceed 5000 km, while for natural gas this

length exceeds 3 million km [11]. The last major bottleneck is the energy loss in hydrogen production through the electrolysis process and in every subsequent conversion of hydrogen in the value chain. Currently, there are 30-35% energy losses in the electrolysis of water for hydrogen production [11]. If hydrogen is further converted into other energy carriers, such as ammonia, there will be 13-25% more losses.

1.2. XINTC B.V.

The literature review and the main thesis project are conducted in collaboration with XINTC B.V., a Dutch start-up company. XINTC produces, and markets Alkaline Water Electrolysers as an Original Equipment Manufacturer (OEM). Therefore, the thesis will be focused on alkaline water electrolysis. The company offers standardized components instead of customized engineered solutions. The capacity of the electrolysers falls in the spectrum of 150 kW to 50 MW making them suitable for middle-range hydrogen applications. Middle-range hydrogen applications are defined as those which are focused on the built environment, mobility sector, and electricity sector. The electrolyser is comprised of gas modules which are interconnected and controlled with electronics.

Electrolysers are delivered together with the balance of plant in the form of containerized solution, delivering hydrogen from 1 to 30 bar. Moreover, they are manufactured with low-cost materials which are abundant in nature to reduce their CAPEX and Operative Expenditures (OPEX). Finally, they have been designed to operate in optimum conditions to maximize their efficiency. As a result, the production cost of hydrogen will be lowered. Finally, due to the lower CAPEX and OPEX, the total cost of ownership (TOC) will be lower.

1.3. Research Questions

The intermittency of renewables results in fluctuations in the power grid. In such conditions, the electrolysers must be able to operate in the part-load range to produce green hydrogen. Normally, the part-load range varies from 20-40% of their nominal load [12]. During the water electrolysis process in the part-load range, produced hydrogen species can be contaminated by oxygen, or the opposite, resulting in the creation of an explosive atmosphere. This contamination is often called gas crossover and is more significant under the part load operational range. When the alkaline water electrolysers operate close to their nominal load range, the gas crossover becomes significantly smaller [12].

The explosive atmosphere is created because the hydrogen-oxygen mixture can lead to spontaneous combustion if the concentration of the contaminating species reaches 4 vol%, which is the Lower Explosive Limit (LEL) [13]. Therefore, when the electrolysers operate in the part-load range, such fluctuations can introduce risks for their safe operation and are forced to shut down. Typically, they shut down when the concentration of impurity reaches 2 vol%, which is 50% of the LEL [14]. In addition, due to the contamination of hydrogen, the resulting gas purity will be reduced as will the overall efficiency of the process. Furthermore, the deactivation of the electrolyser results in financial losses due to the lack of production. Therefore, the scope of this thesis is depicted on the following research questions:

1. *Which are the factors that affect the gas purity of the produced gases in alkaline water electrolysis?*

2. *How can the performance of alkaline water electrolysers, in terms of gas purity, be improved?*

3. *How can the gas purity of alkaline water electrolysers be modeled?*

4. *How can the operating conditions of the process affect the response of the gas purity?*

5. *How can the design characteristics of the system affect the response of gas purity?*

1.4. Thesis outline

To tackle the research questions an extended literature study is conducted. During the literature study, the mechanisms that result in the gas nucleation, growth and detachment are studied. Furthermore, due to the mass transfer limitations, the crossover mechanisms that lead to the purity decline of the product are considered. As a result, a steady-state and dynamic model are developed in Python. These models consider all the aforementioned phenomena. The models are validated with experimental data from the literature, and are compared to experimental data of XINTC. Moreover, in the literature study, in order to reduce the impurity of the produced gases, an alternative operating concept is suggested. This alternative concept is called the dynamic switching of electrolyte cycles. The dynamic switching of electrolyte cycles is tested experimentally and validated by the developed dynamic model. Overall, the proposed thesis outline is the following:

- In *Chapter* 2, a literature study is presented. During the literature study, a brief introduction to the state-of-the-art electrolysis technologies occurs. Next, the mass transfer mechanisms in gas evolving electrodes are analyzed. The mass transfer limitations are the primary sources of gas crossover which are thoroughly analysed for the alkaline water electrolysis. Finally, alternative operating concepts are proposed.

- In *Chapter* 3, the gas crossover model is presented. The model assumptions and the simplified process flow diagram are introduced. The general form of the steady-state and dynamic mass balances is shown. The unknown terms in the mass balances are mathematically expressed by implementing the boundary conditions, empirical correlations, and known fluid dynamics relations. As a result, the final form of the steady-state and dynamic material balances is proposed.

- In *Chapter* 4, the gas crossover experiments are presented. The experimental setup of XINTC is introduced. Next, the experimental results for the steady-state case are shown. Finally, the results of the dynamic switching experiment are analyzed.

- In *Chapter* 5, the developed models are validated with experimental results from the literature. The steady-state and dynamic models are compared with the experimental results from Chapter 4. Finally, a sensitivity analysis is conducted in order to test the robustness of the dynamic model.
- In *Chapter* 6, the closing discussion of the thesis is presented. The conclusions of the thesis are shown. Finally, future recommendations for the developed model are proposed.

2

Literature Study

In this chapter, the literature study is conducted. To approach the research questions, firstly a description of the commercial electrolysis technologies is given. Then, the mass transfer mechanisms which result in the production of the gaseous product and dissolved species in gas evolving electrodes are analyzed. Furthermore, due to the mass transfer limitations, the gas crossover mechanisms in alkaline water electrolysis are described. Finally, the strategies to reduce the gas crossover, as well as the modeling research in alkaline water electrolysis are presented.

2.1. Electrolysis technologies

In this section, a short description of the components and the working principles of the current commercially available water electrolysis technologies for hydrogen production will be given. Firstly, the Alkaline Water Electrolysis (AWE), which is the most mature and robust technology, will be described. Then, the Proton Exchange Membrane Electrolysis (PEM), the Anion Exchange Membrane (AEM) water electrolysis, and the Solid Oxide Electrolysis (SOEC) will be described. Finally, the current research trends on state-of-the-art electrolysis technologies will be presented.

2.1.1. Alkaline water electrolysis

The Alkaline Water Electrolysis (AWE) is the most mature and robust electrolysis technology. The first AWE was demonstrated by Van Troostwijk and Deinman in 1789 [15]. The electrolysis cell consists of two porous electrodes, namely the anode and the cathode. The porous plates are made of non-noble metals which are abundant in nature, such as nickel, iron, or cobalt, and they can be flat, perforated, or consist of wired mesh. The anode and cathode are immersed in a strong liquid alkaline electrolyte which is either potassium hydroxide KOH, or sodium hydroxide NaOH and provides the required ionic conductivity between the electrodes. The KOH concentration ranges from 20 wt% to 40 wt% in a temperature range of 60 – 90 °C [12].

The anode and the cathode are separated by a porous solid diaphragm. The role of the diaphragm is to avoid the gas crossover of the evolved gases and to allow the required conduction of hydroxide ions from the cathode to the anode. The selection of the diaphragm constitutes one of the most important design criteria since its thickness,

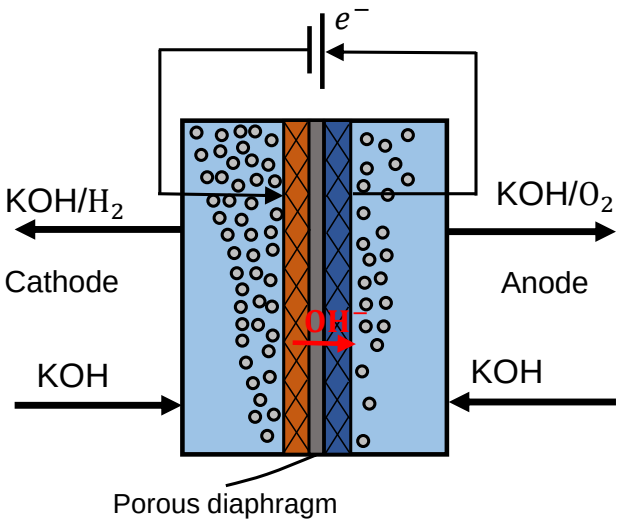

Figure 2.1: Schematic of a zero-gap alkaline water electrolyser. Liquid electrolyte containing KOH, enters the system. The application of DC power results in gaseous H_2 and OH^- ions at the cathode, and gaseous O_2 and H_2O at the anode. OH^- ions are conducted through the diaphragm. The mixture exits the half-cells with the liquid electrolyte. *Orange*: Cathodic electrode. *Blue*: Anodic electrode.

ionic conductivity, and gas permeation influence the ohmic drop and the permeation of the dissolved gases, and thus the overall efficiency of the electrolyser [16]. One example of a commercial type of diaphragm for alkaline water electrolysis is the “Zirfon PERL UTP 500” which is manufactured by Agfa and consists of Zirconium oxide (zirconia) and polyphenylene sulfide fabric, with 500 µm thickness [17].

The latest trend in the design of Alkaline Water Electrolysers is the zero-gap configuration (Figure 2.1). In zero-gap designs, the porous electrodes are pressed directly onto the diaphragm, thus reducing the interelectrode gap from 2 mm in traditional electrolysers to less than 0.5 mm [18]. The reduction of the interelectrode gap results in lower ohmic resistance of the electrolyte between the electrodes, and consequently in higher overall efficiency.

The water decomposition during alkaline electrolysis is based on the following half-reactions, and their standard potential in comparison with standard hydrogen electrode (SHE) at T=298.15 K [19] :

$$\text{Cathode}: \quad 2H_2O + 2e^- \longrightarrow 2OH^- + H_2, \qquad E^o = -0.83V \tag{2.1}$$

$$\text{Anode}: \quad 2OH^- \longrightarrow 0.5O_2 + H_2O + 2e^-, \qquad E^o = 0.4V \tag{2.2}$$

$$\text{Overall Reaction}: \quad H_2O \longrightarrow H_2 + 0.5O_2, \qquad E^o = -1.23V \tag{2.3}$$

When DC potential is applied in the configuration that is shown in Figure 2.1, H_2O molecules are reduced at the cathode and H_2 with OH^- ions are produced. This reaction (2.1) is often called the hydrogen evolution reaction (HER). At the same time, hydroxide ions are conducted via the diaphragm on the anode side, where they are subject to the oxidation reaction, and they lose electrons (2.2). As a result, oxygen and water molecules are produced. This reaction is often called the oxygen evolution reaction (OER). From the reactions (2.1) – (2.3), it can be observed that the electrolyser requires a minimum potential difference of 1.23 V. This is the minimum potential

required for water decomposition and is often called the reversible potential. In realistic applications, electrolysis of water will always require a higher potential for hydrogen production to be applied due to the existence of overpotentials (i.e., diaphragm resistance, bubble resistance).

One major advantage of alkaline water electrolysers is the fact that they consist of cheap and abundant materials in nature. As a result, there is an ease in scaling up this technology and a lot of ongoing research takes place. On the other hand, the existence of porous diaphragms does not allow the differential pressure operation between the half cells, because there will be gas crossover through the diaphragm via convective mass transfer [20]. In addition, during part-load operation, the alkaline electrolysers are subject to gas crossover which will be analyzed later. Usually, alkaline water electrolysers do not operate above 90°C because the diaphragm can be degraded and pose threats to the safe operation of the system. Finally, the operation of the alkaline electrolysers is limited to a low current density range 2-4 $\mathrm{kA} \cdot \mathrm{m}^{-2}$ [21].

2.1.2. Proton exchange membrane water electrolysis

To solve the disadvantages of AWE, the concept of proton exchange membrane (PEM) Water Electrolysers was firstly introduced in the 1960s by General Electric [21]. The idea behind PEM Electrolysis is that the electrolyte is not liquid but consists of a solid polymer electrolyte membrane. The PEM water electrolysers operate in a temperature range of 50 - 80°C and a higher current density range 6-20 $\mathrm{kA} \cdot \mathrm{m}^{-2}$, thus allowing higher hydrogen production, and more compact electrolysers than the AWE. The most usual type of membrane for PEM water electrolysis is the Nafion membrane manufactured by DuPont which has a much lower thickness (20-300 μm) than the Zirfon diaphragm. As a result, due to their small membrane thickness, the PEM electrolysers can have better conductivity, and lower gas crossover due to smaller pore diameter, thus allowing the differential pressure operation between the half cells. However, the fact that the working environment of PEM electrolysers is highly acidic requires the implementation of noble, rare, and expensive catalysts for the electrodes. Usually, the electrodes are manufactured from Ruthenium, Platinum, or Iridium. For example, Iridium is one of the rarest elements on Earth and it has been reported to have an average mass fraction of 0.001 ppm in crustal rock [21]. As a result, the scalability of the PEM electrolysers is questioned, since an increase in the demand for these metals could skyrocket the cost of PEM electrolysers, and consequently the hydrogen production cost.

The water decomposition during PEM water electrolysis (Figure 2.2) occurs via the following half-cell reactions:

$$\text{Cathode}: \quad 2\mathrm{H}^{+} + 2e^{-} \longrightarrow 2\mathrm{H}_2 \tag{2.4}$$

$$\text{Anode}: \quad \mathrm{H}_2\mathrm{O} \longrightarrow 2\mathrm{H}^{+} + 0.5\mathrm{O}_2 + 2e^{-} \tag{2.5}$$

When DC voltage is supplied and electrolysis starts, hydrogen protons cross the membrane, where they are reduced into hydrogen molecules (2.4). At the anode, the supply of deionized water leads to the occurrence of the oxidation reaction (2.5). As a result, oxygen with water leave the anodic half-cell, and hydrogen protons are produced.

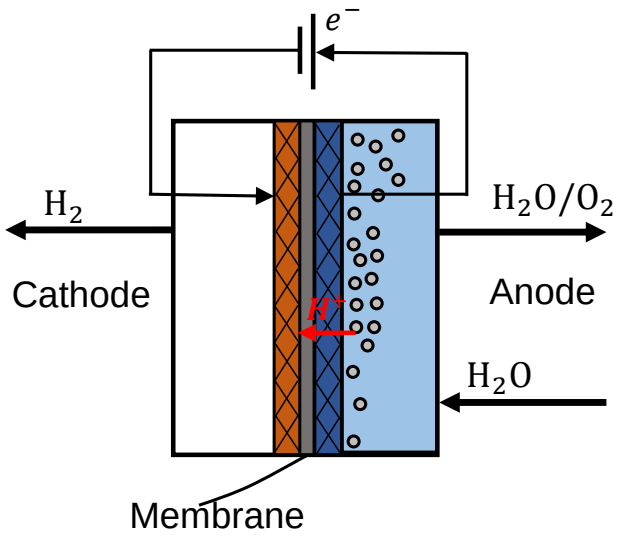

Figure 2.2: Schematic of a PEM water electrolyser. Deionized H_2O is supplied to the anode. During the electrolysis the H^+ protons are conducted to the cathode where they are reduced into H_2 molecules. At the anode, water is oxidized into H^+ protons and O_2 molecules. PEM water electrolysers can operate in a high current density range, and liquid electrolyte is not required.

2.1.3. Anion exchange membrane water electrolysis

The Anion Exchange Membrane (AEM) water electrolysis is an alternative technology to produce hydrogen, by combining the advantages of both the PEM water electrolysis and the AWE [22]. More specifically, the development of AEM water electrolysis focuses on the deployment of non-noble electrocatalysts due to the alkaline nature of the process, and the operation with high differential pressures between the half-cells. Furthermore, the operation focuses on low concentration liquid electrolyte which consists of KOH, NaOH, $\mathrm{K_2CO_3}$ or DI water. Schematically, an AEM water electrolyser is shown in Figure 2.3. The AEM water electrolyser consists of the membrane electrode assembly (MEA). The MEA is the core of this technology and includes the anion exchange membrane, and the electrocatalysts which are sprayed on the surface of the membrane. The layer which is sparayed on the anodic side is called anode catalyst layer (ACL), and the layer which is sprayed on the cathodic side is called cathode catalyst layer (CCL).

The anion exchange membrane consists of anion exchange functional groups which are embedded on a polymer backbone. The polymer backbone is fabricated from polysulfone (PSF) or polysterene cross linked with divinylbenzene (DVB), and the ion exchange groups are $-\mathrm{NH_3^+}$, $-\mathrm{RN_2^+}$, $=\mathrm{R_2N^+}$, $-\mathrm{R_3P^+}$, $-\mathrm{R_2S^+}$ or quaternary ammonium salts [22]. The function of the AEM is to hinder the cross permeation of the gaseous produced species, and the provision of ionic conductivity for the hydroxide ions. The AEM must also have satisfactory mechanical, thermal, and chemical stability. One commercial AEM is the A-201 membrane which is produced by Tokuyama Corporation [23]. Furthermore, PSF ionomers are used in AEM to provide access for transport between the catalyst layers, where the reactions take place, and the membrane.

Regarding the electrocatalysts, there is a lot of research to avoid Ir and Pt based electrocatlysts [22]. Currently the research is focused on deploying Ni-Fe and Ni-Mo electrocatalysts. The Ni-Fe alloy is suitable for the OER, and the Ni-Mo alloy is suitable for HER. A commercial solution for non-noble electrocatalysts is the Acta 4030 ($Ni/CeO_2 - La_2O_3/C$) for HER , and the Acta 3030 ($CuCoO_x$) for OER, manufactured by Acta SpA.

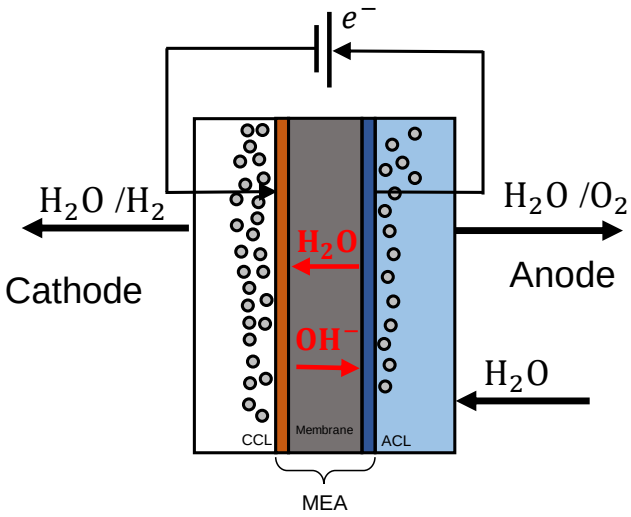

Figure 2.3: Schematic of an AEM water electrolyser. Water with a low KOH concentration is supplied to the anodic compartment. The H_2O molecules are transferred to the cathode where they are reduced to H_2 molecules and OH^- ions. The OH^- ions are conducted to the anode where they are oxidized to O_2 and H_2O. At the exit of the cathode, the produced H_2 species remains ”wet”. The H_2O and O_2 mixture exits the anode for further processing.

The half-cell reactions and the overall reaction which take place during AEM water electrolysis obey the reactions (2.1) – (2.3). During the operation of an AEM water electrolyser, water with 1M KOH is recirculated in the anodic half-cell. The anodic side of the membrane remains soaked with water, while the cathodic side of the membrane remains dry. The water molecules are transferred through the membrane and are reduced to produce hydrogen in the cathodic side, according to reaction (2.1). At the same time, hydroxide ions are transferred to the anodic side, due to the attractive forces. In the ACL, the hydroxide ions are recombined to produce water and oxygen. The hydrogen produced in the cathodic side contains moisture due to water and needs to be further processed after the reaction. AEM water electrolysers operate between 50-70°C. The discharge pressure of hydrogen can be up to 30 bar and the current density range is $2 - 5\ \mathrm{kA\ m^{-2}}$ [22].

Nonetheless, the AEM water electrolysis is mainly in R&D phase. The first attempt to commercialize an AEM water electrolyser was made viable by Enapter in 2018 [24]. In general, the main obstacle in the AEM water electrolysis is the chemical and mechanical stability of the membranes. In Ref. [22] it is reported that a possible reason for the instability of the AEM involves the degradation of the polymer backbone or the ion exchange functional groups. Furthermore, the AEM has lower conductivity than the PEM. As a result potassium hydroxide is required for better ionic conductivity. The usage of DI water results in higher resistances than in the PEM water electrolysis.

Finally, the development of AEM electrolysers that implement non-noble electrocatalysts, show slow progress.

2.1.4. Solid oxide electrolysis cells

The implementation of Solid oxide electrolysis cells (SOECs) could be advantageous when coupled to industrial processes with large amounts of waste heat. Typically, the commercial SOECs operate at 800-1000°C and the reason is that the thermodynamics, the kinetics, and the ion conduction are most favorable for the HER in this range of temperatures [25]. More specifically, the total energy demand (ΔH) for hydrogen production significantly reduces at 100°C, and then, it remains almost constant. Furthermore, for hydrogen production at 800-1000°C, the supplied heat energy continuously increases ($T\Delta S$) and hence, the electric energy demand (ΔG) lowers. As a result, the implementation of SOECs could lead to lower hydrogen production costs when there is sufficient waste heat available. Normally, the electrolyte material for the state-of-the-art commercial SOECs is the yttria-stabilized zirconia (YSZ). YSZ is used for the conduction of oxygen ions. One disadvantage of the SOECs which operate in this temperature range is the degradation and the instability of the electrolyte in the long term. The working principle of a SOEC with a YSZ electrolyte is depicted in Figure 2.4.

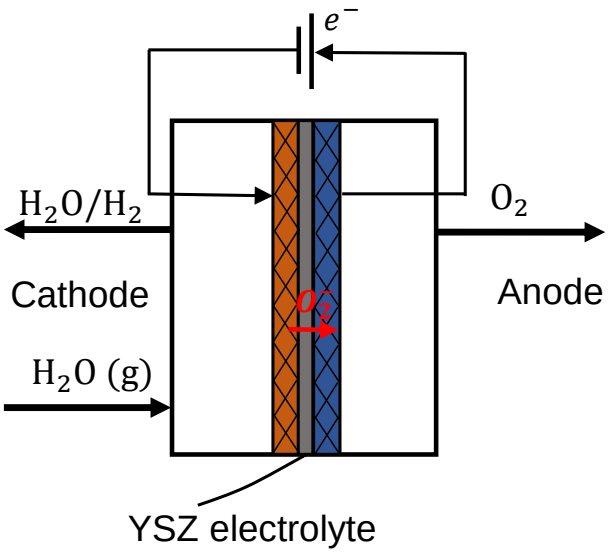

Figure 2.4: Schematic of a SOEC electrolyser. Steam at 800-1000°C is supplied to the cathode. The application of DC power results in the reduction of steam to H_2 molecules and O^{-2} ions. The O^{-2} ions are conducted to the anode where oxygen is extracted. At the exit of the cathode, a mixture of steam and H_2 exits the compartment for further processing.

The half-reactions which take place in SOECs are the following:

$$\text{Cathode}: \quad H_2O + 2e^- \longrightarrow H_2 + O^{2-} \tag{2.6}$$

$$\text{Anode}: \quad O^{2-} \longrightarrow 0.5O_2 + 2e^- \tag{2.7}$$

Firstly, steam at 800 - 1000°C is supplied at the cathodic electrode. When the required voltage is applied, electrolysis of the water starts taking place. More specifically, the

water molecules are reduced into hydrogen molecules and oxygen ions (2.6). Then, the oxygen ions cross the YSZ electrolyte and reach the anode side where oxygen is extracted (2.7).

2.1.5. Current research trends on the state-of-the-art electrolysers

In this subsection, the recent research trends for each of the water electrolysis technologies will be presented briefly.

In AWE, research conducted by Schalenbach et al. [20] has shown that the development of diaphragms with thickness in the same order of magnitude with PEM electrolysers could enhance the overall efficiency of AWE. Moreover, there is ongoing research in the development of anion exchange membranes [22] and ion solvating membranes [26] for AWE. The application of the aforementioned membranes could avoid or significantly reduce the implementation of strongly concentrated KOH electrolyte, and consequently, reduce the gas crossover. However, anion exchange membranes have poor stability and a much lower lifetime than the Zirfon diaphragm.

In PEM electrolysis [21] there is a lot of ongoing research on the development of IrO_2 mixtures as electrocatalysts to mitigate the slowness of the OER. At the same time, the developed electrocatalysts need to be unaffected by the acidic environment of PEM electrolysis. Furthermore, alternative electrocatalysts are investigated for the HER. Typical examples include the investigation of MoS_2 and Pd/CNTs. Finally, there is ongoing research focused on the membranes for cost reduction and the improvement of their mechanical stability.

Finally, even though the SOEC is relatively a new technology there are some projects which will be commercialized [27]. Hauch et al. [28] have reported that the performance of SOEC has increased more than a factor of 2.5 over the last years. Furthermore, the degradation of SOEC electrolysers has been reduced by more than a factor of 100. The ongoing research is mainly focused on the development of more robust and durable electrodes in the long term [28]. When high overpotentials are applied, the Ni network closest to the electrolyte is destroyed and leads to Ni migration in the support layer. As a result, the electrochemical performance is reduced.

2.2. The sources of gas crossover in alkaline water electrolysis

To understand how gas crossover occurs, it is important to consider the mass transfer mechanisms that take place in the half cell and enhance the nucleation, growth, and detachment of the gas bubbles. The mass transfer mechanisms which are analyzed in the following sections are limited to the electrode-electrolyte interface and the bulk electrolyte in the half cell. As a result, the mass transfer mechanisms induce properties and phenomena which are important for the material balance equations that will be presented in Chapter 3.

2.2.1. Prerequisites for gas evolution in gas-evolving electrodes

The electrodes which are immersed in a liquid electrolyte define a two-phase system, since the electrode is solid, and the electrolyte is liquid. When a current is applied to the electrode, bubbles start forming, and gaseous hydrogen is produced. For that

reason, they are defined as gas-evolving electrodes, and the electrode region now becomes a three-phase system.

It is a misconception that the production rate at which species are formed in the electrode region, and obey Faraday's law, is equal to the amount of the product in the gaseous phase. Initially, when the electrochemical reactions take place, the product is transported into the electrode-electrolyte interface in dissolved form. For the transition in the gaseous phase upon the initiation of the electrolysis, several prerequisites exist [29]. More specifically, the operating conditions such as the temperature, pressure, and current density in which the electrolysis takes place are the most basic ones. In addition, the existence of nucleation sites on the solid surface of the electrodes is required. Such nucleation sites exist due to the irregularities on the electrode surface. As a result, gas evolution occurs at these sites due to heterogeneous nucleation.

Another important requirement for gas formation is the existence of supersaturation on the electrode region [30]. The concentration of the dissolved species in the electrolyte at the electrode region must deviate from the equilibrium concentration for the transition in the gaseous phase to start occurring. Typically, this is the case for hydrogen gas evolution since its solubility in strongly concentrated electrolytes is very low. The required supersaturation also strongly depends on the electrode material, its wettability, and the applied current density.

2.2.2. The mass transfer mechanisms on gas-evolving electrodes

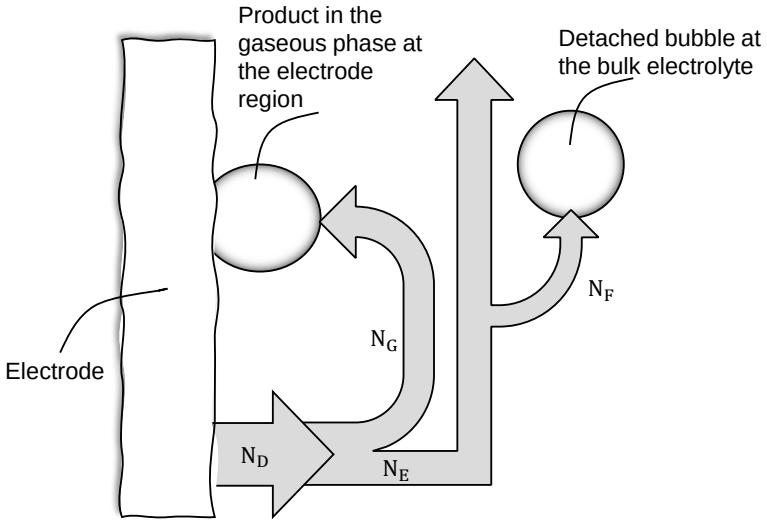

Figure 2.5: Mass transfer mechanisms during alkaline water electrolysis. When DC power is supplied to the electrode, the whole product dissolves in the liquid electrolyte, in the concentration boundary layer of the electrode (Flux N_D). The production rate obeys Faraday's law. Due to the supersaturation in the concentration boundary layer, an amount of the product is subjected to desorption (Flux N_G). Due to the combined effect of diffusion and convection, the rest of the product remains dissolved and is transferred to the electrolyte bulk (Flux N_E). Due to supersaturation in the electrolyte bulk, an amount of the dissolved product desorbs to the detached bubbles (Flux N_F). The rest of the product remains dissolved and exits the electrolysis cell.

Upon the initialization of electrolysis, the product is transferred to the electrolyte-electrode interface in dissolved form. Subsequently, a fraction of the dissolved hydrogen is transferred to the gaseous phase (see Figure 2.5). The amount of the dissolved species which are transported into the gas phase at the electrode region depends on the mass transfer mechanisms which take place when electrochemical reactions start. These mass transfer mechanisms can act on the electrode's boundary layer [29–32].

When the electrochemical reactions take place the reaction product is transferred to the electrode-electrolyte interface in dissolved form according to Faraday's Law (Figure 2.5). This overall production flux density of dissolved species is denoted with N_{D} and is equal to:

$$N_{\mathrm{D}} = \frac{J\nu_i}{nF} \tag{2.8}$$

Where J is the current density, ν_i is the stoichiometric number of species i, n is the charge number of the electrode reaction, and F is the Faraday's constant. Therefore, the effect of current density leads to an increase in the concentration of dissolved H_2 in the boundary layer of the electrode with respect to the concentration of dissolved H_2 in the electrolyte bulk. This concentration gradient builds up to a point where the first nuclei are activated due to supersaturation, and the product is transported into the gaseous phase, due to a desorption flux. The associated flux density is denoted with N_{G}. Afterwards, the bubbles grow and detach from the electrode. A new bubble is created at the same nucleation site and this process keeps on. The nucleation and growth of the bubbles are promoted by mass transfer mechanisms which can enhance the N_G flux density. The most important ones (Figure 2.6) which have been reported by H. Vogt [29, 31] are the following:

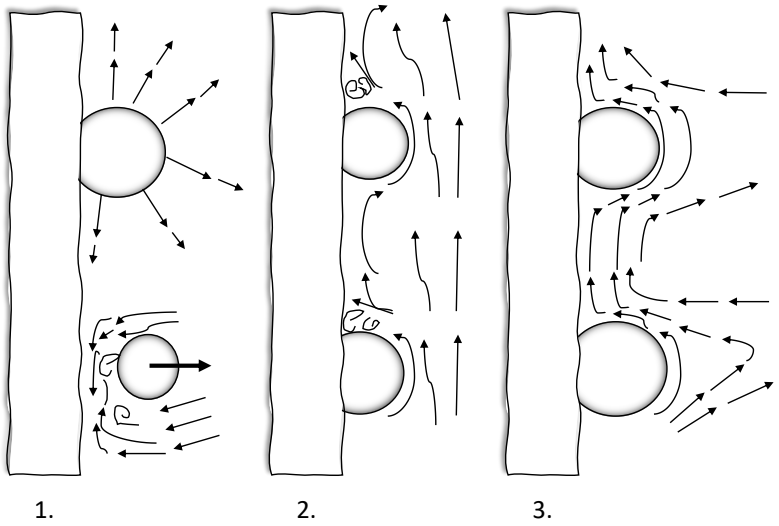

Figure 2.6: Mass transfer mechanisms on the electrode-electrolyte interface. 1. *Micro-convection*: In the electrode region, the growth and detachment of the bubbles induce a stirring effect that enhances the mass transfer. 2. *Two-phase macro-convection*: The combined effect of the forced and free convection influence the momentum in the flow field of the bubbles, and enhance the mass transfer. 3. *Single-phase macro-convection*: Due to the concentration and temperature gradient in the liquid electrolyte, single-phase free convection can influence the flow field, and hence the mass transfer.

1. *Bubble-induced micro-convection:* When the bubbles detach from the electrode and exit the concentration boundary layer, they break up. The growth of the bubbles also influences the neighboring flow field. As a result, the growth and detachment create an intense stirring effect with periodic micro-flow that disturbs the boundary layer. This periodic micro-flow is linked with enhanced mass transfer at the nucleation sites.

2. *Two-phase forced convection (macro-convection):* When the bubbles detach from the electrode, they form a very fine dispersion in the electrolyte. In large-scale electrolysers, this two-phase flow is circulated with pumps and influences the momentum and consequently the mass transfer. The two-phase forced macro-convection can be more prominent at the interelectrode gap.

3. *Two-phase free convection (macro-convection):* This mass transfer mechanism is related to the previous one. Two-phase free convection can also be more prominent in the interelectrode gap, but it influences the momentum, and consequently the mass transfer due to buoyancy effects. More specifically, the buoyancy effects can be induced by the local density differences in the dispersion.

4. *Single-phase free convection:* This mass transfer mechanism is dependent on the concentration and temperature gradient uniquely of the liquid phase between the bulk electrolyte and the electrode-electrolyte interface. Its extent is not related to the two-phase free convection mechanism.

2.2.3. Mass transfer mechanisms from the electrolyte bulk to the gaseous phase

The rest of the product is transferred to the electrolyte bulk by molecular diffusion and superimposed convection. The associated flux leaving from the electrode-electrolyte interface (Figure 2.5) is denoted with N_{E}. As a result, the dissolved H_2 species at the electrolyte bulk can either remain dissolved or be further incorporated into the detached bubbles. More specifically, it is suggested that the electrolyte bulk concentration must be governed by supersaturation [33]. As a result, it is valid to assume that a fraction of the dissolved product which is supersaturated in the electrolyte bulk can be transported into the detached bubbles through a desorptive mass transfer mechanism (flux density N_{F} in Figure 2.5). One of the approaches to model this phenomenon can be via the film theory [33, 34]. This theory is governed by two main assumptions [35]:

1. A thin, laminar film exists in the liquid and gaseous interface

2. In the laminar film, only molecular diffusion takes place

Assuming that in the gaseous interface there is not any mass transfer resistance, the gaseous film can be neglected. In addition, it is assumed that the gas-liquid interface is in phase equilibrium and is governed by an equilibrium concentration c^*, the thin liquid film of a thickness δ_{L} is stagnant, and the concentration gradient is linear. Furthermore, the electrolyte bulk concentration is equal to c_{out}. As a result, molecular

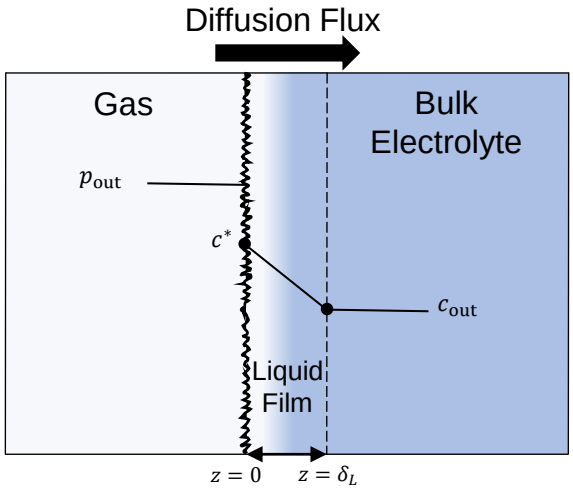

Figure 2.7: The film theory [35]. Mass transfer from the liquid to gaseous phase occurs in a thin laminar film of a thickness δ_{L}, due to diffusion. At $z = 0$, the gas-liquid interface is governed by the equilibrium concentration c^*. In the liquid film, a linear concentration gradient is assumed, where the concentration of the electrolyte bulk equals c_{out}.

diffusion which obeys the film theory only occurs with a driving force $c^* - c_{\mathrm{out}}$ and can be visualized in Figure 2.7.

The diffusion molar flux in the liquid film obeys Fick's Law. Therefore, it will be:

$$\dot{\Phi}_{\mathrm{diff}} = -D_\theta A_{\mathrm{GL}} \frac{dc}{dz} \tag{2.9}$$

Where, D_θ is the molecular mass transfer coefficient between the dissolved species and the liquid electrolyte, at a temperature θ, in $\mathrm{m^2 s^{-1}}$, and A_{GL} is the gas-liquid interface area in $\mathrm{m^2}$. Considering the liquid film assumptions, the diffusion molar flux can be rewritten:

$$\dot{\Phi}_{\mathrm{diff}} = -D_\theta A_{\mathrm{GL}} \frac{c_{\mathrm{out}} - c^*}{\delta_{\mathrm{L}} - 0} \tag{2.10}$$

From equation (2.10) it follows that:

$$\dot{\Phi}_{\mathrm{diff}} = N_{\mathrm{F}} \cdot A_{\mathrm{GL}} \tag{2.11}$$

In the preceding analysis, it is assumed that the equilibrium concentration c^* is larger than the outlet concentration of dissolved species in the electrolyte bulk c_{out}. As a result, the diffusive flux from the film theory, N_{F}, is directed from the gaseous phase to the liquid phase. This phenomenon is called physisorption. When the outlet dissolved concentration of species , c_{out}, is larger than the equilibrium concentration c^*, due to supersaturation, the diffusion flux is directed from the liquid phase to the gaseous phase. This phenomenon is called desorption. Typically, the former case is valid for the dissolved hydrogen in the electrolyte bulk. Rearranging equation (2.10) and using equation (2.11), an expression for the flux density N_{F} can be obtained:

$$N_{\mathrm{F}} = k_{\mathrm{L}} \cdot (c^* - c_{\mathrm{out}}) \tag{2.12}$$

where, k_{L} is the effective liquid mass transfer coefficient in ms^{-1} and is equal to:

$$k_{\mathrm{L}} = \frac{D_\theta}{\delta_L} \tag{2.13}$$

The approximation of the mass transfer coefficient k_{L} can be achieved with two methods. According to De Haan et al. [35], the diffusivity in the liquid phase D_θ is in the order of $10^{-9}\ \mathrm{m^2 s^{-1}}$.From experimental results, the mass transfer coefficient k_{L} is about $10^{-4}\ \mathrm{ms^{-1}}$. Therefore, the boundary layer thickness δ_{L} should be around $10^{-5}\ \mathrm{m}$. For quick estimations, it is valid to assume that the boundary layer thickness is proportional to the radius of the rising gas bubble $\delta_{\mathrm{L}} \sim d_{\mathrm{b}}/2$. Consequently, the mass transfer coefficient can be approximated with equation (2.14).

$$k_{\mathrm{L}} = \frac{2D_\theta}{d_{\mathrm{b}}} \tag{2.14}$$

Where the proportionality constant is equal to 1.

The second way to calculate the mass transfer coefficient $k_{\mathrm{L},i}^{j}$ can be achieved by implementing empirical correlations. More specifically, for mass transfer calculations, the Sherwood number (Sh) can be applied. In general, the Sh number is a function of the Reynolds Re and Schmidt number Sc:

$$Sh = f(Re, Sc) \tag{2.15}$$

To calculate the Sherwood number, the Re and Sc numbers must be found first. The Re number is given by the following formula from Vogt [33]:

$$Re = \frac{u_{\mathrm{rs}} \cdot \rho_{\mathrm{L}} \cdot d_{\mathrm{b}}}{\mu_{\mathrm{L}}} \tag{2.16}$$

Where μ_{L} is the dynamic viscosity of the liquid electrolyte in $\mathrm{Pa \cdot s}$, and ρ_{L} is the density of the liquid electrolyte in $\mathrm{kg \cdot m^{-3}}$. The term u_{rs} refers to the rising swarm velocity of the gas bubbles during gas evolution, in $\mathrm{m \cdot s^{-1}}$. In the literature, Vogt [36] and Haug et al. [34] use the same relation to calculate the rising swarm bubble velocity from Brauer et al. [37]:

$$u_{\mathrm{rs}} = u_{\mathrm{r}} \cdot \frac{1}{1 + \frac{\varepsilon_{\mathrm{g}}}{\left(1-\varepsilon_{\mathrm{g}}\right)^2}} \cdot \frac{1 - \varepsilon_{\mathrm{g}}}{1 + \frac{1.05}{\left(1+\frac{0.0685}{\left(\varepsilon_{\mathrm{g}}\right)^2}\right)^{0.5} - 0.5}} \tag{2.17}$$

Where ε_{g} is the gas hold-up fraction inside the half-cell. The term u_{r} refers to the rising velocity of a single bubble in $\mathrm{m \cdot s^{-1}}$. According to Haug et al. [34] for $1 < Re < 430$ the following relationship could be used:

$$u_{\mathrm{r}} = 0.33 g^{0.76} \left(\frac{\rho_{\mathrm{L}}}{\mu_{\mathrm{L}}}\right)^{0.52} \left(\frac{d_{\mathrm{b}}}{2}\right)^{1.28} \tag{2.18}$$

However, according to Vogt [33] for $Re < 1.4$ the following relation can be used for the single bubble rising velocity:

$$u_{\mathrm{r}}^{j} = \frac{g\,(d_{\mathrm{b}})^2}{12\mu_{\mathrm{L}}} \cdot \left(1 - \frac{\rho_{\mathrm{G}}}{\rho_{\mathrm{L}}}\right) \tag{2.19}$$

From the work of Vogt [33], the Sc number is equal to:

$$Sc_i = \frac{\mu_{\mathrm{L}}}{D_\theta} \tag{2.20}$$

Therefore, the Sh number which is again in accordance to both Vogt [33] and Haug et al.[34], from the paper of Brauer et al. [38], will be equal to:

$$Sh = \frac{k_{\mathrm{L}} \cdot d_{\mathrm{b}}}{D_\theta} = 2 + \frac{0.651 \cdot (Re \cdot Sc)^{1.72}}{1 + (Re \cdot Sc)^{1.22}} \tag{2.21}$$

Finally, according to Vogt [33], the outlet electrolyte bulk concentration c_{out}, which is larger than the equilibrium concentration, increases with the length x of the electrode, that is $c_{\mathrm{out}} = c(x)$. Haug et al. [34] assume that the electrolyte bulk concentration c_{out} does not increase with the length of the electrode, but it remains constant throughout the electrolysis half-cell. This is due to the continuous stirred tank reactor (*CSTR*) assumption.

2.2.4. The gas evolution efficiency

From the preceding sections, it can be concluded that the overall flux density of formation of dissolved gas (Figure 2.5) is equal to:

$$N_{\mathrm{D}} = N_{\mathrm{G}} + N_{\mathrm{E}} \tag{2.22}$$

The gas evolution efficiency, f_{G}, is related to the amount of the dissolved species in the electrode-electrolyte interface which are transported into the gaseous phase via the preceding mass transfer mechanisms. In Ref. [30], the gas evolution efficiency is mathematically defined as:

$$f_{\mathrm{G}} = \frac{N_{\mathrm{G}}}{N_{\mathrm{D}}} = 1 - \frac{N_{\mathrm{E}}}{N_{\mathrm{D}}} \tag{2.23}$$

When $f_{\mathrm{G}} = 1$, the whole dissolved product in the electrode boundary layer is transported into the gaseous phase and a bubble curtain is created. Typically, it occurs when the current density is very high. In this case, it is also suggested that the fractional bubble coverage Θ equals $\Theta = 1$, and both the micro and macro-convective mass transfer mechanisms are negligible [30]. Nevertheless, this case does not seem realistic because the electrode would be completely blocked, and no reactants could be fed for the electrochemical reactions. In real cases, the gas evolution efficiency will have an upper bound close to unity for high current densities.

On the contrary, $f_{\mathrm{G}} = 0$ when the whole product remains dissolved in the bulk electrolyte. This is the case when the current density is very low, $\Theta \ll 1$, and the whole dissolved product is transferred to the electrolyte bulk through macro-convection mass transfer mechanisms. More specifically, in this case, the single-phase free convection becomes the dominant mass transfer mechanism [31] and the role of micro-convection is negligible. In real case applications it has been reported that hydrogen bubbles start forming at current densities as low as $0.01\ \mathrm{kA \cdot m^{-2}}$.

The gas evolution efficiency is a powerful property because it denotes a single quantity that describes all the mass transfer phenomena at the electrode-electrolyte

region. In addition, it is an indication of the desired product which is formed at the electrode region in the gaseous phase. It is also important because the product which remains dissolved in the electrolyte is the primary source of the gas crossover as will be later explained. For these reasons, there has been a lot of effort to quantitatively define the gas evolution efficiency. Vogt [29–32] has reported a series of publications for its calculation by considering the effect of the preceding mass transfer mechanisms, and the fractional bubble coverage Θ. More specifically, the gas evolution efficiency can be calculated by implementing models with empirical relationships [30–32]. Otherwise, it can be calculated as a function of the applied current density [33, 39]. However, the main problem with such relations is the fact that they cannot be generalized for a variety of operating conditions in every application. Among other parameters, the gas evolution efficiency depends on the material properties of the electrode, and its specific design (i.e., perforated/mesh electrodes, membrane electrode assembly). In addition, the fact that the modern alkaline water electrolysers are being developed in a zero-gap configuration further complicates the validity of these models. For these reasons, Haug et al. [34] suggest the gas evolution efficiency being a fitting parameter as a function of the current density. Overall, indicatively, some of these gas evolution efficiency models are listed in Table 2.1.

Table 2.1: Hydrogen gas evolution efficiency according to the literature.

Author	Relation
Vogt [33]	$f_{\mathrm{G}} = 1 - 1.35J^{-0.095}$
Pierre *et al.* [39]	$f_{\mathrm{G}} = 0.5663\left(1 - e^{-0.00206J}\right)$
Haug *et al.* [34]	$f_{\mathrm{G}} = 0.25744J^{0.14134}$

2.3. The crossover mechanisms and their effect on the efficiency of alkaline water electrolysis

As stated in *Chapter 1*, the part-load operation in alkaline water electrolysis varies between 20-40% of the nominal load. The precise definition of the lower bound of operation is important because it signifies the lowest power load range at which the alkaline water electrolyser can work when it is coupled with renewables and produce green hydrogen safely.

When the load is very low, a fraction of the produced hydrogen remains dissolved in the electrolyte. As a result, the dissolved species in the electrolyte are recirculated in the auxiliary equipment, and under the effect of convective and diffusive mass transfer mechanisms, they can cross the opposite half-cell. This phenomenon is called the gas crossover and is of special importance because the dissolved species in the opposite half-cell can result in recombination reactions to produce water, lower the gas purity of the evolved product, or spontaneously combust and pose serious threats to the integrity of the electrolyser.

In this section, it is analyzed how the crossover occurs in alkaline water electrolysis. Firstly, a short description of an alkaline water electrolysis plant is presented and

highlighted how the overall process results in the gas crossover. Then, a complete breakdown of the crossover mechanisms is denoted according to the literature. Finally, it is analyzed how gas crossover affects the faradaic efficiency and the safety of alkaline water electrolysers.

2.3.1. Alkaline water electrolysis in mixed mode operation

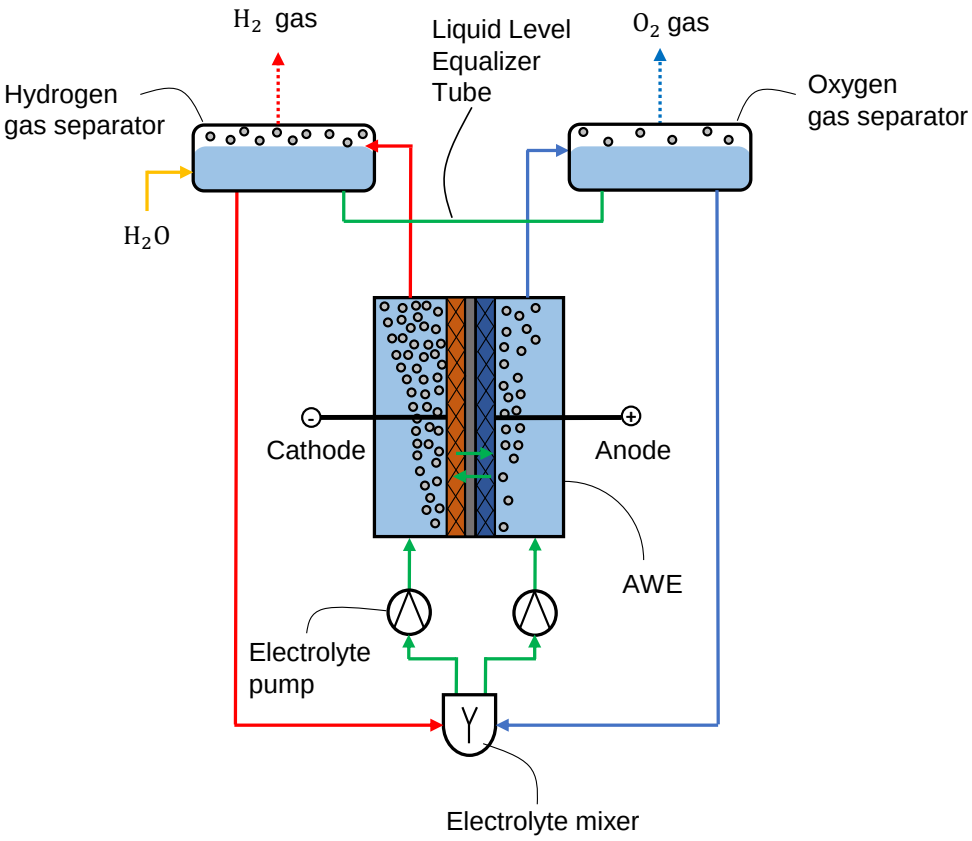

Figure 2.8: Process flow diagram of an alkaline water electrolysis plant in mixed mode. Dissolved hydrogen in the liquid electrolyte is transferred to the hydrogen gas separator and outgases. Dissolved oxygen is transferred to the oxygen gas separator and outgases. The amount that remains dissolved in the liquid electrolyte is recirculated. In the electrolyte mixer, the liquid streams from the gas separators that contain the dissolved species are mixed and re-directed to the electrolysis cell with the use of pumps. Gas crossover due to electrolyte mixing occurs. The dissolved species inside the compartment can cross-permeate to the opposite half-cell through the diaphragm due to concentration or pressure gradient. The amount of gas crossover in the liquid level equalizer tube is negligible. *Red*: Hydrogen circuit. *Blue*: Oxygen circuit. *Yellow*: Feedwater. *Green*: Crossover regions.

In Figure 2.8, the system overview of an alkaline water electrolysis plant is given. The electrolyser is presumed to be in a zero-gap configuration and consists of mesh electrodes. The electrolyte solution contains strongly concentrated KOH for ionic conduction. The half-reactions obey the reactions (2.1) and (2.2). Therefore, when the electrochemical reactions take place, dissolved species will exist in the electrolyte

bulk. In addition, the mixture which contains the electrolyte solution with the dissolved species and the gaseous products exits the electrolyser and is transferred to the gas separators. Typically, there are two gravity gas separators, one for hydrogen and another one for oxygen. When the mixture enters the separator, the gaseous products move upwards, and the electrolyte solution remains at the bottom of the separator. As a result, the gaseous products can be extracted and be further processed. After that, the electrolyte solution and the dissolved species are recirculated, and the flow rate can be adjusted by the means of pumps.

On the cathode side, water is consumed due to the cathodic half-cell reaction, while on the anode side water is produced due to the anodic half-cell reaction. For that reason, the liquid level in the gas separators will be different. Consequently, a liquid level equalizer tube is typically installed to avoid such level differences [12, 40]. Moreover, due to the water consumption and production, the concentration of potassium hydroxide increases on the cathode and reduces on the anode. As a result, an electrolyte mixer is placed to balance the concentration difference between the half-cells. In addition to the electrolyte mixer, an H_2O feed is placed on the hydrogen gas separator to supplement the water lost due to hydrogen production.

Overall, during the electrolysis process, the existence and hence the recirculation and mixing of the dissolved species inside the electrolyser induce crossover due to diffusive and convective mass transfer mechanisms. These mechanisms are further analyzed according to the literature [12, 16, 20, 34, 40, 41].

2.3.2. Crossover due to diffusion

The first mechanism that has been reported in the literature is the crossover of the electrolysis products due to diffusion. The electrolysis products can be diffused across the pores of the diaphragm to the opposite half-cell, as depicted with green arrows in Figure 2.8.

Diffusion can occur in both the half-cells [12]. Therefore, anodic oxygen can cross-permeate on the cathode and contaminate the produced hydrogen, hence reducing the gas purity. The cross-permeated oxygen also combusts with the evolved hydrogen products and results in regenerated water. On the contrary, cathodic hydrogen can cross-permeate the diaphragm and react with or contaminate the evolved anodic oxygen, resulting in direct product loss. Due to the overall reaction for alkaline water electrolysis (2.3), more hydrogen than oxygen is produced. Therefore, more hydrogen than oxygen cross-permeates the diaphragm [40].

In general, the hydrogen species can cross-permeate the diaphragm by diffusion either as a gaseous phase, in the form of bubbles, or dissolved in the electrolyte. Schalenbach et al. [16] reported that the hydrogen bubbles possibly cannot penetrate the Zirfon pores because their diameter is larger than the diameter of Zirfon's pores. This consideration can also be validated by Haug et al. [40] who measured the hydrogen bubble diameter for their experimental setup and found out that the average bubble diameter is larger than 100 µm while the Zirfon's pore diameter is approximately 130 nm [42]. In addition, Schalenbach et al, assume that as the electrolyte penetrates the diaphragm pores, it induces a capillary pressure that may further prevent the penetration of the bubbles in the opposite half-cell. Therefore, it will be assumed that hydrogen cannot penetrate the opposite half-cell in the form of gas bubbles. Con-

sequently, the crossover on the diaphragm is due to the diffusion of the dissolved hydrogen species in the electrolyte bulk.

The driving force of diffusion is the high concentration gradient across the diaphragm. Especially in a zero-gap configuration, the concentration of the cathodic dissolved hydrogen in the vicinity of the diaphragm is supersaturated. On the anode, the concentration of dissolved hydrogen is close to zero. Consequently, this concentration gradient leads to a diffusive mass flux across the diaphragm denoted as $N_{H_2}^{diff}$. The diffusion mass flux obeys Fick's Law, and its mathematical formulation according to Haug et al. [41] is the following:

$$N_{H_2}^{diff} = D_{H_2}^{eff} \frac{\Delta c_{H_2}}{\delta_{sep}} \tag{2.24}$$

Where, Δc_{H_2} is the concentration difference between the cathode and the anode, δ_{sep} is the thickness of the diaphragm, and $D_{H_2}^{eff}$ is the effective diffusion coefficient of hydrogen in the diaphragm. The exact mathematical definition of these parameters will be given in Chapter 3.4.6.

2.3.3. Crossover due to convection

In general, there are several subcategories of convective crossover in alkaline water electrolysis. Here it is taken into consideration the crossover due to differential pressure across the diaphragm, and electrolyte mixing. The crossover due to electro-osmotic drag has been reported to be negligible in alkaline water electrolysis [20, 41].

Differential Pressure: The driving force of the crossover due to differential pressure is the absolute pressure difference between the half-cells. As a result, the electrolyte with the dissolved species can cross-permeate through the diaphragm to the opposite half-cell. The crossover due to differential pressure obeys Darcy's law and its mathematical formulation is the following [20]:

$$N_{H_2}^{dp} = \varepsilon_{H_2}^{Darcy} \frac{\Delta p}{\delta_{sep}} \tag{2.25}$$

Where, $\varepsilon_{H_2}^{Darcy}$ is the hydrogen permeability due to differential pressure, and $\Delta p = p^{cat} - p^{ano}$ is the absolute pressure difference between the cathode and the anode. A similar equation is applied to oxygen permeation.

The Zirfon diaphragm in alkaline water electrolysers has much larger pores than the Nafion membranes in PEM. For that reason, the alkaline water electrolysers are more prone to crossover due to differential pressure. As a result, they normally operate under balanced pressure.

Schalenbach et al. [16] have derived a relation that correlates the crossover due to differential pressure with the crossover due to diffusion for Zirfon diaphragms. Therefore, they can extract which crossover mechanism becomes dominant during alkaline water electrolysis. The relationship is the following:

$$\frac{N_{H_2}^{dp}}{N_{H_2}^{diff}} \approx \frac{\Delta p}{0.01} \tag{2.26}$$

The equation (2.26) is the main reason why balanced pressure operation is normally chosen for alkaline water electrolysis. Even if there is a very small pressure difference, from equation (2.26) it becomes clear that the crossover due to differential pressure becomes dominant.

Electrolyte mixing: In the previous section, the working principles of an alkaline water electrolysis plant in mixed mode operation were described. To avoid the concentration difference in KOH between the half-cells, an electrolyte mixer and a liquid level equalizer tube are typically installed. In the electrolyte mixer and the liquid level equalizer, the electrolyte streams from both the half-cells are mixed. However, as it has already been described, the liquid electrolyte carries dissolved species from each half cell. Therefore, when the mixing of the streams occurs, the dissolved species from each half-cell end up in the opposite one. Now, each stream carries impurities which are simply the dissolved species of the opposite half-cell. As a result, when the dissolved species reach the gas separator of the opposite half-cell, they can outgas and lower the purity of the product. The regions where crossover due to electrolyte mixing occurs are highlighted with green color in Figure 2.8.

2.3.4. Comparison of the crossover mechanisms

Both the diffusive and differential pressure crossover mechanisms are important for the calculation of the cross-permeated flux across the diaphragm. However, their contribution depends on the operating conditions during the electrolysis process. More specifically, according to equation (2.26) the applied pressure is one of the most important parameters because it determines which mechanism becomes dominant. If one of these crossover mechanisms becomes dominant, the other one can be omitted. For example, during their experimental setup, Schalenbach et al. [20] applied 6 bar absolute pressure in each half cell, while Haug et al. [40] applied 1 bar. In addition, they both installed a pressure controller to each half cell and claimed that it has an accuracy within 1%. Therefore, the maximum absolute differential pressure in [20] will be $\Delta p_{\mathrm{Schalenbach}} = 0.06\,\mathrm{bar}$, and in Ref. [40] it will be $\Delta p_{\mathrm{Haug}} = 0.01\,\mathrm{bar}$. The substitution of these Δp in (2.26) leads to a sixfold differential pressure crossover than the diffusive one in Ref. [20], and equal contribution in Ref. [40]. For that reason, Schalenbach et al. assumed that the crossover in the diaphragm was governed by the differential pressure and the diffusive contribution was omitted, while Haug et al. assumed the opposite. In conclusion, from the previous experiments, the applied pressure during alkaline water electrolysis must be close to atmospheric to avoid the crossover due to differential pressure.

Trinke et al. published a report [41] where they performed a series of experiments to measure the contribution of each of the crossover mechanisms that were described previously. The resulting current density was ranging from 0.1-7 $\mathrm{kA \cdot m^{-2}}$ at a constant pressure of 1 bar. From these experiments, they found out that the most influential crossover mechanism in alkaline water electrolysis is the convection due to electrolyte mixing. More specifically, they concluded that the crossover due to electrolyte mixing remained almost constant regardless of the current density. In addition, they claimed that it accounts for 90% of the total crossover. The rest was due to diffusive crossover through the diaphragm.

Finally, in a report by Haug et al. [40], the effect of the liquid level equalizer in the gas crossover was evaluated experimentally. More specifically, they installed a valve in the equalization tube and performed the electrolyser in a partly separated mode of operation. Partly separated is defined as the operation where the valve in the equalization tube remains open and the recirculated electrolyte streams from the gas separators do not conclude in the electrolyte mixer but their corresponding half-cell. They compared the resulting gas crossover with the gas crossover from the separated operation. In a separated operation, the valve in the equalization tube remains closed. From this experiment, they found out that the gas crossover by the electrolyte mixing in the equalization tube is negligible.

2.3.5. The effect of gas crossover on the cell efficiency

In general, the overall cell efficiency is the product of voltaic and faradaic efficiency [20]. The modeling results in Ref. [20] reveal that in low current densities, the faradaic efficiency in alkaline water electrolysis becomes dominant to the decline of the overall cell efficiency. In low current densities, more hydrogen will remain dissolved in the electrolyte bulk, and hence more product will cross-permeate to the anodic compartment. At the same time, the themobalanced voltage will be low, and hence the impact of voltaic efficiency in the overall cell efficiency. On the contrary, in the modeling results of Ref. [20], at higher current densities, the voltaic efficiency becomes dominant to the drop of the overall cell efficiency. In high current densities, gas crossover is significantly reduced and the faradaic efficiency is close to unity. Due to the higher impact of resistances in the thermobalanced voltage at higher current densities, the main reason of the drop in the overall cell efficiency is due to the voltaic efficiency. Therefore, for the part-load operation, the faradaic efficiency is more relevant.

The Faradaic efficiency according to Schalenbach et al. [20] is equal to:

$$\eta_{\mathrm{c}} = 1 - \frac{I_{\mathrm{loss}}}{I} \tag{2.27}$$

Where, I_{loss} is the current which does not lead to the production of hydrogen on the cathode. According to Ref.[20], the main reason for the current loss is the cross-permeation of hydrogen and oxygen species through the diaphragm. Therefore, to estimate the faradaic efficiency the current loss is interrelated with the cross-permeated fluxes through the diaphragm by applying Faraday's law. Using equation (2.8), the total current is estimated. Therefore, the faradaic efficiency is given by:

$$\eta_{\mathrm{c}} = 1 - \frac{N_{\mathrm{H_2}}^{\mathrm{dp}}}{N_{\mathrm{H_2}}} - 2\frac{N_{\mathrm{O_2}}^{\mathrm{dp}}}{N_{\mathrm{H_2}}} \tag{2.28}$$

Equation (2.28) is partially correct because the effect of the crossover due to the electrolyte mixing has not been considered in Ref. [20]. However, equation (2.28) provides a crude estimate and understanding of the influence of gas crossover on the faradaic efficiency, and consequently the overall cell efficiency.

2.3.6. The effect of gas crossover on fire and safety

The cross permeation of dissolved hydrogen species in the anodic half-cell, where oxygen is produced, can create an explosive atmosphere due to the spontaneous

oxidation reaction of hydrogen with oxygen. The opposite case also holds true.

To quantify the ignition of a possible explosion, the vapour concentration of the fuel source in air is typically studied. More specifically, for electrolysis applications, the gaseous concentration of hydrogen in gaseous oxygen is considered. The explosion can take place for a range of concentrations. The limits of this range are called the Lower Explosive Limit (LEL), and the Upper Explosive Limit (UEL). Below the LEL, combustion of hydrogen with oxygen cannot occur because the mixture is too lean. Similarly, above the UEL, combustion of hydrogen with oxygen cannot occur because the mixture is too rich. The limits strongly depend on the applied pressure and temperature, and they are experimentally defined. In the CHEMSAFE database [43], the LEL and UEL limits can be found from a variety of publications. More specifically, for $T = 20°\mathrm{C}$ and $p = 1\ \mathrm{bar}$, the LEL of hydrogen in oxygen is 4 mol%, and the UEL is 95.2 mol% according to Ref. [44]. When there is an ignition source available, and hydrogen in oxygen concentration reaches the LEL which is 4 mol%, the mixture can spontaneously combust. To avoid the risk of spontaneous combustion in electrolysis applications due to gas crossover, the standard ISO 22734:2019 is proposed [14]. In ISO 22734:2019, the hydrogen content in hydrogen-oxygen gas mixtures should never exceed 50% of LEL, which equals 2 mol%. Consequently, when the anodic hydrogen content exceeds 2 mol%, the electrolyser must shut down.

2.4. Gas crossover mitigation strategies

The operation of alkaline water electrolysers requires the avoidance of 2 mol% in the anodic hydrogen content. During the part load operation, there is more dissolved hydrogen in the liquid electrolyte than in the nominal load operation. Furthermore, the anodic hydrogen content in the part load range can approach the 50% of LEL, and can force the electrolyser to shut down.

In the following, some strategies for the mitigation of the gas crossover in alkaline water electrolysis are presented, according to the literature. These strategies are based on reshaping the design of the electrochemical cell and proposing alternative process operations.

2.4.1. Reshaping the design of the electrochemical cell

The first alternative to reduce the gas crossover is the implementation of catalytic recombiners [45]. The catalytic recombiners are applied to the vicinity of the electrode. They are made from a Pt-based catalyst which is sprayed on a porous structure. Their function aims at recombining H_2/O_2 gas mixtures to water by promoting a heterogeneous reaction. The catalytic gas recombiner is activated when H_2 cross permeates the diaphragm and the H_2/O_2 mixture obtains a critical value in terms of H_2 concentration. It has to be noted that the implementation of recombiners does not mitigate the source of the crossover but reduces the risk of spontaneous combustion. Consequently, the faradaic efficiency is not increased, but the resulting stream is hydrogen-free. Another solution to reduce the gas crossover, according to Schalenbach et al. [46], is the implementation of two additional electrodes in the electrochemical cell. One additional electrode is installed on the cathode side to reduce the hydrogen crossover. Similarly, a second additional electrode is installed on the anode side to reduce the

oxygen crossover. In these additional electrodes, the reverse half-reactions of their corresponding primary electrodes are promoted. For example, with the additional electrode installed on the cathode, the reverse cathodic reaction takes place. As a result, if there is a tendency for hydrogen species to cross permeate the diaphragm, the reverse reaction occurs on this additional electrode, and the gases are electrochemically sent back to the primary electrode. Furthermore, similar reasoning is followed for the anodic half-cell. Nevertheless, the main issue with this design configuration is the fact that it can be very complicated and does not tackle the crossover due to electrolyte mixing.

2.4.2. Alternative process operations

The problem with the two previous strategies is that none of them can tackle the crossover due to electrolyte mixing. In the literature, two different process operation strategies have been reported that can reduce this crossover mechanism. These process operations are the lye circulation control [47], and the dynamic switching of electrolyte cycles [40].

Schug published a report [47], where he states that crossover occurs due to diffusion and electrolyte mixing. He also highlights the fact that even if diffusive crossover will be minimized, the crossover due to electrolyte mixing remains dominant in part-load operation. For that reason, it is suggested supplying a minimum lye flow rate to each half cell such that the diaphragm will not “dry out”, and at the same time, the temperature rise of the cell remains small. The reduction of the flow rate can lead to less convective crossover and consequently less electrolyte mixing. Furthermore, it is reported that the control of the lye circulation is achieved by the implementation of some empirical relationships between the current, voltage, and lye flow. However, these relationships are not provided in the paper.

Haug et al. [40], suggest the dynamic switching of electrolyte cycles as an alternative process operation, and experimentally prove that it can reduce the gas crossover. Schematically, the dynamic switching of electrolyte cycles is depicted in Figure 2.9.

The process flow diagram of this method is similar to the mixed-mode operation. The only difference is that each electrolyte pump is now connected with a new branch, and there are four valves. This modification enables the changeover of the operative electrolyte cycle by dynamically switching the valves. More specifically, when the valves V-1.1 and V-1.2 are open, and the valves V-2.1 and V-2.2 are closed, the system works in the partly separated mode operation. On the contrary, when the valves V-1.1 and V-1.2 are closed, and the valves V-2.1 and V-2.2 are open, the system works in the mixed-mode operation.

If the process works in the partly separated mode, there is no crossover due to electrolyte mixing because the valves V-2.1 and V-2.2 are closed. Therefore, there will only be crossover through the diaphragm which is very small. Furthermore, as already described previously, the electrolyte mixing in the equalization tube is negligible. However, the system cannot permanently operate in a partly separated mode. The reason is that a concentration gradient in the KOH between the half-cells is formed and it leads to a reduction in the electrolyte conductivity, and thus a reduction in the overall efficiency. Consequently, in the dynamic switching of electrolyte cycles, the system works for a certain period in partly separated mode and then switches to mixed

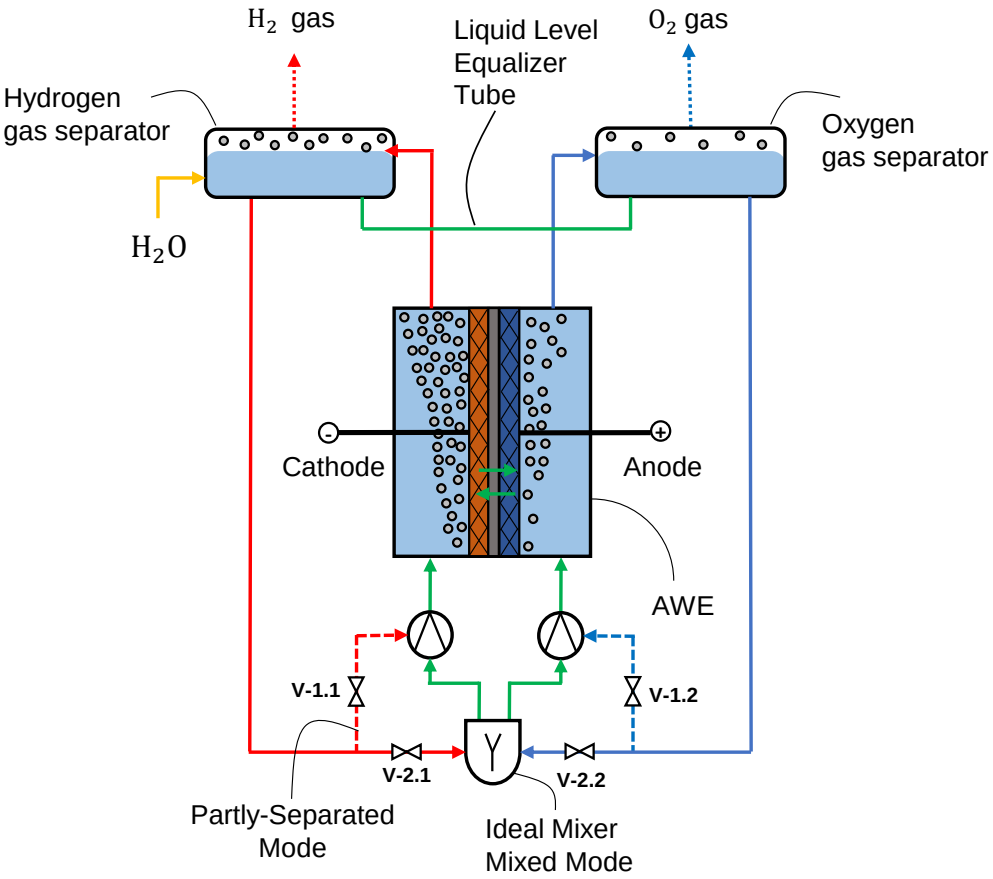

Figure 2.9: The Dynamic Switching of Electrolyte Cycles process. When the valves V-2.1, V-2.2 are opened, and V-1.1, V-1.2 are closed, the plant operates in a mixed mode. Crossover occurs due to diffusion through the diaphragm, and due to electrolyte mixing. When the valves V-2.1, V-2.2 are closed, and V-1.1, V-1.2 are opened, the plant operates in a partly-separated mode. Crossover occurs only due to diffusion through the diaphragm. During the dynamic switching, the electrolysis plant operates for a certain time in a partly-separated mode and then it switches to a mixed mode for the same time. The periodic switching of the active electrolyte cycle results in a sinusoidal trend for the impurity. The average impurity in the dynamic switching is less than the impurity in the mixed mode.

mode.

The dynamic switching of the electrolyte cycles continues as long the electrolyser operates under part-load. According to the experiments conducted by Haug et al. [40], the anodic hydrogen content develops an oscillatory behavior. The extreme values in this oscillatory behavior are the minimum and maximum obtainable anodic hydrogen content when the system works in partly separated mode and mixed mode, respectively. Therefore, the overall anodic hydrogen content is the mean of these extreme values. In conclusion, this method can be a realistic solution that can be applied to the existing equipment and reduce the crossover due to electrolyte mixing under part-load operation.

2.5. Literature on modeling of alkaline water electrolysis

In the literature, only the report of Haug et al. [34] focuses on developing a steady-state model of the gas crossover in alkaline water electrolysers. In this zero-dimensional model, steady-state material balances are applied, and the gas impurity is calculated as a function of current density, temperature, lye flow rate, and KOH concentration. Finally, the results are verified with experimental data.

Schalenbach et al. [20], published a report where they estimate the overall efficiency of the electrochemical cell, for both alkaline water electrolysis and PEM electrolysis. For the calculation of the overall efficiency, they consider all the overpotentials and the gas crossover through the diaphragm and membrane. They claim that the development of thinner diaphragms than Zirfon could reduce the overpotentials and consequently achieve better efficiencies than the PEM electrolysers. Finally, they also validate their modeling results with experimental data.

However, most of the modeling publications are focused on the polarization curve and hydrogen production. Ulleberg [48] developed a model by applying thermodynamics, heat transfer, and electrochemical empirical models to predict the performance of alkaline water electrolysers under dynamic loading. This model drew the attention of many researchers because it can accurately predict the performance of alkaline electrolysers when it is coupled with renewables [49, 50]. Amores et al. [51], extended Ulleberg's model by considering the electrolyte concentration and the distance between the electrodes.

Finally, more recently, CFD models have been developed to study alkaline water electrolysis cells. Lee et al. [52], developed a three-dimensional model in Ansys Fluent to evaluate the gas evolution at the electrodes, the dissolution of products in the electrolyte, and the bubble coverage of the electrodes.

3

The gas crossover model

The development of the model described in this chapter focuses on the prediction of the gas purity during alkaline water electrolysis at the exit of the gas separators, under steady-state transient state. The predicted gas purity depends on the applied temperature, pressure, flow rate, and current density. It also depends on the concentration of potassium hydroxide, and the liquid and gaseous volume of the gas separators.

In the previous chapter, alternative operational concepts were introduced to further increase the purity of the resulting gaseous products. The dynamic switching of the electrolyte cycles seems to be a promising solution to operate the alkaline water electrolyser at the low current density range while maintaining the gas purity high. During the dynamic switching of electrolyte cycles, the electrolyser operates for a specific time range in mixed-mode, and then it switches to partly separated mode. During the mixed-mode operation, the anolyte and catholyte cycles are continuously mixed to maintain the concentration of potassium hydroxide stable due to the half-reactions that take place in the compartments. Then, the process switches to the separated mode where crossover occurs only due to diffusion through the diaphragm. As a result, the impurity acquires a sinusoidal behavior where its average value is lower when compared with the mixed mode [40].

In Chapter 3, dynamic mass balances are used to describe the dynamic switching of the electrolyte cycles. The development of the model that describes the dynamic switching of electrolyte cycles requires the introduction of the steady state case. For this purpose, firstly, the steady-state model will be presented and then the dynamic material balances.

In the first section of this chapter, the assumptions that describe the mass transfer phenomena throughout the whole electrolysis simplified process flow diagram will be shown. The assumptions and the simplified process flow diagram are valid for both the steady-state and dynamic models. In the next section, the generic form of the steady-state material balances will be given. Next, the generic form of the dynamic material balances will be provided. The following section contains the boundary conditions and the mathematical expressions for the parameters of the model. In most of the cases, the mathematical expressions are the same for both models, unless otherwise stated. Finally, the final form of both the steady-state and dynamic material balances that were implemented in Python will be provided.

3.1. System description and assumptions

In the following, a brief system description and the required assumptions of the mathematical models in the alkaline water electrolyser will be introduced. In the first subsection, the assumptions for the steady-state and dynamic mass balances in the electrolysis cell will be provided. For both situations, the assumptions are the same. In the next subsection, the assumptions for the steady-state and dynamic mass balances in the gas separators will be given. The assumptions are valid for both models. Finally, the simplified process flow diagram that was implemented for both mathematical models will be presented.

3.1.1. Mathematical model assumptions for the electrolysis cell

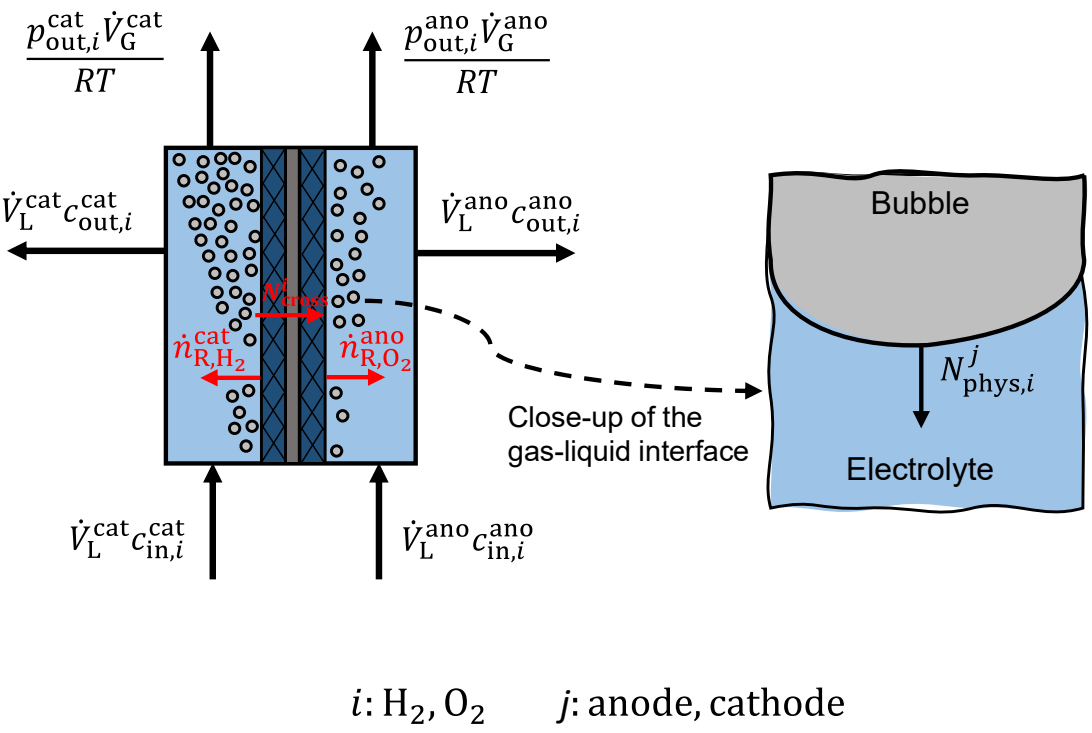

Figure 3.1: The mass balance in the single cell. The reaction rate $\dot{n}^{j}_{\text{R},i}$ obeys Faraday's law. Only liquid stream with dissolved molecules enters the cell $\dot{V}^{j}_{\text{L}}c^{j}_{\text{in},i}$. The stream which exits the cell consists of the liquid electrolyte with the dissolved species $\dot{V}^{j}_{\text{L}}c^{j}_{\text{out},i}$, and the gaseous phase which obeys ideal gas law $\frac{p^{j}_{\text{out},i}\dot{V}^{j}_{\text{G}}}{R\,T}$. The mass transfer in the electrolyte bulk is governed by a desorption flux $N^{j}_{\text{phys},i}$. In the electrolysis cell, cross-permeation in the opposite half cell occurs due to diffusion through the diaphragm N^{i}_{cross}

When the electrolysis process starts, hydrogen is produced in the cathode $\dot{n}^{\text{cat}}_{\text{R,H}_2}$, and oxygen is produced in the anode $\dot{n}^{\text{ano}}_{\text{R,O}_2}$. Due to the mass transfer limitations that were introduced in Chapter 2.2, a part of the total product is transferred to the liquid phase and the rest is directly transferred to the gaseous phase. The part of the product that is transferred to the liquid phase remains dissolved and is described by the variable $c^{j}_{\text{out},i}$. At this point, it is assumed that each compartment follows the

continuous-stirred-tank model (CSTR) [53]. More specifically, each half cell can be considered a reactor whose contents are perfectly mixed. The reactor consists of continuous inflow and outflow. As a result, the concentration and temperature throughout the reactor are uniform. Due to the perfect mixing assumption, the contents of the reactor can outflow immediately. The outlet dissolved concentration of the products is an unknown quantity and is calculated by the developed model. Overall, due to the development of gas crossover mechanisms, each reactor will also contain the product of the opposite half cell.

In practice, the liquid volumetric flow rate that enters the anode $\dot{V}_{\mathrm{L}}^{\mathrm{ano}}$, is equal to the volumetric flow rate that enters the cathode $\dot{V}_{\mathrm{L}}^{\mathrm{cat}}$, since it can be regulated by a pump before the cell entrance (Figure 3.3). Furthermore, it is assumed that the outlet volumetric flow rate equals the inlet. This assumption is required to simplify the material balances. The part of the product that is transferred to the gaseous phase is assumed to obey the ideal gas law, due to atmospheric operation. Given the cathodic and anodic temperature, the model can predict the outlet partial pressure $p_{\mathrm{out},i}^{j}$ as well as the gaseous volumetric flow rate $\dot{V}_{\mathrm{G}}^{j}$. The gaseous volumetric flow rate that leaves the half-cells is not the same between the anode and cathode. The bubbles which contain the gaseous products are assumed to be monodisperse and perfectly spherical, and any coalescence effects due to hydrodynamic phenomena are not taken into consideration. Finally, it is assumed that no gaseous product can be recirculated throughout the system. Therefore, the inlet volumetric flow rate is gas-free.

The products that remain dissolved in the electrolyte bulk can be transferred to the gaseous phase via a subsequent mass transfer step $N_{\mathrm{phys},i}^{j}$ or can cross permeate through the diaphragm to the opposite half cell via the $N_{\mathrm{cross},i}$ flux. In the first case, the subsequent mass transfer step can be achieved via a desorption flux due to the supersaturation of dissolved species in the liquid electrolyte and can be modeled via the film theory (Chapter 3.4.5).The desorption flux takes place between the bulk liquid electrolyte and the product bubbles (Figure 3.1). Even though that there is a desorption flux, the mass transfer in the electrolyte bulk in Figure 3.1 is visualized by a physisorption flux. When the physisorption flux is negative, which is mostly the case, the direction of the $N_{\mathrm{phys},i}^{j}$ flux is opposite to the direction shown in Figure 3.1. In the second case, it is assumed that the cross-permeation flux through the diaphragm is achieved only due to the diffusion of dissolved species in the bulk electrolyte (Fick's Law). The gaseous phase cannot cross-permeate because the diaphragm is hydrophilic. The electrolyser operates in low pressure, close to atmospheric, and hence the convective mass transfer due to differential pressure through the diaphragm (Darcy's Law) can be neglected. Finally, it is assumed that there is no additional mass transfer in the interconnecting piping.

3.1.2. Mathematical model assumptions for the gas separator

After the dissolution of the products in the liquid electrolyte and the formation of the resulting product gases in the electrolysis cell, the two-phase mixture is directed to the gas separators (Figure 3.2). For visualization purposes, the two-phase mixture is depicted as two different streams. The inflow and outflows of each gas separator consist of the products from both the half cells due to crossover. When the electrolyser operates in "mixed mode", the liquid electrolyte that contains the dissolved species

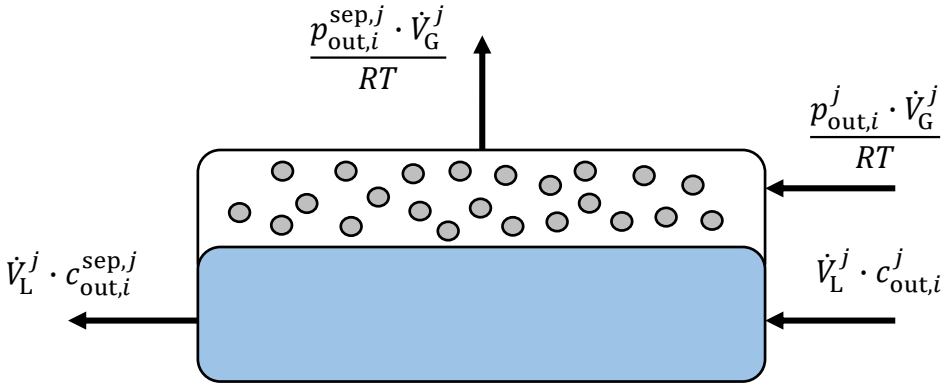

Figure 3.2: The mass balance in the gas separator. The liquid stream with the dissolved species i that exits the electrolysis cell j, $\dot{V}_{\text{L}}^{j} c_{\text{out},i}^{j}$, now enters its corresponding gas separator. The gaseous stream of species i that exits the compartment j, $\frac{p_{\text{out},i}^{j} \dot{V}_{\text{G}}^{j}}{R\,T}$, now enters the gas separator. The produced gas is collected at the exit of the gas separator $\frac{p_{\text{out},i}^{\text{sep},j} \dot{V}_{\text{G}}^{j}}{R\,T}$. The liquid stream that exits the gas separator $\dot{V}_{\text{L}}^{j} c_{\text{out},i}^{\text{sep},j}$, is recirculated.

$c_{\text{out},i}^{\text{sep},j}$ is directed to an ideal mixer, where it is mixed with the dissolved species that exit from the opposite gas separator. Therefore, crossover due to electrolyte mixing occurs. When the electrolyser switches to “partly separated mode”, the liquid electrolyte which outflows from the gas separator $c_{\text{out},i}^{\text{sep},j}$ can be directed to the half cell without mixing. The partial pressures of H_2, O_2 at the outlet of the gas separator, $p_{\text{out},\text{H}_2}^{\text{sep},j}$ and $p_{\text{out},\text{O}_2}^{\text{sep},j}$ are used to compute the impurity of the product gas.

The gas separators are also modeled as CSTR ideal reactors. However, in comparison to the electrolysis cell, there is no reaction. When a specific current density is applied to the electrolyser, there is always a transition time required for the system to reach a steady state. The CSTR assumption is essential such that the transition time to equilibrium can be accurately modeled. The quantities which define the transition time required for the system to reach equilibrium are the liquid $V_{\text{liq}}^{\text{sep},j}$ and the gaseous volume $V_{\text{gas}}^{\text{sep},j}$ of each gas separator. Finally, the gas separators are assumed to be 100% percent efficient, and hence there is no additional mass transfer from the liquid electrolyte to the gaseous phase.

3.1.3. Simplified process flow diagram

In Figure 3.1 and Figure 3.2, the liquid and gaseous flow rates with their corresponding concentrations and partial pressures are given. In Figure 3.3, the liquid and gaseous volumes in the electrolysis cell and the gas separators are also depicted.

The Figure 3.3 shows a simplified process flow diagram of an electrolysis plant that was analyzed in Chapter 2 (see Figure 2.9). In the simplified process flow diagram, the liquid level equalizer tube and the feedwater stream in the cathodic gas separator are not included. The liquid level equalizer tube is required to keep the liquid level of the gas separators equal due to the reduction and oxidation reactions. The conservation of equal liquid levels between the gas separators means that there is no

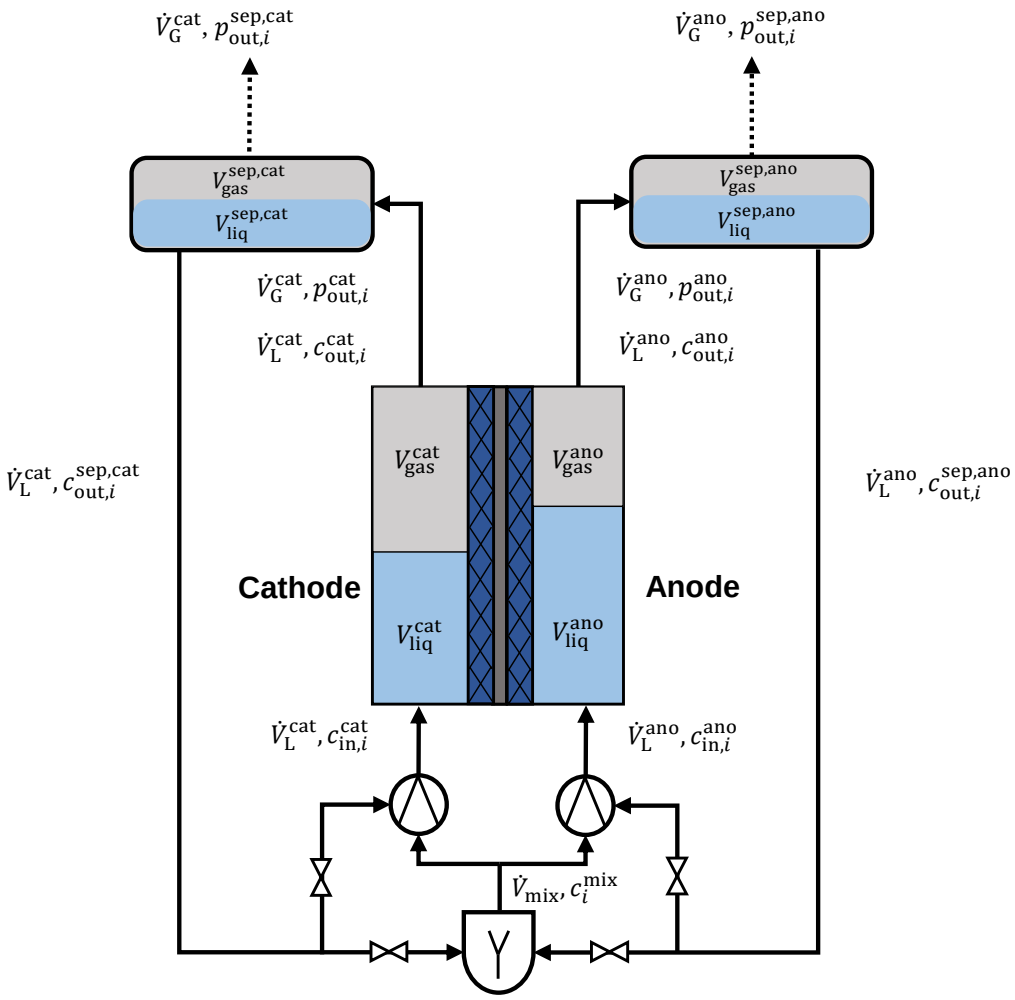

Figure 3.3: The simplified process flow diagram. The liquid and gaseous flow rates that enter and exit the system, are denoted with their corresponding concentration and partial pressure. The liquid and gaseous volumes that are used in the material balances, are shown with different colors (turquoise and grey).

differential pressure build-up between the anodic and cathodic half cells. In addition, as analyzed in Chapter 2.3.4, there is no additional crossover due to the existence of the liquid level equalizer tube. The role of the feedwater stream is to compensate for the water consumed due to gas production. As a result, instead of including these additional streams in the mathematical model, the liquid and gaseous volumes in the gas separators $V_{\mathrm{liq}}^{\mathrm{sep},j}$ and $V_{\mathrm{gas}}^{\mathrm{sep},j}$ are assumed to be steady with time. Additional mass transfer phenomena which may take place inside the gas separator are neglected.

The liquid and gaseous volumes inside the electrolysis half cells V_{liq}^{j} and V_{gas}^{j} are also assumed to be steady with time (see Figure 3.3). Due to the CSTR model, it is reasonable to assume that the application of a current density results in gas evolution immediately. Therefore, for a specific current density, it is assumed that the evolved gases instantly reach their steady state which is represented by the steady liquid and gaseous volumes in the half cells. In practice, the liquid electrolyte and the

evolved gases represent a bubbly flow, where the sum of the bubbles' volume inside the half cell acquires the required gaseous volume, and the liquid electrolyte without the bubbles acquires its corresponding liquid volume. To visualize the liquid and gaseous volumes inside the electrolyser, the bubbly flow is depicted as two distinct areas (turquoise color for liquid volume, grey color for gaseous volume). The same holds for the gas separators.

Finally, the liquid and gaseous flow rates $\dot{V}_{\mathrm{L}}^{j}$ and $\dot{V}_{\mathrm{G}}^{j}$ are depicted in the simplified process flow diagram. It is assumed that the flow rates are determined in the electrolysis cell and do not change throughout the process. As a result, the gaseous flow rate is calculated from the mathematical equations of the electrolysis cell and its value remains the same at the exit of the gas separator. The liquid volumetric flow rate is regulated by the pump, before the entrance of the electrolyser, and remains the same at the entrance and exit of the gas separator. When the system operates in mixed mode, the flow rate at the exit of the ideal mixer is $\dot{V}_{\mathrm{mix}}$.

3.2. The general form of the steady-state material balances

In the following, the general form of the steady-state material balances for alkaline water electrolysers is introduced. In the first subsection, the steady-state material balances for the electrolysis cell are given. Similarly, in the next subsection, the steady-state material balances for the gas separators are provided.

3.2.1. The general form of steady-state material balances in the electrolysis cell

The electrolysis cell consists of the anodic and the cathodic half cell. For each half cell, there is a steady-state material balance for the liquid phase and another for the gaseous phase. Due to the existence of gas crossover, each half cell will also contain the product from the opposite one. For example, in the anode, the primary product is oxygen, but hydrogen will also exist due to gas crossover. Therefore, the anodic side consists of two steady-state material balances for the liquid phase (one for the primary product, one for the product due to crossover), and two material balances for the gaseous phase (one for the primary product, one for the product due to crossover). Similarly, the same holds for the cathode. Consequently, for the liquid and gaseous phase in the electrolysis cell there will be eight steady-state material balances in total. The general form of a material balance in steady-state is the following:

$$0 = \begin{pmatrix} \text{Mass flow rate of component A into system} \end{pmatrix} - \begin{pmatrix} \text{Mass flow rate of component A out of system} \end{pmatrix} + \begin{pmatrix} \text{Rate of generation of mass of component A from reaction} \end{pmatrix}$$

The units of each term in the material balances are in $\mathrm{mol} \cdot \mathrm{s}^{-1}$. The rate of accumulation of mass in the system is not taken into consideration because the system is solved for the steady-state case. The rate of depletion of mass in the material

balance is also neglected because it is assumed that there are no recombination reactions. The applied steady-state mass balance for the electrolysis cell is based on Figure 3.1. For the single cell, the total production rate on the electrode obeys Faraday's Law. The percentage of the total production rate that is transferred directly to the gaseous phase in the vicinity of the electrode is characterized by the gas evolution efficiency $f_{\mathrm{G},i}$. The gas evolution efficiency is zero for hydrogen in the anode and oxygen in the cathode. The crossover flux through the diaphragm N^{i}_{cross} is directed from the cathode to the anode. The crossover flux is integrated over the geometric area of the diaphragm A_{d}. The crossover of species through the diaphragm is characterized by an effective diffusion coefficient $D^{\mathrm{eff}}_{i,\theta}$ over the thickness of the diaphragm. Furthermore, the physisorption flux retains a positive sign when it is directed from the gaseous to the liquid phase. This flux is integrated over the gas-liquid interface A^{j}_{GL} and is governed by a mass transfer coefficient $k^{j}_{\mathrm{L},i}$. As a result, the steady-state mass balances for the liquid and gaseous phase in the electrolysis system are described by equations (3.1)-(3.8).

Dissolved H_2 in the anodic half-cell:

$$0 = \dot{V}^{\mathrm{ano}}_{\mathrm{L}} \cdot \left(c^{\mathrm{ano}}_{\mathrm{in,H_2}} - c^{\mathrm{ano}}_{\mathrm{out,H_2}}\right) + N^{\mathrm{ano}}_{\mathrm{phys,H_2}} \cdot A^{\mathrm{ano}}_{\mathrm{GL}} + N_{\mathrm{cross,H_2}} \cdot A_{\mathrm{d}} \tag{3.1}$$

Dissolved O_2 in the anodic half-cell:

$$0 = \dot{V}^{\mathrm{ano}}_{\mathrm{L}} \cdot \left(c^{\mathrm{ano}}_{\mathrm{in,O_2}} - c^{\mathrm{ano}}_{\mathrm{out,O_2}}\right) + N^{\mathrm{ano}}_{\mathrm{phys,O_2}} \cdot A^{\mathrm{ano}}_{\mathrm{GL}} + N_{\mathrm{cross,O_2}} \cdot A_{\mathrm{d}} + \left(1 - f_{\mathrm{G,O_2}}\right) \cdot \dot{n}^{\mathrm{ano}}_{\mathrm{R,O_2}} \tag{3.2}$$

Gaseous H_2 in the anodic half cell:

$$0 = \frac{\dot{V}^{\mathrm{ano}}_{\mathrm{G}}}{R \cdot T} \cdot \left(p^{\mathrm{ano}}_{\mathrm{in,H_2}} - p^{\mathrm{ano}}_{\mathrm{out,H_2}}\right) - N^{\mathrm{ano}}_{\mathrm{phys,H_2}} \cdot A^{\mathrm{ano}}_{\mathrm{GL}} \tag{3.3}$$

Gaseous O_2 in the anodic half cell:

$$0 = \frac{\dot{V}^{\mathrm{ano}}_{\mathrm{G}}}{R \cdot T} \cdot \left(p^{\mathrm{ano}}_{\mathrm{in,O_2}} - p^{\mathrm{ano}}_{\mathrm{out,O_2}}\right) - N^{\mathrm{ano}}_{\mathrm{phys,O_2}} \cdot A^{\mathrm{ano}}_{\mathrm{GL}} + f_{\mathrm{G,O_2}} \cdot \dot{n}^{\mathrm{ano}}_{\mathrm{R,O_2}} \tag{3.4}$$

Dissolved H_2 in the cathodic half cell:

$$0 = \dot{V}^{\mathrm{cat}}_{\mathrm{L}} \cdot \left(c^{\mathrm{cat}}_{\mathrm{in,H_2}} - c^{\mathrm{cat}}_{\mathrm{out,H_2}}\right) + N^{\mathrm{cat}}_{\mathrm{phys,H_2}} \cdot A^{\mathrm{cat}}_{\mathrm{GL}} - N_{\mathrm{cross,H_2}} \cdot A_{\mathrm{d}} + \left(1 - f_{\mathrm{G,H_2}}\right) \cdot \dot{n}^{\mathrm{cat}}_{\mathrm{R,H_2}} \tag{3.5}$$

Dissolved O_2 in the cathodic half cell:

$$0 = \dot{V}^{\mathrm{cat}}_{\mathrm{L}} \cdot \left(c^{\mathrm{cat}}_{\mathrm{in,O_2}} - c^{\mathrm{cat}}_{\mathrm{out,O_2}}\right) + N^{\mathrm{cat}}_{\mathrm{phys,O_2}} \cdot A^{\mathrm{cat}}_{\mathrm{GL}} - N_{\mathrm{cross,O_2}} \cdot A_{\mathrm{d}} \tag{3.6}$$

Gaseous H_2 in the cathodic half cell:

$$0 = \frac{\dot{V}^{\mathrm{cat}}_{\mathrm{G}}}{R \cdot T} \cdot \left(p^{\mathrm{cat}}_{\mathrm{in,H_2}} - p^{\mathrm{cat}}_{\mathrm{out,H_2}}\right) - N^{\mathrm{cat}}_{\mathrm{phys,H_2}} \cdot A^{\mathrm{cat}}_{\mathrm{GL}} + f_{\mathrm{G,H_2}} \cdot \dot{n}^{\mathrm{cat}}_{\mathrm{R,H_2}} \tag{3.7}$$

Gaseous O_2 in the cathodic half cell:

$$0 = -\frac{\dot{V}_{\mathrm{G}}^{\mathrm{cat}}}{R \cdot T} \cdot \left(p_{\mathrm{in,O_2}}^{\mathrm{cat}} - p_{\mathrm{out,O_2}}^{\mathrm{cat}}\right) - N_{\mathrm{phys,O_2}}^{\mathrm{cat}} \cdot A_{\mathrm{GL}}^{\mathrm{cat}} \tag{3.8}$$

3.2.2. The general form of steady-state material balances in the gas separators

As illustrated in Figure 3.3, the simplified alkaline water electrolysis plant consists of two gas separators. Each gas separator is associated with its corresponding half-cell j. The mass balances for the gas separators are written by considering Figure 3.2. Due to the effect of gas crossover, the two-phase stream that enters the gas separator consists of the primary product of the associated half-cell j, as well as the cross-permeated product. Therefore, each gas separator is characterized by two mass balances for the liquid phase and two mass balances for the gaseous phase. In total, the simplified electrolysis plant consists of eight material balances for the gas separators. The general form of the steady-state mass balance in the gas separators is the following:

$$0 = \begin{pmatrix} \text{Mass flow} \\ \text{rate of} \\ \text{component A} \\ \text{into system} \end{pmatrix} - \begin{pmatrix} \text{Mass flow} \\ \text{rate of} \\ \text{component A} \\ \text{out of system} \end{pmatrix}$$

The units of each term in the dynamic material balances are in $\mathrm{mol} \cdot \mathrm{s}^{-1}$. The gas separators can be modeled as CSTR ideal reactors. Because there is no chemical reaction that takes place inside the gas separators, the reaction rate terms in the generic form of the material balances are neglected. Furthermore, since the mass balances are associated with the steady-state case the rate of accumulation of mass in the system is equal to zero. The inflow of each gas separator is the outflow of its corresponding half-cell j (Figure 3.3). The gaseous inflow to the gas separator obeys the ideal gas law. The liquid inflow to the gas separator is characterized by the outlet dissolved concentration of the products in the bulk liquid electrolyte $c_{\mathrm{out},i}^{j}$. As a result, the steady-state material balances will be the following:

Dissolved H_2 in the anodic gas separator:

$$0 = \dot{V}_{\mathrm{L}}^{\mathrm{ano}} \cdot \left(c_{\mathrm{out,H_2}}^{\mathrm{ano}} - c_{\mathrm{out,H_2}}^{\mathrm{sep,ano}}\right) \tag{3.9}$$

Dissolved O_2 in the anodic gas separator:

$$0 = \dot{V}_{\mathrm{L}}^{\mathrm{ano}} \cdot \left(c_{\mathrm{out,O_2}}^{\mathrm{ano}} - c_{\mathrm{out,O_2}}^{\mathrm{sep,ano}}\right) \tag{3.10}$$

Gaseous H_2 in the anodic gas separator:

$$0 = \frac{\dot{V}_{\mathrm{G}}^{\mathrm{ano}}}{R \cdot T} \cdot \left(p_{\mathrm{out,H_2}}^{\mathrm{ano}} - p_{\mathrm{out,H_2}}^{\mathrm{sep,ano}}\right) \tag{3.11}$$

Gaseous O_2 in the anodic gas separator:

$$0 = \frac{\dot{V}_{\mathrm{G}}^{\mathrm{ano}}}{R \cdot T} \cdot \left(p_{\mathrm{out,O_2}}^{\mathrm{ano}} - p_{\mathrm{out,O_2}}^{\mathrm{sep,ano}} \right) \tag{3.12}$$

Dissolved H_2 in the cathodic gas separator:

$$0 = \dot{V}_{\mathrm{L}}^{\mathrm{cat}} \cdot \left(c_{\mathrm{out,H_2}}^{\mathrm{cat}} - c_{\mathrm{out,H_2}}^{\mathrm{sep,cat}} \right) \tag{3.13}$$

Dissolved O_2 in the cathodic gas separator:

$$0 = \dot{V}_{\mathrm{L}}^{\mathrm{cat}} \cdot \left(c_{\mathrm{out,O_2}}^{\mathrm{cat}} - c_{\mathrm{out,O_2}}^{\mathrm{sep,cat}} \right) \tag{3.14}$$

Gaseous H_2 in the cathodic gas separator:

$$0 = \frac{\dot{V}_{\mathrm{G}}^{\mathrm{cat}}}{R \cdot T} \cdot \left(p_{\mathrm{out,H_2}}^{\mathrm{cat}} - p_{\mathrm{out,H_2}}^{\mathrm{sep,cat}} \right) \tag{3.15}$$

Gaseous O_2 in the cathodic gas separator:

$$0 = \frac{\dot{V}_{\mathrm{G}}^{\mathrm{cat}}}{R \cdot T} \cdot \left(p_{\mathrm{out,O_2}}^{\mathrm{cat}} - p_{\mathrm{out,O_2}}^{\mathrm{sep,cat}} \right) \tag{3.16}$$

In order the liquid material balances that are described by equations (3.9)-(3.10) and (3.13)-(3.14) to be valid, the outlet dissolved concentration of species i in the compartment j, $c_{\mathrm{out},i}^{j}$, must be equal to the separator's outlet dissolved concentration of species i, $c_{\mathrm{out},i}^{\mathrm{sep},j}$.Therefore, for the steady-state liquid material balances in the gas separators, it holds that:

$$c_{\mathrm{out},i}^{\mathrm{sep},j} = c_{\mathrm{out},i}^{j} \tag{3.17}$$

Similarly, in order the gaseous material balances that are described by equations (3.11)-(3.12) and (3.15)-(3.16) to be valid, the outlet partial pressure of species i in the half cell j, $p_{\mathrm{out},i}^{j}$ needs to be equal to the separator's outlet partial pressure of species i in the compartment j, $p_{\mathrm{out},i}^{\mathrm{sep},j}$. Therefore, for the steady-state gaseous material balances in the gas separators, it holds that:

$$p_{\mathrm{out},i}^{\mathrm{sep},j} = p_{\mathrm{out},i}^{j} \tag{3.18}$$

3.3. The general form of the dynamic material balances

In the following, the general form of the dynamic material balances for alkaline water electrolysers are introduced. In the first subsection, the dynamic material balances for the electrolysis cell are given. Similarly, in the next subsection, the dynamic material balances for the gas separators are provided.

3.3.1. The general form of dynamic material balances in the electrolysis cell

As explained in Chapter 3.2.1, in total there are eight material balances. The same also holds for the dynamic material balances. Therefore, the general form of the dynamic material balances for the electrolysis cell will be:

$$\begin{pmatrix}\text{Rate of}\\ \text{accumulation}\\ \text{of mass}\\ \text{in system}\end{pmatrix} = \begin{pmatrix}\text{Mass flow}\\ \text{rate of}\\ \text{component A}\\ \text{into system}\end{pmatrix} - \begin{pmatrix}\text{Mass flow}\\ \text{rate of}\\ \text{component A}\\ \text{out of system}\end{pmatrix} + \begin{pmatrix}\text{Rate of}\\ \text{generation of}\\ \text{mass of}\\ \text{component A}\\ \text{from reaction}\end{pmatrix}$$

The units of each term in the dynamic material balance are in $\mathrm{mol}\cdot\mathrm{s}^{-1}$. The rate of depletion of mass in the material balance is neglected because it is assumed that there are no recombination reactions. For the dynamic material balances the rate of accumulation of mass is not neglected. The applied dynamic mass balance for the electrolysis cell is based on Figure 3.1. The dynamic mass balances for the electrolysis cell are described by equations (3.19)-(3.26).

Dissolved H_2 in the anodic half-cell:

$$\frac{dN^{\mathrm{ano}}_{\mathrm{H_2,liq}}}{dt} = \dot{V}^{\mathrm{ano}}_{\mathrm{L}} \cdot \left(c^{\mathrm{ano}}_{\mathrm{in,H_2}} - c^{\mathrm{ano}}_{\mathrm{out,H_2}}\right) + N^{\mathrm{ano}}_{\mathrm{phys,H_2}} \cdot A^{\mathrm{ano}}_{\mathrm{GL}} + N_{\mathrm{cross,H_2}} \cdot A_{\mathrm{d}} \tag{3.19}$$

Dissolved O_2 in the anodic half-cell:

$$\frac{dN^{\mathrm{ano}}_{\mathrm{O_2,liq}}}{dt} = \dot{V}^{\mathrm{ano}}_{\mathrm{L}} \cdot \left(c^{\mathrm{ano}}_{\mathrm{in,O_2}} - c^{\mathrm{ano}}_{\mathrm{out,O_2}}\right) + N^{\mathrm{ano}}_{\mathrm{phys,O_2}} \cdot A^{\mathrm{ano}}_{\mathrm{GL}} + N_{\mathrm{cross,O_2}} \cdot A_{\mathrm{d}} + \left(1 - f_{\mathrm{G,O_2}}\right) \cdot \dot{n}^{\mathrm{ano}}_{\mathrm{R,O_2}} \tag{3.20}$$

Gaseous H_2 in the anodic half cell:

$$\frac{dN^{\mathrm{ano}}_{\mathrm{H_2,gas}}}{dt} = \frac{\dot{V}^{\mathrm{ano}}_{\mathrm{G}}}{R \cdot T} \cdot \left(p^{\mathrm{ano}}_{\mathrm{in,H_2}} - p^{\mathrm{ano}}_{\mathrm{out,H_2}}\right) - N^{\mathrm{ano}}_{\mathrm{phys,H_2}} \cdot A^{\mathrm{ano}}_{\mathrm{GL}} \tag{3.21}$$

Gaseous O_2 in the anodic half cell:

$$\frac{dN^{\mathrm{ano}}_{\mathrm{O_2,gas}}}{dt} = \frac{\dot{V}^{\mathrm{ano}}_{\mathrm{G}}}{R \cdot T} \cdot \left(p^{\mathrm{ano}}_{\mathrm{in,O_2}} - p^{\mathrm{ano}}_{\mathrm{out,O_2}}\right) - N^{\mathrm{ano}}_{\mathrm{phys,O_2}} \cdot A^{\mathrm{ano}}_{\mathrm{GL}} + f_{\mathrm{G,O_2}} \cdot \dot{n}^{\mathrm{ano}}_{\mathrm{R,O_2}} \tag{3.22}$$

Dissolved H_2 in the cathodic half cell:

$$\frac{dN^{\mathrm{cat}}_{\mathrm{H_2,liq}}}{dt} = \dot{V}^{\mathrm{cat}}_{\mathrm{L}} \cdot \left(c^{\mathrm{cat}}_{\mathrm{in,H_2}} - c^{\mathrm{cat}}_{\mathrm{out,H_2}}\right) + N^{\mathrm{cat}}_{\mathrm{phys,H_2}} \cdot A^{\mathrm{cat}}_{\mathrm{GL}} - N_{\mathrm{cross,H_2}} \cdot A_{\mathrm{d}} + \left(1 - f_{\mathrm{G,H_2}}\right) \cdot \dot{n}^{\mathrm{cat}}_{\mathrm{R,H_2}} \tag{3.23}$$

Dissolved O_2 in the cathodic half cell:

$$\frac{dN^{\mathrm{cat}}_{\mathrm{O_2,liq}}}{dt} = \dot{V}^{\mathrm{cat}}_{\mathrm{L}} \cdot \left(c^{\mathrm{cat}}_{\mathrm{in,O_2}} - c^{\mathrm{cat}}_{\mathrm{out,O_2}}\right) + N^{\mathrm{cat}}_{\mathrm{phys,O_2}} \cdot A^{\mathrm{cat}}_{\mathrm{GL}} - N_{\mathrm{cross,O_2}} \cdot A_{\mathrm{d}} \tag{3.24}$$

Gaseous H_2 in the cathodic half cell:

$$\frac{dN^{\text{cat}}_{\text{H}_2,\text{gas}}}{dt} = \frac{\dot{V}^{\text{cat}}_{\text{G}}}{R \cdot T} \cdot \left(p^{\text{cat}}_{\text{in},\text{H}_2} - p^{\text{cat}}_{\text{out},\text{H}_2}\right) - N^{\text{cat}}_{\text{phys},\text{H}_2} \cdot A^{\text{cat}}_{\text{GL}} + f_{\text{G},\text{H}_2} \cdot \dot{n}^{\text{cat}}_{\text{R},\text{H}_2} \tag{3.25}$$

Gaseous O_2 in the cathodic half cell:

$$\frac{dN^{\text{cat}}_{\text{O}_2,\text{gas}}}{dt} = -\frac{\dot{V}^{\text{cat}}_{\text{G}}}{R \cdot T} \cdot \left(p^{\text{cat}}_{\text{in},\text{O}_2} - p^{\text{cat}}_{\text{out},\text{O}_2}\right) - N^{\text{cat}}_{\text{phys},\text{O}_2} \cdot A^{\text{cat}}_{\text{GL}} \tag{3.26}$$

3.3.2. The general form of dynamic material balances in the gas separators

As analysed in Chapter 3.2.2, in total, there are eight steady-state material balances for the gas separators of the electrolysis plant. The same holds for the case of the dynamic material balances of the gas separators. Therefore, the general form of the dynamic material balances for the electrolysis cell will be:

$$\begin{pmatrix} \text{Rate of} \\ \text{accumulation} \\ \text{of mass} \\ \text{in system} \end{pmatrix} = \begin{pmatrix} \text{Mass flow} \\ \text{rate of} \\ \text{component A} \\ \text{into system} \end{pmatrix} - \begin{pmatrix} \text{Mass flow} \\ \text{rate of} \\ \text{component A} \\ \text{out of system} \end{pmatrix}$$

The units of each term in the dynamic material balances are in $\text{mol} \cdot \text{s}^{-1}$. The gas separators can be modeled as CSTR ideal reactors. Because there is no chemical reaction that takes place inside the gas separators, the reaction rate terms in the generic form of the material balances are neglected. For the dynamic material balances, the rate of accumulation of mass in the system is not neglected. The inflow of each gas separator is the outflow of its corresponding half-cell j (Figure 3.3). The gaseous inflow to the gas separator obeys the ideal gas law. The liquid inflow to the gas separator is characterized by the outlet dissolved concentration of the products in the bulk liquid electrolyte $c^{j}_{\text{out},i}$. As a result, the dynamic material balances will be the following:

Dissolved H_2 in the anodic gas separator:

$$\frac{dN^{\text{ano,sep}}_{\text{H}_2,\text{liq}}}{dt} = \dot{V}^{\text{ano}}_{\text{L}} \cdot \left(c^{\text{ano}}_{\text{out},\text{H}_2} - c^{\text{sep,ano}}_{\text{out},\text{H}_2}\right) \tag{3.27}$$

Dissolved O_2 in the anodic gas separator:

$$\frac{dN^{\text{ano,sep}}_{\text{O}_2,\text{liq}}}{dt} = \dot{V}^{\text{ano}}_{\text{L}} \cdot \left(c^{\text{ano}}_{\text{out},\text{O}_2} - c^{\text{sep,ano}}_{\text{out},\text{O}_2}\right) \tag{3.28}$$

Gaseous H_2 in the anodic gas separator:

$$\frac{dN^{\text{ano,sep}}_{\text{H}_2,\text{gas}}}{dt} = \frac{\dot{V}^{\text{ano}}_{\text{G}}}{R \cdot T} \cdot \left(p^{\text{ano}}_{\text{out},\text{H}_2} - p^{\text{sep,ano}}_{\text{out},\text{H}_2}\right) \tag{3.29}$$

Gaseous O_2 in the anodic gas separator:

$$\frac{dN_{O_2,gas}^{ano,sep}}{dt} = \frac{\dot{V}_G^{ano}}{R \cdot T} \cdot \left(p_{out,O_2}^{ano} - p_{out,O_2}^{sep,ano}\right) \tag{3.30}$$

Dissolved H_2 in the cathodic gas separator:

$$\frac{dN_{H_2,liq}^{cat,sep}}{dt} = \dot{V}_L^{cat} \cdot \left(c_{out,H_2}^{cat} - c_{out,H_2}^{sep,cat}\right) \tag{3.31}$$

Dissolved O_2 in the cathodic gas separator:

$$\frac{dN_{O_2,liq}^{cat,sep}}{dt} = \dot{V}_L^{cat} \cdot \left(c_{out,O_2}^{cat} - c_{out,O_2}^{sep,cat}\right) \tag{3.32}$$

Gaseous H_2 in the cathodic gas separator:

$$\frac{dN_{H_2,gas}^{cat,sep}}{dt} = \frac{\dot{V}_G^{cat}}{R \cdot T} \cdot \left(p_{out,H_2}^{cat} - p_{out,H_2}^{sep,cat}\right) \tag{3.33}$$

Gaseous O_2 in the cathodic gas separator:

$$\frac{dN_{O_2,gas}^{cat,sep}}{dt} = \frac{\dot{V}_G^{cat}}{R \cdot T} \cdot \left(p_{out,O_2}^{cat} - p_{out,O_2}^{sep,cat}\right) \tag{3.34}$$

3.4. Defining the unknown terms in the dynamic mass balances

The mathematical expressions that define the material balances (3.1)-(3.8), (3.17)-(3.18) and (3.19)-(3.34), contain numerous unknown terms. In order to solve the equations, some physical parameters and boundary conditions need to be defined.

The aim of this section is the mathematical definition of the unknown terms in the steady-state and dynamic mass balances. In the first subsection, the boundary conditions will be given. Next, all the terms in the mass balances will be thoroughly analyzed such that the system of equations becomes coupled. The unknown terms will be expressed using empirical relations, or physically based models.

3.4.1. Boundary conditions

During the dynamic switching of electrolyte cycles process, the plant operates for a specific time range in *mixed-mode*, and then it switches to the *partly-separated* mode of operation. The boundary conditions have been implemented in a similar manner to Haug et al. [34]. However, in the dynamic and steady-state mass balances of this modeling approach, the boundary conditions are associated with the outflows of the gas separators.

During the *mixed-mode*, both electrolyte cycles are mixed before re-entering the electrolysis cell. Assuming that the liquid electrolyte is incompressible during both modes of operation, the mixed liquid volumetric flow rate $\dot{V}_{mix}$ will be equal to:

$$\dot{V}_{\mathrm{mix}} = \dot{V}_{\mathrm{L}}^{\mathrm{ano}} + \dot{V}_{\mathrm{L}}^{\mathrm{cat}} \tag{3.35}$$

The mixed liquid concentration of the dissolved species at the exit of the ideal mixer will be equal to the inlet concentration in both half cells:

$$c_i^{\mathrm{mix}} = c_{\mathrm{in},i}^{j} \tag{3.36}$$

Finally, the dissolved mixed concentration c_i^{mix} can be found by applying a mass balance for the ideal mixer before the inlet of the electrolysis cell (see Figure 3.3) for each species.

$$\dot{V}_{\mathrm{mix}} \cdot c_{\mathrm{H_2}}^{\mathrm{mix}} = \dot{V}_{\mathrm{L}}^{\mathrm{ano}} \cdot c_{\mathrm{out,H_2}}^{\mathrm{sep,ano}} + \dot{V}_{\mathrm{L}}^{\mathrm{cat}} \cdot c_{\mathrm{out,H_2}}^{\mathrm{sep,cat}} \tag{3.37}$$

$$\dot{V}_{\mathrm{mix}} \cdot c_{\mathrm{O_2}}^{\mathrm{mix}} = \dot{V}_{\mathrm{L}}^{\mathrm{ano}} \cdot c_{\mathrm{out,O_2}}^{\mathrm{sep,ano}} + \dot{V}_{\mathrm{L}}^{\mathrm{cat}} \cdot c_{\mathrm{out,O_2}}^{\mathrm{sep,cat}} \tag{3.38}$$

When the simplified alkaline water electrolysis plant switches to the *partly-separated mode*, the liquid electrolyte stream that exits its gas separator re-enters its corresponding half-cell without mixing with the stream from the opposite half-cell (see dashed lines in Figure 3.3). As a result, since it is assumed that there is no additional mass transfer in the interconnecting piping, the liquid concentration of the species at the inlet of the half-cell $c_{\mathrm{in},i}^{j}$ will be equal to the liquid concentration of the species at the exit of the gas separators $c_{\mathrm{out},i}^{\mathrm{sep},j}$.

$$c_{\mathrm{in,H_2}}^{\mathrm{ano}} = c_{\mathrm{out,H_2}}^{\mathrm{sep,ano}} \tag{3.39}$$

$$c_{\mathrm{in,H_2}}^{\mathrm{cat}} = c_{\mathrm{out,H_2}}^{\mathrm{sep,cat}} \tag{3.40}$$

$$c_{\mathrm{in,O_2}}^{\mathrm{ano}} = c_{\mathrm{out,O_2}}^{\mathrm{sep,ano}} \tag{3.41}$$

$$c_{\mathrm{in,O_2}}^{\mathrm{cat}} = c_{\mathrm{out,O_2}}^{\mathrm{sep,cat}} \tag{3.42}$$

For the steady-state mode, the outlet dissolved concentration of species i in the separator of the compartment j, $c_{\mathrm{out},i}^{\mathrm{sep},j}$, in equations (3.37)-(3.42), will be substituted by the outlet dissolved concentration in the electrolyte cell, $c_{\mathrm{out},i}^{j}$ due to equation (3.17).

In the present model, the distinction between mixed-mode and partly-separated mode is made by applying the boundary conditions (3.37)-(3.38) and (3.39)-(3.42), respectively. Therefore, the development of the dynamic switching of electrolyte cycles model requires the changeover between these two sets of boundary conditions.

3.4.2. Pressure terms

In this subsection, the partial pressures $p_{\mathrm{in},i}^{j}$ and $p_{\mathrm{out},i}^{j}$ will be analyzed. Furthermore, the total anodic or cathodic pressure exerted on the gaseous product in each half-cell p_{tot}^{j} will be given in terms of known fluid dynamics relations. Based on the assumptions and fluid dynamics definitions some of the terms can be neglected or simplified. For

the steady-state model, the partial pressures appear in the gaseous mass balances (3.3)-(3.4) and (3.7)-(3.8). For the dynamic model, the partial pressures appear in the gaseous mass balances (3.21)-(3.22) and (3.25)-(3.26).

The inlet partial pressures $p^j_{\mathrm{in},i}$ can be neglected. In Chapter 3.1.1, it was assumed that no gaseous product can be recirculated throughout the system. Therefore it holds that:

$$p^j_{\mathrm{in},i} = 0 \tag{3.43}$$

In the work of Leroy et al. [54], hydrogen and oxygen species that are produced in the vicinity of the electrode are “wet”. Therefore, the produced gases consist of water vapor which is in equilibrium with the water from the liquid electrolyte solution. The water vapor partial pressure $p_{\mathrm{H_2O}}$ which is in equilibrium with the electrolyte solution can be calculated based on the work by Balej et al. [55], in Appendix A.1.

Considering the cross-permeated product, the total pressure exerted on the gaseous product in each half cell is equal to:

$$p^{\mathrm{ano}}_{\mathrm{tot}} = p^{\mathrm{ano}}_{\mathrm{out,H_2}} + p^{\mathrm{ano}}_{\mathrm{out,O_2}} + p_{\mathrm{H_2O}} \tag{3.44}$$

$$p^{\mathrm{cat}}_{\mathrm{tot}} = p^{\mathrm{cat}}_{\mathrm{out,H_2}} + p^{\mathrm{cat}}_{\mathrm{out,O_2}} + p_{\mathrm{H_2O}} \tag{3.45}$$

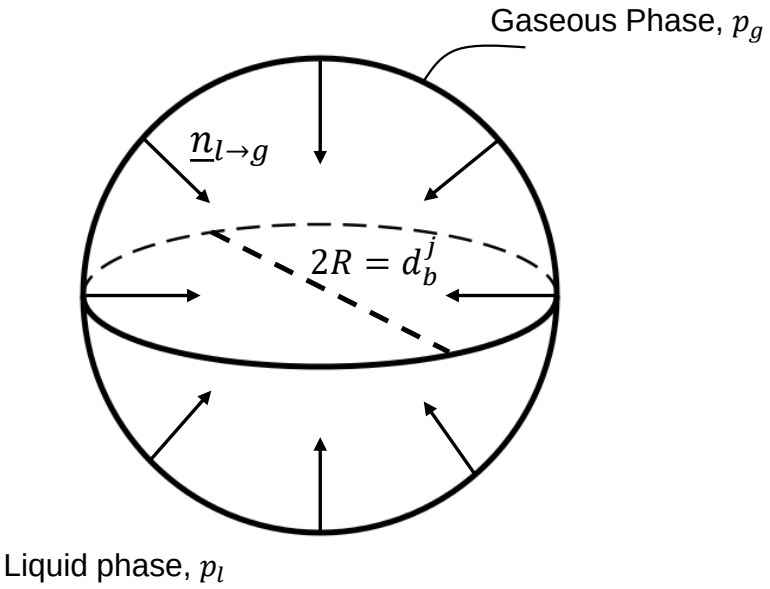

Figure 3.4: Application of the Young-Laplace equation for the calculation of the surface tension in a perfectly spherical bubble.

The definition of the total pressure exerted on the gaseous product in each half cell from the equations (3.44)-(3.45), allows the connection of the outlet partial pressure of the primary product with the outlet partial pressure of the cross-permeated product. To define the total pressure p^j_{tot}, the approach of Haug et al. [34] is followed. More specifically, the connection of the gas separators with the atmosphere results

in the exertion of an absolute pressure p^j on the liquid electrolyte which is equal to the atmospheric pressure. During electrolysis, the gaseous product in the half-cell builds up a pressure difference $\Delta p_{g\to l}$ with respect to the absolute pressure of the liquid electrolyte, due to the effect of the surface tension. The pressure difference $\Delta p_{g\to l}$ between the liquid and gaseous phase can be calculated by implementing the Young-Laplace equation. The general expression for the Young-Laplace equation is the following:

$$\Delta p_{g\to l} \equiv p_l - p_g = \gamma \nabla_s \cdot \underline{n}_{l\to g} = \gamma \left(\frac{1}{R_1} + \frac{1}{R_2} \right)$$

Where γ is the surface tension of the liquid electrolyte in $\mathrm{N\,m^{-1}}$. In Figure 3.4, the term $n_{l\to g}$ is the unit normal pointing towards the gaseous phase and $R_{1,2}$ are the radii of curvature. Since it is assumed that the bubbles are monodisperse and perfectly spherical it holds that:

$$R_1 = R_2 = \frac{d_{\mathrm{b}}^j}{2}$$

Where d_{b}^j is the diameter of produced bubbles in m. Furthermore, from Figure 3.4 the unit normal points towards the center of the bubble. Therefore, the divergence will be negative. As a result, the pressure difference will be equal to:

$$\Delta p_{g\to l} \equiv p_l - p_g = -\gamma \frac{4}{d_{\mathrm{b}}^j}$$

$$p_g = p_l + \gamma \frac{4}{d_{\mathrm{b}}^j}$$

For the alkaline water electrolysis, the term p_g is the total pressure that is exerted on the gaseous phase p_{tot}^j. The term p_l is the absolute pressure that is applied on the liquid electrolyte p^j due to the existence of pumps. Therefore it will be:

$$p_{\mathrm{tot}}^{\mathrm{ano}} = p^{\mathrm{ano}} + \gamma \frac{4}{d_{\mathrm{b}}^{\mathrm{ano}}} \tag{3.46}$$

$$p_{\mathrm{tot}}^{\mathrm{cat}} = p^{\mathrm{cat}} + \gamma \frac{4}{d_{\mathrm{b}}^{\mathrm{cat}}} \tag{3.47}$$

The bubble diameter, d_{b}^j, is shown in Chapter 3.4.5.

Finally,the surface tension of the liquid electrolyte can be approximated as a function of the temperature and the mass fraction of KOH in the liquid electrolyte solution from the work of Feldkamp [56], in Appendix A.2.

3.4.3. The accumulation terms

The left-hand side of every dynamic material balance (3.19)-(3.34) contains the accumulation terms dN/dt. The focus of this subsection is their definition such that the system of the ordinary differential equations becomes solvable. This subsection is not applicable for the steady-state mass balances. In Figure 3.3, the liquid volumes in the electrolysis cell and the gas separators contain the dissolved species $N_{i,\mathrm{liq}}^{j,\mathrm{sep}}$, $N_{i,\mathrm{liq}}^{j}$ in

moles. The amount of species in the gaseous product for the electrolysis cell and the gas separators is given by the quantities $N_{i,\mathrm{gas}}^{j,\mathrm{sep}}$, and $N_{i,\mathrm{gas}}^{j}$ in moles, respectively.

When the species dissolve in the liquid electrolyte, they instantly reach the outlet dissolved concentration $c_{\mathrm{out},i}^{j}$ and $c_{\mathrm{out},i}^{\mathrm{sep},j}$, due to the CSTR assumption. Taking advantage of the fact that the units of the concentration are in $\mathrm{mol} \cdot \mathrm{m}^{-3}$, the amount of the dissolved species in the liquid electrolyte can be re-written:

$$N_{i,\mathrm{liq}}^{j} = c_{\mathrm{out},i}^{j} \cdot V_{\mathrm{liq}}^{j} \tag{3.48}$$

$$N_{i,\mathrm{liq}}^{j,\mathrm{sep}} = c_{\mathrm{out},i}^{\mathrm{sep},j} \cdot V_{\mathrm{liq}}^{\mathrm{sep},j} \tag{3.49}$$

As analyzed in Chapter 3.1.3, the liquid volumes are steady with time. Therefore, the only term that changes with time and remains in the derivative at the left-hand side of the material balances will be the outlet dissolved concentration.

In the gaseous material balances, the amount of species in the gaseous product in the electrolysis cell and the gas separators $N_{i,\mathrm{gas}}^{j}$, $N_{i,\mathrm{gas}}^{j,\mathrm{sep}}$ can be approximated by the ideal gas law:

$$N_{i,\mathrm{gas}}^{j} = \frac{p_{\mathrm{out},i}^{j} \cdot V_{\mathrm{gas}}^{j}}{R \cdot T} \tag{3.50}$$

$$N_{i,\mathrm{gas}}^{j,\mathrm{sep}} = \frac{p_{\mathrm{out},i}^{\mathrm{sep},j} \cdot V_{\mathrm{gas}}^{\mathrm{sep},j}}{R \cdot T} \tag{3.51}$$

Again, as analyzed in Chapter 3.1.3, the gaseous volumes are steady with time. The temperature in the electrolysis cell and the gas separators is also constant with time. Therefore, the only term that remains in the accumulation term will be the outlet partial pressure $p_{\mathrm{out},i}^{j}$ or $p_{\mathrm{out},i}^{\mathrm{sep},j}$.

Finally, the gaseous volumes in the electrolysis cell V_{gas}^{j} are calculated in Chapter 3.4.5. Knowing the geometrical volume of the half cell V_{hcell}, the liquid volumes in the electrolysis cell can be calculated by using equation (3.52).

$$V_{\mathrm{liq}}^{j} = V_{\mathrm{hcell}} - V_{\mathrm{gas}}^{j} \tag{3.52}$$

For the gas separators, their geometrical volume V_{sep}^{j} is also known. Furthermore, the existence of a liquid level detector in the gas separator of XINTC, can help to monitor the liquid volume inside the gas separator $V_{\mathrm{liq}}^{\mathrm{sep},j}$. Therefore, since the $V_{\mathrm{liq}}^{\mathrm{sep},j}$ term is always known, the gaseous volume in the gas separator can be calculated by using equation (3.53).

$$V_{\mathrm{gas}}^{\mathrm{sep}} = V_{\mathrm{sep}}^{j} - V_{\mathrm{liq}}^{\mathrm{sep},j} \tag{3.53}$$

3.4.4. The gas evolution terms

As analyzed in Chapter 2.2.1, when alkaline electrolysis starts occurring, the whole product is transferred to the electrode-electrolyte interface in dissolved form. The reaction rate $\dot{n}_{\mathrm{R},i}^{j}$ obeys Faraday's Law and is given by equation (3.54).

$$\dot{n}_{\mathrm{R},i}^{j} = \frac{J\nu_i}{nF} \cdot A_{\mathrm{el}} \tag{3.54}$$

Where A_{el}, is the electrode area. The stoichiometric number ν_i will be $\nu_{\mathrm{H_2}} = 1$ for hydrogen which is produced in the cathode, and $\nu_{\mathrm{O_2}} = 0.5$ for oxygen which is produced in the anode, when the charge transfer equals $n = 2$ from reactions (2.1) and (2.2).

When the product is transferred to the liquid electrolyte-electrode interface in dissolved form, the concentration boundary layer becomes supersaturated. In the literature [29], it has been reported that the supersaturation can be 80 times higher than the equilibrium concentration. The existence of nucleation sites on the electrode surface enforces heterogeneous nucleation to begin and product bubbles start forming due to desorption of the supersaturated species in the concentration boundary layer. Furthermore, the effect of micro-convection and macro-convection (Chapter 2.2.2) can enhance the mass transfer of the dissolved species to the gaseous phase on the electrode-electrolyte interface.

According to Vogt [29], the activation of the nucleation sites for the release of the product in the gaseous phase strongly depends on the operating conditions of the electrolyser, and more specifically on the current density. When the current density is very low, the concentration of the dissolved species in the electrolyte-electrode interface is very low and the nucleation sites are not activated. On the contrary, in higher current densities the concentration of the dissolved species in the electrolyte-electrode interface is increased such that the product obtains a high degree of supersaturation and the nucleation sites on the electrode surface are activated.

In Chapter 2.2.4 the gas evolution efficiency $f_{\mathrm{G},i}$ was introduced. The gas evolution efficiency can quantify the formation of gas in the concentration boundary layer due to the desorption of supersaturated species and the simultaneous action of the subsequent mass transfer steps of micro-convection and macro-convection. Furthermore, the gas evolution efficiency must be a function of the current density. For the present study, the gas evolution efficiency of hydrogen and oxygen is approximated from the experimental steady-state impurities which are shown in Chapter 4.3. The methodology followed to extract the gas evolution efficiencies is shown in Chapter 5.3.1. The hydrogen and oxygen gas evolution efficiencies are described by equation (5.5) and (5.6), respectively.

$$f_{\mathrm{G,H_2}} = 0.87554 \cdot J^{0.04963}$$

$$f_{\mathrm{G,O_2}} = 0.84$$

Where J is the applied current density and is given in $\mathrm{kA\ m^{-2}}$. The hydrogen and oxygen gas evolution efficiencies are valid for the current density range $0.75\ \mathrm{kA\ m^{-2}} \leq J \leq 3\mathrm{kA\ m^{-2}}$. Finally, for the oxygen gas evolution, it has to be noted that it is was not possible to find a dependency on the current density. A similar trend for the oxygen gas evolution efficiency can be found in the publication of Haug et al. [34].

3.4.5. Mass transfer in the electrolyte bulk

After the initial gas evolution at the electrode-electrolyte interface, the dissolved species leave the boundary layer, and they are transferred to the electrolyte bulk due to diffusion and superimposed convection. The concentration of the dissolved species in the electrolyte bulk is characterized by the quantity $c^j_{\text{out},i}$ in the dynamic material balances. This quantity is unknown and is calculated by solving the system of mass balances for both the steady state and transient state. Depending on the species (hydrogen or oxygen) and the operating conditions (current density, temperature, pressure, flow rate, electrolyte concentration), the electrolyte bulk can be supersaturated.

In the steady-state mass balances (3.1)-(3.8), and the dynamic material balances (3.19)-(3.26), the physisorption mass transfer flux $N^j_{\text{phys},i}$ also appears. According to Vogt [33], besides the gas evolution in the concentration boundary layer on the electrode, additional gas evolution can take place in the electrolyte bulk due to the supersaturation of the dissolved species. The $N^j_{\text{phys},i}$ term, considers the additional gas evolution in the electrolyte bulk. When the $N^j_{\text{phys},i}$ term is negative, desorption takes place, and there is a mass transfer from the supersaturated liquid electrolyte to the gaseous bubbles which rise due to the buoyancy effect.

In general, the total mass transfer from the liquid to the gaseous phase $\dot{\Phi}_{\text{tot}}$ (in mol/s) can be calculated as the superposition of diffusive and convective mass transfer mechanisms:

$$\dot{\Phi}_{\text{tot}} = \dot{\Phi}_{\text{conv}} + \dot{\Phi}_{\text{diff}}$$

Because the solubility of hydrogen and oxygen in the electrolyte bulk is low, the convective mass transfer mechanism can be neglected. As a result, the Φ_{tot} term will be only due to diffusion. Furthermore, the $\dot{\Phi}_{\text{diff}}$ term can be modeled with the film theory [35], as it was shown in Chapter 2.2.3. Therefore, to model the mass transfer in the electrolyte bulk, equation (2.12) can be used:

$$N^j_{\text{phys},i} = k^j_{\text{L},i} \cdot \left(c^{*,j}_i - c^j_{\text{out},i}\right) \tag{3.55}$$

Where, $k^j_{\text{L},i}$ is the effective liquid mass transfer coefficient in $\text{m} \cdot \text{s}^{-1}$, and $c^{*,j}_i$ is the equilibrium concentration of species i, in the compartment j, in $\text{mol} \cdot \text{m}^{-3}$. The goal in the next paragraphs will be to deduce mathematical expressions for the gas-liquid interface area A^j_{GL}, the effective mass transfer coefficient $k^j_{\text{L},i}$ and the equilibrium concentration $c^{*,j}_i$.

In Chapter 3.1.1, it was assumed that the bubbles are monodisperse and perfectly spherical. As a result, the volume V^j_{b} and the surface area S^j_{b} of a single bubble will be equal to:

$$V^j_{\text{b}} = \frac{\pi}{6} \cdot \left(d^j_{\text{b}}\right)^3 \tag{3.56}$$

$$S^j_{\text{b}} = \pi \cdot \left(d^j_{\text{b}}\right)^2 \tag{3.57}$$

To express mathematically the diameter of a single bubble the experimental investigations of Haug et al. [34] will be used. From the performed experiments, it was found

out that the diameter of the single bubble in the cathodic and anodic compartment, in m, can be approximated by:

$$d_{\mathrm{b}}^{\mathrm{cat}} = 593.84 \cdot 10^{-6} \cdot (1 + 0.2J)^{-0.25} \tag{3.58}$$

$$d_{\mathrm{b}}^{\mathrm{ano}} = 10^{-4} \tag{3.59}$$

To approximate the overall gas-liquid interfacial area A_{GL}^{j}, the total gas volume inside the electrolysis cell V_{gas}^{j} must be known. For this purpose, the methodology and experimental results of Haug et al. [34] are used. Since the geometrical volume of the half cell V_{hcell} is a known quantity, the total gas volume can be approximated by experimentally defining the gas hold-up fraction at the outlet of the electrolysis cell $\varepsilon_{\mathrm{g,out}}^{j}$. In general, the liquid electrolyte that consists of concentrated potassium hydroxide has very high conductivity. Due to the gas evolution, the conductivity of the concentrated liquid electrolyte declines. Therefore, Haug et al. [34] performed conductivity measurements to quantify the gas hold-up fraction at the outlet of the electrolysis cell. The gas hold-up fraction at the outlet of the electrolysis cell $\varepsilon_{\mathrm{g,out}}^{j}$ is reported in Appendix A.3.

However, the measurement of the conductivity at the exit of the electrolysis cell results in a higher gas hold-up fraction since the gas bubbles tend to coalesce. Due to the bubble coalescence, the total pressure at the exit of the electrolysis cell will be smaller because of the Young-Laplace equation. More specifically, when the bubbles coalesce, they will have a larger bubble diameter d_{b}^{j}. As a result, the total pressure p_{tot}^{j} on account of the relations (3.46) and (3.47) will be smaller at the exit of the electrolysis cell. To correct the effect of higher gas hold-up fraction due to pressure decrease, Haug et al. [34] propose the implementation of equation (3.60) for the approximation of the total gas volume V_{gas}^{j} in the electrolysis cell.

$$V_{\mathrm{gas}}^{j} = \varepsilon_{\mathrm{g,out}}^{j} \cdot V_{\mathrm{b}}^{j} \cdot \frac{p^{j}}{p_{\mathrm{tot}}^{j}} \tag{3.60}$$

Knowing the total gas volume in the electrolysis cell V_{gas}^{j} in m^3, the gas hold-up fraction inside the electrolysis cell $\varepsilon_{\mathrm{g}}^{j}$ will be equal to:

$$\varepsilon_{\mathrm{g}}^{j} = \frac{V_{\mathrm{gas}}^{j}}{V_{\mathrm{hcell}}} \tag{3.61}$$

Finally, the gas-liquid interface area can be calculated with the following relation:

$$A_{\mathrm{GL}}^{j} = \frac{V_{\mathrm{gas}}^{j}}{V_{\mathrm{b}}^{j}} \cdot S_{\mathrm{b}}^{j} \tag{3.62}$$

To calculate the mass transfer coefficient $k_{\mathrm{L},i}^{j}$, the empirical Sh correlations will be implemented, as it was shown in Chapter 2.2.3. All the required empirical correlations will be re-written to make them consistent with the notation used in this chapter.

The Reynolds number in compartment j, Re^{j} will be calculated by equation (3.63). The literature data for the dynamic viscosity of liquid electrolyte μ_{L} is obtained from

Ref. [34], and can be found in Appendix A.5. The density of the liquid electrolyte ρ_{L} in $\mathrm{kg} \cdot \mathrm{m}^{-3}$ is calculated based on Ref. [57], as a function of the operating temperature and weight concentration of KOH, and can be found in Appendix A.6.

$$Re^{j} = \frac{u_{\mathrm{rs}}^{j} \cdot \rho_{\mathrm{L}} \cdot d_{\mathrm{b}}^{j}}{\mu_{\mathrm{L}}} \tag{3.63}$$

The rising swarm velocity of the gas bubbles during gas evolution in compartment j, u_{rs}^{j}, is calculated by equation (3.64).

$$u_{\mathrm{rs}}^{j} = u_{\mathrm{r}}^{j} \cdot \frac{1}{1 + \frac{\varepsilon_{\mathrm{g}}^{j}}{\left(1-\varepsilon_{\mathrm{g}}^{j}\right)^{2}}} \cdot \frac{1 - \varepsilon_{\mathrm{g}}^{j}}{1 + \frac{1.05}{\left(1+\frac{0.0685}{\left(\varepsilon_{\mathrm{g}}^{j}\right)^{2}}\right)^{0.5} - 0.5}} \tag{3.64}$$

Depending on the operating conditions, the Re number for the cathodic compartment could not be less than 6. As a result, the rising velocity of a single bubble u_{r}^{j} can be calculated by equation (3.65).

$$u_{\mathrm{r}}^{j} = 0.33 g^{0.76} \left(\frac{\rho_{\mathrm{L}}}{\mu_{\mathrm{L}}}\right)^{0.52} \left(\frac{d_{\mathrm{b}}^{j}}{2}\right)^{1.28} \tag{3.65}$$

The Sc_i number, of species i, can be calculated by equation (3.66).

$$Sc_i = \frac{\mu_{\mathrm{L}}}{D_{\mathrm{i},\theta}} \tag{3.66}$$

The calculation of hydrogen and oxygen diffusivities in the liquid electrolyte required for the Sc number, are given by fitting the experimental diffusivities of Tham et al. [58]. The procedure followed to obtain the fitting equations is reported in Appendix A.4. Finally, the Sh number is given by equation (3.67).

$$Sh_i^{j} = \frac{k_{\mathrm{L},i}^{j} \cdot d_{\mathrm{b}}^{j}}{D_{i,\theta}} = 2 + \frac{0.651 \cdot \left(Re^{j} \cdot Sc_i\right)^{1.72}}{1 + \left(Re^{j} \cdot Sc_i\right)^{1.22}} \tag{3.67}$$

The last term that needs to be modeled for the approximation of the mass transfer at the electrolyte bulk is the liquid equilibrium concentration of the species at the gas-liquid interface $c_i^{*,j}$. The calculation of the species' equilibrium concentration can be achieved with the implementation of the Setchenov relation. More specifically, the Setchenov relation correlates the solubility of dissolved gas in the liquid electrolyte $c_i^{*,j}$ with the KOH mass fraction w_{KOH}.

$$\log\left(\frac{c_{i,\mathrm{H_2O}}^{*,j}}{c_i^{*,j}}\right) = K_{\mathrm{S},i} \cdot w_{\mathrm{KOH}} \tag{3.68}$$

where $c_{i,\mathrm{H_2O}}^{*}$ is the solubility of dissolved species i in pure water and $K_{\mathrm{S},i}$ denotes the Setchenov constant of species i. The solubility of dissolved gas in pure water at the gas-liquid interface is the equilibrium concentration. For inert gases like hydrogen and

oxygen that obey the ideal gas law, it is assumed that the equilibrium concentrations can be approximated with Henry's law at low pressures. To estimate $c^*_{i,\mathrm{H_2O}}$, Henry's constant H_i is required and calculated with the correlation equation from Himmelblau's paper [59] in Appendix A.7. In general, Henry's constant H_i can have different types of units [60]. In Himmelblau's publication [59], the Henry's constant H_i is given in atm units. The partial pressure $p^j_{\mathrm{out,i}}$ is given in Pa units. Therefore, to formulate the Henry's Law constant in atm with water being the solvent, the Henry's Law will be:

$$H_i = \frac{\frac{p^j_{\mathrm{out,i}}}{101325Pa}}{c^{*,j}_{i,\mathrm{H_2O}} \cdot \frac{M_{\mathrm{H_2O}}}{\rho_{\mathrm{H_2O}}}} \tag{3.69}$$

where $\rho_{\mathrm{H_2O}}$ is the density of pure water in $\mathrm{kg\ m^{-3}}$. The pure water density is provided in Appendix A.9. The $M_{\mathrm{H_2O}}$ is the molar mass of water. Rearranging equation (3.69) results in equation (3.70).

$$c^{*,j}_{i,\mathrm{H_2O}} = \frac{\rho_{\mathrm{H_2O}}}{M_{\mathrm{H_2O}}} \cdot \frac{p^j_{\mathrm{out,i}}}{H_i \cdot 101325Pa} \tag{3.70}$$

For the solubility of hydrogen and oxygen in liquid electrolyte there are very few experimental data available in the literature. From the report of Walker [61], the most interesting experimental data on solubility of hydrogen and oxygen in concentrated KOH solutions are included in the publication of Jolly et al. (p.34 in [61]). These data have been obtained experimentally by considering the publication of Knaster and Apel'baum [62] and Geffcken [63]. In addition, they provide the solubility of hydrogen and oxygen for a range of temperatures and potassium hydroxide concentrations. From the experimental results, the Setchenov constants can be extracted with fittings and be used in the relation (3.68) to calculate the equilibrium concentration of the species in the liquid electrolyte. The calculation of the Setchenov constants is provided in Appendix A.8.

After the calculation of the Setchenov constant $K_{\mathrm{S},i}$, equation (3.70) can be substituted in equation (3.68) and equation (3.71) will be obtained. In equation (3.71), the equilibrium concentration of the dissolved species in the electrolyte $c^{*,j}_i$ is expressed as a function of the species' outlet partial pressure $p^j_{\mathrm{out},i}$.

$$c^{*,j}_i = \frac{\rho_{\mathrm{H_2O}} \cdot p^j_{\mathrm{out},i}}{M_{\mathrm{H_2O}} \cdot 101325 \cdot H_i \cdot 10^{K_{\mathrm{S},i} \cdot w_{\mathrm{KOH}}}} \tag{3.71}$$

3.4.6. Mass transfer through the diaphragm

The mass transport through the diaphragm can be characterized by the well-known Nernst-Planck equation in 1D.

$$N_{\mathrm{cross},i} = -D^{\mathrm{eff}}_i \frac{dc_i}{dx} + \frac{z_i F}{RT} D^{\mathrm{eff}}_i c_i \, (d\Phi/dx) + c_i U \tag{3.72}$$

where, $d\Phi/dx$ denotes the gradient of the electric field, z_i the charge on ion i, and D^{eff}_i the effective diffusivity of species i through the diaphragm. In the Nernst-Planck

equation, the first term describes the mass transfer due to diffusion, the second term describes the mass transfer due to migration, and the third term describes the mass transfer through the diaphragm due to convection. In addition to the previous mechanisms, a subcategory can be the mass transfer through the diaphragm due to differential pressure. This mass transfer mechanism can be described by Darcy's law (see Chapter 2.3.3).

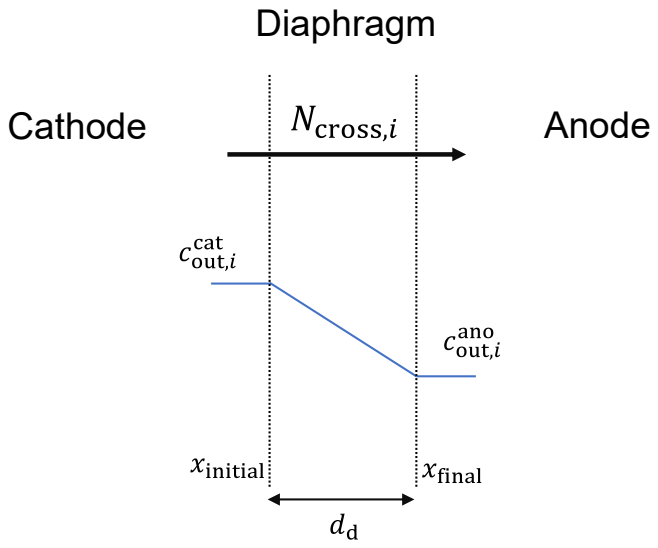

Figure 3.5: Crossover flux through the diaphragm. The positive sign convention for the crossover flux $N_{\mathrm{cross},i}$ is from the cathode to the anode. The concentration gradient through the diaphragm with thickness d_{d}, is linear.

According to the analysis that took place in Chapter 2.3.4, the effect of convectional mass transfer which is described by the Nernst-Planck equation can be neglected, since there is no bulk flow through the diaphragm. Furthermore, the effect of the mass transfer due to differential pressure is negligible. Since the half cells are balanced in terms of pressure, and operate in atmospheric pressure, the absolute pressure difference can be neglected, and hence the mass transfer due to differential pressure. Finally, the effect of migration does not seem to affect the purity of the produced gases [20]. As a result, for the determination of the gas crossover through the diaphragm only the effect of diffusion is considered.

$$N_{\mathrm{cross},i} = -D_i^{\mathrm{eff}} \frac{dc_i}{dx} \tag{3.73}$$

In Figure 3.5, the sign convention for the crossover flux through the diaphragm has been assumed to be from the cathode to the anode. This is the case for hydrogen since its concentration in the cathodic compartment is much higher than in the anodic. The opposite holds true for oxygen. Furthermore, assuming that the concentration gradient across the diaphragm is linear results in equation (3.75).

$$N_{\mathrm{cross},i} = -D_i^{\mathrm{eff}} \frac{dc_i}{dx} = -D_i^{\mathrm{eff}} \frac{c_{\mathrm{out},i}^{\mathrm{ano}} - c_{\mathrm{out},i}^{\mathrm{cat}}}{x_{\mathrm{final}} - x_{\mathrm{initial}}} \tag{3.74}$$

Rearranging equation (3.74) results in equation (3.75).

$$N_{\text{cross},i} = \frac{D_i^{\text{eff}}}{d_{\text{d}}} \cdot \left(c_{\text{out},i}^{\text{cat}} - c_{\text{out},i}^{\text{ano}}\right) \tag{3.75}$$

Where d_{d} is the thickness of the diaphragm in m. For electrochemical applications [64], the effective diffusion coefficient D_i^{eff} can be expressed as a function of the molecular diffusion coefficient $D_{i,\theta}$ and the MacMullin number N_{M}, through equation (3.76).

$$D_i^{\text{eff}} = \frac{D_{i,\theta}}{N_{\text{M}}} \tag{3.76}$$

According to the literature [65, 66], the MacMullin number N_{M} associates the bulk flow properties with the actual mass transfer properties of the diaphragm. It is a dimensionless number of the porosity ε and tortuosity τ of the porous media, and can be experimentally defined by measuring the ionic resistance through the porous media, if the conductivity of the electrolyte is known. For the steady-state and dynamic model, the MacMullin number is given by equation (3.77).

$$N_{\text{M}} = \frac{\tau}{\varepsilon} \tag{3.77}$$

From the preceding analysis, it can be concluded that the effective diffusion coefficient strongly depends on the selection of the appropriate diaphragm. As a result, the diaphragm type can affect the magnitude of the overall crossover flux of species i $N_{\text{cross},i}$.

3.5. Model input and system solution

To solve the steady-state mass balances, as well as the dynamic mass balances, equations (3.1)-(3.8) and (3.19) - (3.34) need to be manipulated and re-arranged in accordance to the boundary conditions and the definition of unknown terms as described in Chapter 3.4. In the following, the required model input are briefly described. Next, the steady-state and dynamic material balances are provided in their final form. The re-arrangements and manipulations are described in Appendix B and Appendix C.

3.5.1. Input data

The properties of the liquid electrolyte and gaseous species which are described in Chapter 3.4 and Appendix A depend on the operational conditions such as the system pressure, temperature, current density and electrolyte mass fraction. In Table 3.1,the input data are given for the case in which the temperature, pressure, current density and electrolyte mass fraction are equal to $T = 313.15\ \text{K}$, $p^{\text{ano}} = p^{\text{cat}} = 1\ \text{bar}$, $J = 0.75\ \text{kA m}^{-2}$ and w_{KOH}=0.35, respectively.

For the crossover through the diaphragm, the material properties must be imported into the developed model. Overall, two diaphragms were used, namely the ”Zirfon PERL UTP 500” and the ”Type A” diaphragm.

The “Zirfon PERL UTP 500” is a composite material that consists of Zirconium oxide (zirconia) and polysulfone. The existence of polysulfone allows the diaphragm to

Table 3.1: Calculated properties for $T = 313.15$ K, $p^{\text{ano}} = p^{\text{cat}} = 1$ bar, $J = 0.75$ kA m^{-2} and w_{KOH}=0.35.

Property	Value	Units	Reference
γ	0.08600	N m^{-1}	(A.3)
$f_{\text{G,H}_2}$	0.86	-	(5.5)
$f_{\text{G,O}_2}$	0.84	-	(5.6)
$d_{\text{b}}^{\text{cat}}$	0.000169	m	(3.58)
$\varepsilon_{\text{g,out}}^{\text{ano}}$	0.11393	-	(A.4)
$\varepsilon_{\text{g,out}}^{\text{cat}}$	0.18656	-	(A.4)
$D_{\text{H}_2,\theta=40}$	2.25124E-09	m^2 s^{-1}	(A.5)
$D_{\text{O}_2,\theta=40}$	6.71637E-10	m^2 s^{-1}	(A.6)
μ_{L}	0.001641	Pa s	(A.7)
ρ_{L}	1340.49425	kg m^{-3}	(A.8)
$\rho_{\text{H}_2\text{O}}$	992.2157	kg m^{-3}	(A.15)
H_{H_2}	74913.35860	atm	(A.9)
H_{O_2}	53781.52404	atm	(A.9)
$K_{\text{S,H}_2}$	3.04641	-	(A.12)
$K_{\text{S,O}_2}$	4.10274	-	(A.14)

be highly flexible, while the zirconia gives good wettability and stiffness. The “Type A” diaphragm is a polymer sheet that consists of polyethylene with hydrophilic treatment. The hydrophilic treatment is required to hinder the cross-permeation of the gaseous phase through the diaphragm. As a result, hydrogen or oxygen can crossover to the opposite half-cell only while being dissolved in the liquid electrolyte. The porosity and tortuosity of “Zirfon PERL UTP 500” are obtained from the technical datasheet provided by AGFA [17], and the literature [34]. Similarly, for the “Type A” diaphragm, the same properties are obtained from the technical datasheet provided by the vendor and from empirical correlations which were found in the literature [67], and provided in Appendix A.10. Overall, the porosity and tortuosity for both diaphragms are depicted in Table 3.2.

Table 3.2: Porosity ε, tortuosity τ, and thickness d_{d} of Zirfon and Type A diaphragms

Diaphragm	ε %	τ	d_{d} (μm)
Zirfon PERL UTP 500	55 ± 10	3.14	500 ± 50
Type A	35	1.95	600 ± 100

The properties which are provided in Table 3.1, and Table 3.2 are inserted in the system of equations for the solution of the model. Considering the required operating conditions, the current density can change with time. Therefore, the properties which are a function of the current density will change accordingly. Besides the current density, the rest of the operational parameters do not change with time and are given as input in the model. The model input is the same for both the steady-state and the dynamic model.

3.5.2. System solution of the steady-state model

In the following, the final form of the set of equations, as well as the unknown terms that describe the model in terms of the gas crossover is presented. The steady-state model is described by equations (3.78)-(3.83). The strategy followed to obtain these equations is described in detail in Appendix B.

Dissolved H_2 in the anodic half-cell:

$$0 = \dot{V}_{\mathrm{L}}^{\mathrm{ano}} \cdot \left(c_{\mathrm{in,H_2}}^{\mathrm{ano}} - c_{\mathrm{out,H_2}}^{\mathrm{ano}}\right) + N_{\mathrm{phys,H_2}}^{\mathrm{ano}} \cdot A_{\mathrm{GL}}^{\mathrm{ano}} + N_{\mathrm{cross,H_2}} \cdot A_{\mathrm{d}} \tag{3.78}$$

Dissolved O_2 in the anodic half-cell:

$$0 = \dot{V}_{\mathrm{L}}^{\mathrm{ano}} \cdot \left(c_{\mathrm{in,O_2}}^{\mathrm{ano}} - c_{\mathrm{out,O_2}}^{\mathrm{ano}}\right) + N_{\mathrm{phys,O_2}}^{\mathrm{ano}} \cdot A_{\mathrm{GL}}^{\mathrm{ano}} + N_{\mathrm{cross,O_2}} \cdot A_{\mathrm{d}} + \left(1 - f_{\mathrm{G,O_2}}\right) \cdot \dot{n}_{\mathrm{R,O_2}}^{\mathrm{ano}} \tag{3.79}$$

Gaseous O_2 in the anodic half-cell:

$$0 = -\frac{\dot{V}_{\mathrm{G}}^{\mathrm{ano}}}{R \cdot T} \cdot p_{\mathrm{out,O_2}}^{\mathrm{ano}} - N_{\mathrm{phys,O_2}}^{\mathrm{ano}} \cdot A_{\mathrm{GL}}^{\mathrm{ano}} + f_{\mathrm{G,O_2}} \cdot \dot{n}_{\mathrm{R,O_2}}^{\mathrm{ano}} \tag{3.80}$$

Dissolved H_2 in the cathodic half-cell:

$$0 = \dot{V}_{\mathrm{L}}^{\mathrm{cat}} \cdot \left(c_{\mathrm{in,H_2}}^{\mathrm{cat}} - c_{\mathrm{out,H_2}}^{\mathrm{cat}}\right) + N_{\mathrm{phys,H_2}}^{\mathrm{cat}} \cdot A_{\mathrm{GL}}^{\mathrm{cat}} - N_{\mathrm{cross,H_2}} \cdot A_{\mathrm{d}} + \left(1 - f_{\mathrm{G,H_2}}\right) \cdot \dot{n}_{\mathrm{R,H_2}}^{\mathrm{cat}} \tag{3.81}$$

Dissolved O_2 in the cathodic half-cell:

$$0 = \dot{V}_{\mathrm{L}}^{\mathrm{cat}} \cdot \left(c_{\mathrm{in,O_2}}^{\mathrm{cat}} - c_{\mathrm{out,O_2}}^{\mathrm{cat}}\right) + N_{\mathrm{phys,O_2}}^{\mathrm{cat}} \cdot A_{\mathrm{GL}}^{\mathrm{cat}} - N_{\mathrm{cross,O_2}} \cdot A_{\mathrm{d}} \tag{3.82}$$

Gaseous H_2 in the cathodic half-cell:

$$0 = -\frac{\dot{V}_{\mathrm{G}}^{\mathrm{cat}}}{R \cdot T} \cdot p_{\mathrm{out,H_2}}^{\mathrm{cat}} - N_{\mathrm{phys,H_2}}^{\mathrm{cat}} \cdot A_{\mathrm{GL}}^{\mathrm{cat}} + f_{\mathrm{G,H_2}} \cdot \dot{n}_{\mathrm{R,H_2}}^{\mathrm{cat}} \tag{3.83}$$

In the steady-state model, the outlet partial pressures of species i, in the compartment j, $p_{\mathrm{out},i}^{j}$, are expressed as functions of the solubility of species i in the liquid electrolyte of the compartment j, $c_i^{*,j}$. As a result, the partial pressures are not considered as unknown quantities in the steady-state model. The outlet partial pressures for the steady-state model are described by equations (3.84)-(3.87). Their detailed derivation is presented in Appendix B.1.

Outlet partial pressure of H_2 in the anodic half-cell:

$$p_{\mathrm{out,H_2}}^{\mathrm{ano}} = \frac{M_{\mathrm{H_2O}}}{\rho_{\mathrm{H_2O}}} \cdot c_{\mathrm{H_2}}^{*,\mathrm{ano}} \cdot 101325Pa \cdot H_{\mathrm{H_2}} \cdot 10^{K_{\mathrm{H_2}} \cdot w_{\mathrm{KOH}}} \tag{3.84}$$

Outlet partial pressure of H_2 in the cathodic half-cell:

$$p_{\mathrm{out,H_2}}^{\mathrm{cat}} = \frac{M_{\mathrm{H_2O}}}{\rho_{\mathrm{H_2O}}} \cdot c_{\mathrm{H_2}}^{*,\mathrm{cat}} \cdot 101325Pa \cdot H_{\mathrm{H_2}} \cdot 10^{K_{\mathrm{H_2}} \cdot w_{\mathrm{KOH}}} \tag{3.85}$$

Outlet partial pressure of O_2 in the anodic half-cell:

$$p_{\mathrm{out,O_2}}^{\mathrm{ano}} = p_{\mathrm{tot}}^{\mathrm{ano}} - p_{\mathrm{H_2O}} - \frac{M_{\mathrm{H_2O}}}{\rho_{\mathrm{H_2O}}} \cdot c_{\mathrm{H_2}}^{*,\mathrm{ano}} \cdot 101325Pa \cdot H_{\mathrm{H_2}} \cdot 10^{K_{\mathrm{H_2}} \cdot w_{\mathrm{KOH}}} \tag{3.86}$$

Outlet partial pressure of O_2 in the cathodic half-cell:

$$p_{\mathrm{out,O_2}}^{\mathrm{cat}} = p_{\mathrm{tot}}^{\mathrm{cat}} - p_{\mathrm{H_2O}} - \frac{M_{\mathrm{H_2O}}}{\rho_{\mathrm{H_2O}}} \cdot c_{\mathrm{H_2}}^{*,\mathrm{cat}} \cdot 101325Pa \cdot H_{\mathrm{H_2}} \cdot 10^{K_{\mathrm{H_2}} \cdot w_{\mathrm{KOH}}} \tag{3.87}$$

Furthermore, the gaseous volumetric flow rates $\dot{V}_{\mathrm{G}}^{\mathrm{ano}}$, and $\dot{V}_{\mathrm{G}}^{\mathrm{cat}}$ are expressed as functions of other variables by using equations (3.88)-(3.89). Their detailed derivation is presented in Appendix B.2.

Outlet gaseous volumetric flow rate in the anodic half-cell:

$$\dot{V}_{\mathrm{G}}^{\mathrm{ano}} = -\frac{R \cdot T}{\frac{M_{\mathrm{H_2O}}}{\rho_{\mathrm{H_2O}}} \cdot c_{\mathrm{H_2}}^{*,\mathrm{ano}} \cdot 101325Pa \cdot H_{\mathrm{H_2}} \cdot 10^{K_{\mathrm{H_2}} \cdot w_{\mathrm{KOH}}}} \cdot N_{\mathrm{phys,H_2}}^{\mathrm{ano}} \cdot A_{\mathrm{GL}}^{\mathrm{ano}} \tag{3.88}$$

Outlet gaseous volumetric flow rate in the cathodic half-cell:

$$\dot{V}_{\mathrm{G}}^{\mathrm{cat}} = -\frac{R \cdot T}{p_{\mathrm{tot}}^{\mathrm{cat}} - p_{\mathrm{H_2O}} - \frac{M_{\mathrm{H_2O}}}{\rho_{\mathrm{H_2O}}} \cdot c_{\mathrm{H_2}}^{*,\mathrm{cat}} \cdot 101325Pa \cdot H_{\mathrm{H_2}} \cdot 10^{K_{\mathrm{H_2}} \cdot w_{\mathrm{KOH}}}} \cdot N_{\mathrm{phys,O_2}}^{\mathrm{cat}} \cdot A_{\mathrm{GL}}^{\mathrm{cat}} \tag{3.89}$$

To solve the system of equations for the steady-state model, it is chosen to reduce the number of unknown variables to the maximum possible. Steady-state systems of equations are solved by implementing optimization solvers from SciPy. More specifically, the optimization solver that is selected for the steady-state model is the Nelder-Mead solver. The Nelder-Mead solver utilizes simplex methods by calling the scipy.optimize.minimize command [68]. To obtain the system solution, an objective function is required. In the steady-state model, the objective function satisfies the minimum norm solution. Therefore, the system of equations (3.78)-(3.83) is expressed as an array that satisfies equation (3.90).

$$\min ||A\mathbf{x} - \mathbf{b}|| \tag{3.90}$$

Where the matrix A contains the coefficients of the unknown quantities, the vector $\mathbf{x}$ contains the unknown quantities, and the vector $\mathbf{b}$ contains the known quantities of equations (3.78)-(3.83), which are expressed as the right-hand-side.

Furthermore, the solution requires a set of initial conditions. The ideal set of initial conditions is chosen by trial and error. Overall, the larger the number of unknown variables, the longer the system takes to be solved. Furthermore, it is more difficult to select a set of initial conditions when the number of unknown variables is large.

As a result, variables such as the partial pressures and the volumetric flow rates are expressed as functions of the solubility of species in the liquid electrolyte and the outlet dissolved concentration of the species in the liquid electrolyte.

In the steady-state model, there are 6 unknown terms. As a result, A will be a 6-by-6 matrix, $\mathbf{x}$ will be a 6-by-1 vector, and $\mathbf{b}$ will be a 6-by-1 vector. The unknown terms of the steady-state model are shown in Table 3.3.

Finally, the H_2 in O_2 impurity is obtained as the mole fraction of gaseous H_2 without taking into account water vapour. The same reasoning is followed for the O_2 in H_2 impurity. Due to equation (3.18), the outlet partial pressure of species i, in the separator j, is equal to the outlet partial pressure of the corresponding half cell j. As a result, both impurities are calculated from equations (3.91), (3.92).

$$y_{\mathrm{H_2}} = \frac{p^{\mathrm{ano}}_{\mathrm{out,H_2}}}{p^{\mathrm{ano}}_{\mathrm{out,H_2}} + p^{\mathrm{ano}}_{\mathrm{out,O_2}}} \tag{3.91}$$

$$y_{\mathrm{O_2}} = \frac{p^{\mathrm{cat}}_{\mathrm{out,O_2}}}{p^{\mathrm{cat}}_{\mathrm{out,H_2}} + p^{\mathrm{cat}}_{\mathrm{out,O_2}}} \tag{3.92}$$

Table 3.3: The unknown terms of the steady-state model

Unknown Quantity	Symbol	Unit
Dissolved Concentration of hydrogen in the anodic compartment	$c^{\mathrm{ano}}_{\mathrm{out,H_2}}$	$\mathrm{mol \cdot m^{-3}}$
Dissolved Concentration of oxygen in the anodic compartment	$c^{\mathrm{ano}}_{\mathrm{out,O_2}}$	$\mathrm{mol \cdot m^{-3}}$
Solubility of hydrogen in the liquid electrolyte, in the anodic compartment	$c^{*,\mathrm{ano}}_{\mathrm{H_2}}$	$\mathrm{mol \cdot m^{-3}}$
Solubility of hydrogen in the liquid electrolyte, in the cathodic compartment	$c^{*,\mathrm{cat}}_{\mathrm{H_2}}$	$\mathrm{mol \cdot m^{-3}}$
Dissolved Concentration of hydrogen in the cathodic compartment	$c^{\mathrm{cat}}_{\mathrm{out,H_2}}$	$\mathrm{mol \cdot m^{-3}}$
Dissolved Concentration of oxygen in the cathodic compartment	$c^{\mathrm{cat}}_{\mathrm{out,O_2}}$	$\mathrm{mol \cdot m^{-3}}$

3.5.3. System solution of the dynamic model

In the following, the ordinary differential equations which describe the performance of the alkaline water electrolyser, in terms of the gas crossover, are listed in their final form. The strategy followed to obtain the final form of the dynamic material balances is provided in Appendix C. The ordinary differential equations are provided in compact form where necessary. The subscript i denotes the gaseous species $\mathrm{H_2}$ or $\mathrm{O_2}$, and the superscript j denotes the anodic or cathodic compartment.

Dissolved H_2 in the anodic half-cell:

$$\frac{dc^{\mathrm{ano}}_{\mathrm{out,H_2}}}{dt} = \frac{1}{V^{\mathrm{ano}}_{\mathrm{liq}}} \cdot \left[\dot{V}^{\mathrm{ano}}_{\mathrm{L}} \cdot \left(c^{\mathrm{ano}}_{\mathrm{in,H_2}} - c^{\mathrm{ano}}_{\mathrm{out,H_2}}\right) + N^{\mathrm{ano}}_{\mathrm{phys,H_2}} \cdot A^{\mathrm{ano}}_{\mathrm{GL}} + N_{\mathrm{cross,H_2}} \cdot A_{\mathrm{d}}\right] \quad (3.93)$$

Dissolved O_2 in the anodic half-cell:

$$\frac{dc^{\mathrm{ano}}_{\mathrm{out,O_2}}}{dt} = \frac{1}{V^{\mathrm{ano}}_{\mathrm{liq}}} \cdot \left[\dot{V}^{\mathrm{ano}}_{\mathrm{L}} \cdot \left(c^{\mathrm{ano}}_{\mathrm{in,O_2}} - c^{\mathrm{ano}}_{\mathrm{out,O_2}}\right) + N^{\mathrm{ano}}_{\mathrm{phys,O_2}} \cdot A^{\mathrm{ano}}_{\mathrm{GL}} + N_{\mathrm{cross,O_2}} \cdot A_{\mathrm{d}} + \left(1 - f_{\mathrm{G,O_2}}\right) \cdot \dot{n}^{\mathrm{ano}}_{\mathrm{R,O_2}}\right] \quad (3.94)$$

Gaseous H_2 in the anodic half-cell:

$$\frac{dp^{\mathrm{ano}}_{\mathrm{out,H_2}}}{dt} = -\frac{\dot{V}^{\mathrm{ano}}_{\mathrm{G}}}{V^{\mathrm{ano}}_{\mathrm{gas}}} \cdot p^{\mathrm{ano}}_{\mathrm{out,H_2}} - \frac{R \cdot T}{V^{\mathrm{ano}}_{\mathrm{gas}}} \cdot N^{\mathrm{ano}}_{\mathrm{phys,H_2}} \cdot A^{\mathrm{ano}}_{\mathrm{GL}} \quad (3.95)$$

Gaseous O_2 in the anodic half-cell:

$$\frac{dp^{\mathrm{ano}}_{\mathrm{out,O_2}}}{dt} = -\frac{\dot{V}^{\mathrm{ano}}_{\mathrm{G}}}{V^{\mathrm{ano}}_{\mathrm{gas}}} \cdot p^{\mathrm{ano}}_{\mathrm{out,O_2}} - \frac{R \cdot T}{V^{\mathrm{ano}}_{\mathrm{gas}}} \cdot \left(N^{\mathrm{ano}}_{\mathrm{phys,O_2}} \cdot A^{\mathrm{ano}}_{\mathrm{GL}} - f_{\mathrm{G,O_2}} \cdot \dot{n}^{\mathrm{ano}}_{\mathrm{R,O_2}}\right) \quad (3.96)$$

Dissolved H_2 in the cathodic half-cell:

$$\frac{dc^{\mathrm{cat}}_{\mathrm{out,H_2}}}{dt} = \frac{1}{V^{\mathrm{cat}}_{\mathrm{liq}}} \cdot \left[\dot{V}^{\mathrm{cat}}_{\mathrm{L}} \cdot \left(c^{\mathrm{cat}}_{\mathrm{in,H_2}} - c^{\mathrm{cat}}_{\mathrm{out,H_2}}\right) + N^{\mathrm{cat}}_{\mathrm{phys,H_2}} \cdot A^{\mathrm{cat}}_{\mathrm{GL}} - N_{\mathrm{cross,H_2}} \cdot A_{\mathrm{d}} + \left(1 - f_{\mathrm{G,H_2}}\right) \cdot \dot{n}^{\mathrm{cat}}_{\mathrm{R,H_2}}\right] \quad (3.97)$$

Dissolved O_2 in the cathodic half-cell:

$$\frac{dc^{\mathrm{cat}}_{\mathrm{out,O_2}}}{dt} = \frac{1}{V^{\mathrm{cat}}_{\mathrm{liq}}} \cdot \left[\dot{V}^{\mathrm{cat}}_{\mathrm{L}} \cdot \left(c^{\mathrm{cat}}_{\mathrm{in,O_2}} - c^{\mathrm{cat}}_{\mathrm{out,O_2}}\right) + N^{\mathrm{cat}}_{\mathrm{phys,O_2}} \cdot A^{\mathrm{cat}}_{\mathrm{GL}} - N_{\mathrm{cross,O_2}} \cdot A_{\mathrm{d}}\right] \quad (3.98)$$

Gaseous H_2 in the cathodic half-cell:

$$\frac{dp^{\mathrm{cat}}_{\mathrm{out,H_2}}}{dt} = -\frac{\dot{V}^{\mathrm{cat}}_{\mathrm{G}}}{V^{\mathrm{cat}}_{\mathrm{gas}}} \cdot p^{\mathrm{cat}}_{\mathrm{out,H_2}} - \frac{R \cdot T}{V^{\mathrm{cat}}_{\mathrm{gas}}} \cdot \left(N^{\mathrm{cat}}_{\mathrm{phys,H_2}} \cdot A^{\mathrm{cat}}_{\mathrm{GL}} - f_{\mathrm{G,H_2}} \cdot \dot{n}^{\mathrm{cat}}_{\mathrm{R,H_2}}\right) \quad (3.99)$$

Gaseous O_2 in the cathodic half-cell:

$$\frac{dp^{\mathrm{cat}}_{\mathrm{out,O_2}}}{dt} = -\frac{\dot{V}^{\mathrm{cat}}_{\mathrm{G}}}{V^{\mathrm{cat}}_{\mathrm{gas}}} \cdot p^{\mathrm{cat}}_{\mathrm{out,O_2}} - \frac{R \cdot T}{V^{\mathrm{cat}}_{\mathrm{gas}}} \cdot N^{\mathrm{cat}}_{\mathrm{phys,O_2}} \cdot A^{\mathrm{cat}}_{\mathrm{GL}} \quad (3.100)$$

Dissolved species i, in the gas separator of j half-cell:

$$\frac{dc^{\mathrm{sep},j}_{\mathrm{out},i}}{dt} = \frac{\dot{V}^{j}_{\mathrm{L}}}{V^{\mathrm{sep},j}_{\mathrm{liq}}} \cdot \left(c^{j}_{\mathrm{out},i} - c^{\mathrm{sep},j}_{\mathrm{out},i}\right) \quad (3.101)$$

Gaseous species i, in the gas separator of j half-cell:

$$\frac{dp_{\mathrm{out},i}^{\mathrm{sep},j}}{dt} = \frac{\dot{V}_{\mathrm{G}}^{j}}{V_{\mathrm{gas}}^{\mathrm{sep},j}} \cdot \left(p_{\mathrm{out},i}^{j} - p_{\mathrm{out},i}^{\mathrm{sep},j}\right) \tag{3.102}$$

Where, the gaseous volumetric flow rate in the anodic and cathodic compartment $\dot{V}_{\mathrm{G}}^{\mathrm{ano}}$, $\dot{V}_{\mathrm{G}}^{\mathrm{cat}}$ are coupled with other variables using equations (3.103)-(3.104), in $\mathrm{m}^3\ \mathrm{s}^{-1}$ units.

$$\dot{V}_{\mathrm{G}}^{\mathrm{ano}} = -\frac{R \cdot T}{p_{\mathrm{tot}}^{\mathrm{ano}} - p_{\mathrm{H_2O}}} \cdot \left(N_{\mathrm{phys,H_2}}^{\mathrm{ano}} \cdot A_{\mathrm{GL}}^{\mathrm{ano}} + N_{\mathrm{phys,O_2}}^{\mathrm{ano}} \cdot A_{\mathrm{GL}}^{\mathrm{ano}} - f_{\mathrm{G,O_2}} \cdot \dot{n}_{\mathrm{R,O_2}}^{\mathrm{ano}}\right) \tag{3.103}$$

$$\dot{V}_{\mathrm{G}}^{\mathrm{cat}} = -\frac{R \cdot T}{p_{\mathrm{tot}}^{\mathrm{cat}} - p_{\mathrm{H_2O}}} \cdot \left(N_{\mathrm{phys,H_2}}^{\mathrm{cat}} \cdot A_{\mathrm{GL}}^{\mathrm{cat}} + N_{\mathrm{phys,O_2}}^{\mathrm{cat}} \cdot A_{\mathrm{GL}}^{\mathrm{cat}} - f_{\mathrm{G,H_2}} \cdot \dot{n}_{\mathrm{R,H_2}}^{\mathrm{cat}}\right) \tag{3.104}$$

In total, equations (3.93)-(3.104) include 16 unknowns. The ensemble of the unknown terms is depicted in Table 3.4. The ordinary differential equations are solved by implementing the odeint function from the SciPy package [69]. The scipy.integrate.odeint function is a numerical solver for first order ordinary differential equations which implements LSODA from the FORTRAN library. The LSODA is a backward or forward multistep method that automatically selects the solver and the timestep that is implemented, depending on the stability of the problem. The solution requires the assignment of initial conditions. The initial condition given to the set of ordinary differential equations is the zero value at $t = 0$ for every unknown term of Table 3.4. This typically means that the the alkaline water electrolyser is inactive when it starts up. Finally, the H_2 in O_2 impurity is obtained as the mole fraction of gaseous H_2 without taking into account water vapour. The same reasoning is followed for the O_2 in H_2 impurity. Both impurities are calculated from equations (3.105), (3.106).

$$y_{\mathrm{H_2}} = \frac{p_{\mathrm{out,H_2}}^{\mathrm{sep,ano}}}{p_{\mathrm{out,H_2}}^{\mathrm{sep,ano}} + p_{\mathrm{out,O_2}}^{\mathrm{sep,ano}}} \tag{3.105}$$

$$y_{\mathrm{O_2}} = \frac{p_{\mathrm{out,O_2}}^{\mathrm{sep,cat}}}{p_{\mathrm{out,H_2}}^{\mathrm{sep,cat}} + p_{\mathrm{out,O_2}}^{\mathrm{sep,cat}}} \tag{3.106}$$

Table 3.4: The unknown terms of the system of ordinary differential equations

Unknown Quantity	Symbol	Unit
Dissolved Concentration of hydrogen in the anodic compartment	$c^{\text{ano}}_{\text{out},\text{H}_2}$	$\text{mol} \cdot \text{m}^{-3}$
Dissolved Concentration of oxygen in the anodic compartment	$c^{\text{ano}}_{\text{out},\text{O}_2}$	$\text{mol} \cdot \text{m}^{-3}$
Outlet partial pressure of hydrogen in the anodic compartment	$p^{\text{ano}}_{\text{out},\text{H}_2}$	Pa
Outlet partial pressure of oxygen in the anodic compartment	$p^{\text{ano}}_{\text{out},\text{O}_2}$	Pa
Dissolved Concentration of hydrogen in the cathodic compartment	$c^{\text{cat}}_{\text{out},\text{H}_2}$	$\text{mol} \cdot \text{m}^{-3}$
Dissolved Concentration of oxygen in the cathodic compartment	$c^{\text{cat}}_{\text{out},\text{O}_2}$	$\text{mol} \cdot \text{m}^{-3}$
Outlet partial pressure of hydrogen in the cathodic compartment	$p^{\text{cat}}_{\text{out},\text{H}_2}$	Pa
Outlet partial pressure of oxygen in the cathodic compartment	$p^{\text{cat}}_{\text{out},\text{O}_2}$	Pa
Dissolved Concentration of hydrogen in the anodic gas separator	$c^{\text{sep,ano}}_{\text{out},\text{H}_2}$	$\text{mol} \cdot \text{m}^{-3}$
Dissolved Concentration of oxygen in the anodic gas separator	$c^{\text{sep,ano}}_{\text{out},\text{O}_2}$	$\text{mol} \cdot \text{m}^{-3}$
Outlet partial pressure of hydrogen in the anodic gas separator	$p^{\text{sep,ano}}_{\text{out},\text{H}_2}$	Pa
Outlet partial pressure of oxygen in the anodic gas separator	$p^{\text{sep,ano}}_{\text{out},\text{O}_2}$	Pa
Dissolved Concentration of hydrogen in the cathodic gas separator	$c^{\text{sep,cat}}_{\text{out},\text{H}_2}$	$\text{mol} \cdot \text{m}^{-3}$
Dissolved Concentration of oxygen in the cathodic gas separator	$c^{\text{sep,cat}}_{\text{out},\text{O}_2}$	$\text{mol} \cdot \text{m}^{-3}$
Outlet partial pressure of hydrogen in the cathodic gas separator	$p^{\text{sep,cat}}_{\text{out},\text{H}_2}$	Pa
Outlet partial pressure of oxygen in the cathodic gas separator	$p^{\text{sep,cat}}_{\text{out},\text{O}_2}$	Pa

4

Gas crossover experiments

In this chapter, the experiments of gas crossover are presented. In the first section, the experimental setup will be briefly described. Next, the operating conditions for both the steady-state and dynamic switching of electrolyte cycles experiments will be shown. Finally, the experimental gas crossover results will be presented for both cases.

4.1. Description of the experimental setup

In Figure 4.1, the experimental setup of XINTC is shown. The main components of the alkaline water electrolysis setup include the electrolysis single cell, the gas separators, the gas chromatograph, the main pumps, and the valves. For the accomplishment of the experiments, a single cell is chosen instead of a stack. Since the availability of the literature data for gas crossover in alkaline water electrolysers is limited to the single cell setup, it is believed that the demonstration of the experiment and the model in similar conditions is more appropriate for comparison and validation.

The single cell consists of the electrodes in the anode and cathode. Each electrode has an area A_{el} of 51x145 mm^2. The dimensions of each half-cell are (LxWxH) 15x5x0.38 cm^3. For the experiments, the "Type A" diaphragm was used. Its properties are shown in Table 3.2. The "Type A" diaphragm has an area A_{d} of 61x145 mm^2. The anodic gas separator is cylindrical and has a volume of 16 L. Similarly, the cathodic gas separator has a volume of 32 L. Furthermore, they include a liquid level detector to measure the level of the liquid electrolyte during operation. The liquid level of the gas separators during the operation is approximately 42% of the total volume of the gas separators. The produced gases are manually collected from the exit of the electrolysis cell. The sampling point is located at the exit of the electrolysis cell to accelerate the response of the system, and reach the steady-state impurities faster. Next, they are imported for purity analysis in the gas chromatograph. In such a way, it is possible to determine the impurity of the produced gases. The pumps are located before the entrance of the electrolysis cell. The pumps are required to regulate the flow of the liquid electrolyte in the electrolysis cell. The distinction between the mixed-mode and the partly separated mode takes place with the installation of two 3-way valves (Valve 1.1 and Valve 2.1). These valves are actuated simultaneously, and their normally open position (denoted as NO) can be seen in Figure 4.1. During

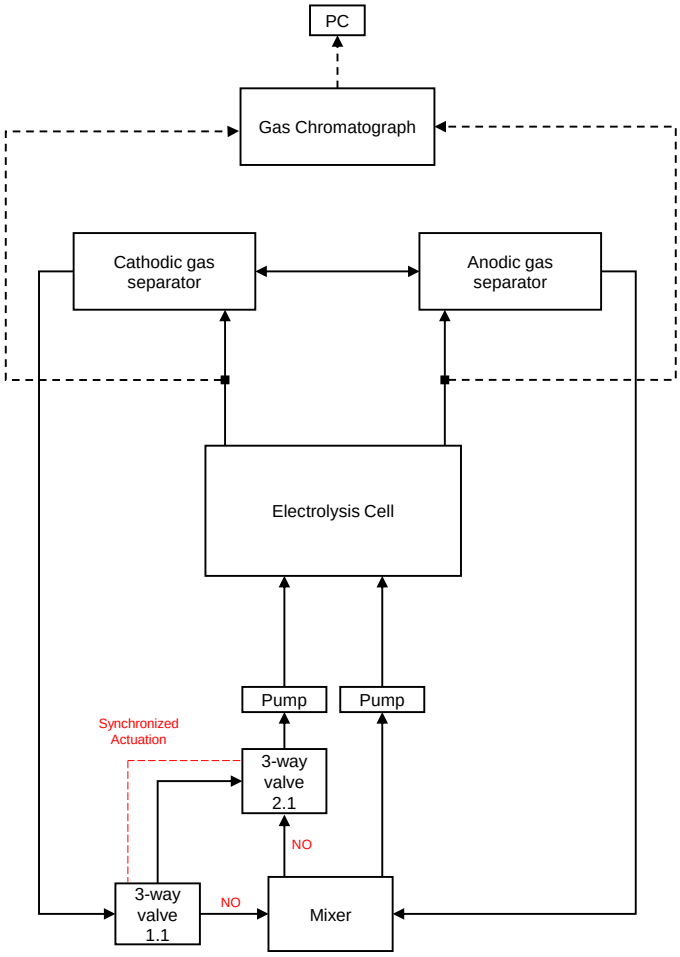

Figure 4.1: The experimental setup of XINTC. The gas impurity measurements take place at the exit of the electrolysis cell, before the gas separators. The changeover from the mixed to the partly-separated mode occurs with the use of two 3-way valves, which are synchronized . In their normally open position (NO), the plant operates in mixed mode. In their normally closed position, the plant operates in partly-separated mode.

their normally open position, the anolyte and catholyte are directed to the mixer and the mixed-mode operation takes place. When they switch to their normally closed position, the catholyte bypasses the mixer. As a result, the electrolysis plant operates in a partly-separated mode. The design characteristics of the electrolysis plant in the experimental setup are summarized in Table 4.1.

4.2. Operating conditions

In the following, the operating conditions for conducting the steady-state and dynamic switching of electrolyte cycles experiments, are presented. The measured impurities from the steady-state experiment will be imported in the steady-state model to approximate the gas evolution efficiency. The measured impurities from the dynamic switching of electrolyte cycles are required to model this alternative process. Both of these models will be presented in Chapter 5.

Table 4.1: Design characteristics of the experimental electrolysis setup.

Property	Symbol	Value	Units
Electrode area	A_{el}	51x145	mm^2
Diaphragm area	A_{d}	61x145	mm^2
Diaphragm thickness	d_{d}	600	μm
Half-cell volume	V_{hcell}	15x5x0.38	cm^3
Anodic gas separator volume	$V_{\mathrm{sep}}^{\mathrm{ano}}$	16	L
Cathodic gas separator volume	$V_{\mathrm{sep}}^{\mathrm{cat}}$	32	L

4.2.1. Steady-state experiment

The steady-state experiments are conducted in a mixed-mode operation. Therefore, the 3-way valves in the experimental setup (see Figure 4.1) are always in their normally open position. The experimental setup is filled in with liquid electrolyte containing 35 wt% KOH. Before the initiation of the impurity measurements, the setup must have a uniform temperature in the electrolysis cell and the auxiliary equipment. For this reason, during the startup conditions, the liquid electrolyte is heated up to the desired operating temperature. At the same time, DC power is supplied to the electrolysis cell. The gaseous product starts being produced in the anode and cathode leaving the electrolysis cell with the liquid electrolyte. After approximately two hours, the impurity measurements start.

The measurements take place at a temperature of $T = 40°\mathrm{C}$. The system operates in atmospheric pressure and with a flow rate of $\dot{V}_{\mathrm{L}} = 150\ \mathrm{ml\ min}^{-1}$. Due to the very low value, the flow meter indicates that the volumetric flow rate fluctuates between $0\ \mathrm{ml\ min}^{-1} \leq \dot{V}_{\mathrm{L}} \leq 150\mathrm{ml\ min}^{-1}$. Therefore, it is assumed that the actual flow rate is the average, $\dot{V}_{\mathrm{L}} = 75\ \mathrm{ml\ min}^{-1}$. During the experiment, the current density is changed between 0.75-3 $\mathrm{kA\ m}^{-2}$. The produced gas with the liquid electrolyte that contains the dissolved species leave the electrolysis cell and they are directed to the gas separators as a bubbly flow. The gaseous bubbles tend to coalesce in the interconnecting piping and the gas separators. Due to the density difference between the produced gas and the liquid electrolyte, the produced gas leaves the gas separators from the upper part. The liquid electrolyte with the dissolved species leave the gas separators from its lower part. The anolyte and catholyte with the dissolved species are directed to the mixer because the 3-way valves are in the normally open position. As a result, they are continuously being mixed and re-directed to the electrolysis cell.

During the steady-state experiments, the current density is changed between 0.75-3 $\mathrm{kA\ m}^{-2}$. As a result, the gas evolution and hence the impurity of the gaseous product will also change. For the steady-state experiments, the gaseous samples are collected manually at the exit of the single cell 30 mins after the application of the existing current density. The gaseous samples are imported into the gas chromatograph, where they are analyzed in terms of their purity and measured in vol% units. The impurity measured in the anodic compartment denotes the anodic hydrogen content (AHC). The impurity measured in the cathodic compartment denotes the cathodic

oxygen content (COC). For the existing current density, five consecutive measurements are executed to ensure that the impurity has reached its steady state. After the five consecutive measurements are completed, the current density is changed, and the same procedure is repeated. From the steady-state experiments, both the anodic hydrogen content and the cathodic oxygen content are experimentally defined. The operating conditions for the steady-state experiments are listed in Table 4.2.

Table 4.2: Operating conditions during the steady-state experiments.

Variable	Symbol	Value	Units
Liquid flow rate	$\dot{V}_{\mathrm{L}}$	75	$\mathrm{mL\ min^{-1}}$
KOH mass fraction	w_{KOH}	35	$\mathrm{wt\%}$
Operating temperature	T	313.15	K
Operating pressure in the compartment j	p^j	101325	Pa
Current density	J	0.75-3	$\mathrm{kA\ m^{-2}}$

4.2.2. The dynamic switching of electrolyte cycles

The dynamic switching of electrolyte cycles is conducted by changing the lye circulation from the mixed mode to the partly separated and the opposite, as a function of time. When the 3-way valves are normally open, the alkaline water electrolyser operates in mixed mode. The normally open position of the 3-way valves results in the mixing of the catholyte with the anolyte. When the 3-way valves close (see Figure 4.1), the alkaline water electrolyser operates in a partly-separated mode. It is a partly separated mode of operation because the anolyte and catholyte do not mix before the pumps. Due to the closed position of the valves, the catholyte bypasses the mixer. At the same time, the anolyte continues entering the mixer, but due to the closed position of valves 1.1 and 2.1, it cannot be mixed with the catholyte. To successfully perform the dynamic switching of electrolyte cycles, the experimental setup operates for a specific time in a mixed mode, and then it switches to a partly separated mode. The switching time from one mode to another remains constant during the execution of the experiment.

In the beginning, the experimental setup is manually filled in with liquid electrolyte with a mass fraction of 35 wt% KOH. During the start-up of the alkaline water electrolyser, the 3-way valves are opened. As a result, the electrolysis is conducted in a mixed mode. Next, DC power is supplied to the electrolysis cell, and the gaseous product starts forming in the anode and the cathode. The supplied power is set to a current density of $J = 0.75\ \mathrm{kA\ m^{-2}}$. For the dynamic switching of electrolyte cycles, the current density remains steady during the experiment. As soon as the temperature becomes uniform in the electrolysis cell and the auxiliary equipment, the impurity measurements can start.

The measurements are conducted at a temperature of T=40°C. The electrolysis takes place at atmospheric pressure. The average flow rate is equal to 75 mL $\mathrm{min^{-1}}$. During the start-up period, while the electrolyser operates in mixed mode, some con-

secutive impurity measurements are conducted to verify whether the electrolyser has reached its steady state in terms of the anodic hydrogen content. For the dynamic switching of electrolyte cycles, there is interest only in the anodic hydrogen content because the H_2 in O_2 is always greater than the O_2 in H_2. When the impurity measurements converge to the steady-state value, the dynamic switching begins. The 3-way valves change to their closed position and the catholyte does not mix with the anolyte. The changeover from the mixed mode to the partly separated mode lasts for 30 min. During the 30 mins of the partly separated mode, 3 measurements are executed to quantify the anodic hydrogen content. The gaseous samples are manually collected every 10 min at the exit of the single cell and are fed into the gas chromatograph. After 30 mins, the 3-way valves are placed again in the normally open position. As a result, the anolyte and catholyte are continuously mixed. Again, the gaseous samples to quantify the anodic hydrogen content are collected manually every 10 mins. After 30 mins of mixed mode, the 3-way valves switch to the closed position, and the same procedure is repeated. The continuous changeover from the mixed mode to the partly separated mode, every 30 mins, lasts for 2 hours. The operating conditions of the dynamic switching of electrolyte cycles are listed in Table 4.3.

Table 4.3: Operating conditions during the dynamic switching of the electrolyte cycles.

Variable	Symbol	Value	Units
KOH mass fraction	w_{KOH}	35	$\mathrm{wt\%}$
Liquid flow rate	$\dot{V}_{\mathrm{L}}$	75	$\mathrm{mL\ min^{-1}}$
Operating temperature	T	313.15	K
Operating pressure in the compartment j	p^j	101325	Pa
Current density	J	0.75	$\mathrm{kA\ m^{-2}}$
Liquid volume fraction in the j gas separator	$h_{\mathrm{liq}}^{\mathrm{sep},j}$	42	%
Switching time	t_{switch}	30	min
Total time of the experiment	t_{tot}	2	h

4.3. Results of the steady-state experiment

In Figure 4.2, the anodic hydrogen content and the cathodic oxygen content are depicted for the operating conditions which are shown in Table 4.2. The experimental results are also listed in Table 4.4.

First of all, it can be experimentally verified that the anodic hydrogen content is always larger than the cathodic oxygen content. This observation can be justified because of the higher production rate of hydrogen in the cathode than the production rate of oxygen in the anode. Furthermore, in the experimental operating conditions, the solubility and diffusivity of hydrogen in the liquid electrolyte is higher than the solubility and diffusivity of oxygen in the KOH solution. Due to the higher production rate, solubility and diffusivity, more hydrogen will be dissolved in the liquid electrolyte

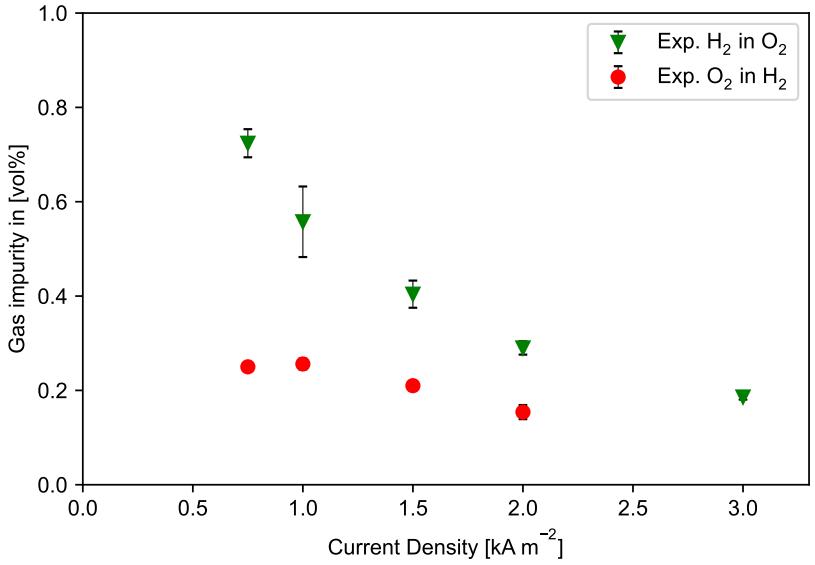

Figure 4.2: The experimental steady-state impurity as a function of the current density. The gaseous samples are collected at the exit of the single cell.

Table 4.4: Steady-state experimental impurity as a function of the current density

J (kA m^{-2})	H_2 in O_2 (vol%)	O_2 in H_2 (vol%)
0.75	0.724 ±0.029	0.250 ±0.015
1	0.557 ±0.074	0.256 ±0.011
1.5	0.404 ±0.029	0.210 ±0.010
2	0.290 ±0.014	0.154 ±0.015
3	0.186 ±0.005	-

and cross permeate through the diaphragm or by electrolyte mixing. As a result, the anodic hydrogen content will always be higher than the cathodic oxygen content.

Furthermore, both impurities decrease as the current density increases. In the lower current densities, the production rate is low, and hence there is no high concentration gradient between the boundary layer of the electrode and the electrolyte bulk. The supersaturation in the concentration boundary layer is reduced in the lower current densities and nucleation, growth and detachment of the gaseous bubbles is challenging. Consequently, more product remains dissolved in the electrolyte bulk and can outgas from the opposite half-cell, and hence result in higher impurity.

On the other hand, when the current density is large, the generation of product in the concentration boundary layer increases. Due to the higher production rate, the concentration gradient between the boundary layer of the electrode and the electrolyte bulk becomes higher. Therefore, the higher supersaturation can result in higher amounts of gaseous product, and hence less dissolved species remain in the system.

From the experimental results it can be observed that the measurements of H_2 in O_2 which took place in the lower current densities, $0.5\ \text{kA m}^{-2} \leq J \leq 1.5\ \text{kA m}^{-2}$,

present more deviation than the measurements in the higher current densities. According to Haug et al. [40], the transition time to the steady-state value strongly depends on the gaseous volume in the system. When the total gaseous volume of the products is low, the system needs more time to reach its steady-state impurity. In low current densities, due to the lower supersaturation, the production rate is low as will the gaseous volume in the system. In addition, the impurity samples were manually collected and may have increased the inaccuracy of the measurements. Consequently, the large standard deviation of the H_2 in O_2 impurities, in the low current density range, can be attributed to the inconsistency of the measurements, as well as the fact that the system did not reach its steady-state values when the measurements were received.

Finally, it is found that the value of the anodic hydrogen content depends on the location where the gas sample is taken from the experimental setup. During the experiments, the gaseous samples are collected at the exit of the electrolysis cell and not at the exit of the gas separators. As a result, the additional mass transfer that takes place inside the separator tank is not taken into consideration from the the experimental measurements.

4.4. Results of the dynamic switching experiment

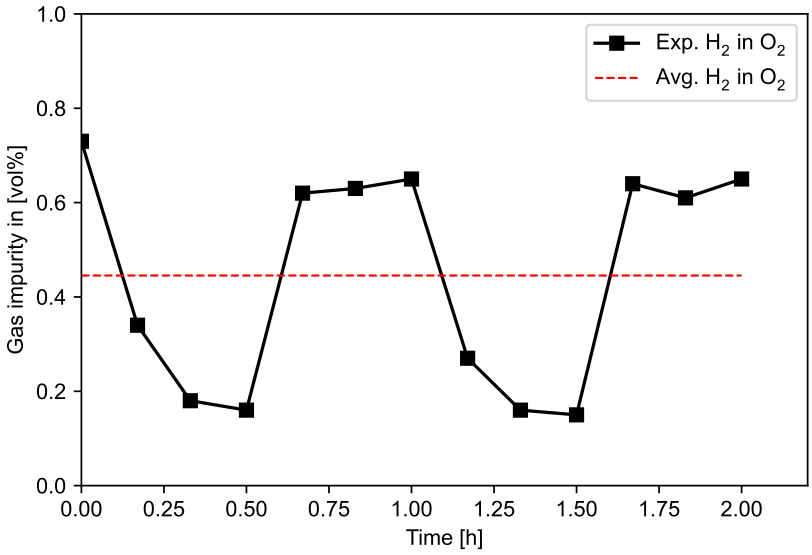

Figure 4.3: The experimental dynamic switching of the electrolyte cycles. The anodic hydrogen content as a function of time (black squares). The average anodic hydrogen content is shown with a red dashed line. The gaseous samples are collected at the exit of the single cell.

In Figure, 4.3, the experimental results of the dynamic switching of electrolyte cycles are shown. On the vertical axis of the graph, the experimental H_2 in O_2 is depicted, in vol%. In the horizontal axis, the time can be seen in h. Before the experiment begins, the valves are positioned to their normally open position and the system operates in the mixed mode. Therefore, the first measurement at $t = 0$ h corresponds to the steady-state value when the system operates in mixed mode.

At $t = 0$ h, the valves are positioned to their normally closed position, and the system switches to the partly-separated mode for 30 min. Since, the valves are closed,

the catholyte does not mix with the anolyte. The absence of mixing leads to gas crossover only due to diffusion through the diaphragm. According to Trinke et al. [41], the gas crossover due to electrolyte mixing can be responsible for up to 90% of the total crossover. Therefore, when the valves close, and the system operates in partly-separated mode, the H_2 in O_2 impurity reduces because the share of the gas crossover due to diffusion through the diaphragm is considerably smaller than the gas crossover due to electrolyte mixing. In the experimental results, the H_2 in O_2 impurity gradually decreases when the system operates in the partly separated mode at $0\ \mathrm{h} < t \leq 0.5\ \mathrm{h}$ and $1\ \mathrm{h} < t \leq 1.5\ \mathrm{h}$. As a result, the experimental observations can be validated from the literature.

At $t = 0.5\ \mathrm{h}$, the valves are positioned to their normally open position and the system switches to the mixed mode for 30 min. In the mixed mode, the catholyte is being continuously mixed with the anolyte, and the dissolved hydrogen species in the liquid electrolyte will eventually be in the anodic compartment due to electrolyte mixing. At the same time, the gas crossover due to the diffusion of the dissolved species through the diaphragm is also active. Since the share of the gas crossover due to electrolyte mixing is significantly larger than the gas crossover due to the diffusion through the diaphragm, the H_2 in O_2 impurity will be increased. Furthermore, the final measurement of the anodic hydrogen content every time the system operates in mixed mode, shows that its value is always smaller than the steady-state impurity. This means that with the dynamic switching, we managed to keep the anodic hydrogen content lower compared to the corresponding state-state value. From the experimental results, at $0.5\ \mathrm{h} < t \leq 1\ \mathrm{h}$ and $1.5\ \mathrm{h} < t \leq 2\ \mathrm{h}$, the increase of the anodic hydrogen content due to electrolyte mixing can be clearly observed.

The H_2 in O_2 impurity in the dynamic switching of electrolyte cycles attains a sinusoidal trend which is similar to the trend observed by Haug et al. [40]. This behavior can be attributed to the continuous switching of the active electrolyte cycles. The traditional operation of the alkaline water electrolysers relies on the mixed mode. The continuous switching of the electrolyte cycles from the mixed to the partly-separated mode allows the reduction of the impurity when the system operates in the partly-separated mode, and the increase of the impurity when it operates in mixed mode. As a result, an average anodic hydrogen content is obtained. The average H_2 in O_2 impurity is shown in Figure 4.3 with a red dashed line, and is equal to $y_{\mathrm{H_2}}^{\mathrm{avg}} = 0.445\ \mathrm{vol\%}$. This results verifies that the operation of the system with the dynamic switching results in less anodic hydrogen content than the mixed mode operation ($y_{\mathrm{H_2}} = 0.724\ \mathrm{vol\%}$).

Finally, in Figure 4.3, it can be observed that the activation of the mixed mode, during the dynamic switching of electrolyte cycles, results in a steep increase of the anodic hydrogen content. The sharp increase of the H_2 in O_2 impurity can be attributed to the fact that the measurements are collected at the exit of the electrolysis cell. As a result, the total liquid and gaseous volume is small, and the impurity takes little time to reach equilibrium. Furthermore, the fact that the measurements are presented as a function of time does not allow the acquisition of multiple samples to calculate an average value and the error bars for the same point. Ideally, the measurements should be performed in shorter periods of time. However, the experimental setup allows the collection of the samples, and their analysis in the gas chromatograph, every 10 min. Overall, the experimental results are also listed in Table 4.5.

Table 4.5: The experimental dynamic switching of the electrolyte cycles. The anodic hydrogen content as a function of time. The gaseous samples are collected at the exit of the single cell.

Time (h)	H_2 in O_2 (vol%)	Time (h)	H_2 in O_2 (vol%)
0	0.73	1.17	0.27
0.17	0.34	1.33	0.16
0.33	0.18	1.5	0.15
0.5	0.16	1.67	0.64
0.67	0.62	1.83	0.61
0.83	0.63	2	0.65
1	0.65		

5

Modeling results

In this chapter, the modeling results are presented. In the first section, the validity of the models is tested with literature data. Next, the results of the model are shown for the setup of XINTC in comparison with the experimental results that were presented in Chapter 4. Finally, a sensitivity analysis is conducted to test the robustness of the model.

5.1. Validation of the steady-state model

The validity of the steady-state model is tested for the experimental results found by Haug et al. [40]. The design characteristics of the electrolysis cell are presented in Table 5.1.

Table 5.1: Design characteristics of the experimental electrolysis setup of Haug et al.[40].

Property	Symbol	Value	Units
Electrode area	A_{el}	150	cm^2
Diaphragm area	A_{d}	232	cm^2
Diaphragm thickness	d_{d}	500	$\mu\mathrm{m}$
Half-cell volume	V_{hcell}	0.16x0.015x0.145	m^3
Gas volume in the half-cell and the gas separator j	$V_{\mathrm{gas}}^{\mathrm{tot},j}$	1.6	L
Liquid volume in the half-cell and the gas separator j	$V_{\mathrm{liq}}^{\mathrm{tot},j}$	1.9	L

In Ref. [40], it is reported that the total liquid volume in each gas separator j equals $V_{\mathrm{liq}}^{\mathrm{sep},j} = 1.2\ \mathrm{L}$. The liquid and gaseous volumes in the half-cell can be calculated from equations (3.52) and (3.60). The total gas and liquid volumes in the half-cell j including its associated gas separator, $V_{\mathrm{gas}}^{\mathrm{tot},j}$, and $V_{\mathrm{liq}}^{\mathrm{tot},j}$ are given by equations (5.1)-(5.2). Since the gaseous volume in the half-cell can be calculated, the implementation of equation

(5.1) results in the gaseous volume of the products in the gas separator j, $V_{\text{gas}}^{\text{sep},j}$.

$$V_{\text{gas}}^{\text{tot},j} = V_{\text{gas}}^{\text{sep},j} + V_{\text{gas}}^{j} \tag{5.1}$$

$$V_{\text{liq}}^{\text{tot},j} = V_{\text{liq}}^{\text{sep},j} + V_{\text{liq}}^{j} \tag{5.2}$$

The operating conditions which were implemented in the model are listed in Table 5.2. The experimental setup operates in mixed mode. Therefore, the mixed mode boundary conditions, which are given by equations (3.35)-(3.38), are applied in the steady-state model. Furthermore, the diaphragm used in the experiments of Haug et al. [40], is the Zirfon. The properties of the Zirfon diaphragm are shown in Table 3.2.

Table 5.2: Operating conditions during the steady-state experiments of Haug et al.[40].

Variable	Symbol	Value	Units
KOH mass fraction	w_{KOH}	31.2	$\text{wt}\%$
Liquid flow rate	$\dot{V}_{\text{L}}$	0.33	L min^{-1}
Operating temperature	T	80	$^{\circ}\text{C}$
Operating pressure in the compartment j	p^{j}	101325	Pa
Current density	J	0.5 - 4	kA m^{-2}

The hydrogen gas evolution efficiency is given as a function of the current density, and the oxygen gas evolution efficiency is given as constant. Both gas evolution efficiencies are described by equations (5.3)-(5.4).

$$f_{\text{G,H}_2} = 0.25744 \cdot J^{0.14134} \tag{5.3}$$

$$f_{\text{G,O}_2} = 1 \tag{5.4}$$

Where the current density J is given in A m^{-2}.The implementation of the steady-state material balances that were described in Chapter 3 result in Figure 5.1.

In Figure 5.1, the vertical axis contains the gas impurity in vol%, and the horizontal axis shows the current density in kA m^{-2}. The experimental values of the anodic hydrogen content (green triangles) are provided for current densities ranging from 0.5-4 kA m^{-2}. Similarly, the experimental values of the cathodic oxygen content (red circles) are provided for current densities ranging from 0.5-1.5 kA m^{-2}. The experimental anodic hydrogen content ranges from 1.090-0.146 vol%. The experimental cathodic oxygen content ranges from 0.290-0.063 vol%. The increase of the current density results in the reduction of the impurity.

In Figure 5.1, the modeled anodic hydrogen content is represented by the green dashed line. Similarly, the modeled cathodic oxygen content is shown with the red dashed line. For current densities below 0.5 kA m^{-2} the anodic hydrogen content can exceed the threshold of 2 vol%, and the cathodic oxygen content is below 1.5 vol%. The increase of the current density results in the decline of the impurities for both models. Furthermore, the anodic hydrogen content is always larger than the cathodic oxygen content. This trend is due to the higher production rate of hydrogen

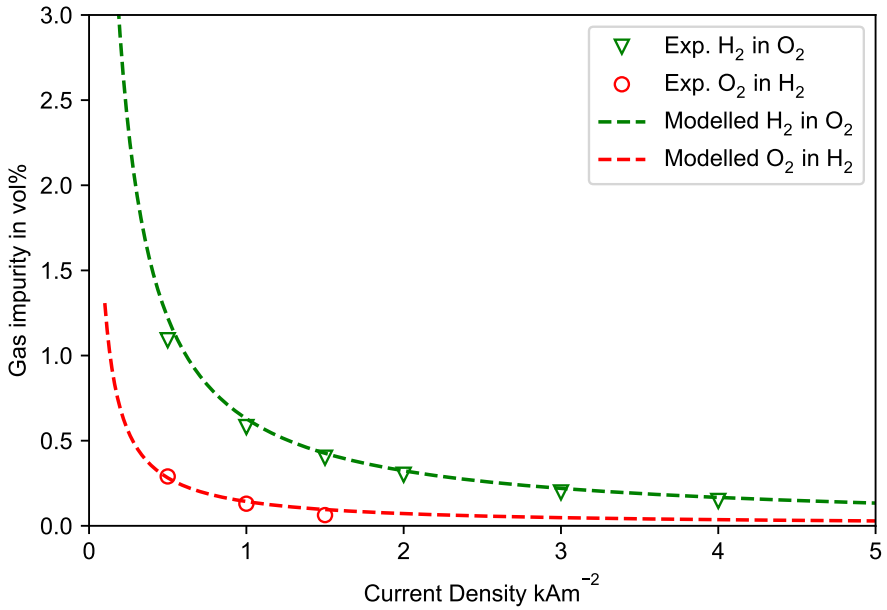

Figure 5.1: Validation of the steady-state model with the experimental results of Haug et al.[40].

with respect to oxygen. Since more hydrogen than oxygen is produced, the electrolyte bulk contains more dissolved hydrogen than oxygen species and hence the anodic hydrogen is larger than the cathodic oxygen content. Consequently, it is valid to say that the developed steady-state model comes in agreement with the experimental results and is almost identical with the model developed by Haug et al. [34].

5.2. Validation of the dynamic model

The validity of the model that describes the dynamic switching of electrolyte cycles is tested for the experimental results which are published by Haug et al.[40]. The design characteristics of the electrolysis cell are given in Table 5.1. The operating conditions during the experimental dynamic switching of electrolyte cycles are listed in Table 5.3.

Table 5.3: Operating conditions during the experimental dynamic switching of electrolyte cycles [40].

Variable	Symbol	Value	Units
KOH mass fraction	w_{KOH}	31.2	$\mathrm{wt\%}$
Liquid flow rate	$\dot{V}_{\mathrm{L}}$	0.33	$\mathrm{L\,min^{-1}}$
Operating temperature	T	80	$^{\circ}\mathrm{C}$
Operating pressure in the compartment j	p^{j}	101325	Pa
Current density	J	1	$\mathrm{kA\,m^{-2}}$
Duration of switching	t_{switch}	30	min

In the dynamic switching of electrolyte cycles, the volume of the liquid electrolyte and gaseous product in the electrolysis cell and the gas separators plays a significant role in the time required for the transition of the system to its steady-state. More specifically, the transition of the experimental setup to its steady-state, in terms of the anodic hydrogen content, strongly depends on the total volume of the produced gas in each half-cell and its associated gas separator $V_{\mathrm{gas}}^{\mathrm{tot},j}$. As stated in Chapter 5.1, the experimental total gaseous volume in each half-cell and its associated gas separator equals $V_{\mathrm{gas}}^{\mathrm{tot},j} = 1.6\ \mathrm{L}$. The introduction of this value in the developed model reveals that the gaseous volume in the gas separator of the compartment j equals $V_{\mathrm{gas}}^{\mathrm{sep},j} = 1.55\ \mathrm{L}$. The rest of the gaseous product can be found in the half-cell j, and has a volume of $V_{\mathrm{gas}}^{j} = 0.05\ \mathrm{L}$.

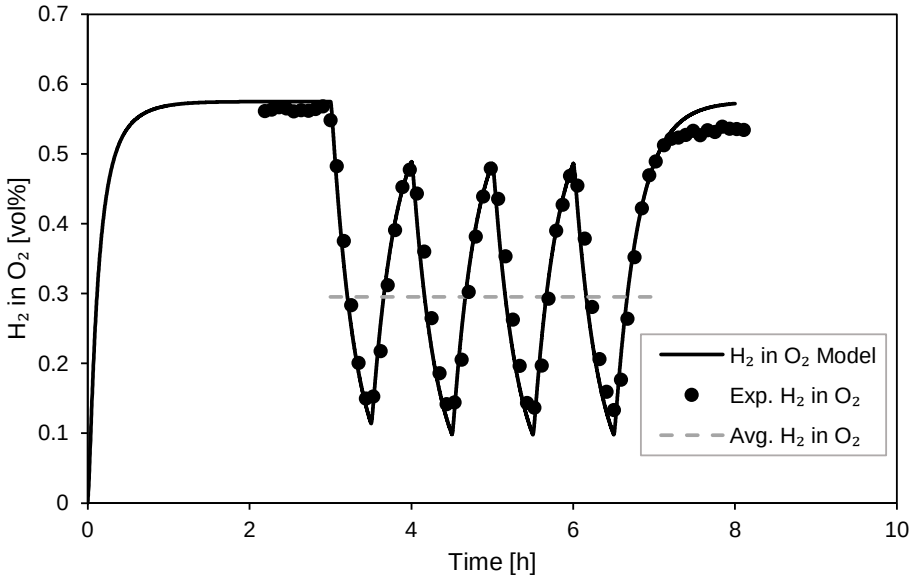

Figure 5.2: Validation of the dynamic switching model with the experimental results of Haug et al.[40].

In Figure 5.2, the validation of the model that describes the dynamic switching of electrolyte cycles with the experimental data of Haug et al. [40] is presented. On the vertical axis of the graph, the anodic hydrogen content is shown in vol%. Similarly, on the horizontal axis, the time is displayed, in h. The black circles show the experimental results found in Ref. [40]. The solid black line shows the prediction of the anodic hydrogen content as a function of time from the developed dynamic model. The grey dashed line shows the average anodic hydrogen content from the modeling results, when the dynamic switching starts.

In the beginning of the experiment, when $2\ \mathrm{h} \leq t_{\mathrm{tot}} \leq 3\ \mathrm{h}$, the system operates in mixed-mode until and has reached its steady state in terms of the anodic hydrogen content. When $3\ \mathrm{h} < t_{\mathrm{tot}} \leq 3.5\ \mathrm{h}$, the dynamic switching starts by importing into the model the boundary conditions of the partly-separated mode. The boundary conditions of the partly-separated mode are given by equations (3.39)-(3.42). Instantly,

there is a drop in the anodic hydrogen content. From the material balances, and the boundary conditions, the gas crossover in the partly-separated mode occurs only due to diffusion through the diaphragm. The partly-separated mode lasts for 30 min. Therefore, when $t_{\mathrm{tot}} = 3.5\ \mathrm{h}$, the boundary conditions of the mixed-mode are imported into the dynamic model. As a result, the anodic hydrogen content starts increasing due to electrolyte mixing before the entrance of the electrolysis cell. The continuous switching between the mixed-mode and the partly-separated mode takes place every 30 min, until $t_{\mathrm{tot}} = 6.5\ \mathrm{h}$. At this point, the mixed-mode boundary conditions are imported into the model, and the system approaches its steady-state anodic hydrogen content until $t_{\mathrm{tot}} = 8\ \mathrm{h}$.

In the beginning, the model approaches successfully the experimental steady-state anodic hydrogen content until $t_{\mathrm{tot}} = 3\ \mathrm{h}$. When the dynamic switching starts, the H_2 in O_2 impurity decreases because of the activation of the partly-separated mode. The model follows the fall successfully. When $t_{\mathrm{tot}} = 3.5,\ 4.5,\ 5.5,\ 6.5\ \mathrm{h}$, the model predicts a slightly lower anodic hydrogen content in the end of the partly-separated mode. Furthermore, the maximum H_2 in O_2 content matches the experimental results, when $t_{\mathrm{tot}} = 4,\ 5,\ 6\ \mathrm{h}$. When the system operates for the last time in mixed-mode and approaches its steady-state, at $6.5\ \mathrm{h} \leq t_{\mathrm{tot}} \leq 8\ \mathrm{h}$, the model predicts a higher impurity in comparison with the experimental results. Finally, in Ref. [40] it is reported that the average anodic hydrogen content during the dynamic switching of electrolyte cycles equals $y_{\mathrm{H_2}}^{\mathrm{avg}} = 0.306\ \mathrm{vol\%}$. The average anodic hydrogen content predicted from the model equals $y_{\mathrm{H_2}}^{\mathrm{avg,mod}} = 0.295\ \mathrm{vol\%}$.

Overall, the dynamic model sufficiently validates the experimental results in Ref.[40] and adapts to the sinusoidal trend during the dynamic switching of electrolyte cycles. The average anodic hydrogen content, which is calculated by the model, slightly deviates from the experimental average value . Despite the lower anodic hydrogen content which is predicted from the model when switching occurs from the partly-separated to the mixed mode, the results from the model and the experiment are in good agreement.

5.3. Results of the steady-state model

In the following, the calculation of the gas evolution efficiency is firstly presented. The gas evolution efficiency is required for the material balances of the steady-state and the dynamic model. Then, the results of the steady-state model in comparison with the experimental data from the setup of XINTC are shown.

5.3.1. Calculation of the gas evolution efficiency

The gas evolution efficiency is an indispensable term for the accurate solution of the material balances. Its value strongly depends on the cell design and the operating conditions of the cell.

The gas evolution efficiency of hydrogen and oxygen can be calculated by importing into the steady-state model the experimental values of the anodic hydrogen content and cathodic oxygen content which were introduced in Figure 4.2. When these impurities are known, the anodic partial pressure of hydrogen, $p_{\mathrm{out,H_2}}^{\mathrm{ano}}$ and the cathodic partial pressure of oxygen, $p_{\mathrm{out,O_2}}^{\mathrm{cat}}$ can be calculated from equations (3.91)-

(3.92), respectively. As a result, the solubility of hydrogen in the liquid electrolyte, in the anodic compartment, $c_{H_2}^{*,ano}$ can also be calculated because of equation (3.84). Furthermore, due to the knowledge of p_{out,O_2}^{cat}, the partial pressure of hydrogen in the cathodic compartment can be calculated, because of equation (3.45). As a result, the solubility of hydrogen in the liquid electrolyte, in the cathodic compartment, $c_{H_2}^{*,cat}$ can be calculated due to equation (3.85).

In Table 3.3, the unknown terms of the steady-state model are listed. When the experimental anodic hydrogen and cathodic oxygen content are imported into the model, the anodic and cathodic solubility of hydrogen in the liquid electrolyte, $c_{H_2}^{*,ano}$, $c_{H_2}^{*,cat}$ can be calculated and are not included as unknown quantities for the calculation of the gas evolution efficiency. At the same time, the gas evolution efficiency of hydrogen and oxygen are imported as unknown terms into the steady-state model. Due to the knowledge of the solubility, the number of unknowns is maintained and the steady-state model can be solved. In this case, the steady-state model can calculate the gas evolution efficiency of hydrogen and oxygen as a function of the current density.

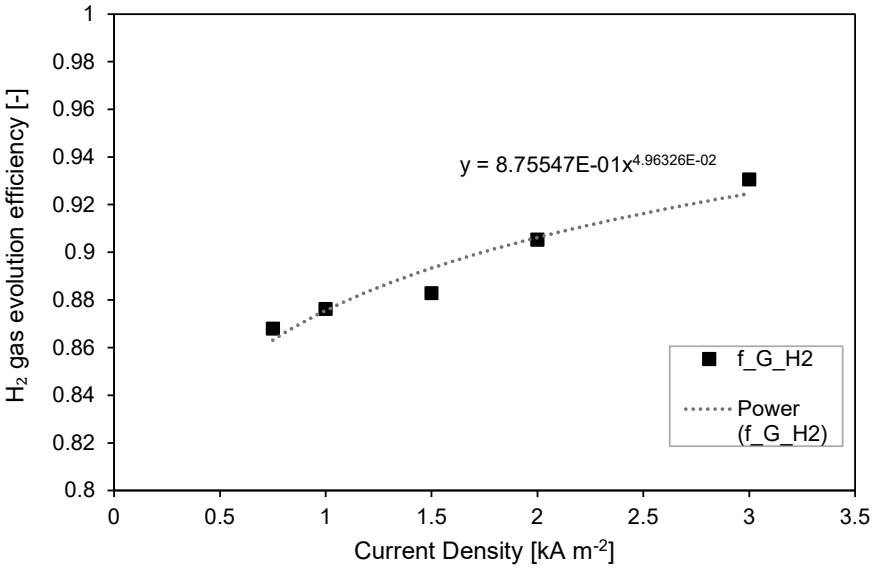

Figure 5.3: Calculated hydrogen gas evolution efficiency for the experimental results of XINTC, at the exit of the single cell.

In Figure 5.3, the calculated gas evolution of hydrogen is presented as a function of the current density. The calculated results are also listed in Table 5.4. In Chapter 2.2.4, it was mentioned that the gas evolution efficiency depends on the operating conditions that are applied in the electrolysis cell. More specifically, it was stated that it presents a significant dependence on the applied current density. Therefore, a considerable effort was presented in expressing the gas evolution efficiency as a function of the current density (see Table 2.1). The introduction of the experimental impurities in the steady-state model results in a moderate increase of the hydrogen gas evolution efficiency, which is expressed as a function of the applied current density. The modeled results are fitted to a power law trendline which is expressed from equation (5.5).

$$f_{G,H_2} = 0.87554 \cdot J^{0.04963} \tag{5.5}$$

Where the current density J is given in $\mathrm{kA\ m^{-2}}$. The modeling results validate that the increase of the current density can lead to a higher gas evolution efficiency. This observation can be explained from Faraday's law and the mass transfer mechanisms which act on the concentration boundary layer of the electrodes. A high reaction rate results in more dissolved product in the concentration boundary layer of the electrode. As a result, a large supersaturation builds up with respect to the electrolyte bulk, and hence more product is transferred to the gaseous phase. Finally, the steady-state model indicates a relatively higher gas evolution efficiency in comparison with the equations listed in Table 2.1. The higher value can be due to the dependency on other operating conditions such as the flow rate and the bubble coverage on the electrode area. Furthermore, it can be due to the underestimation of the anodic hydrogen content with the steady-state experiment. Despite the higher result, the hydrogen gas evolution efficiency does not exceed the unity for current densities up to 4 $\mathrm{kA\ m^{-2}}$.

The steady-state model can also calculate the gas evolution efficiency of oxygen. The solution of the steady-state model indicates that the gas evolution efficiency of oxygen is equal to unity. However, its implementation in the steady-state model resulted in a much lower cathodic oxygen content than the experimental. In general, it is not realistic to accept that the gas evolution efficiency is equal to unity, because it is assumed that the whole product is transferred to the gaseous phase in the boundary layer of the electrode. As a result, when the gas evolution efficiency is equal to unity, the calculated impurity is lower. To correct this effect, it is expressed by equation (5.6) to fit the experimental cathodic oxygen content.

$$f_{\mathrm{G,O_2}} = 0.84 \tag{5.6}$$

Table 5.4: The hydrogen gas evolution efficiency calculated from the steady-state model by importing the experimental anodic hydrogen content.

J ($\mathrm{kA\ m^{-2}}$)	$f_{\mathrm{G,H_2}}$ (-)
0.75	0.868
1	0.876
1.5	0.882
2	0.905
3	0.930

5.3.2. Comparison of the steady-state model with the experimental results

In Figure 5.4, the comparison of the steady state model with the experimental results from the alkaline water electrolyser of XINTC, is shown. On the vertical axis, the gas impurity is given, in vol%. On the horizontal axis, the current density is depicted in $\mathrm{kA\ m^{-2}}$. The approximated gas evolution efficiencies from equations (5.5)-(5.6) are imported into the steady-state model. Furthermore, the design characteristics of the

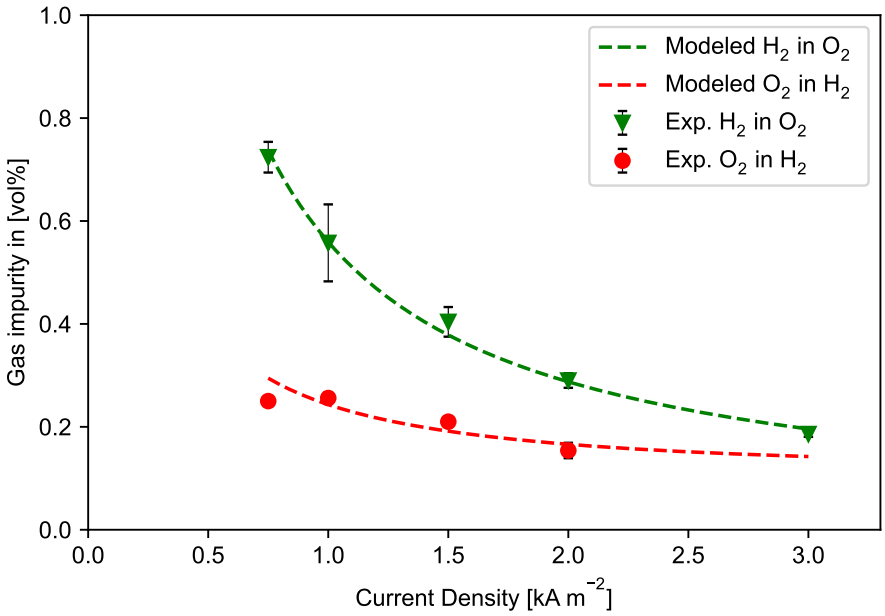

Figure 5.4: Comparison of the model in mixed mode with the experimental results of XINTC.

experimental setup, and the input operating conditions are listed in Table 4.1 and Table 4.2, respectively. The mixed-mode boundary conditions are given from equations (3.37)-(3.38). The material balances for the steady-state model which operates in mixed mode are solved by implementing simplex methods. The solution begins by introducing a set of initial conditions to the solver.

For both impurities, the model sufficiently verifies the experimental results. The solution presents a similar trend to the validated model. More specifically, it can be observed that the H_2 in O_2 content is always larger than the O_2 in H_2 content. The larger reaction rate estimated by the Faraday's law leads to a higher hydrogen production, and a hence higher anodic hydrogen than cathodic oxygen content. Furthermore, as the current density increases, the H_2 in O_2 impurity shows a gradually descending tendency. This can be explained by the growing hydrogen gas evolution efficiency as a function of the current density. Since the hydrogen gas evolution efficiency interprets the gas formation due to supersaturation in the electrode area, then a higher gas evolution efficiency results in a larger amount of gas on the electrode surface without O_2 species. Therefore, in the high current densities, the bulk concentration and partial pressure of the anodic hydrogen will be less, compared to the low current densities. The lower bulk concentration results in a low anodic hydrogen content, due to the desorption flux.

Similarly, the drop of the O_2 in H_2 impurity is due to the increasing hydrogen gas evolution efficiency with the current density. However, the variation of the O_2 in H_2 impurity is small due to the significantly high production rate of hydrogen in the cathode. The oxygen species which dissolve in the anodic compartment, cross permeate the opposite half cell due to the mixed boundary conditions. In the cathodic compartment, the bulk concentration of dissolved oxygen is significantly smaller than the bulk concentration of dissolved hydrogen. This can be explained by the 50% smaller reaction rate of oxygen in comparison with hydrogen. Furthermore, the diffusivity of oxygen in

the liquid electrolyte is an order magnitude smaller than the diffusivity of hydrogen. As a result, the desorption flux of oxygen in the cathodic compartment, is substantially smaller than the desorption flux of hydrogen, and hence the O_2 in H_2 impurity will show a small drop.

5.4. Results of the dynamic model

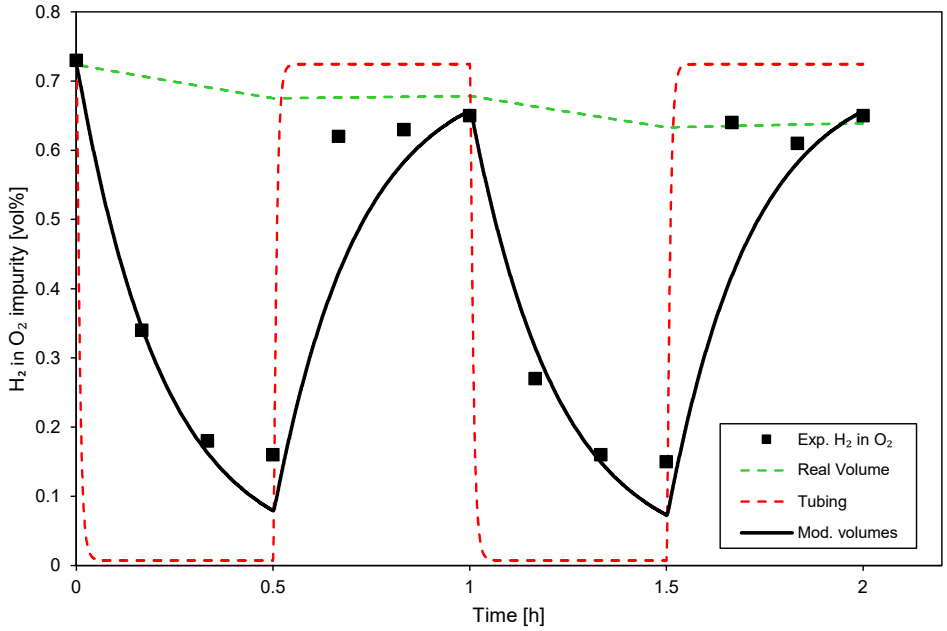

Figure 5.5: Comparison of three cases of the dynamic switching model with the experimental results of XINTC. *Green dashed line*: In the dynamic model the real volumes of the separator tanks are applied, $V_{\text{sep}}^{\text{ano}}$=16 L, $V_{\text{sep}}^{\text{cat}}$=32 L. *Red dashed line*: In the dynamic model the volumes of the separator tanks correspond to the volume of the interconnecting piping between the cell and the sampling point, $V_{\text{sep}}^{\text{ano}} = V_{\text{sep}}^{\text{cat}}$=0.06 L. *Black solid line*: Comparison of the dynamic model with the experimental data by applying a correction factor of 0.03 to the volume of the separator tanks,$V_{\text{sep}}^{\text{ano}}$=0.48 L, $V_{\text{sep}}^{\text{cat}}$=0.96 L .

In Figure 5.5, the dynamic model is shown in comparison with the experimental results from Table 4.5. The vertical axis contains the gas impurity in vol%. On the horizontal axis, the time is shown in h. The operating conditions which are applied in the dynamic switching model are listed in Table 4.3. The hydrogen gas evolution efficiency which is applied in the dynamic switching model is given by equation (5.7).

$$f_{\text{G,H}_2} = 0.868 \tag{5.7}$$

This is the gas evolution efficiency that corresponds to the current density of 0.75 kA m^{-2}, in Table 5.4. The oxygen gas evolution efficiency is given by equation (5.6).

In the dynamic model, the volume of the gas separators strongly influences the transition time to the steady state. For the experimental results of XINTC, it is not wise to use the actual volume of the separator tank because the impurity measurements took place at the exit of the electrolysis cell. However, the response of the anodic hydrogen content at the exit of the cell is not the same as at the exit of the gas separator. The modeling procedure to successfully predict the response of the

system must include the volume of the gas separators. Otherwise, the system will have an instant response to its steady state due to the CSTR assumption, and the transition time will not be modeled properly. As a result, in order to find the volume of the gas separators that better fit the experimental results, three cases of the dynamic model are considered. In these cases, the liquid volume fraction in the gas separators is kept constant at 42% of their geometrical volume.

In the first case (Real volumes), the actual volumes of the gas separators are imported from Table 4.1. At t=0, the model has reached its steady-state gas impurity, and the dynamic switching starts. In this case, because the volume ratio of the gas separator to the half-cell is extremely large ($R_{\mathrm{v}} = 561$ for the anode, and $R_{\mathrm{v}} = 1122$ for the cathode), the calculated response is significantly slow (green dashed line). The model does not agree with the experimental data because the anodic hydrogen content is predicted at the exit of the gas separators, where the inertia of the separator tank affects the calculated result. The response of the experimental setup is faster than the calculated result because the measurements are collected at the exit of the electrolysis cell, and the sample does not experience further mass transfer inside the separator tanks.

In the second case (Tubing), the volume of the gas separators corresponds to the volume of the interconnecting piping between the single cell and the sampling point. The total volume of the interconnecting piping equals approximately 0.06 L for each compartment. The examination of the calculated result reveals that the model (Tubing) reaches very fast its steady state (red dashed line). In this case, the volume ratio of the tubing to the half-cell is low ($R_{\mathrm{v}} = 2.1$ for the anode and cathode) and the system response is significantly fast due to the CSTR assumption. The low volume ratio in conjunction with the CSTR assumption accelerate the response to such an extent that the system instantly reaches its steady state.

To eliminate the difference in response time due to the large volume difference of the gas separators with the half-cell in the first case, and the immensely fast response due to the CSTR assumption in the second case, a correction factor is applied to the total volumes of the gas separators. The correction factor is equal to 0.03 and is applied to the real volumes of the gas separators. As a result, the corrected volumes of the new model (Modified volume) are $V_{\mathrm{sep}}^{\mathrm{ano}}$=0.48 L and $V_{\mathrm{sep}}^{\mathrm{cat}}$=0.96 L. In the following, only the model with the modified volumes is considered (black solid line).

To simulate the experimental dynamic switching, the model starts in mixed mode, reaches its steady-state impurity, and then the switching between the partly-separated and the mixed mode begins. At $t = 0\ \mathrm{h}$, the modeled steady-state impurity (black solid line) in mixed mode verifies the experimental value (black squares). Subsequently, at $0\ \mathrm{h} < t \leq 0.5\ \mathrm{h}$, the boundary conditions for the partly separated mode are imported into the model. The impurity decreases because the boundary conditions dictate that the gas crossover occurs only due to the effect of diffusion through the diaphragm. The decrease in the anodic hydrogen content can be interpreted from the significantly smaller magnitude of the crossover through the diaphragm than the crossover due to electrolyte mixing. It can be observed that the model presents the same trend with the experimental results when it operates in the partly-separated mode. The trend strongly depends on the correction factor which is applied to the geometrical volume of the gas separators. However, at $t = 0.5\ \mathrm{h}$, the anodic hydrogen content is

underestimated by the model. The underestimation of the impurity can be due to the gradual build up of a local supersaturation, in close proximity to the diaphragm, that leads to a high concentration gradient between the half cells, because the electrolyte mixing is inactive. For example, the dissolved cathodic hydrogen is supersaturated in the boundary layer, which is very close to the diaphragm area. At the same time, due to the absence of electrolyte mixing, the bulk concentration of the anodic hydrogen gradually decreases. As a result, a large concentration gradient between the half-cells builds up and leads to a higher gas crossover through the diaphragm in comparison with the model. This phenomenon results in a higher anodic hydrogen content than the predicted value, at $t = 0.5\ \mathrm{h}$. The dynamic model cannot capture phenomena of local supersaturation because it is developed on the basis of the CSTR assumption. The same tendency can be detected when $1\ \mathrm{h} < t \leq 1.5\ \mathrm{h}$. Finally, in Figure 5.2, when the validated model operates in partly-separated mode it shows a similar trend with the current model.

At $0.5\ \mathrm{h} < t \leq 1\ \mathrm{h}$, the system operates in the mixed mode, and the H_2 in O_2 impurity increases because the gas crossover develops due to electrolyte mixing in conjunction with the diffusion through the diaphragm. The model predicts a gradual increase of the anodic hydrogen content even though the experimental results indicate a steeper growth. The steeper growth can be due to the fact that the gaseous samples are collected at the exit of the electrolysis cell. At $t = 1\ \mathrm{h}$, before switching to the partly-separated mode, the approximated impurity is less than the initial one, at $t = 0\ \mathrm{h}$. This observation can be attributed to the fact that the system has not reached its steady-state anodic hydrogen content and is well-captured by the model and the experimental results.

From the modeling results of the dynamic switching (Modified volumes), the average H_2 in O_2 impurity can be approximated. The average modeled anodic hydrogen content equals $y_{\mathrm{H_2}}^{\mathrm{avg,mod}} = 0.423\ \mathrm{vol\%}$. From the experimental results of dynamic switching, the average anodic hydrogen content is equal to $y_{\mathrm{H_2}}^{\mathrm{avg}} = 0.445\ \mathrm{vol\%}$. Therefore, the modified model develops a sinusoidal trend which is similar to the experimental impurities.

Overall, the proper implementation of the dynamic model to any experimental results reveals that the applied volume ratio of the gas separator to the half-cell should be kept in moderate values. Furthermore, when the impurity is not calculated at the exit of the gas separators, the response of the model becomes significantly fast, due to the CSTR assumption. As a result, a correction factor to the geometrical volumes needs to be applied. The modified model which is applied to the experimental results of XINTC shows that the trend of the dynamic switching experiment can be sufficiently predicted. However, the existence of any local supersaturation inside the half-cell cannot be predicted properly due to the CSTR assumption.

5.5. Sensitivity Analysis

In the following, a sensitivity analysis for the dynamic model is provided. The boundary conditions of the dynamic model correspond to the operation in mixed mode. The sensitivity analysis focuses on the dynamic model because it can provide information about the response of the system and the steady-state impurity at the same time.

Furthermore, only the anodic hydrogen content is shown because it presents larger variation than the cathodic oxygen content. The sensitivity analysis is materialized with varying the gas evolution efficiency of the model, the design characteristics of the system and the operating conditions. The design characteristics include the variation of the volume in the gas separators and the diaphragm. The operating conditions include the variation of the liquid volumetric flow rate, the liquid and gaseous volume in the gas separators, the temperature in the system and the KOH mass fraction. The models with the varying input parameters are compared to the default model. The input parameters of the default model are listed in Table 5.5.

Table 5.5: Input parameters of the default model.

Variable	Symbol	Value	Units
KOH mass fraction	w_{KOH}	30	$\mathrm{wt\%}$
Liquid flow rate	$\dot{V}_{\mathrm{L}}$	100	$\mathrm{mL\ min^{-1}}$
Operating temperature	T	313.15	K
Operating pressure in the compartment *j*	p^j	101325	Pa
Current density	J	1	$\mathrm{kA\ m^{-2}}$
Anodic gas separator volume	$V_{\mathrm{sep}}^{\mathrm{ano}}$	1	L
Cathodic gas separator volume	$V_{\mathrm{sep}}^{\mathrm{cat}}$	1	L
Liquid volume in the anodic gas separator	$V_{\mathrm{liq}}^{\mathrm{sep,ano}}$	0.5	L
Liquid volume in the cathodic gas separator	$V_{\mathrm{liq}}^{\mathrm{sep,cat}}$	0.5	L
Hydrogen gas evolution efficiency	$f_{\mathrm{G,H_2}}$	0.875	-
Oxygen gas evolution efficiency	$f_{\mathrm{G,O_2}}$	0.830	-

5.5.1. Variation of the gas evolution efficiency

In Figure 5.6, the effect of the variation of the gas evolution efficiency in the anodic hydrogen content as a function of time is shown. The dynamic model operates in mixed mode until it reaches its steady state, and the models with the varied gas evolution efficiency are compared with the default model (black dashed line).

In Figure 5.6a, the variation of the hydrogen gas evolution is shown. Firstly, it can be observed that a decrease in the hydrogen gas evolution efficiency leads to an increase in the anodic hydrogen content. The decrease of the hydrogen gas evolution results in a lower gaseous production rate of hydrogen and more dissolved cathodic hydrogen. The dissolved hydrogen in the cathode cross permeates to the anodic half-cell due to the mixed boundary conditions. An increase in the bulk concentration of the anodic hydrogen, results in a higher desorption flux in the anodic electrolyte bulk, and hence a higher H_2 in O_2 impurity. On the contrary, an increase in the hydrogen gas evolution efficiency leads to a higher gaseous hydrogen production rate in the cathode and hence less dissolved cathodic hydrogen. The dissolved cathodic hydrogen which

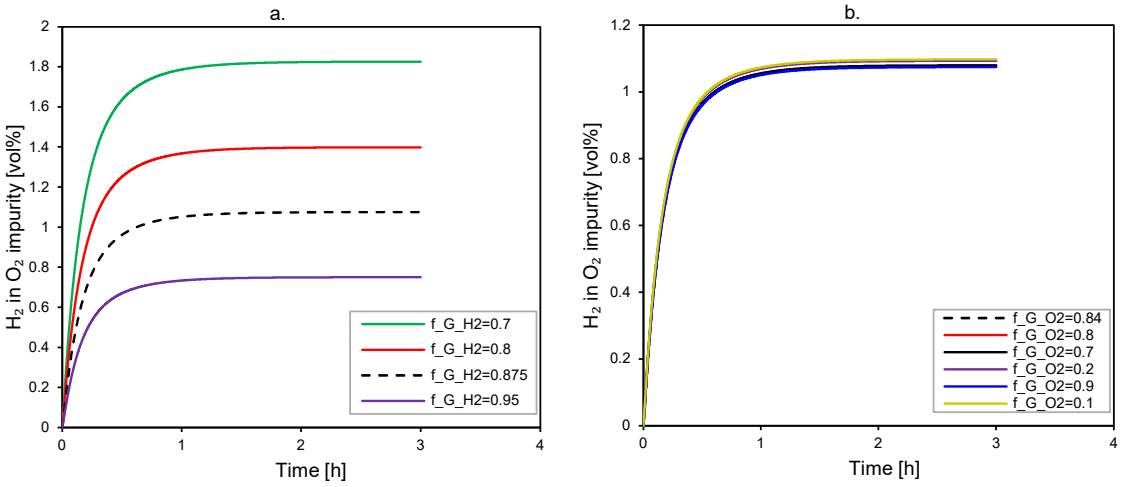

Figure 5.6: Variation of the gas evolution efficiency: (a) Hydrogen gas evolution efficiency. (b) Oxygen gas evolution effiency

ends up to the anodic half-cell, results in a lower H_2 in O_2 impurity due to the reduced anodic bulk concentration of hydrogen. The variation of the hydrogen gas evolution efficiency does not affect the transition time to the steady state.

In Figure 5.6b, the variation of the oxygen gas evolution is shown. The variation of the oxygen gas evolution efficiency seems to negligibly affect the anodic hydrogen content. However, it seems that the implementation of extreme values ($f_{\mathrm{G,O_2}} = 0.9$ and $f_{\mathrm{G,O_2}} = 0.1$) slightly affects the steady-state value. When the oxygen gas evolution efficiency decreases, to some extent less pure oxygen product is generated in the anodic compartment. As a result, the anodic oxygen partial pressure will be slightly reduced and the H_2 in O_2 slightly increases due to equation (3.105). At the same time, when the oxygen gas evolution efficiency decreases to $f_{\mathrm{G,O_2}} = 0.1$, the degree of desorption of the dissolved oxygen in the anodic half-cell is increased by an order of magnitude. As a result, the anodic oxygen partial pressure is kept constant and the anodic hydrogen content is not significantly affected. Finally, the variation of the oxygen gas evolution efficiency does not affect the response of the model to its steady state.

Overall, it can be concluded that the calculation of the hydrogen gas evolution efficiency significantly affects the final results of the model. Therefore, accurate experimental data are required for the approximation of the hydrogen gas evolution efficiency. On the contrary, the small variation in the oxygen gas evolution efficiency does not seem to substantially affect the final result.

5.5.2. Variation of the operating conditions

In Figure 5.7, the sensitivity analysis due to the variation of the operating conditions is presented. More specifically, the varying operating conditions include the liquid flow rate $\dot{V}_{\mathrm{L}}$ (Figure 5.7a), the temperature T of the process (Figure 5.7b), the mass fraction of KOH w_{KOH} (Figure 5.7c), and the liquid $V_{\mathrm{liq}}^{\mathrm{sep},j}$ and gaseous volume in the gas separator $V_{\mathrm{gas}}^{\mathrm{sep},j}$ (Figure 5.7d). The dynamic model simulates the operation of an alkaline water electrolyser in mixed mode. As a result, the mixed boundary conditions

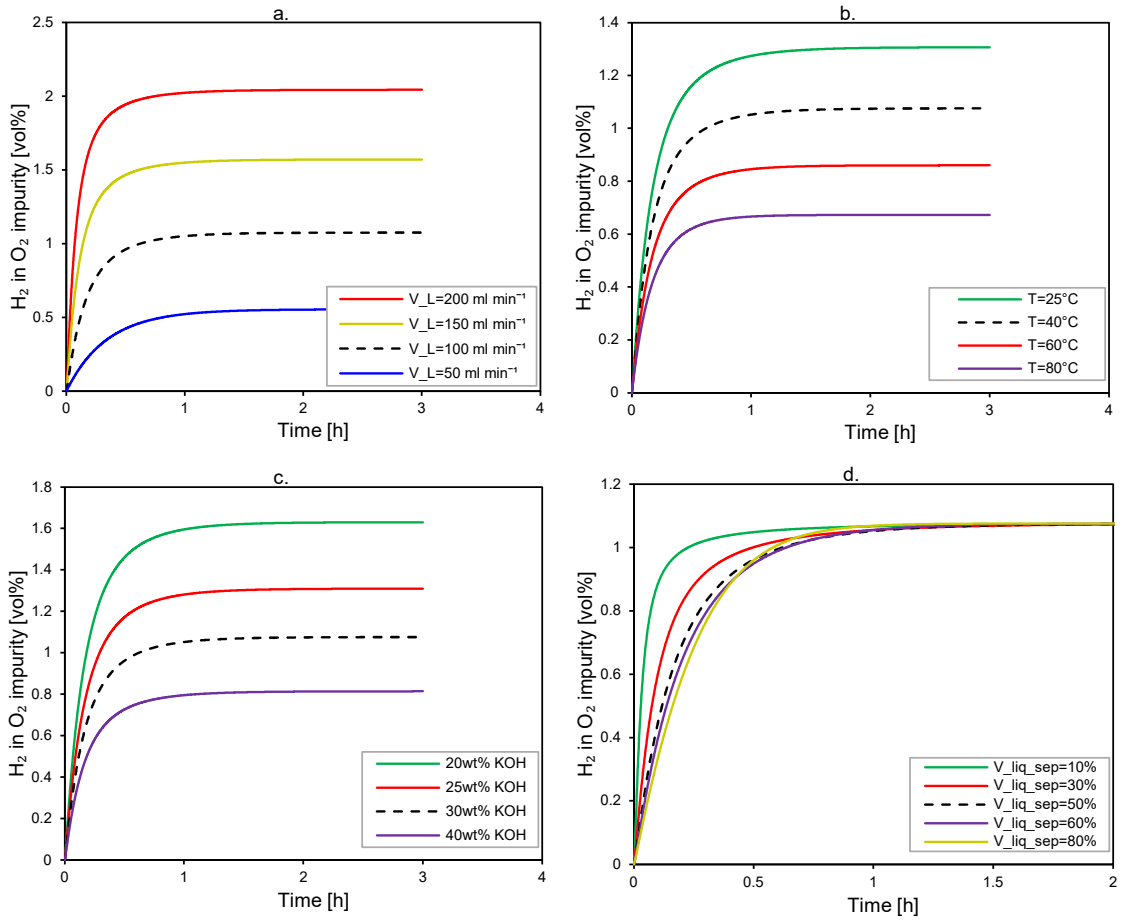

Figure 5.7: Variation of the operating conditions: (a) Liquid flow rate. (b) Temperature. (c) KOH wt%. (d) Liquid and gaseous volume in the gas separator

are given. The models with the varying operating conditions are compared with the default model (black dashed line).

In Figure 5.7a, the variation of the liquid flow rate is presented. It can be observed that a increase in the liquid flow rate results in a rise of the steady-state H_2 in O_2 impurity. This trend can be attributed to the electrolyte mixing gas crossover mechanism. More specifically, an increase in the liquid flow rate leads to a higher convective mass transfer from the mass balance equations. Therefore, more dissolved cathodic hydrogen will conclude in the anodic compartment. The bulk concentration of hydrogen in the anodic half-cell increases as the liquid flow rate rises. As a result, the desorption flux is governed by higher supersaturation, and hence more hydrogen will outgas in the anodic compartment. Similarly, as the liquid flow rate decreases, the anodic hydrogen content reduces. The transition time to the steady-state, does not seem to be affected from the variation of liquid flow rate.

In Figure 5.7b, the variation of the temperature is presented. An increase in the temperature results in a lower steady-state H_2 in O_2 impurity. The solubility data which are imported in the model by implementing the Setchenov relation (see Table A.9 and Table A.12), indicate that an increase in the temperature slightly reduces the solubility of hydrogen and oxygen in the liquid electrolyte. Therefore, in higher temperatures,

the dissolved hydrogen species experiences a higher degree of supersaturation than in lower temperatures and can outgas more efficiently. At the same time, the diffusivity data which are imported in the model (see Table A.2 and Table A.4) indicate that an increase in the temperature results in a higher hydrogen and oxygen diffusivity. Therefore, the hydrogen and oxygen species experience a higher rate of diffusion, which is a fundamental property for the calculation of the mass transfer coefficient in the electrolyte bulk. The combined reduction in the solubility and the rise in diffusivity lead to a higher desorptive flux in the electrolyte bulk. As a result, the gas crossover due to the electrolyte mixing reduces and the dissolved species outgas more efficiently in the compartment in which they are generated. Similarly, the opposite holds true when the temperature is reduced. Finally, the variation of the temperature does not affect the transition time to the steady state.

In Figure 5.7c, the sensitivity analysis for the variation of the KOH mass fraction is shown. It can be observed that an increase in the KOH mass fraction leads to a decrease in the anodic hydrogen content. The decrease of the H_2 in O_2 impurity can be explained from the imported solubility literature data. An examination of the imported data (see Table A.9 and Table A.12) reveals that an increase in the KOH mass fraction results in the fall of the solubility of hydrogen and oxygen species due to the salting out effect. As a result, the dissolved species in the electrolyte bulk, achieve a higher degree of supersaturation with an increasing KOH mass fraction. Due to the higher degree of supersaturation, the desorptive flux in the electrolyte bulk also increases and a higher amount of pure hydrogen or oxygen is released in the compartment in which they are produced. As a result the H_2 in O_2 impurity decreases with an increasing KOH mass fraction. The KOH mass fraction does not affect the transition time to the steady-state impurity.

In Figure 5.7d, the variation of the liquid and gaseous volume in the gas separators is presented. The total volume of the separator tank is kept constant. The liquid volume is expressed as a percentage of the total geometrical volume of the gas separator. For example, the indication V_liq_sep=30% means that the gas separator consists of 30% liquid electrolyte and 70% gaseous product. In Figure 5.7d, it can be noticed that a decrease in the liquid volume of the gas separator results in a faster system response.

The response of the system in terms of the anodic hydrogen content presents a dependency on the gaseous volumetric flow rate, which is visualized in Figure 5.8. More specifically, a decrease in the liquid volume means that gas separator consists of more gaseous product and the bulk concentration of the dissolved species develops faster to its steady state. Due to the quick response of the bulk concentration, the desorption flux in the single cell will follow a similar trend. Therefore, from equation (3.103), the anodic volumetric flow rate develops faster as the liquid volume of the gas separator decreases. Subsequently, the anodic hydrogen content reaches its steady state faster. On the contrary, when the liquid volume of the gas separator increases, the gaseous flow rate develops slower. At the same time, the partial pressure increases fast. Hence, the response of the anodic hydrogen content does not slow down significantly. For this reason, when the liquid volume increases, the anodic hydrogen content does not show a significant difference with the case where V_liq_sep=50%. Finally, all the models conclude in the same steady-state anodic

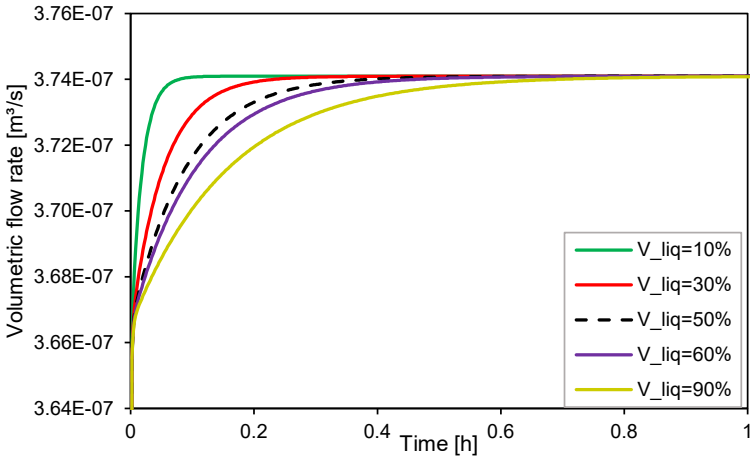

Figure 5.8: Response of the gaseous volumetric flow rate as a function of the liquid volume of the separator tank.

hydrogen content.

Overall, the variation of the operating conditions in the dynamic model results in a realistic behavior during the alkaline water electrolysis. Finally, it has to be noted that the dynamic material balances strongly depend on the input properties, such as the diffusivity and the solubility. Therefore, the input properties need to be selected carefully.

5.5.3. Variation of the design characteristics

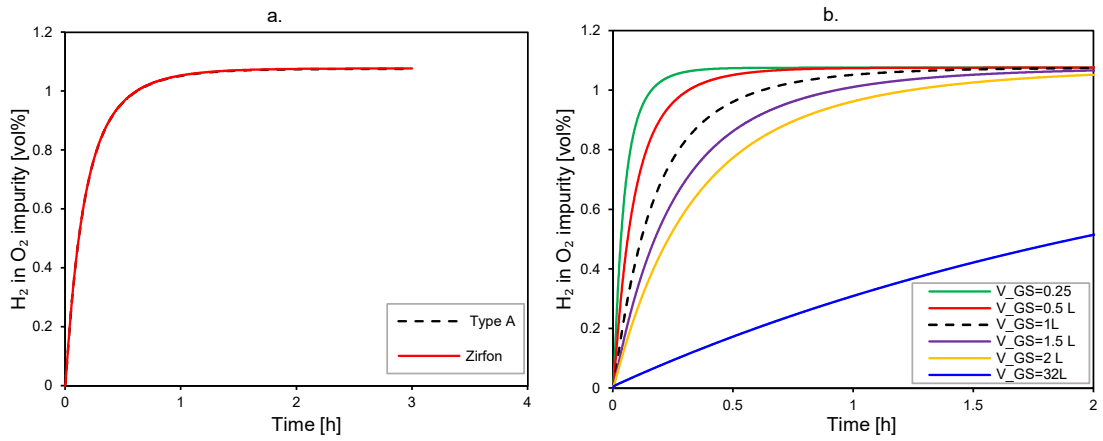

Figure 5.9: Variation of the design characteristics: (a) Porous diaphragm. (b) Geometrical volume of the gas separators.

In Figure 5.9, the sensitivity analysis for the design characteristics is shown. The design characteristics consist of the porous diaphragm, and the geometrical volume of the gas separators. The dynamic models simulate the transition to the steady state in mixed mode, and hence the mixed boundary conditions are imported. The varied dynamic models are compared with the default model (black dashed line).

In Figure 5.9a, the effect of Type A and Zirfon diaphragm in the anodic hydrogen content is compared. From the modeling results, it can be observed that the selec-

tion of alternative porous diaphragm has a negligible effect on the variation of the H_2 in O_2 impurity. The negligible effect on the anodic hydrogen content can be justified from the definition of the hydrogen gas evolution efficiency in this model. The hydrogen gas evolution was calculated by importing into the model the experimental H_2 in O_2 and O_2 in H_2 impurities. The measured impurities are the the result of the gas crossover mechanisms due to the diffusion through the diaphragm, and the electrolyte mixing. Therefore, the gas evolution acts as a lumped parameter which includes both of these gas crossover mechanisms. The CSTR assumption cancels out the existence of any local supersatution phenomena close to the electrode area which may result in a larger diffusion through the diaphragm. Finally, in an attempt to quantify the effect of gas crossover flux through the diaphragm, the anodic hydrogen content is evaluated for the dynamic model in the partly-separated mode. When the model reaches its steady state, the results indicate that for the Zirfon separator the H_2 in O_2 impurity equals to $y_{H_2}^{\text{Zirfon}} = 0.0103$ vol% and for the Type A it is equal to $y_{H_2}^{\text{TypeA}} = 0.0088$ vol%. Therefore, the maximum calculated contribution of the gas crossover through the diaphragm is negligible in comparison with the electrolyte mixing, which is above 1% according to Figure 5.9a.

In Figure 5.9b, the effect of the variation of the geometrical volume of the gas separators is studied. The liquid volume of the electrolyte in the gas separator is 42% of the geometrical volume of the separator tank. It is noticed that an increase in the geometrical volume results in a slower transition to the steady-state. The enlargement of the geometrical volume of the gas separator leads to an increase of both the liquid and gaseous volume inside the gas separator. Therefore, it causes a slower response in the dissolved species in the liquid electrolyte and a slower response in the outlet partial pressures of the species in the gas separator. This observation can be justified from equations (3.101)-(3.102). In Figure 5.10, the response of the anodic gaseous volu-

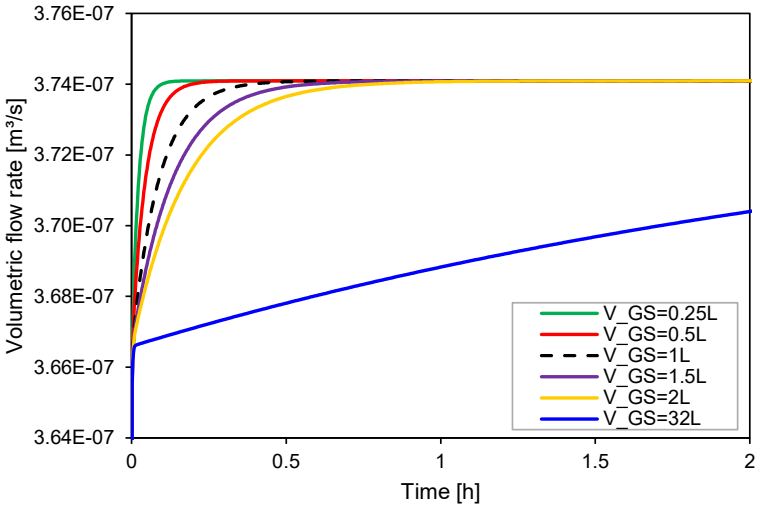

Figure 5.10: Response of the gaseous volumetric flow rate as a function of the total volume of the separator tank.

metric flow rate is shown. The transition time of the anodic hydrogen content presents a strong dependency on the gaseous volumetric flow rate. Since the response time of the bulk concentration increases with the enlargement of the separator tank, the gaseous volumetric flow rate will evolve slower due to equation (3.103). The comparison of Figure 5.10 with Figure 5.9b reveals that the anodic hydrogen content develops a similar trend. Therefore, when the volume of the separator tank increases, the H_2 in O_2 impurity reaches its steady state slower. On the contrary, when the volume of the gas separators decreases, the anodic hydrogen content will evolve faster to its steady state because the bulk concentration and the partial pressures in the gas separator develop faster. Finally, in the extreme case where the geometrical volume of the gas separator is oversized (V_GS=32L), the system will need even more time to reach its steady state.

Overall, the model is not sensitive to different diaphragms. The possible overestimation of the hydrogen gas evolution efficiency in combination with the negligence of local supersaturation in the electrode area, results in a significantly underestimated diffusion flux through the separator. Thus, the modeled anodic hydrogen content is not affected by the change of diaphragms.

Finally, the dynamic model can calculate the system response, in terms of the anodic hydrogen content, by taking into account the geometrical volume of the gas separators. In the steady-state model, the effect of the gas separators is neglected because the accumulation terms are zero. It is found that the geometrical volume of the gas separators can substantially influence the transition time to the steady-state gas impurity.

6

Conclusions and recommendations

In this thesis, the gas crossover in alkaline water electrolysis has been experimentally characterized and calculated by developing a steady-state and a dynamic model. More specifically:

- The motivation of the thesis has been provided. The factors which affect the gas purity in alkaline water electrolysis are thoroughly analyzed. It has been proven that the gas purity can be modeled both in steady-state and dynamically. The design characteristics and operating conditions of the electrolyser affect the response of the model, in terms of the anodic hydrogen content. As a result, the model can predict the gas crossover, in low current densities and the threshold of the LEL which is 4 vol% can be avoided.

- The literature study has introduced the theoretical framework of the gas crossover mechanisms in alkaline water electrolysis plants (Schalenbach et al. [20], Trinke et al. [41]). Furthermore, the mitigation strategies were analyzed (Haug et al. [40]) with a focus given on the dynamic switching of electrolyte cycles.

- The material balances have been derived for the steady-state and dynamic model. The steady-state model is based on the theoretical considerations of Haug et al. [34]. The dynamic mass balances are an extended version of the steady-state case and they have been developed from the scratch. In the dynamic model, the effect of the gas separators on the response of the system has been included.

- Gas impurity experiments have been conducted for the single cell of XINTC. The samples were collected at the exit of the electrolysis cell. The first experiment shows the steady-state gas impurity in mixed mode as a function of the current density. The second experiment presents the dynamic response of the system when it is subjected to the dynamic switching of electrolyte cycles.

- The results of the models have been provided. The validity of the steady-state and dynamic model has been tested for the experimental results of Haug et al. [40]. The experimental impurities allow the calculation of the gas evolution

efficiency with the use of the steady-state model. Next, the steady-state and dynamic models are compared with the experimental findings. Finally, a sensitivity analysis is provided for the dynamic model which operates in mixed mode.

The conclusions of this thesis can help in improving the experimental setup for single-cell measurements. Furthermore, they assist in the evaluation or the recalculation of important model properties, such as the gas evolution efficiency for hydrogen, $f_{\mathrm{G,H_2}}$. Finally, the outcome of this thesis gives a better understanding on the steady-state and dynamic models. Overall, the conclusions of the thesis are summarized below:

Experiments

1. The results of the steady-state experiment agree with the trend of the results found in the literature. The anodic hydrogen content is larger than the cathodic oxygen content because the production rate of hydrogen is double the oxygen. Furthermore, the anodic hydrogen content decreases as the current density increases because the amount of H_2 species that dissolves in the electrolyte bulk is reduced. The deviation of the experimental H_2 in O_2 impurities, in low current densities, is attributed to the possibility that the system did not reach its steady state.

2. When the system operates in mixed mode, during the experimental dynamic switching, it develops a fast response because the samples are collected at the exit of the single cell. The sampling point is positioned before the gas separators and the inertia of the gas separators is neglected. For this reason, the measurements indicate a faster response in comparison to the modeling results. Nonetheless, the experimental dynamic switching shows that the impurity achieves a sinusoidal trend, where the average H_2 in O_2 content ($y_{\mathrm{H_2}}^{\mathrm{avg}} = 0.445\ \mathrm{vol\%}$) is less than the steady-state impurity in mixed mode ($y_{\mathrm{H_2}} = 0.724\ \mathrm{vol\%}$).

3. When the system operates in a partly-separated mode, during the dynamic switching experiment, it shows that the anodic hydrogen content is larger than the value which is calculated by the modified model, at $t = 0.5,\ 1.5\ \mathrm{h}$. This is due to the existence of areas of local supersaturation, in close proximity to the diaphragm.

4. The existence of the gas separators not only affects the system response but the magnitude of the steady-state anodic hydrogen content. The fact that the samples are collected at the outlet of the electrolysis cell means that the additional mass transfer phenomena that take place into the separator tank are neglected. As a result, the experiment underestimates the anodic hydrogen content.

Steady-state model

1. The steady state model validates the literature data. Furthermore, it shows good agreement with the experimental data from XINTC.

2. The gas evolution efficiency of hydrogen strongly depends on the measured impurities. This is due to the fact that it is calculated by importing the experimental data into the steady state model.

3. The gas evolution efficiency of hydrogen validates that its value is affected from the applied current density. However, in this thesis, it is larger than the calculated value from other relations found in literature. This can be due to the underestimation of the experimental steady-state anodic hydrogen content.

Dynamic model

1. The modified model with the correction factor shows that it can verify the dynamic switching of electrolyte cycles. As a result, it acquires a sinusoidal behavior similar to the trend of the experimental data. The value of the average calculated anodic hydrogen content ($y_{\mathrm{H_2}}^{\mathrm{avg,mod}} = 0.423$ vol%) is close to the experimental ($y_{\mathrm{H_2}}^{\mathrm{avg}} = 0.445$ vol%). Similarly, the calculated value of the validated model is equal to $y_{\mathrm{H_2}}^{\mathrm{avg,mod}} = 0.295$ vol%, and the experimental one equals $y_{\mathrm{H_2}}^{\mathrm{avg}} = 0.306$ vol%.

2. The dynamic model shows that its implementation requires the sampling and calculation of the anodic hydrogen content at the exit of the gas separators. Otherwise, a correction factor has to be applied to the geometrical volume of the gas separators. For example, in the validated model, the anodic hydrogen content was sampled and calculated at the exit of the gas separators. As a result, the calculated transition time agrees with the experimental data. On the contrary, in the experimental data of XINTC, due to the large real volume of the gas separators, the transition time to the steady state is significantly slow. Therefore, a correction factor needs to be applied.

3. The imported volume ratio of the separator tank to the half-cell must have moderate values. The implementation of low volume ratios, such as the Tubing case in Figure 5.5, leads to an instant transition to the steady state, due to the CSTR assumption.

4. When the dynamic model operates in a partly-separated mode, it cannot calculate phenomena of local supersaturation close to the diaphragm, due to the CSTR assumption. As a result, it underestimates the anodic hydrogen content.

5. Overall, the variation of the operating conditions shows that the model is robust and has a realistic behavior.

6. In the dynamic model, the transition time to the steady state depends on the geometrical volume of the separator tank, the volume of the half-cell, and the liquid volume ratio in the gas separator. The rest of the input properties do not affect the response of the system.

7. The steady-state value of the anodic hydrogen content strongly depends on the calculated gas evolution efficiency of hydrogen. As a result, the experimental H_2 in O_2 impurity measurements must be reliable.

8. In the mixed-mode operation, the steady-state anodic hydrogen content is not affected by the diaphragm change. This happens because the gas evolution efficiency acts as a lumped parameter that includes the crossover through the diaphragm and the electrolyte mixing.

Future recommendations

The dynamic switching of the electrolyte cycles seems to be a promising alternative operation to reduce the gas crossover in low current densities. In this thesis, it has been shown that the average anodic hydrogen content is less than the impurity in mixed mode. However, when the system switches to the partly-separated mode, a concentration gradient in KOH builds up due to the half-reactions. A future experimental project regarding the dynamic switching can include the durability of the cell in the long term. Furthermore, it would be interesting to study a complete stack which operates with the dynamic switching. Another alternative process which is interesting to study is the minimum lye flow rate [47]. It is based on the supply of a minimum flow rate such that the diaphragm does not ”dry out”. As a result, the gas crossover due to electrolyte mixing is minimized.

In the model of the thesis, the half-cells were modeled as ideal CSTR reactors. The ideal CSTR follows from the assumption of perfect mixing of the reactants in the half-cell. However, in real cases, the liquid electrolyte may not have a uniform bulk concentration inside the half-cell. Due to the flow configuration in the half-cell, the resulting outlet bulk concentration can vary throughout the reactor. Therefore, the half cells can also be modeled with non-ideal reactors, such as the plug flow model with superimposed dispersion. Another reactor model can include the tank-in-series model. Both models require the experimental determination of the residence time distribution. Furthermore, both models consider the non-ideal behavior of a plug flow reactor. The plug flow reactor model may be more appropriate than the CSTR because it results in a concentration gradient throughout the half-cell. Therefore, it can be possible to capture phenomena of local supersaturation that cannot be tracked with the ideal CSTR assumption.

A more complete version of the current model can also include alternative methods for calculating the gas evolution efficiency. Even though the gas evolution efficiency presents a strong dependence on the applied current density, it is also affected from other operating conditions such as the liquid flow rate and the bubble coverage on the electrode. Vogt [70], has made a significant effort in quantifying the gas evolution efficiency with analytical methods. More specifically, he extracted a function for the gas evolution efficiency, where the variables are the diffusivity of the dissolved species, the pressure, the temperature, the current density, the bubble diameter and the fraction surface coverage of the electrode. Therefore, the implementation of experiments to define the fraction surface coverage and the bubble diameter could result in a different definition of the gas evolution efficiency which is independent of the experimental anodic hydrogen content. Finally, in a future model that calculates the gas crossover, the effect of the gas separators in terms of the additional mass transfer must be included.

A

Appendix - Model properties from literature

In this chapter, the literature data which are required for the calculation of the model's properties will be introduced.

A.1. Water vapour partial pressure

In Ref. [55], the water vapour partial pressure is a function of the potassium hydroxide molality and electrolyte temperature.

$$\begin{aligned}\log_{10} p_{\mathrm{H_2O}} = &-0.01508m - 0.0016788m^2 + 2.25887 \cdot 10^{-5}m^3 \\ &+ \left(1 - 0.0012062m + 5.6024 \cdot 10^{-4}m^2 - 7.8228 \cdot 10^{-6}m^3\right) \\ &\cdot (35.4462 - 3343.93/T - 10.9\log_{10} T + 0.0041645T)\end{aligned} \tag{A.1}$$

In equation A.1, the water vapor pressure is calculated in bar and the temperature T in K. The molality m, is defined as the mols of water per kg of KOH solution. Therefore, the molality is given in $\mathrm{mol/kg}$. Given the molar mass of potassium hydroxide M_{KOH}, the molality can be calculated by:

$$m = \frac{w_{\mathrm{KOH}}}{M_{\mathrm{KOH}} \cdot (1 - w_{\mathrm{KOH}})} \tag{A.2}$$

In which, w_{KOH} is the mass fraction of potassium hydroxide in the electrolyte solution.

A.2. Surface tension of liquid electrolyte

The surface tension of the liquid electrolyte can be calculated as a function of the temperature and the mass fraction of KOH in the liquid electrolyte solution using [56]:

$$\gamma(\theta, w_{\mathrm{KOH}}) = \sum_{i=1}^{5} \left(\sum_{i=k}^{5} \alpha_{ik} \theta^{k-1} \right) w_{\mathrm{KOH}}^{i-1} \cdot 10^{-3} \tag{A.3}$$

where the temperature T is given in $^{\circ}C$, and the matrix coefficient a_{ik} is equal to:

$$\alpha_{ik} = \begin{pmatrix} +75.4787 & -0.138489 & -0.336392 \cdot 10^{-3} & +0.475362 \cdot 10^{-6} & -0.264479 \cdot 10^{-9} \\ -32.889 & +1.34382 & -0.910138 \cdot 10^{-2} & +0.396124 \cdot 10^{-4} & -0.57365 \cdot 10^{-7} \\ +614.527 & -12.8736 & +0.104855 & -0.449076 \cdot 10^{-3} & +0.651193 \cdot 10^{-6} \\ -1455.06 & +39.8511 & -0.344234 & +0.144383 \cdot 10^{-2} & -0.207599 \cdot 10^{-5} \\ +1333.62 & -38.3316 & +0.335129 & -0.137313 \cdot 10^{-2} & +0.194911 \cdot 10^{-5} \end{pmatrix}$$

A.3. Gas hold-up fraction

As explained in Chapter 3.4.5, the gas hold-up fraction is given by the publication of Haug et al.[34]. From their experimental investigations they deduced the following relation for the gas hold-up fraction $\varepsilon^{j}_{\mathrm{g,out}}$:

Table A.1: Mathematical expression for the gas hold-up fraction according to Haug et al.[34].

Compartment	X_1	X_2	X_3
Anode	0.59438	0.59231	0.75647
Cathode	0.76764	0.73233	0.73457

$$\varepsilon^{j}_{\mathrm{g,out}} = \mathrm{X}_1 - \mathrm{X}_2 \cdot X_3^{J} \tag{A.4}$$

where J is the current density in $\mathrm{kA} \cdot \mathrm{m}^{-2}$.

A.4. Hydrogen and Oxygen diffusivity in aqueous KOH solutions

The diffusivities of both hydrogen and oxygen have been estimated by fitting the experimental data of Tham et al. [58].

A.4.1. Hydrogen diffusivity in aqueous KOH solutions

The experimental data for hydrogen are given for different temperatures and depend on the potassium hydroxide weight concentration. Next, by plotting the diffusivities as a function of the weight concentration of potassium hydroxide in a semilog plot, a trendline is added in the Excel such that it fits the experimental data. For better accuracy a 4th order polynomial fitting has been chosen.

For intermediate temperatures, the diffusivity is estimated by calculating the average value between the two neighbouring points. The example of 50°C is illustrated in Figure A.1. The coefficients of the 4th order polynomial fitting are listed in Table A.3 including the example of 50°C.

Table A.2: Experimental data for the diffusivity of hydrogen in aqueous KOH solutions [58].

KOH $wt\%$	$\theta = 25°C$	$\theta = 40°C$	$\theta = 60°C$	$\theta = 80°C$	$\theta = 100°C$
0.050	$3.01 \cdot 10^{-9}$	$4.60 \cdot 10^{-9}$	$7.55 \cdot 10^{-9}$	$1.16 \cdot 10^{-8}$	
0.130	$2.36 \cdot 10^{-9}$	$3.60 \cdot 10^{-9}$	$5.82 \cdot 10^{-9}$	$8.70 \cdot 10^{-9}$	
0.240	$1.85 \cdot 10^{-9}$	$2.74 \cdot 10^{-9}$	$4.46 \cdot 10^{-9}$	$6.70 \cdot 10^{-9}$	$9.90 \cdot 10^{-9}$
0.325	$1.55 \cdot 10^{-9}$	$2.40 \cdot 10^{-9}$	$3.46 \cdot 10^{-9}$	$5.40 \cdot 10^{-9}$	
0.425	$1.25 \cdot 10^{-9}$	$1.95 \cdot 10^{-9}$	$2.89 \cdot 10^{-9}$	$4.40 \cdot 10^{-9}$	
0.515	$1.10 \cdot 10^{-9}$	$1.80 \cdot 10^{-9}$	$2.53 \cdot 10^{-9}$	$3.80 \cdot 10^{-9}$	$5.59 \cdot 10^{-9}$

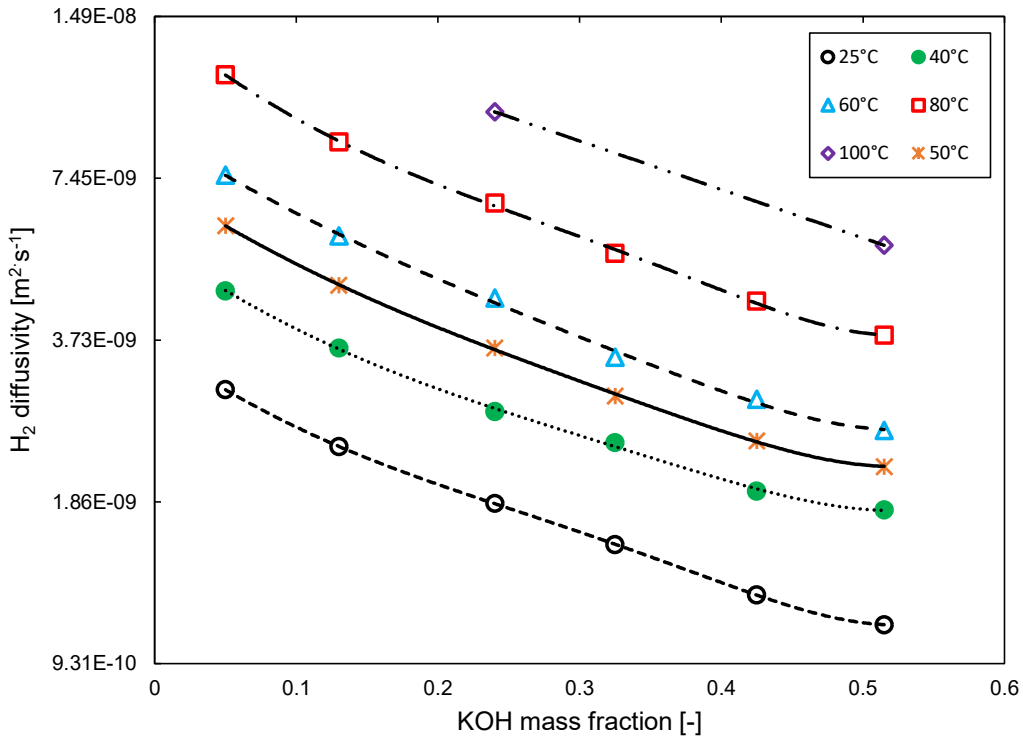

Figure A.1: Experimental hydrogen diffusivity in liquid KOH electrolyte including 4th order polynomial trendlines

Table A.3: Polynomial fitting coefficients for hydrogen diffusivity in aqueous KOH solutions [58].

$\theta(°C)$	α_0	α_1	α_2	α_3	α_4
25	$3.64123 \cdot 10^{-9}$	$-1.49501 \cdot 10^{-8}$	$5.13645 \cdot 10^{-8}$	$-1.03646 \cdot 10^{-7}$	$8.09202 \cdot 10^{-8}$
40	$5.57910 \cdot 10^{-9}$	$-2.28371 \cdot 10^{-8}$	$7.36629 \cdot 10^{-8}$	$-1.37782 \cdot 10^{-7}$	$1.03210 \cdot 10^{-7}$
50	$7.29139 \cdot 10^{-9}$	$-2.81042 \cdot 10^{-8}$	$8.12707 \cdot 10^{-8}$	$-1.46003 \cdot 10^{-7}$	$1.09998 \cdot 10^{-7}$
60	$9.00369 \cdot 10^{-9}$	$-3.33713 \cdot 10^{-8}$	$8.88785 \cdot 10^{-8}$	$-1.54224 \cdot 10^{-7}$	$1.16784 \cdot 10^{-7}$
80	$1.44122 \cdot 10^{-8}$	$-6.70191 \cdot 10^{-8}$	$2.33116 \cdot 10^{-7}$	$-4.54111 \cdot 10^{-7}$	$3.42760 \cdot 10^{-7}$

$$D_{\mathrm{H}_2,\theta} = \sum_{n=0}^{4} \alpha_n \cdot w_{\mathrm{KOH}}^n \tag{A.5}$$

The diffusion coefficient of hydrogen in the liquid electrolyte is calculated for each temperature T in $m^2 s^{-1}$ units and is valid for $0.05 \leqslant w_{\mathrm{KOH}} \leqslant 0.515$.

A.4.2. Oxygen diffusivity in aqueous KOH solutions

The same procedure that has been followed for hydrogen will now be followed for oxygen. From the experimental data of Tham et al. [58], the diffusivity of oxygen in KOH solutions for different temperatures is listed in Table A.4, and plotted in Figure A.2.

Table A.4: Experimental data for the diffusivity of oxygen in aqueous KOH solutions [58].

w_{KOH}	$\theta = 25°\mathrm{C}$	$\theta = 40°\mathrm{C}$	$\theta = 60°\mathrm{C}$	$\theta = 80°\mathrm{C}$	$\theta = 100°\mathrm{C}$
0.035		$2.45 \cdot 10^{-9}$			
0.050			$3.40 \cdot 10^{-9}$	$5.15 \cdot 10^{-9}$	
0.060	$1.45 \cdot 10^{-9}$				
0.102	$1.18 \cdot 10^{-9}$	$1.75 \cdot 10^{-9}$			
0.130			$2.45 \cdot 10^{-9}$	$3.70 \cdot 10^{-9}$	
0.190	$8.50 \cdot 10^{-10}$	$1.25 \cdot 10^{-9}$	$1.80 \cdot 10^{-9}$		
0.240				$2.22 \cdot 10^{-9}$	$3.70 \cdot 10^{-9}$
0.260	$6.00 \cdot 10^{-10}$	$9.00 \cdot 10^{-10}$			
0.325			$1.05 \cdot 10^{-9}$	$1.64 \cdot 10^{-9}$	
0.402	$4.00 \cdot 10^{-10}$	$5.70 \cdot 10^{-10}$			
0.425			$8.50 \cdot 10^{-10}$	$1.25 \cdot 10^{-9}$	$1.71 \cdot 10^{-9}$
0.515	$3.00 \cdot 10^{-10}$	$4.50 \cdot 10^{-10}$	$7.20 \cdot 10^{-10}$	$1.04 \cdot 10^{-9}$	$1.48 \cdot 10^{-9}$

This study is limited to temperatures up to $T = 80°\mathrm{C}$. In Figure A.2 the trendlines added with Excel are visualized. For most of the temperatures, they are 4th order polynomial fittings. However for $T = 60°\mathrm{C}$ and $T = 80°\mathrm{C}$ they are 3rd order polynomials. For intermediate temperatures, such as for $T = 50°\mathrm{C}$ the coefficients are calculated by averaging the neighbouring points. The coefficients for the polynomial fittings of oxygen diffusivity are listed in Table A.5.

$$D_{\mathrm{O}_2,\theta} = \sum_{n=0}^{4} \beta_n \cdot w_{\mathrm{KOH}}^n \tag{A.6}$$

The diffusion coefficient of oxygen in the liquid electrolyte is calculated for each temperature T in $m^2 s^{-1}$ units and is valid for $0.035 \leqslant w_{\mathrm{KOH}} \leqslant 0.515$.

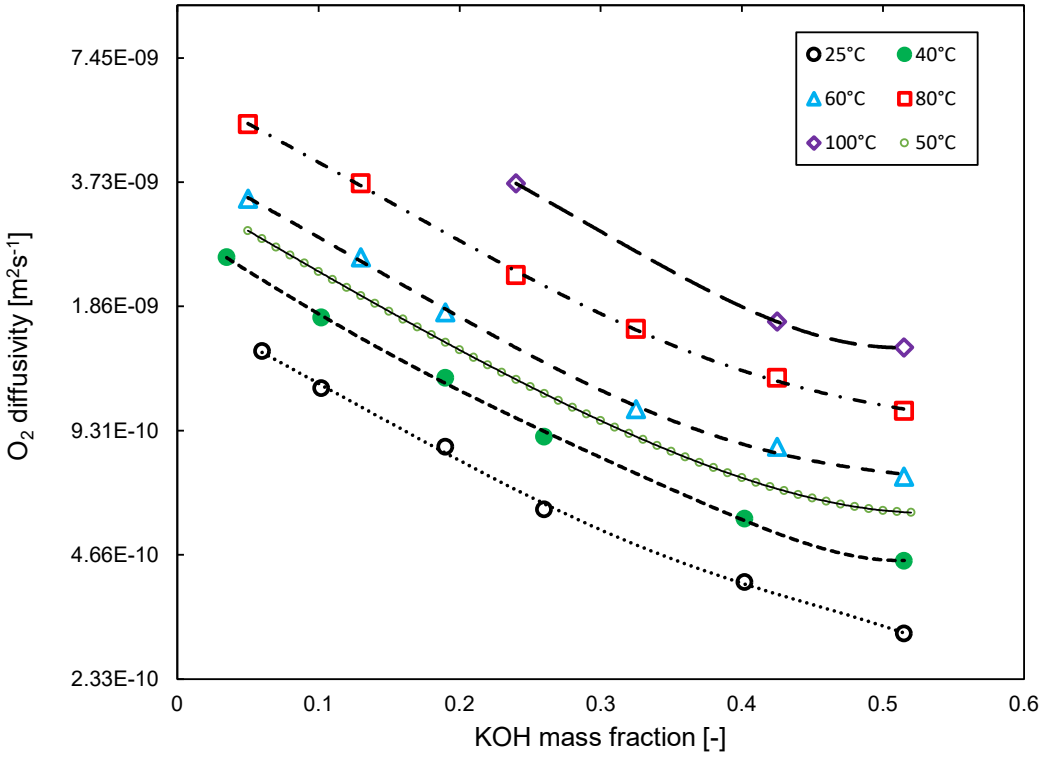

Figure A.2: Experimental oxygen diffusivity in liquid KOH electrolyte, including higher order polynomial trendlines

Table A.5: Diffusivity of oxygen in aqueous potassium hydroxide solutions [58].

$\theta(^{\circ}C)$	β_0	β_1	β_2	β_3	β_4
25	$1.85738 \cdot 10^{-9}$	$-7.71692 \cdot 10^{-9}$	$1.33495 \cdot 10^{-8}$	$-7.01990 \cdot 10^{-9}$	$-2.33205 \cdot 10^{-9}$
40	$2.91827 \cdot 10^{-9}$	$-1.49841 \cdot 10^{-8}$	$4.34515 \cdot 10^{-8}$	$-7.18134 \cdot 10^{-8}$	$5.02453 \cdot 10^{-8}$
50	$3.57483 \cdot 10^{-9}$	$-1.63852 \cdot 10^{-8}$	$3.70667 \cdot 10^{-8}$	$-4.49795 \cdot 10^{-8}$	$2.51226 \cdot 10^{-8}$
60	$4.23140 \cdot 10^{-9}$	$-1.77863 \cdot 10^{-8}$	$3.06820 \cdot 10^{-8}$	$-1.81457 \cdot 10^{-8}$	0
80	$6.37560 \cdot 10^{-9}$	$-2.63261 \cdot 10^{-8}$	$4.48021 \cdot 10^{-8}$	$-2.67261 \cdot 10^{-8}$	0

A.5. Dynamic viscosity

The dynamic viscosity is calculated in $\mathrm{Pa} \cdot \mathrm{s}$ according to Ref. [34] which is valid for $273.15\mathrm{K} \leqslant T \leqslant 363.15\mathrm{K}$.

$$\mu_{\mathrm{L}} = \sum_{n=0}^{4} \alpha_n \cdot T^n \tag{A.7}$$

A.6. KOH density

The density of the liquid electrolyte in $\mathrm{kg\ m^{-3}}$ can be calculated by the paper of Gilliam et al. [57] by taking into account the Table A.7 and equation A.8.

Table A.6: Higher order polynomial coefficients for the calculation of KOH dynamic viscosity [34].

α_0	$+0.9105535967$
α_1	-0.01062211683
α_2	$+4.680761561 \cdot 10^{-5}$
α_3	$-9.209312883 \cdot 10^{-8}$
α_4	$+6.814919843 \cdot 10^{-11}$

Table A.7: Relationship between density of KOH and w_{KOH} for various temperatures according to Gilliam et al. [57].

$\theta(^{\circ}\mathrm{C})$	A	$\theta(^{\circ}\mathrm{C})$	A
0	1001.9	50	988.45
5	1001.0	55	985.66
10	1000.0	60	983.2
15	999.06	65	980.66
20	998.15	70	977.88
25	997.03	80	971.89
30	995.75	90	965.43
35	994.05	100	958.35
40	992.07	150	916.99
45	990.16	200	867.07

$$\rho_{\mathrm{L}} = A \cdot e^{0.086 \cdot w_{\mathrm{KOH}}} \tag{A.8}$$

A.7. Henry's law constant

The Henry's law constant H_i for species i in pure water, has been calculated from [59] in atm.

Table A.8: Constants for the general solubility correlation equation from [59].

Gas	A	B	C	D	E
$\mathrm{O_2}$	-0.0005943	-0.1470	-0.05120	-0.1076	0.8447
$\mathrm{H_2}$	-0.1233	-0.1366	0.02155	-0.2368	0.8249

$$A\left(\log\overline{\mathrm{H_i}}\right)^2 + B\left(1/\overline{\mathrm{T}}\right)^2 + C\left(\log\overline{\mathrm{H_i}}\right)\left(1/\overline{\mathrm{T}}\right) + D\left(\log\overline{\mathrm{H_i}}\right) + E\left(1/\overline{\mathrm{T}}\right) - 1 = 0 \tag{A.9}$$

where $\overline{\mathrm{H_i}} = H_i \cdot 10^{-4}$, and $\overline{\mathrm{T}} = 1/T(^{\circ}K^{-1}) \cdot 10^{3}$.

A.8. Setchenov constants

A.8.1. Hydrogen Setchenov constant

The solubility of hydrogen in liquid KOH has been found experimentally by J. Jolly and S K. Shoor, and Knaster and Apel'baum. The experimental results are presented in the report of Walker et al. [61]. The results of Jolly and S K. Shoor are listed in Table A.9, and the results of Knaster and Apel'baum are listed in Table A.10. They are plotted together in Figure A.3, which is a semilog plot. For the present study, the calculation of hydrogen solubility in the liquid KOH electrolyte will be limited to temperatures below $80^{\circ}\mathrm{C}$.

Table A.9: Experimental results for the solubility of hydrogen in aqueous KOH solutions [61] from J. Jolly and S K. Shoor.

w_{KOH}	$\theta = 25^{\circ}\mathrm{C}$	$\theta = 40^{\circ}\mathrm{C}$	$\theta = 60^{\circ}\mathrm{C}$	$\theta = 80^{\circ}\mathrm{C}$	$\theta = 100^{\circ}\mathrm{C}$
0.000	0.792	0.713	0.712		
0.050	0.583	0.560	0.540	0.539	
0.090	0.465	0.435	0.410	0.394	
0.195	0.226	0.217	0.199	0.196	
0.324		0.082	0.078	0.079	
0.345	0.078				
0.380				0.033	0.047
0.414	0.038	0.035	0.033	0.010	0.034
0.524		0.010	0.009		0.009
0.564	0.011				0.007

Table A.10: Experimental results for the solubility of hydrogen in aqueous KOH solutions [61] from Knaster and Apel'baum.

w_{KOH}	$\theta = 21^{\circ}\mathrm{C}$	$\theta = 45^{\circ}\mathrm{C}$	$\theta = 75^{\circ}\mathrm{C}$
0.053	0.632	0.569	0.542
0.191	0.273	0.239	0.2325
0.305	0.112	0.0952	0.0884
0.401	0.0496	0.0361	0.0328

To calculate the Setchenov constant for any temperature and KOH mass fraction in the required operational range, fittings to the experimental solubility data should be

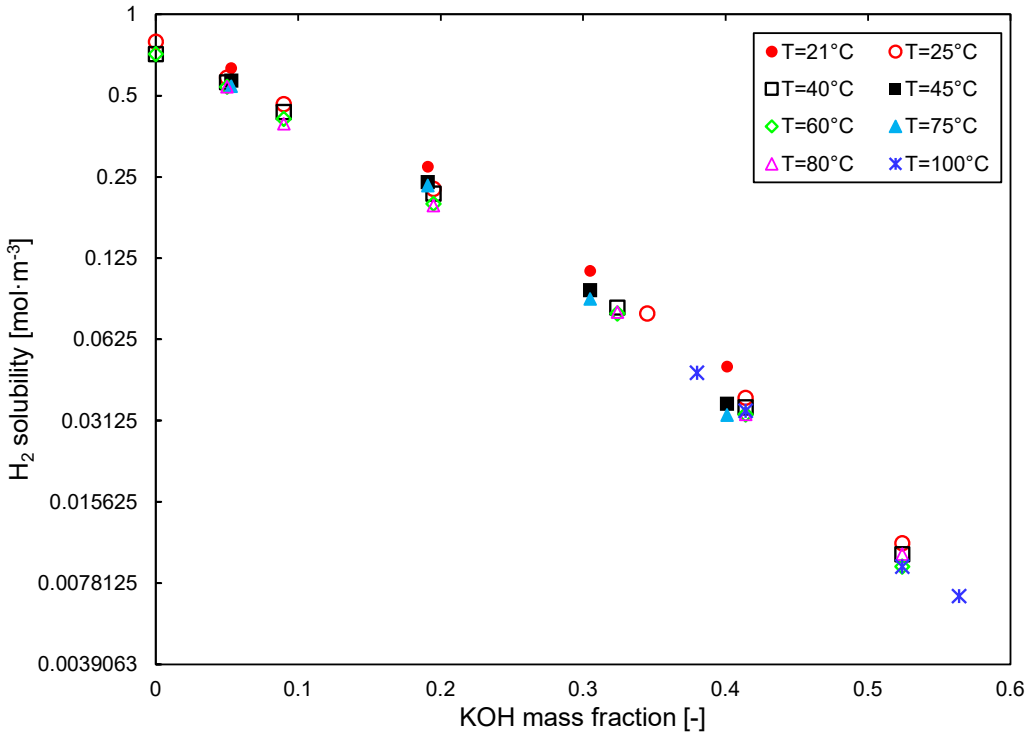

Figure A.3: Experimental solubility of hydrogen, in liquid KOH electrolyte

Table A.11: Coefficients of higher order polynomial trendlines for the experimental solubility results.

$\theta(^{\circ}C)$	α_0	α_1	α_2	α_3	α_4	α_5
25	$+7.91440 \cdot 10^{-1}$	-4.59271	$+11.1859$	-13.6708	6.91981	0
40	$+7.17790 \cdot 10^{-1}$	-3.67249	$+6.58886$	-4.11510	0	0
60	$+7.14536 \cdot 10^{-1}$	-4.05796	$+8.75746$	-7.80221	1.83419	0
80	$+8.26566 \cdot 10^{-1}$	-7.31135	$+36.0550$	-104.680	156.407	-91.5320

provided. Therefore, from the experimental data of J. Jolly and S K. Shoor, higher order polynomial trendlines are introduced. The higher order polynomial trendlines obey equation (A.10). The coefficients of the higher order polynomial trendlines are listed in Table A.11. Finally, since there is not a distinct difference in the solubility of a specific KOH mass fraction between two different temperatures, for intermediate temperatures, the solubility of these points will follow the solubility of the neighbouring point with the higher temperature. For example, in $50^{\circ}\mathrm{C}$ there are not any solubility data. The neighbouring points are $40^{\circ}\mathrm{C}$ and $60^{\circ}\mathrm{C}$. The highest neighbouring temperature is $60^{\circ}\mathrm{C}$. Therefore, the solubility at $50^{\circ}\mathrm{C}$ will follow the trendline of $60^{\circ}\mathrm{C}$.

$$c_{\mathrm{H_2}}^{*,j} = \sum_{n=0}^{5} \alpha_n \cdot w_{\mathrm{KOH}}^{n} \tag{A.10}$$

To calculate the Setchenov constant for hydrogen for any temperature and KOH

weight concentration within the operational range of XINTC, the equations (A.10) and (3.70) will be substituted into the equation (3.68). Solving for K_S results in relation A.11.

$$K_S = \log_{10}\left(\frac{\frac{\rho_{H_2O}}{M_{H_2O}} \cdot \frac{p^j_{out,i}}{H_i \cdot 101325Pa}}{\sum_{n=0}^{5} \alpha_n \cdot w_{KOH}^n}\right) \tag{A.11}$$

If it is further assumed that the produced gas consists of pure hydrogen then the outlet partial pressure will be equal to the applied total pressure in the compartment j. In the case that the total pressure equals the atmospheric pressure, $p^j_{out,i} = 101325Pa$. Therefore, the equation (A.11) results in equation (A.12).

$$K_{S,H_2} = \log_{10}\left[\frac{\rho_{H_2O}}{M_{H_2O} \cdot H_{H_2} \cdot \left(\sum_{n=0}^{5} \alpha_n \cdot w_{KOH}^n\right)}\right] \tag{A.12}$$

A.8.2. Oxygen Setchenov constant

The same procedure that has been followed for hydrogen will now be repeated for oxygen. From the report of Walker et al. [61], the experimental results of J. Jolly and S K. Shoor are listed in Table A.12. The experimental results of Knaster and Apel'baum are listed in Table A.13. Together, they are plotted in Figure A.4 which is a semilog plot. The results are limited to $80°C$.

Table A.12: Experimental results of J. Jolly and S K. Shoor for the solubility of oxygen in aqueous KOH solutions [61].

w_{KOH}	$\theta = 25°C$	$\theta = 40°C$	$\theta = 60°C$	$\theta = 80°C$
0.0000	1.263	1.049	0.875	0.786
0.0500	0.825	0.684	0.605	0.584
0.1350	0.413	0.365	0.339	0.315
0.2300	0.155	0.145	0.139	0.137
0.3160	0.061	0.059	0.056	0.055
0.4070	0.018	0.020	0.019	0.020
0.5030		0.006		
0.5065	0.006		0.005	0.006

Table A.13: Experimental results for the solubility of oxygen in aqueous KOH solutions [61] from Knaster and Apel'baum.

w_{KOH}	$\theta = 21°C$	$\theta = 45°C$	$\theta = 75°C$
0.053	0.897	0.712	0.597
0.191	0.336	0.288	0.244
0.305	0.102	0.0884	0.0812
0.401	0.0232	0.0201	0.01835

For the calculation of the oxygen Setchenov constant at any temperature and KOH weight concentration within the required operational range, fittings to the experimental solubility data should be provided. For the results of J. Jolly and S. K. Shoor, higher order polynomial trendlines are introduced. The higher order polynomial trendlines are described by equation (A.13). The coefficients of the higher order polynomial trendlines are listed in Table A.14. Similarly to the hydrogen case, for intermediate temperatures, the oxygen Setchenov constant will be estimated by giving as input the solubility curve of the neighbouring point with the higher temperature.

$$c_{O_2}^{*,j} = \sum_{n=0}^{4} \beta_n \cdot w_{KOH}^n \tag{A.13}$$

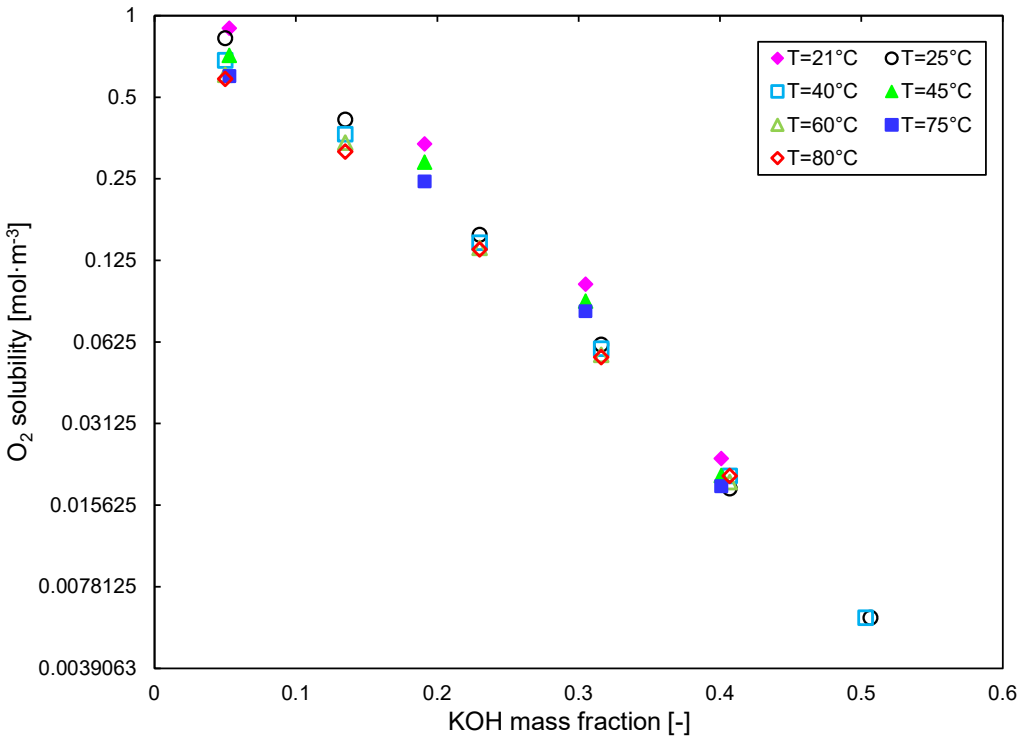

Figure A.4: Experimental oxygen solubility in liquid KOH electrolyte

Table A.14: Coefficients of higher order polynomial trendlines for the oxygen experimental solubility results.

$\theta(^{\circ}C)$	β_0	β_1	β_2	β_3	β_4
25	+1.18090	-8.07030	+20.2617	-21.1267	+6.98302
40	+0.948527	-5.87422	+12.5331	-9.10380	0
60	+0.777288	-3.40450	-2.26070	+30.6480	-38.7919
80	+0.801473	-4.84106	+10.1746	-7.36633	0

The oxygen Setchenov constant can be calculated in a similar way to the hydrogen case. The final relation that describes the oxygen Setchenov constant will be the equation (A.14).

$$K_{S,O_2} = \log_{10}\left[\frac{\rho_{H_2O}}{M_{H_2O} \cdot H_{O_2} \cdot \left(\sum_{n=0}^{4} \beta_n \cdot w_{KOH}^{n}\right)}\right] \tag{A.14}$$

A.9. Density of pure water

In the Setchenov constants for both H_2 and O_2 the pure water density is required. The water density can be calculated from Ref. [71] as a function of temperature in θ°C. The water density will be equal to:

$$\begin{aligned}\rho_{H_2O} = &\left(999.83952 + 16.945176 \cdot \theta - 7.9870401 \cdot 10^{-3} \cdot \theta^2\right.\\ &-46.170461 \cdot 10^{-6} \cdot \theta^3 + 105.56302 \cdot 10^{-9} \cdot \theta^4\\ &\left.-280.54253 \cdot 10^{-12} \cdot \theta^5\right) \cdot \left(1 + 16.879850 \cdot 10^{-3} \cdot \theta\right)\end{aligned} \tag{A.15}$$

Where θ is the temperature in °C. The water density is calculated in $\mathrm{kg\ m^{-3}}$.

A.10. Properties of "Type A" diaphragm

From the datasheet of the Type A diaphragm, it can be seen that the thickness of the separator d_d is 0.6 ± 10 mm, and the pore volume is larger than 35%.

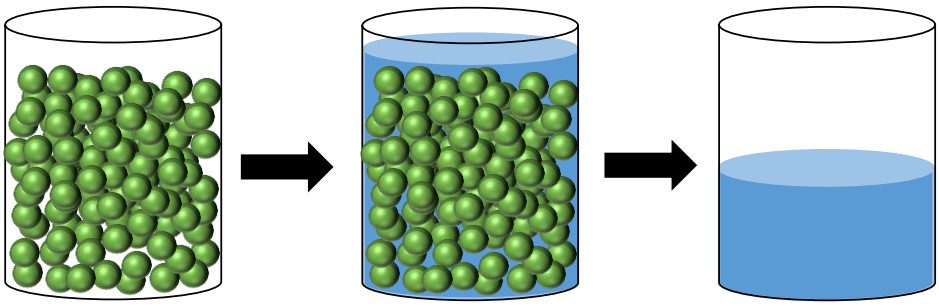

Figure A.5: Visualization of pore volume.

According to the manufacturer, the pore volume is defined as the percentage of air that is trapped inside the cavities of the porous media. In Figure A.5, the porous media is visualized by solid spheres in a cylindrical container. When the cylindrical container is filled in with a liquid and the porous media is removed, the liquid that is left in the cylindrical container represents the liquid volume that remained in the pores. The volume of the liquid over the bulk volume of the porous media represents the pore volume in %. In this sense, the pore volume is another definition for the porosity ε. From the datasheet of the manufacturer, the porosity is higher than 35%. Therefore, for the developed model, the porosity of Type A diaphragm will be represented by equation (A.16).

$$\varepsilon = 0.35 \tag{A.16}$$

The tortuosity τ is not given in the datasheet of the manufacturer. However, it can be approximated by implementing a geometrical approach where the tortuosity is a

function of the porosity. More specifically, according to Pisani et al. [67], the tortuosity in porous media can be approximated with equation (A.17).

$$\tau = [1 - \alpha \cdot (1 - \varepsilon)] \tag{A.17}$$

where α is a shape factor that determines the configuration of the porous medium which acts as an obstacle for the bulk flow. Assuming that the shape of polyethylene in the Type A diaphragm is spherical, the shape factor will be $\alpha \approx 0.75$. The substitution of the shape factor α in equation (A.17) results in:

$$\tau = 1.951 \tag{A.18}$$

B

Appendix - Derivation of the final form of steady-state material balances

The derivation of the final form of the steady-state material balances will be given for the mass balances in the electrolysis cell. As explained in Chapter 3.2.2, the outlet dissolved concentration of species i, in the half-cell j, equals the outlet dissolved concentration of species i in the gas separator of the half-cell j. Therefore, it is not further required to analyze the mass balances in the gas separators.

B.1. Partial pressures in the steady-state model

In Chapter 3.5.2, it was explained that the goal in the steady-state model is the reduction of the unknown terms to the maximum possible. The existence of many unknown terms complicates the selection of a correct set of initial conditions. Furthermore, it increases the solution time. As a result, it is chosen to couple the outlet partial pressures of the steady-state model with other unknown terms. In the following, the procedure to express the outlet partial pressures as a function of the solubility and the outlet dissolved concentration will be analyzed.

In Chapter 3.4.5, the implementation of Henry's law in combination with the Setchenov relation resulted in equation (3.71).

$$c_i^{*,j} = \frac{\rho_{\mathrm{H_2O}} \cdot p_{\mathrm{out},i}^{j}}{M_{\mathrm{H_2O}} \cdot 101325 \cdot H_i \cdot 10^{K_{\mathrm{S},i} \cdot w_{\mathrm{KOH}}}} \tag{3.73}$$

Rearranging equation (3.71) as to the outlet partial pressure, results in equation (B.1).

$$p_{\mathrm{out,i}}^{j} = \frac{M_{\mathrm{H_2O}}}{\rho_{\mathrm{H_2O}}} \cdot c_i^{*,j} \cdot H_i \cdot 101325Pa \cdot 10^{K_{\mathrm{S},i} \cdot w_{\mathrm{KOH}}} \tag{B.1}$$

For the steady-state model, the hydrogen outlet partial pressures in the anodic and cathodic half-cell are expressed by equation (B.1). Therefore, when $i = \mathrm{H_2}$ and $j = \mathrm{ano}$, equation (3.84) is obtained.

$$p_{\mathrm{out,H_2}}^{\mathrm{ano}} = \frac{M_{\mathrm{H_2O}}}{\rho_{\mathrm{H_2O}}} \cdot c_{\mathrm{H_2}}^{*,\mathrm{ano}} \cdot 101325Pa \cdot H_{\mathrm{H_2}} \cdot 10^{K_{\mathrm{H_2}} \cdot w_{\mathrm{KOH}}} \tag{3.86}$$

When $i = \mathrm{H_2}$ and $j = \mathrm{cat}$, equation (3.85) is obtained.

$$p_{\mathrm{out,H_2}}^{\mathrm{cat}} = \frac{M_{\mathrm{H_2O}}}{\rho_{\mathrm{H_2O}}} \cdot c_{\mathrm{H_2}}^{*,\mathrm{cat}} \cdot 101325Pa \cdot H_{\mathrm{H_2}} \cdot 10^{K_{\mathrm{H_2}} \cdot w_{\mathrm{KOH}}} \tag{3.87}$$

For the oxygen partial pressures, equation (B.1) is not used. The implementation of equation (B.1) for oxygen results in more unknown terms due to the $c_i^{*,j}$ term. To avoid the introduction of new terms, the oxygen outlet partial pressures are coupled with the hydrogen outlet partial pressures.

In Chapter 3.4.2, the definition of the total pressure was given by implementing equations (3.44)-(3.45).

$$p_{\mathrm{tot}}^{\mathrm{ano}} = p_{\mathrm{out,H_2}}^{\mathrm{ano}} + p_{\mathrm{out,O_2}}^{\mathrm{ano}} + p_{\mathrm{H_2O}} \tag{3.44}$$

$$p_{\mathrm{tot}}^{\mathrm{cat}} = p_{\mathrm{out,H_2}}^{\mathrm{cat}} + p_{\mathrm{out,O_2}}^{\mathrm{cat}} + p_{\mathrm{H_2O}} \tag{3.45}$$

Combining equations (3.44) and (3.84):

$$p_{\mathrm{tot}}^{\mathrm{ano}} = \frac{M_{\mathrm{H_2O}}}{\rho_{\mathrm{H_2O}}} \cdot c_{\mathrm{H_2}}^{*,\mathrm{cat}} \cdot 101325Pa \cdot H_{\mathrm{H_2}} \cdot 10^{K_{\mathrm{H_2}} \cdot w_{\mathrm{KOH}}} + p_{\mathrm{out,O_2}}^{\mathrm{ano}} + p_{\mathrm{H_2O}} \tag{B.2}$$

Rearranging equation (B.2) results in equation (3.86).

$$p_{\mathrm{out,O_2}}^{\mathrm{ano}} = p_{\mathrm{tot}}^{\mathrm{ano}} - p_{\mathrm{H_2O}} - \frac{M_{\mathrm{H_2O}}}{\rho_{\mathrm{H_2O}}} \cdot c_{\mathrm{H_2}}^{*,\mathrm{ano}} \cdot 101325Pa \cdot H_{\mathrm{H_2}} \cdot 10^{K_{\mathrm{H_2}} \cdot w_{\mathrm{KOH}}} \tag{3.88}$$

Similarly, the combination of equation (3.45) with (3.85) results in equation (3.87) for the oxygen outlet cathodic partial pressure.

$$p_{\mathrm{out,O_2}}^{\mathrm{cat}} = p_{\mathrm{tot}}^{\mathrm{cat}} - p_{\mathrm{H_2O}} - \frac{M_{\mathrm{H_2O}}}{\rho_{\mathrm{H_2O}}} \cdot c_{\mathrm{H_2}}^{*,\mathrm{cat}} \cdot 101325Pa \cdot H_{\mathrm{H_2}} \cdot 10^{K_{\mathrm{H_2}} \cdot w_{\mathrm{KOH}}} \tag{3.89}$$

B.2. Outlet gaseous volumetric flow rates

From the steady-state material balances it is possible to obtain a relation that expresses the outlet gaseous volumetric flow rates in the anodic and cathodic half-cell as a function of the solubilities and dissolved concentrations. In that sense, the number of unknown terms in the steady-state model is reduced.

In Chapter 3.2.1, the general form of the steady-state materials was given. The general form of gaseous H_2 in the anodic half-cell is given by equation (3.3).

$$0 = \frac{\dot{V}_{\mathrm{G}}^{\mathrm{ano}}}{R \cdot T} \cdot \left(p_{\mathrm{in,H_2}}^{\mathrm{ano}} - p_{\mathrm{out,H_2}}^{\mathrm{ano}}\right) - N_{\mathrm{phys,H_2}}^{\mathrm{ano}} \cdot A_{\mathrm{GL}}^{\mathrm{ano}} \tag{3.3}$$

In equation (3.3), the inlet partial pressure is zero since gaseous product cannot re-enter the electrolysis cell. Rearranging equation (3.3) as to the anodic gaseous volumetric flow rate will give (B.3).

$$\dot{V}_{\mathrm{G}}^{\mathrm{ano}} = -\frac{R \cdot T}{p_{\mathrm{out,H_2}}^{\mathrm{ano}}} \cdot N_{\mathrm{phys,H_2}}^{\mathrm{ano}} \cdot A_{\mathrm{GL}}^{\mathrm{ano}} \tag{B.3}$$

Combining equations (B.3) and (3.84) will result in equation (3.88)

$$\dot{V}_{\mathrm{G}}^{\mathrm{ano}} = -\frac{R \cdot T}{\frac{M_{\mathrm{H_2O}}}{\rho_{\mathrm{H_2O}}} \cdot c_{\mathrm{H_2}}^{*,\mathrm{ano}} \cdot 101325Pa \cdot H_{\mathrm{H_2}} \cdot 10^{K_{\mathrm{H_2}} \cdot w_{\mathrm{KOH}}}} \cdot N_{\mathrm{phys,H_2}}^{\mathrm{ano}} \cdot A_{\mathrm{GL}}^{\mathrm{ano}} \tag{3.90}$$

Similarly, the general form of the cathodic gaseous oxygen material balance is given by equation (3.8).

$$0 = -\frac{\dot{V}_{\mathrm{G}}^{\mathrm{cat}}}{R \cdot T} \cdot \left(p_{\mathrm{in,O_2}}^{\mathrm{cat}} - p_{\mathrm{out,O_2}}^{\mathrm{cat}}\right) - N_{\mathrm{phys,O_2}}^{\mathrm{cat}} \cdot A_{\mathrm{GL}}^{\mathrm{cat}} \tag{3.8}$$

Since gaseous product cannot re-enter the electrolysis cell, the inlet partial pressure in equation (3.8) can be neglected. Rearranging equation (3.8) as to the cathodic gaseous volumetric flow rate will result in equation (B.4).

$$\dot{V}_{\mathrm{G}}^{\mathrm{cat}} = -\frac{R \cdot T}{p_{\mathrm{out,O_2}}^{\mathrm{cat}}} \cdot N_{\mathrm{phys,O_2}}^{\mathrm{cat}} \cdot A_{\mathrm{GL}}^{\mathrm{cat}} \tag{B.4}$$

The combination of equation (B.4) with equation (3.87) will give equation (3.89).

$$\dot{V}_{\mathrm{G}}^{\mathrm{cat}} = -\frac{R \cdot T}{p_{\mathrm{tot}}^{\mathrm{cat}} - p_{\mathrm{H_2O}} - \frac{M_{\mathrm{H_2O}}}{\rho_{\mathrm{H_2O}}} \cdot c_{\mathrm{H_2}}^{*,\mathrm{cat}} \cdot 101325Pa \cdot H_{\mathrm{H_2}} \cdot 10^{K_{\mathrm{H_2}} \cdot w_{\mathrm{KOH}}}} \cdot N_{\mathrm{phys,O_2}}^{\mathrm{cat}} \cdot A_{\mathrm{GL}}^{\mathrm{cat}} \tag{3.91}$$

Overall, in Chapter 3.2.1, 8 mass balances were introduced. Since equations (3.3) and (3.8) were used to deduce expressions for outlet gaseous volumetric flow rates in the anodic and cathodic compartment, the mass balances in the final form will be 6, in total.

C

Appendix - Derivation of the final form of dynamic material balances

The derivation of the final form of the dynamic material balances will be firstly analyzed for the liquid phase which contains dissolved species in the electrolysis cell. Next, the gaseous material balances for the electrolysis cell will be introduced. Similarly, the same procedure will be followed for the gas separators.

C.1. Liquid material balances in the electrolysis cell

The generic form of the liquid material balances is described by equations (3.19), (3.20), (3.23) and (3.24). To obtain the final form, equation (3.48) will be introduced into the accumulation term of the material balances.

$$N_{i,\mathrm{liq}}^{j} = c_{\mathrm{out},i}^{j} \cdot V_{\mathrm{liq}}^{j} \tag{3.48}$$

In addition, due to the assumption that the liquid volume remains constant, the liquid volume V_{liq}^{j} remains outside of the derivative. Taking as example the mass balance that describes the dissolved hydrogen in the anodic half cell (3.19), it will be:

$$\frac{dN_{\mathrm{H_2,liq}}^{\mathrm{ano}}}{dt} = \dot{V}_{\mathrm{L}}^{\mathrm{ano}} \cdot \left(c_{\mathrm{in,H_2}}^{\mathrm{ano}} - c_{\mathrm{out,H_2}}^{\mathrm{ano}}\right) + N_{\mathrm{phys,H_2}}^{\mathrm{ano}} \cdot A_{\mathrm{GL}}^{\mathrm{ano}} + N_{\mathrm{cross,H_2}} \cdot A_{\mathrm{d}} \tag{3.19}$$

Combining equation (3.48) with equation (3.19):

$$V_{\mathrm{liq}}^{\mathrm{ano}} \cdot \frac{dc_{\mathrm{out,H_2}}^{\mathrm{ano}}}{dt} = \dot{V}_{\mathrm{L}}^{\mathrm{ano}} \cdot \left(c_{\mathrm{in,H_2}}^{\mathrm{ano}} - c_{\mathrm{out,H_2}}^{\mathrm{ano}}\right) + N_{\mathrm{phys,H_2}}^{\mathrm{ano}} \cdot A_{\mathrm{GL}}^{\mathrm{ano}} + N_{\mathrm{cross,H_2}} \cdot A_{\mathrm{d}} \tag{C.1}$$

Rearranging the left hand side of equation (C.1), it leads to the final form which is described by equation (3.93).

$$\frac{dc_{\mathrm{out,H_2}}^{\mathrm{ano}}}{dt} = \frac{1}{V_{\mathrm{liq}}^{\mathrm{ano}}} \cdot \left[\dot{V}_{\mathrm{L}}^{\mathrm{ano}} \cdot \left(c_{\mathrm{in,H_2}}^{\mathrm{ano}} - c_{\mathrm{out,H_2}}^{\mathrm{ano}}\right) + N_{\mathrm{phys,H_2}}^{\mathrm{ano}} \cdot A_{\mathrm{GL}}^{\mathrm{ano}} + N_{\mathrm{cross,H_2}} \cdot A_{\mathrm{d}}\right] \tag{3.95}$$

Equation (3.93) describes the final form of the dynamic material balance for hydrogen

being dissolved in the liquid electrolyte in the anodic compartment. Similar reasoning can be followed for equations (3.20), (3.23) and (3.24) which results in equations (3.94), (3.97) and (3.98), respectively.

C.2. Gaseous material balances in the electrolysis cell

The generic form of the gaseous material balances is described by equations (3.21), (3.22), (3.25) and (3.26). To obtain the final form of gaseous material balances, equation (3.50) needs to be introduced in the accumulation term of the gaseous material balances.

$$N_{i,\mathrm{gas}}^{j} = \frac{p_{\mathrm{out},i}^{j} \cdot V_{\mathrm{gas}}^{j}}{R \cdot T} \tag{3.50}$$

Due to the assumption made in Chapter 3.1.3, the gaseous volume in the j compartment remains steady and hence the term V_{gas}^{j} remains outside the derivative. Furthermore, the temperature T is assumed to be constant with time. Taking as example the mass balance for gaseous hydrogen in the anodic half-cell, its general form is described by equation (3.21).

$$\frac{dN_{\mathrm{H_2,gas}}^{\mathrm{ano}}}{dt} = \frac{\dot{V}_{\mathrm{G}}^{\mathrm{ano}}}{R \cdot T} \cdot \left(p_{\mathrm{in,H_2}}^{\mathrm{ano}} - p_{\mathrm{out,H_2}}^{\mathrm{ano}}\right) - N_{\mathrm{phys,H_2}}^{\mathrm{ano}} \cdot A_{\mathrm{GL}}^{\mathrm{ano}} \tag{3.21}$$

Combining equation (3.50) with (3.21) and considering the previously mentioned assumptions, will lead to equation (C.2):

$$\frac{V_{\mathrm{gas}}^{\mathrm{ano}}}{R \cdot T} \cdot \frac{dp_{\mathrm{out,H_2}}^{\mathrm{ano}}}{dt} = -\frac{\dot{V}_{\mathrm{G}}^{\mathrm{ano}}}{R \cdot T} \cdot p_{\mathrm{out,H_2}}^{\mathrm{ano}} - N_{\mathrm{phys,H_2}}^{\mathrm{ano}} \cdot A_{\mathrm{GL}}^{\mathrm{ano}} \tag{C.2}$$

Re-arranging (C.2) will result in the final form of gaseous hydrogen in the anodic half-cell, which is described by equation (3.95).

$$\frac{dp_{\mathrm{out,H_2}}^{\mathrm{ano}}}{dt} = -\frac{\dot{V}_{\mathrm{G}}^{\mathrm{ano}}}{V_{\mathrm{gas}}^{\mathrm{ano}}} \cdot p_{\mathrm{out,H_2}}^{\mathrm{ano}} - \frac{R \cdot T}{V_{\mathrm{gas}}^{\mathrm{ano}}} \cdot N_{\mathrm{phys,H_2}}^{\mathrm{ano}} \cdot A_{\mathrm{GL}}^{\mathrm{ano}} \tag{3.97}$$

In equation (3.95), the gaseous volumetric flow rate $\dot{V}_{\mathrm{G}}^{\mathrm{ano}}$ remains an unknown quantity. To define $\dot{V}_{\mathrm{G}}^{\mathrm{ano}}$, the final form of the dynamic material balance for oxygen in the anode is also required. The dynamic material balance for oxygen in the anode is given by equation (3.22).

$$\frac{dN_{\mathrm{O_2,gas}}^{\mathrm{ano}}}{dt} = \frac{\dot{V}_{\mathrm{G}}^{\mathrm{ano}}}{R \cdot T} \cdot \left(p_{\mathrm{in,O_2}}^{\mathrm{ano}} - p_{\mathrm{out,O_2}}^{\mathrm{ano}}\right) - N_{\mathrm{phys,O_2}}^{\mathrm{ano}} \cdot A_{\mathrm{GL}}^{\mathrm{ano}} + f_{\mathrm{G,O_2}} \cdot \dot{n}_{\mathrm{R,O_2}}^{\mathrm{ano}} \tag{3.22}$$

Combining equation (3.50) with (3.22) will result in equation (C.3).

$$\frac{V_{\mathrm{gas}}^{\mathrm{ano}}}{R \cdot T} \cdot \frac{dp_{\mathrm{out,O_2}}^{\mathrm{ano}}}{dt} = -\frac{\dot{V}_{\mathrm{G}}^{\mathrm{ano}}}{R \cdot T} \cdot p_{\mathrm{out,O_2}}^{\mathrm{ano}} - N_{\mathrm{phys,O_2}}^{\mathrm{ano}} \cdot A_{\mathrm{GL}}^{\mathrm{ano}} + f_{\mathrm{G,O_2}} \cdot \dot{n}_{\mathrm{R,O_2}}^{\mathrm{ano}} \tag{C.3}$$

Re-arranging equation (C.3) leads to the final form of gaseous oxygen in the anodic half-cell which is described by equation (3.96).

$$\frac{dp_{\mathrm{out,O_2}}^{\mathrm{ano}}}{dt} = -\frac{\dot{V}_{\mathrm{G}}^{\mathrm{ano}}}{V_{\mathrm{gas}}^{\mathrm{ano}}} \cdot p_{\mathrm{out,O_2}}^{\mathrm{ano}} - \frac{R \cdot T}{V_{\mathrm{gas}}^{\mathrm{ano}}} \cdot \left(N_{\mathrm{phys,O_2}}^{\mathrm{ano}} \cdot A_{\mathrm{GL}}^{\mathrm{ano}} - f_{\mathrm{G,O_2}} \cdot \dot{n}_{\mathrm{R,O_2}}^{\mathrm{ano}}\right) \tag{3.98}$$

Even though equation (3.96) describes the final form of the gaseous material balance for oxygen in the anode, it must be rearranged to obtain the anodic gaseous volumetric flow rate $\dot{V}_{\mathrm{G}}^{\mathrm{ano}}$. For that reason, the relation which describes the total pressure in the anodic compartment as a function of the partial pressures can be introduced in the accumulation term of equation (3.96). The total pressure in the anodic half-cell is given by equation (3.44).

$$p_{\mathrm{tot}}^{\mathrm{ano}} = p_{\mathrm{out,H_2}}^{\mathrm{ano}} + p_{\mathrm{out,O_2}}^{\mathrm{ano}} + p_{\mathrm{H_2O}} \tag{3.44}$$

Introducing equation (3.44) in the accumulation term of equation (3.96) results in equation (C.4):

$$\frac{d\left(p_{\mathrm{tot}}^{\mathrm{ano}} - p_{\mathrm{out,H_2}}^{\mathrm{ano}} - p_{\mathrm{H_2O}}\right)}{dt} = -\frac{\dot{V}_{\mathrm{G}}^{\mathrm{ano}}}{V_{\mathrm{gas}}^{\mathrm{ano}}} \cdot p_{\mathrm{out,O_2}}^{\mathrm{ano}} - \frac{R \cdot T}{V_{\mathrm{gas}}^{\mathrm{ano}}} \cdot \left(N_{\mathrm{phys,O_2}}^{\mathrm{ano}} \cdot A_{\mathrm{GL}}^{\mathrm{ano}} - f_{\mathrm{G,O_2}} \cdot \dot{n}_{\mathrm{R,O_2}}^{\mathrm{ano}}\right) \tag{C.4}$$

Assuming that the total pressure and the water vapour pressure remain constant with time, equation (C.4) can be rewritten:

$$-\frac{dp_{\mathrm{out,H_2}}^{\mathrm{ano}}}{dt} = -\frac{\dot{V}_{\mathrm{G}}^{\mathrm{ano}}}{V_{\mathrm{gas}}^{\mathrm{ano}}} \cdot p_{\mathrm{out,O_2}}^{\mathrm{ano}} - \frac{R \cdot T}{V_{\mathrm{gas}}^{\mathrm{ano}}} \cdot \left(N_{\mathrm{phys,O_2}}^{\mathrm{ano}} \cdot A_{\mathrm{GL}}^{\mathrm{ano}} - f_{\mathrm{G,O_2}} \cdot \dot{n}_{\mathrm{R,O_2}}^{\mathrm{ano}}\right) \tag{C.5}$$

The final step required to obtain the anodic gaseous volumetric flow rate will be to add up equations (3.22) and (C.5). In this way, the derivative with the hydrogen outlet partial pressure will cancel out, and the term $\dot{V}_{\mathrm{G}}^{\mathrm{ano}}$ will be a function of the unknown terms of Table 3.4.

$$\frac{dp_{\mathrm{out,H_2}}^{\mathrm{ano}}}{dt} = -\frac{\dot{V}_{\mathrm{G}}^{\mathrm{ano}}}{V_{\mathrm{gas}}^{\mathrm{ano}}} \cdot p_{\mathrm{out,H_2}}^{\mathrm{ano}} - \frac{R \cdot T}{V_{\mathrm{gas}}^{\mathrm{ano}}} \cdot N_{\mathrm{phys,H_2}}^{\mathrm{ano}} \cdot A_{\mathrm{GL}}^{\mathrm{ano}} \tag{3.22}$$

$$-\frac{dp_{\mathrm{out,H_2}}^{\mathrm{ano}}}{dt} = -\frac{\dot{V}_{\mathrm{G}}^{\mathrm{ano}}}{V_{\mathrm{gas}}^{\mathrm{ano}}} \cdot p_{\mathrm{out,O_2}}^{\mathrm{ano}} - \frac{R \cdot T}{V_{\mathrm{gas}}^{\mathrm{ano}}} \cdot \left(N_{\mathrm{phys,O_2}}^{\mathrm{ano}} \cdot A_{\mathrm{GL}}^{\mathrm{ano}} - f_{\mathrm{G,O_2}} \cdot \dot{n}_{\mathrm{R,O_2}}^{\mathrm{ano}}\right) \tag{C.5}$$

$$\xrightarrow{(3.22)+(C.5)} \quad 0 = -\frac{\dot{V}_{\mathrm{G}}^{\mathrm{ano}}}{V_{\mathrm{gas}}^{\mathrm{ano}}} \cdot \left(p_{\mathrm{out,H_2}}^{\mathrm{ano}} + p_{\mathrm{out,O_2}}^{\mathrm{ano}}\right) - \frac{R \cdot T}{V_{\mathrm{gas}}^{\mathrm{ano}}} \cdot \left(N_{\mathrm{phys,H_2}}^{\mathrm{ano}} \cdot A_{\mathrm{GL}}^{\mathrm{ano}} + N_{\mathrm{phys,O_2}}^{\mathrm{ano}} \cdot A_{\mathrm{GL}}^{\mathrm{ano}} - f_{\mathrm{G,O_2}} \cdot \dot{n}_{\mathrm{R,O_2}}^{\mathrm{ano}}\right) \tag{C.6}$$

Rearranging equation (C.6) results in the required expression for the gaseous outlet volumetric flow rate which is described by equation (3.103).

$$\dot{V}_{\mathrm{G}}^{\mathrm{ano}} = -\frac{R \cdot T}{p_{\mathrm{tot}}^{\mathrm{ano}} - p_{\mathrm{H_2O}}} \cdot \left(N_{\mathrm{phys,H_2}}^{\mathrm{ano}} \cdot A_{\mathrm{GL}}^{\mathrm{ano}} + N_{\mathrm{phys,O_2}}^{\mathrm{ano}} \cdot A_{\mathrm{GL}}^{\mathrm{ano}} - f_{\mathrm{G,O_2}} \cdot \dot{n}_{\mathrm{R,O_2}}^{\mathrm{ano}}\right) \tag{3.105}$$

Following the same procedure for the gaseous material balances in the cathodic compartment, the final form of equations (3.25) and (3.26) will be represented by equations (3.99) and (3.100), respectively. Similarly, it can be proven that the gaseous volumetric flow rate in the cathode will be given by equation (3.104).

C.3. Liquid material balances in the gas separators

The general form of the liquid material balances for the gas separators is given by the equations (3.27), (3.28), (3.31) and (3.32). Taking as example the liquid material balance for hydrogen in the anodic gas separator, its general material balance is given by equation (3.27).

$$\frac{dN_{\mathrm{H_2,liq}}^{\mathrm{ano,sep}}}{dt} = \dot{V}_{\mathrm{L}}^{\mathrm{ano}} \cdot \left(c_{\mathrm{out,H_2}}^{\mathrm{ano}} - c_{\mathrm{out,H_2}}^{\mathrm{sep,ano}}\right) \tag{3.27}$$

To obtain the final form of the dynamic material balances, equation (3.49) must be introduced into the accumulation term of the general form of the liquid material balances.

$$N_{i,\mathrm{liq}}^{j,\mathrm{sep}} = c_{\mathrm{out},i}^{\mathrm{sep},j} \cdot V_{\mathrm{liq}}^{\mathrm{sep},j} \tag{3.49}$$

Due to the assumption that the liquid volume in the gas separator remains constant with time, the term $V_{\mathrm{liq}}^{\mathrm{sep},j}$ remains outside of the derivative.

Introducing equation (3.49) into the accumulation term of equation (3.27) leads to (C.7):

$$\frac{d\left(c_{\mathrm{out,H_2}}^{\mathrm{sep,ano}} \cdot V_{\mathrm{liq}}^{\mathrm{sep,ano}}\right)}{dt} = \dot{V}_{\mathrm{L}}^{\mathrm{ano}} \cdot \left(c_{\mathrm{out,H_2}}^{\mathrm{ano}} - c_{\mathrm{out,H_2}}^{\mathrm{sep,ano}}\right) \tag{C.7}$$

Rearranging equation (C.7), results in equation (C.8), which is the final form of the mass balance for dissolved hydrogen in the anodic gas separator, and obeys equation (3.101).

$$\frac{dc_{\mathrm{out,H_2}}^{\mathrm{sep,ano}}}{dt} = \frac{\dot{V}_{\mathrm{L}}^{\mathrm{ano}}}{V_{\mathrm{liq}}^{\mathrm{sep,ano}}} \cdot \left(c_{\mathrm{out,H_2}}^{\mathrm{ano}} - c_{\mathrm{out,H_2}}^{\mathrm{sep,ano}}\right) \tag{C.8}$$

Following the same procedure for the general form of the material balances (3.28), (3.31) and (3.32), the final form will also obey equation (3.101).

C.4. Gaseous material balances in the gas separators

The general form of the gaseous material balances in the gas separators is given by equations (3.29), (3.30), (3.33) and (3.34). Taking as example the gaseous material balance for hydrogen in the anodic gas separator, its general material balance is given by equation (3.29).

$$\frac{dN_{\mathrm{H_2,gas}}^{\mathrm{ano,sep}}}{dt} = \frac{\dot{V}_{\mathrm{G}}^{\mathrm{ano}}}{R \cdot T} \cdot \left(p_{\mathrm{out,H_2}}^{\mathrm{ano}} - p_{\mathrm{out,H_2}}^{\mathrm{sep,ano}}\right) \tag{3.29}$$

To obtain the final form of the dynamic material balances equation (3.51) must be introduced into the accumulation term of the general form of the gaseous material balances.

$$N_{i,\mathrm{gas}}^{j,\mathrm{sep}} = \frac{p_{\mathrm{out},i}^{\mathrm{sep},j} \cdot V_{\mathrm{gas}}^{\mathrm{sep},j}}{R \cdot T} \tag{3.51}$$

Due to the assumption that the gaseous volume in the gas separator remains constant with time, the term $V_{\mathrm{gas}}^{\mathrm{sep},j}$ remains outside of the derivative. Furthermore, the temperature in the gas separator can be assumed to be steady with time.

Introducing equation (3.51) into the accumulation term of equation (3.29), leads to equation (C.9):

$$\frac{d\left(\frac{p_{\mathrm{out,H_2}}^{\mathrm{sep,ano}} \cdot V_{\mathrm{gas}}^{\mathrm{sep,ano}}}{R \cdot T}\right)}{dt} = \frac{\dot{V}_{\mathrm{G}}^{\mathrm{ano}}}{R \cdot T} \cdot \left(p_{\mathrm{out,H_2}}^{\mathrm{ano}} - p_{\mathrm{out,H_2}}^{\mathrm{sep,ano}}\right) \tag{C.9}$$

Rearanging equation (C.9) by considering the previously mentioned assumptions, equation (C.10) is obtained. The equation (C.10) is the final form of the general material balance for gaseous hydrogen in the anodic gas separator, and obeys equation (3.102).

$$\frac{dp_{\mathrm{out,H_2}}^{\mathrm{sep,ano}}}{dt} = \frac{\dot{V}_{\mathrm{G}}^{\mathrm{ano}}}{V_{\mathrm{gas}}^{\mathrm{sep,ano}}} \cdot \left(p_{\mathrm{out,H_2}}^{\mathrm{ano}} - p_{\mathrm{out,H_2}}^{\mathrm{sep,ano}}\right) \tag{C.10}$$

Following the same procedure for the general form of the material balances (3.30), (3.33) and (3.34), their final form will also obey equation (3.102).

D

Dynamic modeling for safe operation of alkaline water electrolysers to control gas crossover

Abstract

Climate change due to the extensive use of fossil fuels has led to the deployment of green hydrogen. Due to the intermittency of renewable sources, alkaline water electrolysers are forced to operate in their part-load range, where the gas crossover is high. The increasing gas crossover lowers the purity of the produced gases and poses a threat to the safe operation of the system. To mitigate the gas crossover in the part-load range we propose to operate the alkaline water electrolysers with the dynamic switching of electrolyte cycles. This alternative process operation is mathematically modeled and validated with literature data. Furthermore, a sensitivity analysis is performed for the dynamic model. From the results of the sensitivity analysis, we find that the system response, in terms of the anodic hydrogen content, is significantly affected by the liquid and gaseous volume of the gas separators.

D.1. Introduction

Global warming is one of the greatest challenges of the 21st century. It can be attributed to greenhouse gas (GHG) emissions that trap the heat in the atmosphere and cause the temperature to rise [2]. The main contributor to GHG is carbon dioxide (CO_2). An option to reduce the CO_2 emissions can be made by using Green Hydrogen. It contains the term green because renewable electricity is used to produce hydrogen via the application of the water-splitting reaction in the electrolysis process (reaction D.3). Its production does not give rise to CO_2 emissions if the carbon intensity of the used electricity is zero.

In this paper, the dynamic model to calculate the gas crossover is applied to an alkaline water electrolyser. Alkaline water electrolysis (AWE) is the most mature and robust electrolysis technology. The first AWE was demonstrated by Van Troostwijk and Deinman in 1789 [15]. The electrolysis cell consists of two porous electrodes, namely the anode and the cathode. The electrodes are immersed in a strong liquid

alkaline electrolyte which is either potassium hydroxide KOH, or sodium hydroxide NaOH and provides the required ionic conductivity. The anode and the cathode are separated by a porous solid diaphragm. The role of the diaphragm is to avoid the gas crossover of the evolved gases and to allow the required conduction of hydroxide ions from the cathode to the anode.

$$\text{Cathode}: \quad 2H_2O + 2e^- \longrightarrow 2OH^- + H_2 \tag{D.1}$$

$$\text{Anode}: \quad 2OH^- \longrightarrow 0.5O_2 + H_2O + 2e^- \tag{D.2}$$

$$\text{Overall Reaction}: \quad H_2O \longrightarrow H_2 + 0.5O_2 \tag{D.3}$$

When DC power is supplied to the electrolysis cell, H_2O molecules are reduced at the cathode, and H_2 with OH^- ions are produced. This reaction (D.1) is often called the hydrogen evolution reaction (HER). At the same time, hydroxide ions are conducted via the diaphragm on the anode side, where they are subject to the oxidation reaction, and they lose electrons (D.2). As a result, oxygen and water molecules are produced. This reaction is often called the oxygen evolution reaction (OER).

The intermittency of renewables results in fluctuations in the power grid. In such conditions, the electrolysers must be able to operate in the part-load range to produce green hydrogen. Normally, the part-load range varies from 20-40% of their nominal load [12]. During the alkaline water electrolysis process in the part-load range, produced hydrogen species can be contaminated by oxygen, or the opposite, resulting in the creation of an explosive atmosphere. This contamination is often called gas crossover and is more significant under the part load operational range. When the alkaline water electrolysers operate close to their nominal load range, the gas crossover becomes significantly smaller [12].

The explosive atmosphere is created because the hydrogen-oxygen mixture can lead to spontaneous combustion if the concentration of the contaminating species reaches 4 vol%, which is the Lower Explosive Limit (LEL) [14]. Therefore, when the electrolysers operate in the part-load range, such fluctuations can introduce risks to their safe operation and are forced to shut down. Typically, they shut down when the concentration of impurity reaches 2 vol%, which is 50% of the LEL [14]. Due to the contamination of hydrogen, the resulting gas purity will be reduced as will the overall efficiency of the process.

To mitigate gas crossover we study the operation of alkaline water electrolysers with the dynamic switching of electrolyte cycles which was first introduced by Haug et al. [40]. During the dynamic switching, the system operates for a specific time in a mixed mode, and then it switches to a partly-separated mode. In the mixed mode, the anolyte and catholyte are continuously being mixed and gas crossover occurs due to electrolyte mixing and diffusion through the diaphragm. The electrolyte mixing is required to avoid the concentration gradient of KOH due to the half-reactions. According to Trinke et al. [41], electrolyte mixing is the major contributor to the total gas crossover in the alkaline water electrolysis process. When the system switches to a partly-separated mode, gas crossover occurs due to diffusion through the diaphragm and the gas impurity reduces. The switching from the mixed to the partly-separated mode results in a sinusoidal trend where the average impurity is lower than the impurity in the mixed mode.

In the literature, the report of Haug et al. [34] focuses on modeling the gas crossover

mechanisms in an alkaline water electrolyser plant. In this zero-dimensional model, steady-state material balances consider the gas crossover mechanisms due to electrolyte mixing and diffusion through the diaphragm. The model is a function of current density, temperature, lye flow rate, and KOH concentration. The results are verified with experimental data.

Sanchez et al. [72] developed a MATLAB model where the anodic hydrogen content is calculated with semi empirical correlations as a function of the current density. However, since this model is developped with semi empirical correlations based on experiments, the gas crossover mechanisms are not considered in detail.

Sakas et al. [73] developed a dynamic Simulink model to calculate the produced mass flow rate and the polarization curve. This model does not consider the purity of the produced gas at the exit of the gas separators and the gas crossover mechanisms.

Finally, de Groot et al. [74] developed a steady state model which calculates the gas impurity. The difference with the model of Haug et al. [34] lies in the fact that gas crossover due to differential pressure through the diaphragm is also considered.

D.2. Mathematical Model

The present paper focuses on the development of a zero-dimensional dynamic model that can simulate the dynamic switching operation in terms of the anodic hydrogen content. The dynamic model can calculate the gas purity at the exit of the gas separators as a function of the operating conditions of the process. The operating conditions are the current density, the applied pressure, the KOH mass fraction, the liquid volumetric flow rate and the liquid volume in the gas separators.

D.2.1. Assumptions for the electrolysis cell

In Figure D.1, the mass balance in the single-cell is shown. When the electrolysis process starts, hydrogen is produced in the cathode $\dot{n}^{\mathrm{cat}}_{\mathrm{R,H_2}}$, and oxygen is produced in the anode $\dot{n}^{\mathrm{ano}}_{\mathrm{R,O_2}}$. The production rate on the electrodes obeys Faraday's law. Due to the mass transfer limitations in gas evolving electrodes [33, 36], a part of the total product is transferred to the liquid phase and the rest is directly transferred to the gaseous phase. The part of the product that is transferred to the liquid phase remains dissolved and is described by the variable $c^{j}_{\mathrm{out},i}$. At this point, it is assumed that each compartment follows the continuous-stirred-tank model (CSTR) [53]. More specifically, each half cell can be considered a reactor whose contents are perfectly mixed. The reactor consists of continuous inflow and outflow. As a result, the concentration and temperature throughout the reactor are uniform. Due to the perfect mixing assumption, the contents of the reactor can outflow immediately.

In practice, the liquid volumetric flow rate that enters the anode $\dot{V}^{\mathrm{ano}}_{\mathrm{L}}$, is equal to the volumetric flow rate that enters the cathode $\dot{V}^{\mathrm{cat}}_{\mathrm{L}}$, since it can be regulated by a pump before the cell entrance (Figure D.3). Furthermore, it is assumed that the outlet volumetric flow rate equals the inlet. This assumption is required to simplify the material balances. The part of the product that is transferred to the gaseous phase is assumed to obey the ideal gas law, due to atmospheric operation. The bubbles which contain the gaseous products are assumed to be monodisperse and perfectly spherical, and any coalescence effects due to hydrodynamic phenomena are not taken into consid-

eration. Finally, it is assumed that no gaseous product can be recirculated throughout the system. Therefore, the inlet volumetric flow rate is gas-free.

The products that remain dissolved in the electrolyte bulk can be transferred to the gaseous phase via a subsequent mass transfer step $N^{j}_{\mathrm{phys},i}$ or can cross permeate through the diaphragm to the opposite half cell via the $N_{\mathrm{cross},i}$ flux. In the first case, the subsequent mass transfer step can be achieved by a desorption flux due to the supersaturation of dissolved species in the liquid electrolyte and can be modeled via the film theory [35]. The desorption flux takes place between the bulk liquid electrolyte and the product bubbles (close-up in Figure D.1). In the second case, it is assumed that the cross-permeation flux through the diaphragm is achieved only due to the diffusion of dissolved species in the bulk electrolyte (Fick's Law). The gaseous phase cannot cross-permeate through the diaphragm. The electrolyser operates in low pressure, close to atmospheric, and hence the convective mass transfer due to differential pressure through the diaphragm (Darcy's Law) can be neglected. Finally, it is assumed that there is no additional mass transfer in the interconnecting piping.

D.2.2. Assumptions for the gas separators

After the dissolution of the products in the liquid electrolyte and the formation of the resulting product gases in the electrolysis cell, the two-phase mixture is directed to the gas separators (Figure D.2). For visualization purposes, the two-phase mixture is depicted as two different streams. The inflow and outflows of each gas separator consist of the products from both the half cells due to gas crossover. When the electrolyser operates in "mixed mode", the liquid electrolyte that contains the dissolved species $c^{\mathrm{sep},j}_{\mathrm{out},i}$ is directed to an ideal mixer, where it is mixed with the dissolved species that exit from the opposite gas separator. Therefore, crossover due to electrolyte mixing occurs. When the electrolyser switches to "partly separated mode", the liquid electrolyte which outflows from the gas separator $c^{\mathrm{sep},j}_{\mathrm{out},i}$ can be directed to the half-cell without mixing.

The gas separators are also modeled as CSTR ideal reactors. However, in comparison to the electrolysis cell, there is no reaction. When a specific current density is applied to the electrolyser, there is always a transition time required for the system to reach its steady state. The CSTR assumption is essential such that the transition time to equilibrium can be accurately modeled. The quantities which define the transition time required for the system to reach equilibrium are the liquid $V^{\mathrm{sep},j}_{\mathrm{liq}}$ and the gaseous volume $V^{\mathrm{sep},j}_{\mathrm{gas}}$ of each gas separator. Finally, the gas separators are assumed to be 100% percent efficient, and hence there is no additional mass transfer from the liquid electrolyte to the gaseous phase.

D.2.3. Simplified process flow diagram

Figure D.3 shows the simplified process flow diagram of the modeled electrolysis plant. In the simplified process flow diagram, the liquid level equalizer tube and the feedwater stream in the cathodic gas separator are not included. The liquid level equalizer tube is required to keep the liquid level of the gas separators equal due to the reduction and oxidation reactions. The conservation of equal liquid levels between the gas separators means that there is no differential pressure build-up between the

anodic and cathodic half cells. In addition the gas crossover due to the existence of the liquid level equalizer tube is negligible [40]. The role of the feedwater stream is to compensate for the water consumed due to gas production. As a result, instead of including these additional streams in the mathematical model, the liquid and gaseous volumes in the gas separators $V_{\mathrm{liq}}^{\mathrm{sep},j}$ and $V_{\mathrm{gas}}^{\mathrm{sep},j}$ are assumed to be steady with time. Additional mass transfer phenomena which may take place inside the gas separator are neglected.

The liquid and gaseous volumes inside the electrolysis half cells V_{liq}^{j} and V_{gas}^{j} are also assumed to be steady with time (see Figure D.3). Due to the CSTR model, it is reasonable to assume that the application of a current density results in gas evolution immediately. Therefore, for a specific current density, it is assumed that the evolved gases instantly reach their steady state which is represented by the steady liquid and gaseous volumes in the half cells. To visualize the liquid and gaseous volumes inside the electrolyser, the bubbly flow is depicted as two distinct areas (turquoise color for liquid volume, grey color for gaseous volume). The same holds for the gas separators.

Finally, the liquid and gaseous flow rates $\dot{V}_{\mathrm{L}}^{j}$ and $\dot{V}_{\mathrm{G}}^{j}$ are depicted in the simplified process flow diagram. It is assumed that the flow rates are determined in the electrolysis cell and do not change throughout the process. As a result, the gaseous flow rate is calculated from the mathematical equations of the electrolysis cell and its value remains the same at the exit of the gas separator. When the system operates in mixed mode, the flow rate at the exit of the ideal mixer is $\dot{V}_{\mathrm{mix}}$.

D.2.4. Material balances

In Figure D.1 it is assumed that the positive sign convention for the crossover flux, N_{cross}^{i}, is from the cathodic to the anodic compartment. This is due to the higher cathodic bulk concentration of hydrogen in comparison to the anodic. For the oxygen species, the crossover flux will have a negative sign. The crossover flux is integrated over the diaphragm area A_{d}. The positive sign convention for the mass transfer flux in the electrolyte bulk, $N_{\mathrm{phys},i}^{j}$, is from the gaseous to the liquid phase (Close-up in Figure D.1). However, due to the fact that electrolyte bulk is supersaturated, the mass transfer flux has a negative sign and is governed by desorption [33]. The desorptive mass flux is integrated over the gas-liquid interface A_{GL}. The produced species in the electrode region, $n_{\mathrm{R,H_2}}^{\mathrm{cat}}$ and $n_{\mathrm{R,O_2}}^{\mathrm{ano}}$, firstly dissolve in the concentration boundary layer [30]. However, due to high supersaturation in the concentration boundary layer a part of the produced species is transferred directly to the gaseous phase [29, 75]. The amount of the produced species that is transferred to the gaseous phase, in the concentration boundary layer, can be quantified by the gas evolution efficiency $f_{\mathrm{G},i}$ [70]. The dynamic material balances for the electrolysis cell and the gas separators are given from equations (D.4)-(D.8).

Dissolved species i, in the anodic half-cell:

$$\frac{dc_{\mathrm{out},i}^{\mathrm{ano}}}{dt} = \frac{1}{V_{\mathrm{liq}}^{\mathrm{ano}}} \cdot \Big[\dot{V}_{\mathrm{L}}^{\mathrm{ano}} \cdot \left(c_{\mathrm{in},i}^{\mathrm{ano}} - c_{\mathrm{out},i}^{\mathrm{ano}}\right) + N_{\mathrm{phys},i}^{\mathrm{ano}} \cdot A_{\mathrm{GL}}^{\mathrm{ano}} + N_{\mathrm{cross},i} \cdot A_{\mathrm{d}} + \left(1 - f_{\mathrm{G},i}\right) \cdot \dot{n}_{\mathrm{R},i}^{\mathrm{ano}}\Big] \quad \text{(D.4)}$$

Dissolved species i, in the cathodic half-cell:

$$\frac{dc_{\mathrm{out},i}^{\mathrm{cat}}}{dt} = \frac{1}{V_{\mathrm{liq}}^{\mathrm{cat}}} \cdot \left[\dot{V}_{\mathrm{L}}^{\mathrm{cat}} \cdot \left(c_{\mathrm{in},i}^{\mathrm{cat}} - c_{\mathrm{out},i}^{\mathrm{cat}}\right) + N_{\mathrm{phys},i}^{\mathrm{cat}} \cdot A_{\mathrm{GL}}^{\mathrm{cat}} - N_{\mathrm{cross},i} \cdot A_{\mathrm{d}} + \left(1 - f_{\mathrm{G},i}\right) \cdot \dot{n}_{\mathrm{R},i}^{\mathrm{cat}}\right] \quad \text{(D.5)}$$

Gaseous species i in the j half-cell:

$$\frac{dp_{\mathrm{out},i}^{j}}{dt} = -\frac{\dot{V}_{\mathrm{G}}^{j}}{V_{\mathrm{gas}}^{j}} \cdot p_{\mathrm{out},i}^{j} - \frac{R \cdot T}{V_{\mathrm{gas}}^{j}} \cdot \left(N_{\mathrm{phys},i}^{j} \cdot A_{\mathrm{GL}}^{j} - f_{\mathrm{G},i} \cdot \dot{n}_{\mathrm{R},i}^{j}\right) \quad \text{(D.6)}$$

Dissolved species i, in the gas separator of j half-cell:

$$\frac{dc_{\mathrm{out},i}^{\mathrm{sep},j}}{dt} = \frac{\dot{V}_{\mathrm{L}}^{j}}{V_{\mathrm{liq}}^{\mathrm{sep},j}} \cdot \left(c_{\mathrm{out},i}^{j} - c_{\mathrm{out},i}^{\mathrm{sep},j}\right) \quad \text{(D.7)}$$

Gaseous species i, in the gas separator of j half-cell:

$$\frac{dp_{\mathrm{out},i}^{\mathrm{sep},j}}{dt} = \frac{\dot{V}_{\mathrm{G}}^{j}}{V_{\mathrm{gas}}^{\mathrm{sep},j}} \cdot \left(p_{\mathrm{out},i}^{j} - p_{\mathrm{out},i}^{\mathrm{sep},j}\right) \quad \text{(D.8)}$$

Where the species i can be H_2 or O_2, and the compartment j can be the anodic or cathodic. Therefore, in total there are 16 mass balances and 16 unknowns.

The reaction rate $\dot{n}_{\mathrm{R},i}^{j}$ obeys Faraday's Law and is given by equation (D.9).

$$\dot{n}_{\mathrm{R},i}^{j} = \frac{J\nu_i}{nF} \quad \text{(D.9)}$$

The stoichiometric number ν_i will be $\nu_{\mathrm{H_2}} = 1$ for hydrogen which is produced in the cathode, and $\nu_{\mathrm{O_2}} = 0.5$ for oxygen which is produced in the anode, when the charge transfer equals $n = 2$ from reactions (D.1) and (D.2).

The mass transfer flux in the electrolyte bulk $N_{\mathrm{phys},i}^{j}$ can be modeled with the liquid film theory. Assuming that in the gaseous interface there is not any mass transfer resistance, the gaseous film can be neglected. In addition, it is assumed that the gas-liquid interface is in phase equilibrium and is governed by an equilibrium concentration $c_i^{*,j}$, the concentration gradient is linear, and the electrolyte bulk concentration is equal to $c_{\mathrm{out},i}^{\mathrm{ano}}$. As a result, molecular diffusion which obeys the film theory only occurs with a driving force $c^* - c_{\mathrm{out}}$ and is given by equation (D.10).

$$N_{\mathrm{phys},i}^{j} = k_{\mathrm{L},i}^{j} \cdot \left(c_i^{*,j} - c_{\mathrm{out},i}^{j}\right) \quad \text{(D.10)}$$

Where $k_{\mathrm{L},i}^{j}$, is the mass transfer coefficient and can be modeled by applying the empirical Sherwood correlations [34]. The equilibrium concentration of species i in the j compartment, $c_i^{*,j}$, can be expressed as a function of the outlet partial pressure, $p_{\mathrm{out},i}^{j}$, which is given in Pa, by combining Henry's law and the Setchenov relation, in equation

(D.11). This equation requires experimental data for the Henry's constant of species i [59], the Setchenov constant of species i [34], and the density of pure water [71].

$$c_i^{*,j} = \frac{\rho_{\mathrm{H_2O}} \cdot p_{\mathrm{out},i}^{j}}{M_{\mathrm{H_2O}} \cdot 101325 \cdot H_i \cdot 10^{K_{\mathrm{S},i} \cdot w_{\mathrm{KOH}}}} \tag{D.11}$$

Where, $\rho_{\mathrm{H_2O}}$ is the density of pure water in $\mathrm{kg\,m^{-3}}$, $M_{\mathrm{H_2O}}$ is the molar mass of water in $\mathrm{kg\,mol^{-1}}$, H_i is the Henry's constant in atm, $K_{\mathrm{S},i}$ is the Setchenov constant of species i, and w_{KOH} is the KOH mass fraction in wt%.

The crossover flux $N_{\mathrm{cross},i}$ can be modeled with the Nernst-Planck equation in 1D, by considering only the contribution due to diffusion through the diaphragm. The concentration gradient through the diaphragm is assumed to be linear.

$$N_{\mathrm{cross},i} = \frac{D_i^{\mathrm{eff}}}{d_{\mathrm{d}}} \cdot \left(c_{\mathrm{out},i}^{\mathrm{cat}} - c_{\mathrm{out},i}^{\mathrm{ano}}\right) \tag{D.12}$$

Where d_d is the thickness of the diaphragm, and D_i^{eff} is the effective diffusion coefficient of species i. The effective diffusion coefficient is a function of the molecular diffusion coefficient of species i in the liquid electrolyte, and the design characteristics of the diaphragm which are the porosity ε and tortuosity τ.

$$D_i^{\mathrm{eff}} = D_{i,\theta} \frac{\varepsilon}{\tau} \tag{D.13}$$

The molecular diffusion coefficient of species i, $D_{i,\theta}$ is given by the experimental results of Tham et al. [58], in $\mathrm{m^2\,s^{-1}}$. The diaphragm used in the dynamic model is the Zirfon UTP 500 by Agfa. The thickness of the diaphragm is $d_d = 500\,\mu m$ and its porosity is $\varepsilon = 55\,\%$ [17]. The tortuosity of the Zirfon diaphragm is found from the work of Haug et al.[34] and is equal to $\tau = 3.14$.

Finally, the gas evolution efficiencies for hydrogen and oxygen are given from equations (D.14)-(D.15) which are experimentally characterized by Haug et al. [34].

$$f_{\mathrm{G,H_2}} = 0.25744 \cdot \left(J/\mathrm{A\,m^{-2}}\right)^{0.14134} \tag{D.14}$$

$$f_{\mathrm{G,O_2}} = 1 \tag{D.15}$$

Where J is the applied current density.

D.2.5. Boundary conditions

During the dynamic switching of electrolyte cycles process, the plant operates for a specific time range in a mixed mode, and then it switches to the partly-separated mode. The boundary conditions are associated with the outflows of the gas separators.

During the mixed-mode, both electrolyte cycles are mixed before re-entering the electrolysis cell. Assuming that the liquid electrolyte is incompressible during both modes of operation, the mixed liquid volumetric flow rate $\dot{V}_{\mathrm{mix}}$ is equal to:

$$\dot{V}_{\mathrm{mix}} = \dot{V}_{\mathrm{L}}^{\mathrm{ano}} + \dot{V}_{\mathrm{L}}^{\mathrm{cat}} \tag{D.16}$$

The mixed liquid concentration of the dissolved species at the exit of the ideal mixer are equal to the inlet concentration in both half cells:

$$c_i^{\text{mix}} = c_{\text{in},i}^{j} \tag{D.17}$$

The dissolved mixed concentration c_i^{mix} can be found by applying a mass balance for the ideal mixer before the inlet of the electrolysis cell (see Figure D.3) for each species i.

$$\dot{V}_{\text{mix}} \cdot c_i^{\text{mix}} = \dot{V}_{\text{L}}^{\text{ano}} \cdot c_{\text{out},i}^{\text{sep,ano}} + \dot{V}_{\text{L}}^{\text{cat}} \cdot c_{\text{out},i}^{\text{sep,cat}} \tag{D.18}$$

When the simplified alkaline water electrolysis plant switches to the partly-separated mode, the liquid electrolyte stream that exits its gas separator re-enters its corresponding half-cell without mixing with the stream from the opposite half-cell. As a result, since it is assumed that there is no additional mass transfer in the interconnecting piping, the liquid concentration of the species at the inlet of the half-cell $c_{\text{in},i}^{j}$ is equal to the liquid concentration of the species at the exit of the gas separators $c_{\text{out},i}^{\text{sep},j}$.

$$c_{\text{in},i}^{\text{ano}} = c_{\text{out},i}^{\text{sep,ano}} \tag{D.19}$$

The simulation of the dynamic switching can be achieved by the changeover of the mixed and partly-separated mode via the boundary conditions (D.18) and (D.19), as a function of time.

In the work of Leroy et al. [54], hydrogen and oxygen species that are produced in the vicinity of the electrode are “wet”. Therefore, the produced gases consist of water vapor which is in equilibrium with the water from the liquid electrolyte solution. The water vapor partial pressure $p_{\text{H}_2\text{O}}$ which is in equilibrium with the electrolyte solution can be calculated based on the work by Balej et al. [55].

Considering the cross-permeated product, the total pressure exerted on the gaseous product in each half cell is equal to the sum of the partial pressures of the produced gases and water vapour.

$$p_{\text{tot}}^{j} = p_{\text{out,H}_2}^{j} + p_{\text{out,O}_2}^{j} + p_{\text{H}_2\text{O}} \tag{D.20}$$

To define the total pressure p_{tot}^{j}, the approach of Haug et al. [34] is followed. More specifically, the connection of the gas separators with the atmosphere results in the exertion of an absolute pressure p^j on the liquid electrolyte which is equal to the atmospheric pressure. During electrolysis, the gaseous product in the half-cell builds up a pressure difference $\Delta p_{g\to l}$ with respect to the absolute pressure of the liquid electrolyte, due to the effect of the surface tension. The pressure difference $\Delta p_{g\to l}$ between the liquid and gaseous phase can be calculated by implementing the Young-Laplace equation [76].

$$p_{\text{tot}}^{j} = p^j - \Delta p_{g\to l} = p^j + \gamma \frac{4}{d_{\text{b}}^{j}} \tag{D.21}$$

Where the bubble diameter has been experimentally characterized by Haug et al. [34], and the surface tension in the liquid electrolyte can be calculated in $\mathrm{N\,m^{-1}}$, as a

function of the applied temperature and KOH mass fraction from the work of Feldkamp [56].

Finally, the H_2 in O_2 impurity is obtained as the mole fraction of gaseous H_2 without taking into account water vapour.

$$y_{\mathrm{H_2}} = \frac{p_{\mathrm{out,H_2}}^{\mathrm{sep,ano}}}{p_{\mathrm{out,H_2}}^{\mathrm{sep,ano}} + p_{\mathrm{out,O_2}}^{\mathrm{sep,ano}}} \tag{D.22}$$

D.2.6. Input parameters and system solution

The dynamic mass balances require the definition of the liquid and gaseous volumes inside the half-cells, V_{liq}^{j} and V_{gas}^{j}, and the gas separators $V_{\mathrm{liq}}^{\mathrm{sep},j}$ $V_{\mathrm{gas}}^{\mathrm{sep},j}$. The gaseous volume in the half-cell j can be calculated by considering the experimental investigations of Haug et al. [34], for the gas hold-up fraction $\varepsilon_{\mathrm{g,out}}^{j}$. More specifically, the gaseous volume in the half-cell j can be calculated from equation (D.23).

$$V_{\mathrm{gas}}^{j} = \varepsilon_{\mathrm{g,out}}^{j} \cdot V_{\mathrm{b}}^{j} \cdot \frac{p^{j}}{p_{\mathrm{tot}}^{j}} \tag{D.23}$$

Where $\varepsilon_{\mathrm{g,out}}^{j}$ is the gas hold-up fraction at the outlet of the half-cell j, and V_{b}^{j} is the volume of a single bubble in m^3. The gas hold-up fraction is given as a function of the current density and can be calculated from equation.

$$\varepsilon_{\mathrm{g,out}}^{j} = X_1 - X_2 \cdot X_3^{J} \tag{D.24}$$

where J is the current density in $\mathrm{kA\,m^{-2}}$ and the coefficients X_1, X_2 and X_3 are given in Table D.1, depending on the half-cell. The volume of the single bubble, V_{b}^{j}, is given from equation (D.25).

$$V_{\mathrm{b}}^{j} = \frac{\pi}{6} \cdot \left(d_{\mathrm{b}}^{j}\right)^3 \tag{D.25}$$

where the diameter of the produced bubbles in the half-cell j is calculated by the experimental results of Haug et al. [34], in m.

$$d_{\mathrm{b}}^{\mathrm{cat}} = 593.84 \cdot 10^{-6} \cdot (1 + 0.2J)^{-0.25} \tag{D.26}$$

$$d_{\mathrm{b}}^{\mathrm{ano}} = 10^{-4} \tag{D.27}$$

Considering the volume of the half-cell, the liquid volume in the half-cell can be calculated from equation (D.28).

$$V_{\mathrm{liq}}^{j} = V_{\mathrm{hcell}} - V_{\mathrm{gas}}^{j} \tag{D.28}$$

The total gaseous volume in each half-cell and its associated gas separator is reported to be equal to $V_{\mathrm{gas}}^{\mathrm{tot},j} = 1.6\ \mathrm{L}$ [34]. Furthermore, the liquid volume in each gas separator j is reported to be equal to $V_{\mathrm{liq}}^{\mathrm{sep},j} = 1.2\ \mathrm{L}$ [34]. Therefore, the liquid and gaseous volumes in the gas separators are equal to:

$$V_{\mathrm{gas}}^{\mathrm{sep},j} = 1.6 \cdot 10^{-3} - V_{\mathrm{gas}}^{j}\ \mathrm{m^3} \tag{D.29}$$

$$V_{\mathrm{liq}}^{\mathrm{sep},j} = 1.2 \cdot 10^{-3}\ \mathrm{m^3} \tag{D.30}$$

The gas liquid interface can be calculated from equation (D.31).

$$A_{\mathrm{GL}}^{j} = \frac{V_{\mathrm{gas}}^{j}}{V_{\mathrm{b}}^{j}} \cdot S_{\mathrm{b}}^{j} \tag{D.31}$$

Where S_{b}^{j} is the surface area of a single bubble in the half-cell j and is given from equation (D.32).

$$S_{\mathrm{b}}^{j} = \pi \cdot \left(d_{\mathrm{b}}^{j}\right)^{2} \tag{D.32}$$

For the calculation of the mass transfer coefficient $k_{\mathrm{L},i}^{j}$ and the implementation of the Sherwood empirical correlations, it is required the density of the liquid electrolyte ρ_{L} which is given in $\mathrm{kg\,m^{-3}}$ from the paper of Gilliam et al. [57], as a function of the operating temperature and KOH mass fraction in wt%. Furthermore, it is required the dynamic viscosity of liquid electrolyte, μ_{L}, which is obtained from Ref. [34] and is calculated in $\mathrm{Pa\,s}$.

The model that simulates the dynamic switching of electrolyte cycles runs for the operating conditions of the experiment [40]. More specifically, the applied current density equals $J = 1\ \mathrm{kA\,m^{-2}}$, the applied temperature is $T = 80\ ^{\circ}\mathrm{C}$, the applied pressure is $p^{\mathrm{ano}} = p^{\mathrm{cat}} = 1\ \mathrm{bar}$, the liquid volumetric flow rate is $\dot{V}_{\mathrm{L}}^{\mathrm{ano}} = \dot{V}_{\mathrm{L}}^{\mathrm{cat}} = 0.33\ \mathrm{L\,min^{-1}}$, and the KOH mass fraction of the liquid electrolyte is $w_{\mathrm{KOH}} = 32\ \mathrm{wt\%}$. The calculated properties for the operating conditions of the model are shown in Table D.2. The design characteristics of the electrolysis plant are summarized in Table.

Finally, the ordinary differential equations are solved by implementing the odeint function from the SciPy package [69]. The scipy.integrate.odeint function is a numerical solver for first order ordinary differential equations which implements LSODA from the FORTRAN library. The LSODA is a backward or forward multistep method that automatically selects the solver and the timestep that is implemented, depending on the stability of the problem. The solution requires the assignment of initial conditions. The initial condition given to the set of ordinary differential equations is the zero value at $t = 0$ for every unknown term of the ordinary differential equations. This typically means that the the alkaline water electrolyser is inactive when it starts up.

D.3. Results

In the following, the validation of the dynamic switching model with the experimental results of Haug et al. [40] is shown. Furthermore, a sensitivity analysis is conducted to test the validity of the dynamic model in terms of the operating conditions and the design characteristics of the plant.

D.3.1. Validation of the dynamic switching model

The validity of the model that describes the dynamic switching of electrolyte cycles is tested for the experimental results which are published by Haug et al. [40]. The input properties for the operating conditions of the experimental dynamic switching of electrolyte cycles are listed in Table D.2. The design characteristics of the electrolysis cell are given in Table D.3.

In Figure D.4, the validation of the model that describes the dynamic switching of electrolyte cycles with the experimental data of Haug et al. [40] is presented. On the

vertical axis of the graph, the anodic hydrogen content is shown in vol%. Similarly, on the horizontal axis, the time is displayed, in h. The black circles show the experimental results found in Ref. [40]. The solid black line shows the prediction of the anodic hydrogen content as a function of time from the developed dynamic model. The grey dashed line shows the average anodic hydrogen content from the modeling results, when the dynamic switching starts.

In the beginning of the experiment, when $2\ \mathrm{h} \leq t_{\mathrm{tot}} \leq 3\ \mathrm{h}$, the system operates in mixed-mode until it reaches its steady state in terms of the anodic hydrogen content. When $3\ \mathrm{h} < t_{\mathrm{tot}} \leq 3.5\ \mathrm{h}$, the dynamic switching starts by importing into the model the boundary conditions of the partly-separated mode. The boundary conditions of the partly-separated mode are given by equation (D.19). Instantly, there is a drop in the anodic hydrogen content. From the material balances, and the boundary conditions, the gas crossover in the partly-separated mode occurs only due to diffusion through the diaphragm. The partly-separated mode lasts for 30 min. Therefore, when $t_{\mathrm{tot}} = 3.5\ \mathrm{h}$, the boundary conditions of the mixed-mode are imported into the dynamic model. As a result, the anodic hydrogen content starts increasing due to electrolyte mixing before the entrance of the electrolysis cell. The continuous switching between the mixed-mode and the partly-separated mode takes place every 30 min, until $t_{\mathrm{tot}} = 6.5\ \mathrm{h}$. At this point, the mixed-mode boundary conditions are imported into the model, and the system approaches its steady-state anodic hydrogen content until $t_{\mathrm{tot}} = 8\ \mathrm{h}$.

In the beginning, the model approaches successfully the experimental steady-state anodic hydrogen content until $t_{\mathrm{tot}} = 3\ \mathrm{h}$. When the dynamic switching starts, the H_2 in O_2 impurity decreases because of the activation of the partly-separated mode. The model follows the fall successfully. When $t_{\mathrm{tot}} = 3.5,\ 4.5,\ 5.5,\ 6.5\ \mathrm{h}$, the model predicts a slightly lower anodic hydrogen content in the end of the partly-separated mode. Furthermore, the maximum H_2 in O_2 content matches the experimental results, when $t_{\mathrm{tot}} = 4,\ 5,\ 6\ \mathrm{h}$. When the system operates for the last time in mixed-mode and approaches its steady-state, at $6.5\ \mathrm{h} \leq t_{\mathrm{tot}} \leq 8\ \mathrm{h}$, the model predicts a higher impurity in comparison with the experimental results. The underestimation of the anodic hydrogen content can be due to a large concentration gradient through the diaphragm. Due to the CSTR model and the uniform concentration throughout the half-cell the model cannot capture phenomena of local supersaturation. Finally, in Ref. [40] it is reported that the average anodic hydrogen content during the dynamic switching of electrolyte cycles equals $y_{\mathrm{H_2}}^{\mathrm{avg}} = 0.306\ \mathrm{vol\%}$. The average anodic hydrogen content predicted from the model equals $y_{\mathrm{H_2}}^{\mathrm{avg,mod}} = 0.295\ \mathrm{vol\%}$.

Overall, the dynamic model sufficiently validates the experimental results in Ref.[40] and adapts to the sinusoidal trend during the dynamic switching of electrolyte cycles. The average anodic hydrogen content, which is calculated by the model, slightly deviates from the experimental average value . Despite the lower anodic hydrogen content which is predicted from the model when switching occurs from the partly-separated to the mixed mode, the results from the model and the experiment are in good agreement.

D.3.2. Sensitivity analysis

In the following, a sensitivity analysis for the dynamic model is provided. The boundary conditions of the dynamic model correspond to the operation in mixed mode. The sensitivity analysis is materialized with varying the operating conditions of the system and its design characteristics. The design characteristics include the variation of the volume in the gas separators and the diaphragm. The operating conditions include the variation of the liquid volumetric flow rate, the liquid and gaseous volume in the gas separators, the temperature in the system and the KOH mass fraction. The models with the varying input parameters are compared to the default model. The input parameters of the default model are listed in Table D.4.

Variation of the operating conditions

In Figure D.5, the sensitivity analysis due to the variation of the operating conditions is presented. More specifically, the varying operating conditions include the liquid flow rate $\dot{V}_{\mathrm{L}}$ (Figure D.5a), the temperature T of the process (Figure D.5b), the mass fraction of KOH w_{KOH} (Figure D.5c), and the liquid $V_{\mathrm{liq}}^{\mathrm{sep},j}$ and gaseous volume in the gas separator $V_{\mathrm{gas}}^{\mathrm{sep},j}$ (Figure D.5d). The dynamic model simulates the operation of an alkaline water electrolyser in mixed mode. As a result, the mixed boundary conditions are given. The models with the varying operating conditions are compared with the default model (black dashed line).

In Figure D.5a, the variation of the liquid flow rate is presented. It can be observed that an increase in the liquid flow rate results in a rise of the steady-state H_2 in O_2 impurity. This trend can be attributed to the electrolyte mixing gas crossover mechanism. More specifically, an increase in the liquid flow rate leads to a higher convective mass transfer from the mass balance equations. Therefore, more dissolved cathodic hydrogen ends up in the anodic compartment. The bulk concentration of hydrogen in the anodic half-cell increases as the liquid flow rate rises. As a result, the desorption flux is governed by higher supersaturation, and hence more hydrogen will outgas in the anodic compartment. Similarly, as the liquid flow rate decreases, the anodic hydrogen content reduces. The transition time to the steady-state, does not seem to be affected from the variation of liquid flow rate.

In Figure D.5b, the variation of the temperature is presented. An increase in the temperature results in a lower steady-state H_2 in O_2 impurity. The solubility data which are imported in the model by implementing the Setchenov relation, indicate that an increase in the temperature slightly reduces the solubility of hydrogen and oxygen in the liquid electrolyte [61]. Therefore, in higher temperatures, the dissolved hydrogen species experiences a higher degree of supersaturation than in lower temperatures and can outgas more efficiently. At the same time, the diffusivity data which are imported in the model indicate that an increase in the temperature results in a higher hydrogen and oxygen diffusivity [58]. Therefore, the hydrogen and oxygen species experience a higher rate of diffusion, which is a fundamental property for the calculation of the mass transfer coefficient in the electrolyte bulk. The combined reduction in the solubility and the rise in diffusivity lead to a higher desorptive flux in the electrolyte bulk. As a result, the gas crossover due to the electrolyte mixing reduces and the dissolved species outgas more efficiently in the compartment in which they are generated. Similarly, the opposite holds true when the temperature is reduced. Finally,

the variation of the temperature does not affect the transition time to the steady state.

In Figure D.5c, the sensitivity analysis for the variation of the KOH mass fraction is shown. It can be observed that an increase in the KOH mass fraction leads to a decrease in the anodic hydrogen content. The decrease of the H_2 in O_2 impurity can be explained from the imported solubility literature data. An examination of the imported data reveals that an increase in the KOH mass fraction results in the fall of the solubility of hydrogen and oxygen species due to the salting out effect [61]. As a result, the dissolved species in the electrolyte bulk, achieve a higher degree of supersaturation with an increasing KOH mass fraction. Due to the higher degree of supersaturation, the desorptive flux in the electrolyte bulk also increases and a higher amount of pure hydrogen or oxygen is released in the compartment in which they are produced. As a result the H_2 in O_2 impurity decreases with an increasing KOH mass fraction. The KOH mass fraction does not affect the transition time to the steady-state impurity.

In Figure D.5d, the variation of the liquid and gaseous volume in the gas separators is presented. The total volume of the separator tank is kept constant. The liquid volume is expressed as a percentage of the total geometrical volume of the gas separator. In Figure D.5d, it can be noticed that a decrease in the liquid volume of the gas separator results in a faster system response. The response of the system in terms of the anodic hydrogen content presents a dependency on the gaseous volumetric flow rate. A decrease in the liquid volume means that gas separator consists of more gaseous product and the bulk concentration of the dissolved species develops faster to its steady state. Due to the quick response of the bulk concentration, the desorption flux in the single cell will follow a similar trend. Therefore, the anodic volumetric flow rate develops faster as the liquid volume of the gas separator decreases. Subsequently, the anodic hydrogen content reaches its steady state faster. On the contrary, when the liquid volume of the gas separator increases, the gaseous flow rate develops slower. At the same time, the partial pressure increases fast. Hence, the response of the anodic hydrogen content does not slow down significantly. For this reason, when the liquid volume increases, the anodic hydrogen content does not show a significant difference with the case where V_liq_sep=50%. Finally, all the models conclude in the same steady-state anodic hydrogen content.

Overall, the variation of the operating conditions in the dynamic model results in a realistic behavior during the alkaline water electrolysis. Finally, it has to be noted that the dynamic material balances strongly depend on the input properties, such as the diffusivity and the solubility. Therefore, the input properties need to be selected carefully.

Variation of the design characteristics

In Figure D.6, the sensitivity analysis for the design characteristics is shown. The design characteristics consist of the porous diaphragms, and the geometrical volume of the gas separators. The dynamic model simulates the transition to the steady state in mixed mode, and hence the mixed boundary conditions are imported. The varied dynamic models are compared with the default model (black dashed line).

In Figure D.6a, the effect of Type A and Zirfon diaphragm in the anodic hydrogen content is compared. The Type A diaphragm is 500 μm thick, has a porosity of $\varepsilon = 35\ \%$ and the tortuosity equals $\tau = 1.95$. The design characteristics of the Zirfon

diaphragm are shown in Table D.2. From the modeling results, it can be observed that the selection of alternative porous diaphragm has a negligible effect on the variation of the H_2 in O_2 impurity. The negligible effect on the anodic hydrogen content can be justified from the definition of the hydrogen gas evolution efficiency in this model. The hydrogen gas evolution is fitted to the experimental H_2 in O_2 and O_2 in H_2 impurities [34]. The measured impurities are the result of the gas crossover mechanisms due to the diffusion through the diaphragm, and the electrolyte mixing. Therefore, the gas evolution efficiency acts as a lumped parameter which includes both of these gas crossover mechanisms. The CSTR assumption cancels out the existence of any local supersatution phenomena close to the electrode area which may result in a larger diffusion through the diaphragm. Finally, in an attempt to quantify the effect of gas crossover flux through the diaphragm, the anodic hydrogen content is evaluated for the dynamic model in the partly-separated mode. When the model reaches its steady state, the results indicate that for the Zirfon separator the H_2 in O_2 impurity equals to $y_{\mathrm{H_2}}^{\mathrm{Zirfon}} = 0.0103\ \mathrm{vol\%}$ and for the Type A it is equal to $y_{\mathrm{H_2}}^{\mathrm{TypeA}} = 0.0088\ \mathrm{vol\%}$. Therefore, the maximum calculated contribution of the gas crossover through the diaphragm is negligible in comparison with the electrolyte mixing, which is above 1% according to Figure D.6a.

In Figure D.6b, the effect of the variation of the geometrical volume of the gas separators is studied. The liquid volume of the electrolyte in the gas separator is 50% of the geometrical volume of the separator tank. It is noticed that an increase in the geometrical volume results in a slower transition to the steady-state. The enlargement of the geometrical volume of the gas separator leads to an increase of both the liquid and gaseous volume inside the gas separator. Therefore, it causes a slower response in the dissolved species in the liquid electrolyte and a slower response in the outlet partial pressures of the species in the gas separator. This observation can be justified from equations (D.7)-(D.8). Furthermore, the transition time of the anodic hydrogen content presents a strong dependency on the gaseous volumetric flow rate. Since the response time of the bulk concentration increases with the enlargement of the separator tank, the gaseous volumetric flow rate will evolve slower. Therefore, when the volume of the separator tank increases, the H_2 in O_2 impurity reaches its steady state slower. On the contrary, when the volume of the gas separators decreases, the anodic hydrogen content will evolve faster to its steady state because the bulk concentration and the partial pressures in the gas separator develop faster. Finally, in the extreme case where the geometrical volume of the gas separator is oversized (V_GS=32L), the system will need even more time to reach its steady state.

Overall, the model is not sensitive to different diaphragms. The possible overestimation of the hydrogen gas evolution efficiency in combination with the negligence of local supersaturation in the electrode area, results in a significantly underestimated diffusion flux through the separator. Thus, the modeled anodic hydrogen content is not affected by the change of diaphragms.

Finally, the dynamic model can calculate the system response, in terms of the anodic hydrogen content, by taking into account the geometrical volume of the gas separators. In the steady-state model, the effect of the gas separators is neglected because the accumulation terms are zero. It is found that the geometrical volume of the gas separators can substantially influence the transition time to the steady-state

gas impurity.

D.4. Conclusions

The outcome of this paper gives a better understanding on the dynamic model. Overall, the conclusions are summarized below:

1. The dynamic model validates the dynamic switching of electrolyte cycles by changing the boundary conditions as a function of time. As a result, it acquires a sinusoidal behavior similar to the trend of the experimental data. The value of the average calculated anodic hydrogen content ($y_{\mathrm{H_2}}^{\mathrm{avg,mod}} = 0.295$ vol%) is close to the experimental ($y_{\mathrm{H_2}}^{\mathrm{avg}} = 0.306$ vol%).

2. When the dynamic model operates in a partly-separated mode, it cannot calculate phenomena of local supersaturation close to the diaphragm, due to the CSTR assumption. As a result, it underestimates the anodic hydrogen content.

3. Overall, the variation of the operating conditions shows that the model is robust and has a realistic behavior.

4. In the dynamic model, the transition time to the steady state depends on the geometrical volume of the separator tank, the volume of the half-cell, and the liquid volume ratio in the gas separator. The rest of the input properties do not affect the response of the system.

5. In the mixed-mode operation, the steady-state anodic hydrogen content is not affected by the diaphragm change. This happens because the gas evolution efficiency acts as a lumped parameter that includes the crossover through the diaphragm and the electrolyte mixing.

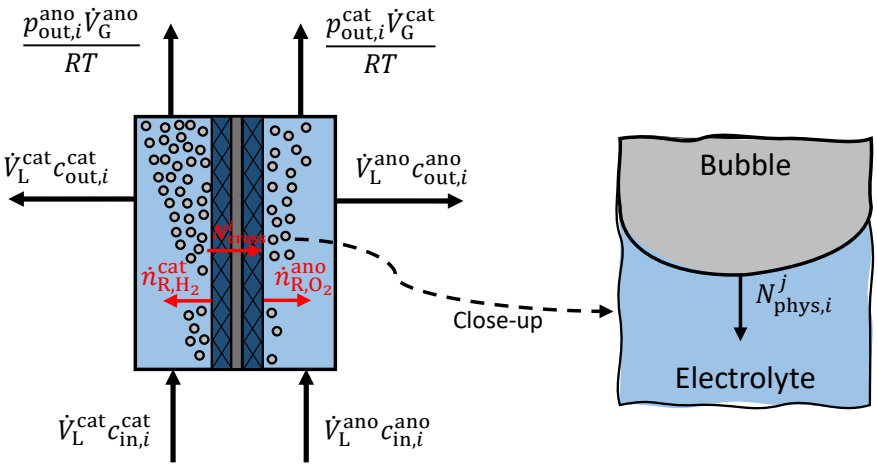

Figure D.1: The mass balance in the single cell. The reaction rate $\dot{n}^{j}_{\text{R},i}$ obeys Faraday's law. Only liquid stream with dissolved molecules enters the cell $\dot{V}^{j}_{\text{L}}c^{j}_{\text{in},i}$. The stream which exits the cell consists of the liquid electrolyte with the dissolved species $\dot{V}^{j}_{\text{L}}c^{j}_{\text{out},i}$, and the gaseous phase which obeys ideal gas law $\frac{p^{j}_{\text{out},i}\dot{V}^{j}_{\text{G}}}{R\,T}$. The mass transfer in the electrolyte bulk is governed by a desorption flux $N^{j}_{\text{phys},i}$. In the electrolysis cell, cross-permeation in the opposite half cell occurs due to diffusion through the diaphragm N^{i}_{cross}

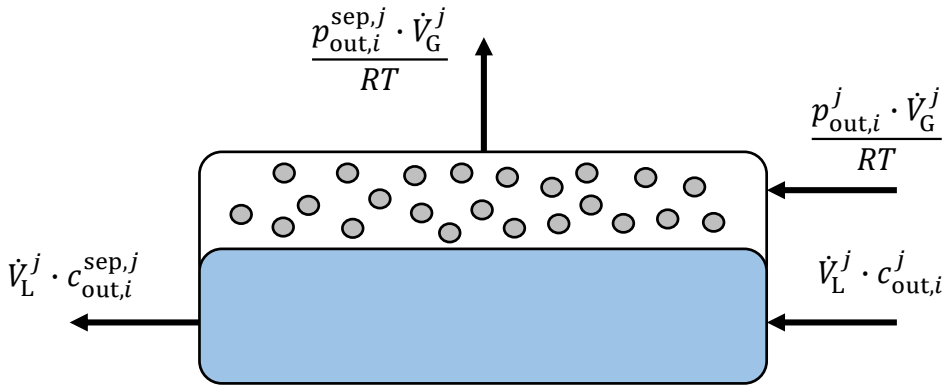

Figure D.2: The mass balance in the gas separator. The liquid stream with the dissolved species i that exits the electrolysis cell j, $\dot{V}_{\mathrm{L}}^{j} c_{\mathrm{out},i}^{j}$, now enters its corresponding gas separator. The gaseous stream of species i that exits the compartment j, $\frac{p_{\mathrm{out},i}^{j} \dot{V}_{\mathrm{G}}^{j}}{R\,T}$, now enters the gas separator. The produced gas is collected at the exit of the gas separator $\frac{p_{\mathrm{out},i}^{\mathrm{sep},j} \dot{V}_{\mathrm{G}}^{j}}{R\,T}$. The liquid stream that exits the gas separator $\dot{V}_{\mathrm{L}}^{j} c_{\mathrm{out},i}^{\mathrm{sep},j}$, is recirculated.

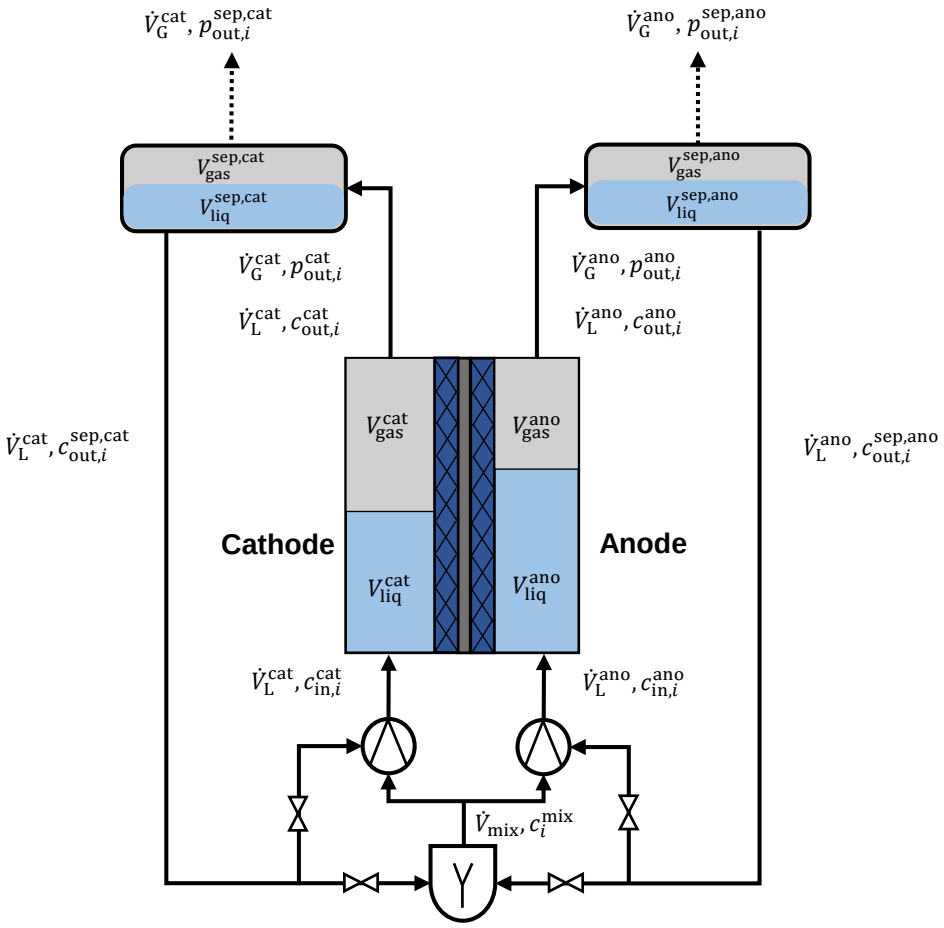

Figure D.3: The simplified process flow diagram. The liquid and gaseous flow rates that enter and exit the system, are denoted with their corresponding concentration and partial pressure. The liquid and gaseous volumes that are used in the material balances, are shown with different colors (turquoise and grey).

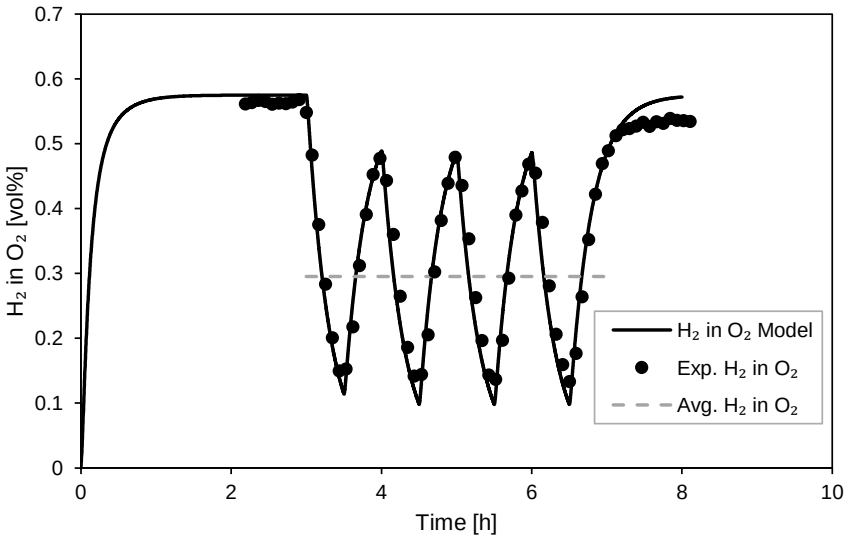

Figure D.4: Validation of the dynamic switching model with the experimental results of Haug et al.[40].

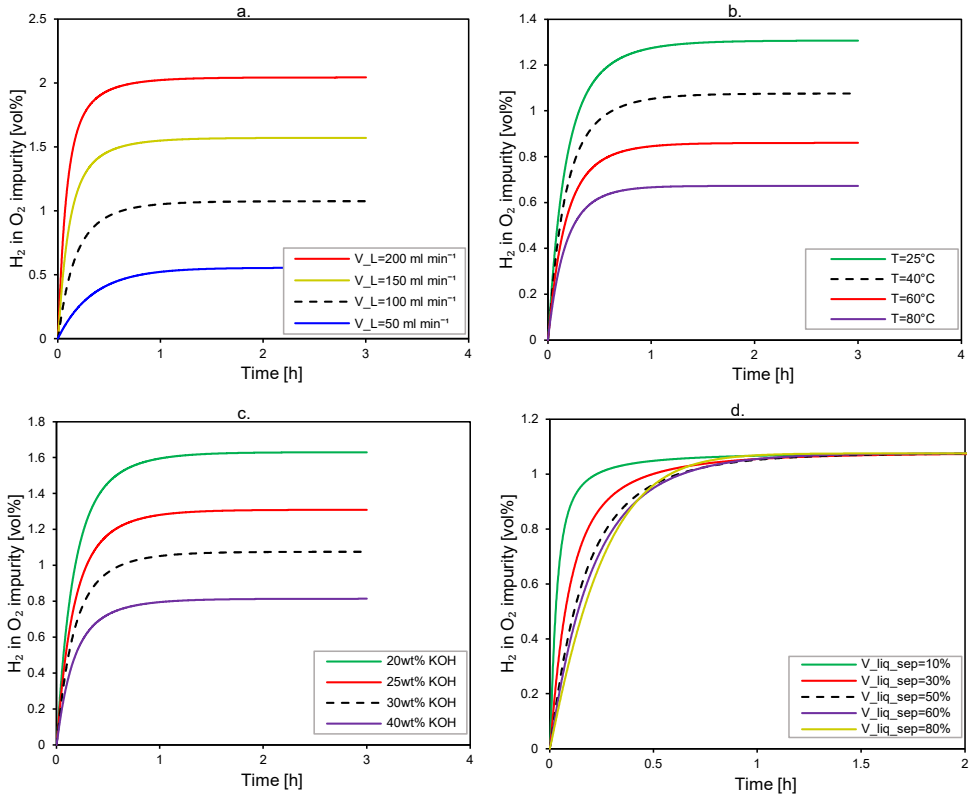

Figure D.5: Variation of the operating conditions: (a) Liquid flow rate. (b) Temperature. (c) KOH wt%. (d) Liquid and gaseous volume in the gas separator

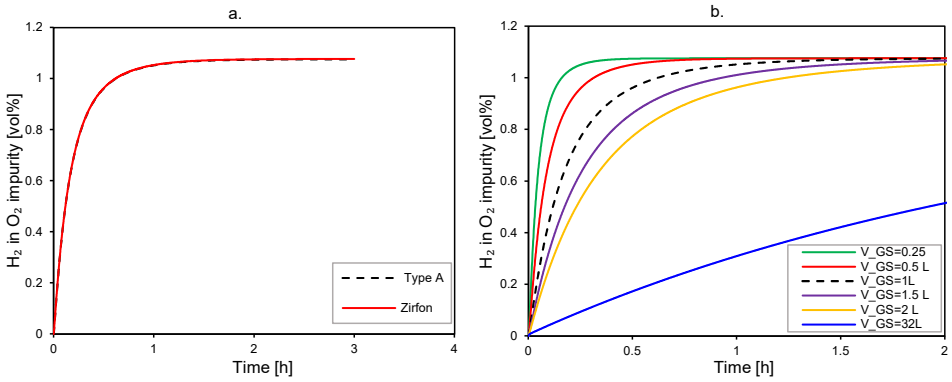

Figure D.6: Variation of the design characteristics: (a) Porous diaphragm. (b) Geometrical volume of the gas separators.

Table D.1: Mathematical expression for the gas hold-up fraction according to Haug et al.[34].

Compartment	X_1	X_2	X_3
Anode	0.59438	0.59231	0.75647
Cathode	0.76764	0.73233	0.73457

Table D.2: The input model properties for the dynamic switching of electrolyte cycles at $T = 80\ ^{\circ}\mathrm{C}$, $p^{\mathrm{ano}} = p^{\mathrm{cat}} = 1\ \mathrm{bar}$, $J = 1\ \mathrm{kA\ m^{-2}}$ and w_{KOH}=0.32.

Property	Value	Units	Reference
γ	0.08267	$\mathrm{N\,m^{-1}}$	[56]
$f_{\mathrm{G,H_2}}$	0.68	-	[34]
$f_{\mathrm{G,O_2}}$	1	-	[34]
$p_{\mathrm{H_2O}}$	27583.85058	Pa	[34]
$d_{\mathrm{b}}^{\mathrm{cat}}$	0.000157	m	[34]
$A_{\mathrm{GL}}^{\mathrm{ano}}$	2.95850	$\mathrm{m^2}$	[34]
$A_{\mathrm{GL}}^{\mathrm{cat}}$	2.97927	$\mathrm{m^2}$	[34]
$\varepsilon_{\mathrm{g,out}}^{\mathrm{ano}}$	0.14631	-	[34]
$\varepsilon_{\mathrm{g,out}}^{\mathrm{cat}}$	0.22969	-	[34]
$D_{\mathrm{H_2},\theta=80}$	$5.58823 \cdot 10^{-9}$	$\mathrm{m^2\,s^{-1}}$	[58]
$D_{\mathrm{O_2},\theta=80}$	$1.68098 \cdot 10^{-9}$	$\mathrm{m^2\,s^{-1}}$	[58]
μ_{L}	0.00087	Pa s	[34]
ρ_{L}	1276.48135	$\mathrm{kg\,m^{-3}}$	[57]
$\rho_{\mathrm{H_2O}}$	971.79778	$\mathrm{kg\,m^{-3}}$	[71]
$H_{\mathrm{H_2}}$	71661.82123	atm	[59]
$H_{\mathrm{O_2}}$	69577.49411	atm	[59]
$K_{\mathrm{S,H_2}}$	3.14	-	[34]
$K_{\mathrm{S,O_2}}$	3.96	-	[34]
$k_{\mathrm{L,H_2}}^{\mathrm{ano}}$	0.00042	$\mathrm{m\,s^{-1}}$	[34]
$k_{\mathrm{L,H_2}}^{\mathrm{cat}}$	0.00033	$\mathrm{m\,s^{-1}}$	[34]
$k_{\mathrm{L,O_2}}^{\mathrm{ano}}$	0.00020	$\mathrm{m\,s^{-1}}$	[34]
$k_{\mathrm{L,O_2}}^{\mathrm{cat}}$	0.00016	$\mathrm{m\,s^{-1}}$	[34]

Table D.3: Design characteristics of the experimental electrolysis setup of Haug et al. [40].

Property	Symbol	Value	Units
Electrode area	A_{el}	150	cm^2
Diaphragm area	A_{d}	232	cm^2
Diaphragm thickness	d_{d}	500	$\mu\mathrm{m}$
Diaphragm porosity	ε	0.55	-
Diaphragm tortuosity	τ	3.14	-
Half-cell volume	V_{hcell}	0.16x0.015x0.145	m^3
Liquid volume in the gas separator j	$V_{\mathrm{liq}}^{\mathrm{sep},j}$	1.2	L
Liquid volume in the anodic half-cell	$V_{\mathrm{liq}}^{\mathrm{ano}}$	$29.86916 \cdot 10^{-5}$	m^3
Liquid volume in the cathodic half-cell	$V_{\mathrm{liq}}^{\mathrm{cat}}$	$26.96877 \cdot 10^{-5}$	m^3
Gaseous volume in the anodic the gas separator	$V_{\mathrm{gas}}^{\mathrm{sep,ano}}$	1.55	L
Gaseous volume in the cathodic the gas separator	$V_{\mathrm{gas}}^{\mathrm{sep,cat}}$	1.52	L
Gaseous volume in the anodic half-cell	$V_{\mathrm{gas}}^{\mathrm{ano}}$	$4.93083 \cdot 10^{-5}$	m^3
Gaseous volume in the cathodic half-cell	$V_{\mathrm{gas}}^{\mathrm{cat}}$	$7.83122 \cdot 10^{-5}$	m^3

Table D.4: Input parameters of the default model.

Variable	Symbol	Value	Units
KOH mass fraction	w_{KOH}	30	$\mathrm{wt\%}$
Liquid flow rate	$\dot{V}_{\mathrm{L}}$	100	$\mathrm{mL\ min^{-1}}$
Operating temperature	T	313.15	K
Operating pressure in the compartment j	p^j	101325	Pa
Current density	J	1	$\mathrm{kA\ m^{-2}}$
Anodic gas separator volume	$V_{\mathrm{sep}}^{\mathrm{ano}}$	1	L
Cathodic gas separator volume	$V_{\mathrm{sep}}^{\mathrm{cat}}$	1	L
Liquid volume in the anodic gas separator	$V_{\mathrm{liq}}^{\mathrm{sep,ano}}$	0.5	L
Liquid volume in the cathodic gas separator	$V_{\mathrm{liq}}^{\mathrm{sep,cat}}$	0.5	L
Hydrogen gas evolution efficiency	$f_{\mathrm{G,H_2}}$	0.875	-
Oxygen gas evolution efficiency	$f_{\mathrm{G,O_2}}$	0.830	-

Bibliography

[1] Kemal Dervis. “Climate Change Threatens the Development Gains Already Achieved”. In: (). URL: https://www.uncclearn.org/wp-content/uploads/library/undp30.pdf (visited on 03/02/2022).

[2] Samer Fawzy et al. *Strategies for mitigation of climate change: a review*. May 2020. DOI: 10.1007/s10311-020-01059-w.

[3] Xi Liu YUE and Qing Xian GAO. “Contributions of natural systems and human activity to greenhouse gas emissions”. In: *Advances in Climate Change Research* 9.4 (May 2018), pp. 243–252. ISSN: 16749278. DOI: 10.1016/j.accre.2018.12.003.

[4] EDGAR - Emissions Database for Global Atmospheric Research. *Greenhouse Gases Emissions and Climate*. URL: https://edgar.jrc.ec.europa.eu/climate_change (visited on 05/02/2022).

[5] Unfccc. *ADOPTION OF THE PARIS AGREEMENT - Paris Agreement text English*. URL: https://unfccc.int/sites/default/files/english_paris_agreement.pdf (visited on 05/02/2022).

[6] EUROPEAN COMMISSION. *The European Green Deal*. Dec. 2019. URL: https://eur-lex.europa.eu/legal-content/EN/TXT/HTML/?uri=CELEX:52019DC0640&from=EN (visited on 02/07/2022).

[7] Government of the Netherlands. *Dutch goals within the EU*. URL: https://www.government.nl/topics/climate-change/eu-policy (visited on 07/02/2022).

[8] Climate Agreement Progress Council. *Climate Agreement*. June 2019. URL: https://www.klimaatakkoord.nl/documenten/publicaties/2019/06/28/national-climate-agreement-the-netherlands (visited on 07/02/2022).

[9] *Government Strategy on Hydrogen*. Apr. 2020. URL: https://www.government.nl/documents/publications/2020/04/06/government-strategy-on-hydrogen (visited on 10/02/2022).

[10] COMMITTEE and THE COMMITTEE OF THE REGIONS. *A hydrogen strategy for a climate-neutral Europe*. July 2020. URL: https://eur-lex.europa.eu/legal-content/EN/TXT/HTML/?uri=CELEX:52020DC0301&from=EN (visited on 11/02/2022).

[11] International Renewable Energy Agency. *Green hydrogen: A guide to policy making*. 2020. ISBN: 978-92-9260-286-4. URL: www.irena.org.

[12] Geert Tjarks, Jürgen Mergel, and Detlef Stolten. *Dynamic Operation of Electrolyzers - Systems Design and Operating Strategies*. May 2016. DOI: 10.1002/9783527674268.ch14.

[13] Office of Energy Efficiency and Renewable Energy. *Hydrogen: Similar but Different*. URL: https://www1.eere.energy.gov/hydrogenandfuelcells/pdfs/h2_safety_fsheet.pdf (visited on 11/02/2022).

[14] ISO 22734:2019. *Hydrogen generators using water electrolysis — Industrial, commercial, and residential applications*. Tech. rep. Geneva: International Organization of Standarization, Sept. 2019. URL: https://www.iso.org/standard/69212.html.

[15] S Trasatti. “Water electrolysis: who first?” In: *Journal of Electroanalytical Chemistry* 476.1 (Oct. 1999), pp. 90–91. ISSN: 15726657. DOI: 10.1016/S0022-0728(99)00364-2.

[16] Maximilian Schalenbach, Wiebke Lueke, and Detlef Stolten. “Hydrogen Diffusivity and Electrolyte Permeability of the Zirfon PERL Separator for Alkaline Water Electrolysis”. In: *Journal of The Electrochemical Society* 163.14 (2016), F1480–F1488. ISSN: 0013-4651. DOI: 10.1149/2.1251613jes.

[17] Agfa. *Technical Data Sheet, ZIRFON PERL UTP 500*. Sept. 2020. URL: https://www.agfa.com/specialty-products/wp-content/uploads/sites/8/2020/06/TDS_ZIRFON_PERL_UTP_500_20200525.pdf.

[18] Robert Phillips and Charles W Dunnill. *Zero gap alkaline electrolysis cell design for renewable energy storage as hydrogen gas*. 2016. DOI: 10.1039/c6ra22242k.

[19] Steven G Bratsch. “Standard Electrode Potentials and Temperature Coefficients in Water at 298.15 K”. In: *Journal of Physical and Chemical Reference Data* 18.1 (1989), pp. 1–21. ISSN: 15297845. DOI: 10.1063/1.555839.

[20] Maximilian Schalenbach et al. “Acidic or Alkaline? Towards a New Perspective on the Efficiency of Water Electrolysis”. In: *Journal of The Electrochemical Society* 163.11 (2016), F3197–F3208. ISSN: 0013-4651. DOI: 10.1149/2.0271611jes.

[21] Marcelo Carmo et al. *A comprehensive review on PEM water electrolysis*. May 2013. DOI: 10.1016/j.ijhydene.2013.01.151.

[22] Immanuel Vincent and Dmitri Bessarabov. *Low cost hydrogen production by anion exchange membrane electrolysis: A review*. May 2018. DOI: 10.1016/j.rser.2017.05.258.

[23] Hiroyuki Yanagi and Kenji Fukuta. “Anion Exchange Membrane and Ionomer for Alkaline Membrane Fuel Cells (AMFCs)”. In: *ECS Transactions* 16.2 (Oct. 2008), pp. 257–262. DOI: 10.1149/1.2981860.

[24] Enapter. *Bringing AEM Electrolysers to the World*. URL: https://www.enapter.com/ (visited on 10/08/2022).

[25] Lei Bi, Samir Boulfrad, and Enrico Traversa. *Steam electrolysis by solid oxide electrolysis cells (SOECs) with proton-conducting oxides*. May 2014. DOI: 10.1039/c4cs00194j.

[26] Mikkel Rykær Kraglund et al. “Zero-Gap Alkaline Water Electrolysis Using Ion-Solvating Polymer Electrolyte Membranes at Reduced KOH Concentrations”. In: *Journal of The Electrochemical Society* 163.11 (2016), F3125–F3131. ISSN: 0013-4651. DOI: 10.1149/2.0161611jes.

[27] Press Conference. *TOTALENERGIES, SUNFIRE AND FRAUNHOFER GIVE THE GO-AHEAD FOR GREEN METHANOL IN LEUNA*. May 2021. URL: https://www.sunfire.de/en/news/detail/totalenergies-sunfire-and-fraunhofer-give-the-go-ahead-for-green-methanol-in-leuna (visited on 03/04/2022).

[28] A Hauch et al. “Recent advances in solid oxide cell technology for electrolysis”. In: *Science* 370.6513 (May 2020). ISSN: 0036-8075. DOI: 10.1126/science.aba6118.

[29] Helmut Vogt et al. “Electrochemical Reactors”. In: *Ullmann’s Encyclopedia of Industrial Chemistry*. Weinheim, Germany: Wiley-VCH Verlag GmbH & Co. KGaA, Jan. 2014, pp. 1–49. DOI: 10.1002/14356007.l09_l01.pub2.

[30] H Vogt. “The rate of gas evolution of electrodes—I. An estimate of the efficiency of gas evolution from the supersaturation of electrolyte adjacent to a gas-evolving electrode”. In: *Electrochimica Acta* 29.2 (May 1984), pp. 167–173. ISSN: 00134686. DOI: 10.1016/0013-4686(84)87043-7.

[31] H Vogt. “The role of single-phase free convection in mass transfer at gas evolving electrodes—I. Theoretical”. In: *Electrochimica Acta* 38.10 (May 1993), pp. 1421–1426. ISSN: 00134686. DOI: 10.1016/0013-4686(93)80079-F.

[32] H Vogt. “On the gas-evolution efficiency of electrodes i - Theoretical”. In: *Electrochimica Acta* 56.3 (May 2011), pp. 1409–1416. ISSN: 00134686. DOI: 10.1016/j.electacta.2010.08.101.

[33] H Vogt. “Studies on gas-evolving electrodes: The concentration of dissolved gas in electrolyte bulk”. In: *Electrochimica Acta* 30.2 (May 1985), pp. 265–270. ISSN: 00134686. DOI: 10.1016/0013-4686(85)80092-X.

[34] Philipp Haug et al. “Process modelling of an alkaline water electrolyzer”. In: *International Journal of Hydrogen Energy* 42.24 (June 2017), pp. 15689–15707. ISSN: 03603199. DOI: 10.1016/j.ijhydene.2017.05.031.

[35] André B. de Haan, H. Burak Eral, and Boelo Schuur. “Chapter 4. General Design of Gas/Liquid Contactors”. In: *Industrial Separation Processes*. De Gruyter, July 2020, pp. 81–116. DOI: 10.1515/9783110654806-004.

[36] Helmut Vogt. “Gas-Evolving Electrodes”. In: *Comprehensive Treatise of Electrochemistry*. Boston, MA: Springer US, 1983, pp. 445–489. DOI: 10.1007/978-1-4615-6690-8_7.

[37] H. Brauer and H. Thiele. “Bewegung von Partikelschwärmen”. In: *Chemie Ingenieur Technik* 45.13 (July 1973), pp. 909–912. ISSN: 0009286X. DOI: 10.1002/cite.330451317.

[38] H. Brauer and D. Mewes. “Strömungswiderstand sowie stationärer Stoff- und Wärmeübergang an Blasen und Tropfen”. In: *Chemie Ingenieur Technik - CIT* 44.15 (Aug. 1972), pp. 953–956. ISSN: 0009-286X. DOI: 10.1002/cite.330441513.

[39] Jean St-Pierre, Normand Massé, and Mario Bergeron. “Dissolved oxygen concentration in a divided rotating cylinder electrode reactor”. In: *Electrochimica Acta* 40.8 (May 1995), pp. 1013–1024. ISSN: 00134686. DOI: 10.1016/0013-4686(94)00337-Z.

[40] Philipp Haug, Matthias Koj, and Thomas Turek. “Influence of process conditions on gas purity in alkaline water electrolysis”. In: *International Journal of Hydrogen Energy* 42.15 (May 2017), pp. 9406–9418. ISSN: 03603199. DOI: 10.1016/j.ijhydene.2016.12.111.

[41] P Trinke et al. “Hydrogen Crossover in PEM and Alkaline Water Electrolysis: Mechanisms, Direct Comparison and Mitigation Strategies”. In: *Journal of The Electrochemical Society* 165.7 (May 2018), F502–F513. ISSN: 0013-4651. DOI: 10.1149/2.0541807jes.

[42] Hae In Lee et al. “The synthesis of a Zirfon□type porous separator with reduced gas crossover for alkaline electrolyzer”. In: *International Journal of Energy Research* 44.3 (May 2020), pp. 1875–1885. ISSN: 0363-907X. DOI: 10.1002/er.5038.

[43] CHEMSAFE. *A Database for Safety Characteristic Data*. URL: https://dechema.de/en/chemsafe.html (visited on 12/09/2022).

[44] Volkmar Schröder. *Explosionsgrenzen von Wasserstoff und Wasserstoff/Methan-Gemischen*. Tech. rep. Bremerhaven, 2003, pp. 1–40. URL: https://nbn-resolving.org/urn:nbn:de:kobv:b43-1987.

[45] S A Grigoriev et al. “Hydrogen safety aspects related to high-pressure polymer electrolyte membrane water electrolysis”. In: *International Journal of Hydrogen Energy* 34.14 (2009), pp. 5986–5991. ISSN: 03603199. DOI: 10.1016/j.ijhydene.2009.01.047.

[46] Maximilian Schalenbach and Detlef Stolten. “High-pressure water electrolysis: Electrochemical mitigation of product gas crossover”. In: *Electrochimica Acta* 156 (May 2015), pp. 321–327. ISSN: 00134686. DOI: 10.1016/j.electacta.2015.01.010.

[47] C A Schug. “Operational characteristics of high-pressure, high-efficiency water-hydrogen-electrolysis”. In: *International Journal of Hydrogen Energy* 23.12 (May 1998), pp. 1113–1120. ISSN: 03603199. DOI: 10.1016/S0360-3199(97)00139-0.

[48] Iystein Ulleberg. *Modeling of advanced alkaline electrolyzers: a system simulation approach*. 2003. URL: www.elsevier.com/locate/ijhydene.

[49] Mitja Mori et al. “Integral Characteristics of Hydrogen Production in Alkaline Electrolysers”. In: *Strojniški vestnik – Journal of Mechanical Engineering* 10.59 (May 2013), pp. 585–594. ISSN: 00392480. DOI: 10.5545/sv-jme.2012.858.

[50] Ankica Đukić and Mihajlo Firak. “Hydrogen production using alkaline electrolyzer and photovoltaic (PV) module”. In: *International Journal of Hydrogen Energy* 36.13 (May 2011), pp. 7799–7806. ISSN: 03603199. DOI: 10.1016/j.ijhydene.2011.01.180.

[51] Ernesto Amores, Jesús Rodríguez, and Christian Carreras. “Influence of operation parameters in the modeling of alkaline water electrolyzers for hydrogen production”. In: *International Journal of Hydrogen Energy* 39.25 (May 2014), pp. 13063–13078. ISSN: 03603199. DOI: 10.1016/j.ijhydene.2014.07.001.

[52] Jaeseung Lee et al. “Modeling of gas evolution processes in porous electrodes of zero-gap alkaline water electrolysis cells”. In: *Fuel* 315 (May 2022), p. 123273. ISSN: 00162361. DOI: 10.1016/j.fuel.2022.123273.

[53] R Smith. *Chemical Process: Design and Integration*. Wiley, 2005. ISBN: 9780470011911. URL: https://books.google.nl/books?id=cdyiWR0d1o8C.

[54] Rodney L. LeRoy, Christopher T. Bowen, and Donald J. LeRoy. “The Thermodynamics of Aqueous Water Electrolysis”. In: *Journal of The Electrochemical Society* 127.9 (Sept. 1980), pp. 1954–1962. ISSN: 0013-4651. DOI: 10.1149/1.2130044.

[55] J BALEJ. “Water vapour partial pressures and water activities in potassium and sodium hydroxide solutions over wide concentration and temperature ranges”. In: *International Journal of Hydrogen Energy* 10.4 (1985), pp. 233–243. ISSN: 03603199. DOI: 10.1016/0360-3199(85)90093-X.

[56] K. Feldkamp. “Die Oberflächenspannung wäßriger NaOH- und KOH-Lösungen”. In: *Chemie Ingenieur Technik - CIT* 41.21 (Nov. 1969), pp. 1181–1183. ISSN: 0009-286X. DOI: 10.1002/cite.330412107.

[57] R GILLIAM et al. “A review of specific conductivities of potassium hydroxide solutions for various concentrations and temperatures”. In: *International Journal of Hydrogen Energy* 32.3 (Mar. 2007), pp. 359–364. ISSN: 03603199. DOI: 10.1016/j.ijhydene.2006.10.062.

[58] Min J. Tham, Robert Dixon Walker, and Keith E. Gubbins. “Diffusion of oxygen and hydrogen in aqueous potassium hydroxide solutions”. In: *The Journal of Physical Chemistry* 74.8 (Apr. 1970), pp. 1747–1751. ISSN: 0022-3654. DOI: 10.1021/j100703a015.

[59] D. M. Himmelblau. “Solubilities of Inert Gases in Water. 0° C. to Near the Critical Point of Water.” In: *Journal of Chemical & Engineering Data* 5.1 (Jan. 1960), pp. 10–15. ISSN: 0021-9568. DOI: 10.1021/je60005a003.

[60] R. Sander. “Compilation of Henry’s law constants (version 4.0) for water as solvent”. In: *Atmospheric Chemistry and Physics* 15.8 (Apr. 2015), pp. 4399–4981. ISSN: 1680-7324. DOI: 10.5194/acp-15-4399-2015.

[61] Jr. Walker R. D. *A study of gas solubilities and transport properties in fuel cell electrolytes*. Tech. rep. Florida Univ. Gainesville, FL, United States, Feb. 1968. URL: https://ntrs.nasa.gov/citations/19690031817.

[62] M. B. Knaster and L.A. Apel'baum. *Solubility of hydrogen and oxygen in concentrated potassium hydroxide solution*. Tech. rep. Russian J. Phys. Chem., 1964, pp. 38–120.

[63] Geffcken. "Solubility of hydrogen in potassium hydroxide". In: *G.Z.Phys.Chem* 49 (1904), pp. 257–302.

[64] K. Scott. "Membranes and separators for microbial fuel cells". In: *Microbial Electrochemical and Fuel Cells*. Elsevier, 2016, pp. 153–178. DOI: 10.1016/B978-1-78242-375-1.00005-8.

[65] Michael J. Martínez-Rodríguez et al. "Characterization of Microporous Layer in Carbon Paper GDL for PEM Fuel Cell". In: *ECS Transactions* 33.1 (Oct. 2010), pp. 1133–1141. ISSN: 1938-5862. DOI: 10.1149/1.3484607.

[66] R. B. MacMullin and G. A. Muccini. "Characteristics of porous beds and structures". In: *AIChE Journal* 2.3 (Sept. 1956), pp. 393–403. ISSN: 0001-1541. DOI: 10.1002/aic.690020320.

[67] L. Pisani. "Simple Expression for the Tortuosity of Porous Media". In: *Transport in Porous Media* 88.2 (June 2011), pp. 193–203. ISSN: 0169-3913. DOI: 10.1007/s11242-011-9734-9.

[68] SciPy Optimization and root finding. *scipy.optimize.minimize*. URL: https://docs.scipy.org/doc/scipy/reference/generated/scipy.optimize.minimize.html.

[69] SciPy Integration and ODEs. *scipy.integrate.odeint*. July 2022. URL: https://docs.scipy.org/doc/scipy/reference/generated/scipy.integrate.odeint.html#scipy-integrate-odeint.

[70] H. Vogt. "The rate of gas evolution at electrodes—II. An estimate of the efficiency of gas evolution on the basis of bubble growth data". In: *Electrochimica Acta* 29.2 (Feb. 1984), pp. 175–180. ISSN: 00134686. DOI: 10.1016/0013-4686(84)87044-9.

[71] George S. Kell. "Density, thermal expansivity, and compressibility of liquid water from 0.deg. to 150.deg.. Correlations and tables for atmospheric pressure and saturation reviewed and expressed on 1968 temperature scale". In: *Journal of Chemical & Engineering Data* 20.1 (Jan. 1975), pp. 97–105. ISSN: 0021-9568. DOI: 10.1021/je60064a005.

[72] Mónica Sánchez et al. "Semi-empirical model and experimental validation for the performance evaluation of a 15 kW alkaline water electrolyzer". In: *International Journal of Hydrogen Energy* 43.45 (Nov. 2018), pp. 20332–20345. ISSN: 03603199. DOI: 10.1016/j.ijhydene.2018.09.029.

[73] Georgios Sakas et al. "Dynamic energy and mass balance model for an industrial alkaline water electrolyzer plant process". In: *International Journal of Hydrogen Energy* 47.7 (Jan. 2022), pp. 4328–4345. ISSN: 03603199. DOI: 10.1016/j.ijhydene.2021.11.126.

[74] Matheus T. de Groot, Joost Kraakman, and Rodrigo Lira Garcia Barros. “Optimal operating parameters for advanced alkaline water electrolysis”. In: *International Journal of Hydrogen Energy* (Sept. 2022). ISSN: 03603199. DOI: 10.1016/j.ijhydene.2022.08.075.

[75] H. Vogt. “Mechanisms of mass transfer of dissolved gas from a gas-evolving electrode and their effect on mass transfer coefficient and concentration overpotential”. In: *Journal of Applied Electrochemistry* 19.5 (Sept. 1989), pp. 713–719. ISSN: 0021-891X. DOI: 10.1007/BF01320646.

[76] E.A. Guggenheim. “Interfacial tension of curved interface”. In: *Thermodynamics: An Advanced Treatment for Chemists and Physicists*. 7th ed. Amsterdam, North-Holland: Elsevier, 1985. Chap. 1, pp. 50–53. ISBN: 0444869514.